Migration radiale dans les disques galactiques et applications à la Voie Lactée

Maxime Kubryk

UPMC
SORBONNE UNIVERSITÉS

THÈSE DE DOCTORAT DE
l'UNIVERSITÉ PIERRE ET MARIE CURIE

Spécialité

Astrophysique

École doctorale Astronomie et Astrophysique d'île-de-france (ED127)

Présentée par

Maxime KUBRYK

Pour obtenir le grade de

DOCTEUR de l'UNIVERSITÉ PIERRE ET MARIE CURIE

Sujet de la thèse :

Migration radiale des étoiles dans les disques galactiques et applications à la Voie Lactée

soutenue le 9 septembre 2014

devant le jury composé de :

M. Nikos PRANTZOS	Directeur de thèse
Mme. Lia ATHANASSOULA	Directrice de thèse
M. Benoît SEMELIN	Président du jury
Mme. Cristina CHIAPPINI	Rapporteur
M. Benoît FAMAEY	Rapporteur
M. François HAMMER	Membre du jury

À mes parents

Remerciements

Tout d'abord, je tiens à remercier chaleureusement mes directeurs de thèse, Nicolas Prantzos et Lia Athanassoula, pour tout le temps qu'ils m'ont consacré, pour leur aide précieuse, et parce qu'ils ont été pour moi de très bons encadrants, à la fois patients, sympathiques, et scientifiquement exigeants.

Je remercie aussi les membres du jury et les rapporteurs pour la relecture du manuscrit et ...(à complèter)

Je remercie également les autres chercheurs du troisième étage, pour la bonne humeur qu'ils apportent à ce coin légèrement isolé de l'IAP... Je remercie Robert Mochkovitch et Frédéric Daigne, pour les expériences de coucher de soleil en aquarium, et les balles rebondissantes dans le couloir ; ainsi qu'Elisabeth Vangioni, qui a de nombreuses fois partager avec nous des chocolats, ou autres friandises !

Je remercie également mes co-bureau, Hélène Dupuy pour sa gentillesse et sa bonne humeur, et Pierre Fleury, pour son entrain, son humour, les passages entiers de Kaamelott récités par coeur, et pour ses imitations d'accents un peu hasardeuses... Je remercie également les autres thésards de l'IAP, avec lesquels les conversations du midi ou du café finissent toujours par s'aventurer sur des terrains surprenants, que ce soit vers les problèmes scientifiques les plus complexes, ou comment élever des girafes naines sur Mars !

Et je remercie également l'IAP, son personnel compétant et d'une grande aide, et ses deux directeurs successifs : Laurent Vigroux, et Francis Bernardeau. Ainsi que le LAM à Marseille, et Jean-Charles Lambert, qui a élaboré des outils numériques qui m'ont été d'une aide précieuse.

Un grand merci à l'ensemble de mes amis, évidemment je ne pourrai pas citer tout le monde... Je remercie notamment Ronan Capron, Sébastien Péray, Johann Buch, et Serge Demoulin pour leurs encouragements et les moments passés ensemble. J'espère que les liens que nous avons créés résisteront au temps et aux distances !

J'adresse un grand merci à Sophie Félix, pour sa joie de vivre, son affection, son réconfort dans les moments difficiles, et aussi sa patience, sa force, parce que partager la vie d'un thésard n'est pas toujours facile !

Enfin, je remercie tous les membres de ma famille ! En particulier ma mère Marie-Hélène Trichard, parce qu'elle a toujours cru en moi, m'a encouragé et soutenu en toute occasion, et parce qu'elle a su comment me guider dans cette passion pour les étoiles, qui me tient depuis tout petit. Je remercie également mon père Gérard Kubryk, pour ses encouragements,

pour les discussions que nous avons, et pour avoir soutenu ma passion en me conseillant de nombreuses lectures. Je remercie mon oncle, pour son regard particulier sur les phénomènes physiques obscurs auxquels je me suis intéressé. Je me souviens en particulier des ondes d'Alfven et des chocs-C, qui l'ont beaucoup fait rire ! Et mon cousin, pour tout ce que nous avons partagé, et parce qu'il m'a fait découvrir la guitare il y a environ 15 ans, ce qui aujourd'hui me permet de me changer les idées quand j'en ai besoin. Et enfin, je remercie mon grand père, Maurice Trichard, parce qu'il a été le premier à me parler des étoiles et des constellations, un soir d'été quand je devais avoir six ou sept ans !

Paris, 9 Septembre 2014 Maxime Kubryk

Résumé

Nous étudions la migration radiale des étoiles, et testons son impact sur l'évolution chimique de la Voie Lactée. Pour cela nous utilisons une simulation N-corps+SPH (Gadget-3) de galaxie fortement barrée, afin d'étudier la migration radiale induite par la barre. Nous examinons un nouveau mécanisme de migration radiale : une fraction des étoiles piégées à la corotation de la barre, se déplacent avec le rayon de corotation lorsque celui-ci va vers l'extérieur (quand la vitesse de rotation de la barre diminue, du fait de son évolution séculaire). Nous montrons que ce mécanisme affecte principalement les régions externes du disque, à condition que la corotation atteigne ces régions. Nous montrons également que ce mécanisme n'a pas d'effets dans la Voie Lactée, car les estimations observationnelles des caractéristiques de la barre, indiquent que la corotation est loin des zones externes. Nous analysons également la migration radiale dans cette simulation, afin de construire un modèle empirique de diffusion stellaire dans le disque, et nous incluons ce modèle dans un code semi-analytique d'évolution chimique de galaxie. Nous testons la validité de cette approche en vérifiant que les galaxies simulées N-corps+SPH et semi-analytique ont des propriétés morphologiques et chimiques similaires. Nous appliquons ensuite notre modèle à la Voie Lactée, en adaptant les paramètres du modèle. Puis, nous comparons les résultats obtenus avec un grand nombre d'observations concernant le voisinage solaire (relation âge-métallicité, distribution de métallicité, relation α/Fe vs Fe/H et la bimodalité disque mince - disque épais) , et les gradients radiaux d'abondance.

Mots clefs : migration radiale, évolution galactique, Voie Lactée, abondances chimique, milieux interstellaire, modélisation

Table des matières

1 Introduction

Les galaxies se forment à partir à partir de la matière noire, et des du gaz primordial formé après le Big Big, qui contient essentiellement de l'hydrogène, un peu d'hélium, et des traces d'éléments légers. Ce gaz primordial tombe en s'enroulant dans les halos de matière noire, se refroidit par viscosité et rayonnement thermique, et ainsi forme des disques de gaz dans les halos. Le gaz est alors soit de l'hydrogène atomique, soit de l'hydrogène moléculaire H_2. Les premières étoiles se forment par effondrements gravitationnels locaux du gaz. À partir d'environ 1 milliard d'années après le Big Bang, les premières galaxies sont formées, et elles évolueront jusqu'à aujourd'hui en continuant à accréter du gaz primordial, et en fusionnant entre elles pour former des galaxies de plus en plus massives, et de formes variées.

En fonction de leur histoire, les galaxies peuvent alors prendre des formes variées. Les observations de galaxies ont amené Edwin Hubble à construire le premier système de classement des galaxies selon leurs morphologies : la séquence de Hubble (Fig. 1.1). Dans la partie gauche de cette séquence on trouve les galaxies elliptiques E, classées de 0 à 5 selon leur ellipticité. Et dans la partie droite de la séquence, on trouve les galaxies spirales, séparées en deux branches selon la présence ou non d'une barre en leur centre, notées SB et S respectivement. Les spirales sont classées de a à d selon la morphologie des spirales. La Fig. 1.1, illustre la séquence de Hubble avec des galaxies réelles.

À l'origine, ce classement était aussi censé décrire les différentes étapes de l'évolution morphologique des galaxies : partant des galaxies elliptiques considérées comme primitives, qui évoluaient ensuite en galaxies disques. Aujourd'hui, la théorie de l'évolution des galaxies indique que cette évolution n'est pas valide, et que la séquence de Hubble doit se lire dans le sens inverse : les galaxies primitives sont des disques, qui évoluent en galaxies disques, soit par des processus internes aux galaxies qui sont encore mal connus, soit par fusion entre galaxies disques de tailles comparables (on parle alors de fusion majeure, par opposition aux fusions mineures qui impliquent un rapport de masse inférieur à ~0.1).

Les galaxies elliptiques sont généralement très pauvres en gaz, et ne forment pratiquement plus d'étoiles. Leur évolution ne se fait plus que part interaction, voire, par fusion avec d'autres

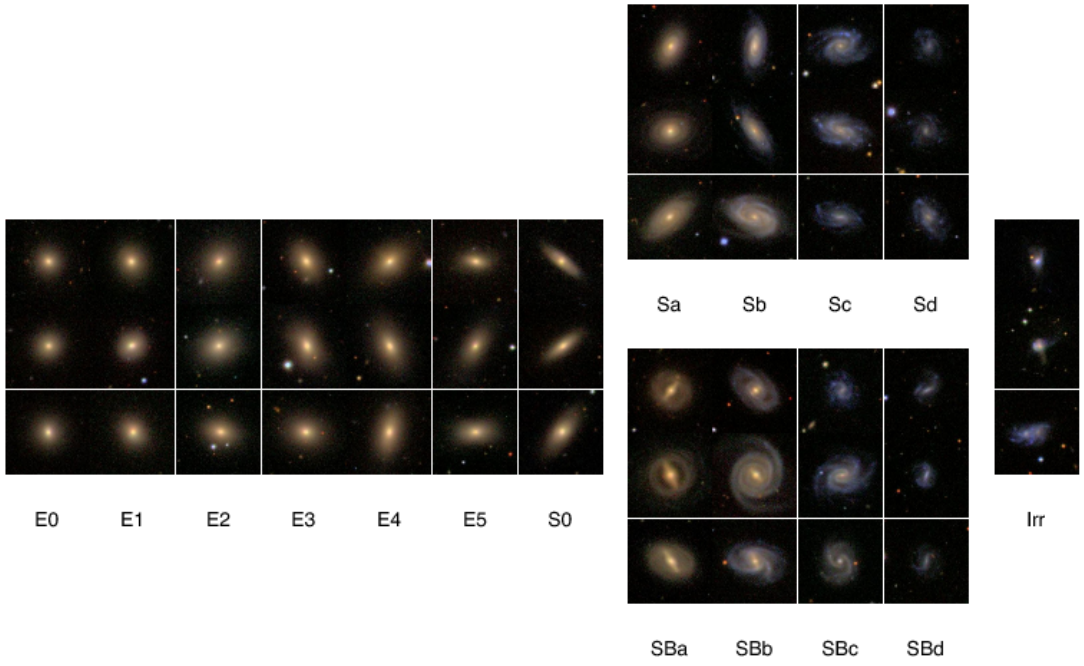

FIGURE 1.1 – Illustration de la séquence de Hubble avec des observations de galaxies réelles. la catégorie "Irr" représente les galaxies irrégulières, qui ne rentrent pas dans la séquence de Hubble.

galaxies. Dans ces galaxies le mouvement des étoiles est principalement radial. À l'inverse, les galaxies disques sont souvent riches en gaz, et ont alors des taux de formation stellaire plus importants. L'évolution de ces galaxies peut se faire par des processus externes (accrétion de gaz, interaction avec des galaxies voisines ou satellites, fusion de galaxies) ; mais aussi par des processus internes, liés au fait qu'un disque d'étoiles est hors de l'équilibre thermodynamique, et va alors former spontanément des structures comme une barre ou des spirales, pour tendre vers l'équilibre (voir Sec. 2.3).

La formation des galaxies est encore mal connue aujourd'hui. La théorie est testée grâce à des simulations N-corps+gaz. Une simulation N-corps+gaz, est constitué d'une partie N-corps, qui résout les équations de la gravitation pour une quantité N d'objets ponctuels, représentant des ensembles d'étoiles, et les particules de matière noire ; et d'une partie permettant de résoudre les équations de l'hydrodynamique du gaz. Ces deux partie sont couplées grâce à la formation stellaire, et aux interactions gravitationnelles entre le gaz et les objets ponctuels. Les codes les plus connus permettant de réaliser ce genre de simulation sont *Gadget* (Springel, Yoshida & White, 2001; Springel, 2005) et *Ramses* (Teyssier, 2002). Ces deux codes, utilisent un algorithme d'optimisation "en arbre" pour le calcul de la partie N-corps, permettant de ne pas calculer pour chaque particule la force gravitationnelle exercée par chacune des autres particules. Concernant la partie hydrodynamique, Gadget utilise un schéma de résolution

SPH (Smothed Particles Hydrodynamics) (Lucy, 1977; Gingold & Monaghan, 1977). Dans ce formalisme le gaz est représenté par des particules "étalées" par un algorithme de lissage. Le code Ramses, quant à lui, utilise un schéma AMR (Adaptive Mesh Refinement), consistant en une résolution Eulérienne avec une grille adaptative. Récemment, le schéma AREPO (Springel, 2010) a été développé pour traiter également l'hydrodynamique avec un schéma AMR dans les simulations Gadget.

Ces codes servent notamment à produire des simulations cosmologiques, reproduisant l'évolution d'un cube d'Univers selon le modèle ΛCDM, depuis l'âge sombre (avant la formation des premières étoiles et galaxies), jusqu'à aujourd'hui. Citons, par exemple, la simulation *Millenium* (Lemson & Virgo Consortium, 2006) (basée sur une version modifiée de *GADGET-2*), dont l'étude montre notamment que le nombre de fusions majeures donnant des galaxies elliptiques n'est pas assez élevé dans la simulation pour reproduire le pourcentage de ces galaxies dans les observations. Ce qui indique que l'évolution des disques en ellipses se fait grâce à des processus internes et également que la croissance des galaxies se fait majoritairement par accrétion du gaz environnant (Genel et al., 2008). La simulation DEUS, est un exemple plus récent de simulation cosmologique (Alimi et al., 2012), utilisant le code Ramses.

Les simulations "zoom" consistant à re-simuler, avec une plus grande résolution, des petites parties de simulations cosmologiques permettent d'étudier plus précisément la formation des disques galactiques (Navarro & White, 1993; Springel, 2000; Semelin & Combes, 2005). Ces simulations ont mis évidence la nécessité de processus de "feedback" de la formation stellaire et des noyaux actifs de galaxies, pour former des disques galactiques ayant des propriétés conformes aux observations (e.g. échelle radiale, fraction de gaz, taux de formation stellaire, etc). Le feedback stellaire décrit l'effet rétroactif de la formation stellaire sur le gaz du milieu interstellaire. En effet, les étoiles renvoient du gaz chaud dans le milieu interstellaire sous forme de vents stellaires ou bien lors de leur explosion en supernovae (pour les étoiles suffisamment massives), les explosions de supernovae créent également des turbulences dans le gaz. Le feedback des noyaux actifs de galaxies, est créé par l'interaction du trou noir super-massif en leur centre, avec le gaz du disque galactique. Les modèles (Springel, Di Matteo & Hernquist, 2005; Booth & Schaye, 2009; Teyssier et al., 2011) montrent que l'accrétion de gaz interstellaire par le trou noir crée une émission de radiation intense, qui réchauffe le gaz du disque galactique.

Les phénomènes de feedback transmettent donc de l'énergie au gaz interstellaire, le chauffent, ce qui régule la formation de nouvelles étoiles, car plus le gaz est chaud moins il est instable gravitationnellement i.e. moins il forme d'étoiles. Sans ces mécanismes, le gaz se refroidit trop rapidement, forme beaucoup d'étoiles dans les premiers milliards d'années de l'existence des galaxies. Les galaxies sont alors vidées de leur gaz, et ne pouvant pratiquement plus former de nouvelles étoiles, sont composées essentiellement d'étoiles très âgées.

Le simulations ont également permis de montrer que l'évolution des galaxies est très sensible au feedback, ce qui pose problème dans la mesure où les phénomènes de rétroaction sont

encore très mal connus et donc difficiles à modéliser proprement.

Pour tester les phénomènes d'évolution internes des disques galactiques dans un environnement plus contrôlé, on utilise des simulations N-corps+gaz de disques isolés, en contrôlant avec précision l'état initial du disque. Ces simulations permettent en particulier de tester la dynamique des étoiles dans les galaxies, et les phénomènes d'évolution séculaire, comme nous le verrons dans la partie 2.

Concernant l'évolution chimique des galaxies, des progrès considérables ont été réalisés grâce à des modèles semi-analytiques "classiques" (modèles en anneaux indépendants, i.e. sans migration radiale), qui consistent à résoudre les équations de l'évolution chimique détaillée. Ces modèles ont permis d'interpréter la grande quantité d'observations concernant les abondances du gaz et des étoiles dans le halo, le bulbe et le disque de la Voie Lactée et les galaxies externes. Ces dernières années, des travaux ont été menés sur ces modèles pour les augmenter grâce à des prescriptions de migration radiale, pour étudier les effets du couplage entre la migration et l'évolution chimique, nous aborderons ce sujet en partie 3. Notons toutefois que les simulations N-corps+gaz de disques galactiques sont en nette progression concernant l'évolution chimique, en incluant de plus en plus d'éléments chimiques, mais ne permettent toujours pas d'inclure des phénomènes comme l'accrétion de gaz intergalactique, qui a pourtant une grande influence sur la composition chimique du milieu interstellaire.

les modèles les plus performants sont les modèles semi-analytiques, qui , couplées à des équations décrivant l'évolution dynamique des étoiles, et du gaz interstellaire. Nous aborderons ce sujet en partie 3.

Comme nous venons de la voir, il reste encore beaucoup de phénomènes à comprendre pour réussir à modéliser correctement la formation des galaxies. Dans ce cadre, la galaxie dans laquelle nous vivons, la Voie Lactée, nous sert de laboratoire pour tester les modèles d'évolution galactique. En effet, puisque nous sommes dans cette galaxie, nous pouvons l'observer avec plus de détails que les galaxies extérieures. D'où l'importance des observations et des études de la Voie Lactée. Dans la Fig. 1.2, nous montrons une carte de la Voie Lactée, comme si nous la voyions de l'extérieur. Sur cette carte, on voit les deux bras spiraux majeures, les bras spiraux plus faibles, la barre/bulbe centrale, et la position du Soleil qui est à environ 8 kpc du centre de la Galaxie, entre les deux bras majeurs.

La Voie Lactée est un système chimiquement inhomogène dont les composantes principales sont (avec les données sur la morphologies issues de Jurić et al. (2008)) :

- Le halo de matière noire, constitué d'une matière encore inconnue aujourd'hui, a une masse estimée de $\sim 10^{12}$ $M_\odot$.
- Le bulbe/barre a une masse de $\sim 1.5 \times 10^{10} M_\odot$ (majoritairement des étoiles), qui représente environ 25% de la masse stellaire totale de la Voie Lactée. Le rayon de la barre est estimé à environ 2.5-3 kpc. Cette région est constituée majoritairement d'étoiles vieilles, dont la métallicité peut atteindre 3 $Z_\odot$ (avec $Z_\odot$ la métallicité solaire).

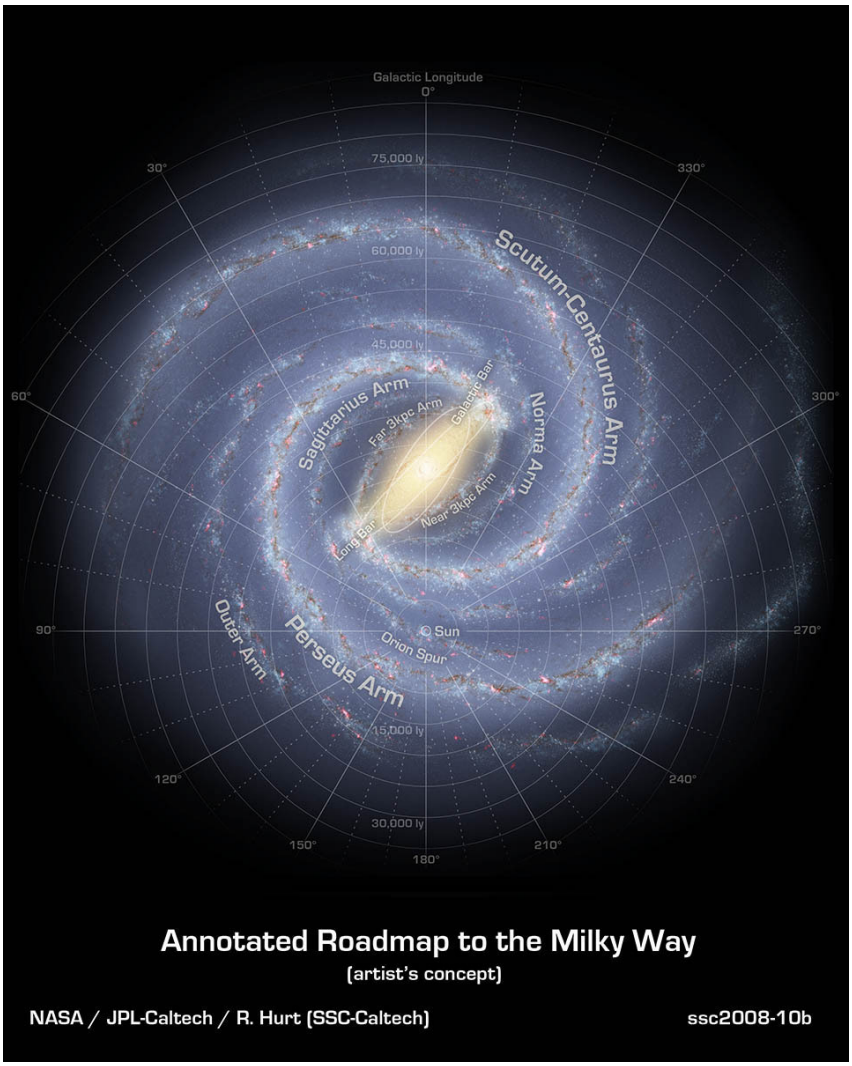

FIGURE 1.2 – Vue d'artiste de la Voie Lactée observée de l'extérieur, à partir d'observations infra-rouges du disque par le satellite Spitzer. Les bras majeurs et mineurs sont indiqués, ainsi que la position de la barre. Le repère est centré sur le Soleil et les distances sont indiquées en années-lumières. (Source : NASA, Spitzer Space Telescope)

- Le disque mince a une masse totale de $\sim 3 \times 10^{10} M_{\odot}$, il est la composante la plus massive de la galaxie, pour ce qui est de la matière baryonique. Son profil radial de densité surfacique d'étoiles décroit exponentiellement avec une échelle de 2600±520 pc : $\Sigma_{thin} = \rho_{0,\odot} e^{-\frac{R-R_{\odot}}{2600}}$. Ce profil est valable jusqu'à un rayon d'environ 30 kpc. Son profil vertical de densité volumique d'étoiles décroit exponentiellement avec une échelle de hauteur de 300±60 pc au voisinage solaire. Il est composé d'étoiles d'âges divers, allant environ de 10 à 0 Gyr, et ces étoiles ont des métallicités très variées en fonction de leur position radiale, avec des métallicité décroissantes en fonction du rayon. Sa métallicité moyenne est $[Fe/H] \sim -0.1$. C'est dans le disque mince que les étoiles se forment, à partir du gaz moléculaire H_2.
- Le disque épais, quant à lui, a une masse de ~20% celle du disque mince. Sa vitesse de rotation autour du centre galactique est plus faible que celle du disque mince (50 à 100 km/s de moins). Il est constitué de vieilles étoiles (~ 10 Gyr) de métallicité plutôt faible ([Fe/H]~ −0.7). Son échelle de hauteur est de 900±180 pc au voisinage solaire, et son échelle radiale est de 3600±720 pc.
- Le gaz a une masse de $\sim 5 \times 10^{9} M_{\odot}$, il est en rotation autour du centre et est confiné prés du plan Galactique. La majorité de ce gaz est de l'hydrogène atomique neutre HI (~ 80%). Les 20% restant sont sous forme de gaz moléculaire essentiellement, et une très faible proportion est sous forme de gaz ionisé. La densité de HI est presque constante entre 4 et 17 kpc. Hors de cet intervalle, sa densité décroit rapidement. Au voisinage solaire, il a une échelle de hauteur de ~ 150 pc. Quant au gaz moléculaire, il est concentré sur un anneau de densité maximale au rayon ~ 4.5 kpc, et hors de se rayon sa densité décroit suivant une gaussienne de largeur à mi-hauteur ~ 2 kpc. Au voisinage solaire, ce gaz a une échelle de hauteur de ~ 60 pc.
- Le halo stellaire est la composante galactique la moins massive, sa masse vaut 3% de la masse du bulbe, mais c'est la composante baryonique la plus étendue : il peut atteindre un rayon de 40 kpc. Il est constitué d'étoiles vieilles (>10 Gyr), et pauvres en métaux([Fe/H]~-1.5).

L'étude des galaxies, et notamment de la Voie Lactée, à la fois par les observations et par les simulations N-corps+gaz ou semi-analytiques, est d'une grande importance pour notre compréhension de l'Univers, car leur formation et évolution fait appel à de nombreux phénomènes physiques, allant de l'échelle atomique (pour la nucléosynthèse au cœur des étoiles) jusqu'à l'échelle cosmologique (formation des galaxies, interactions avec leur environnement, etc). Par ailleurs les différents phénomènes en jeux sont souvent couplés entre eux. Les galaxies sont donc au croisement de divers domaines de l'astrophysique.

Ainsi, l'observation des galaxies, permet de retracer leur histoire via des traceurs chimiques ou morphologique (nous y reviendrons en partie 3 au sujet de la Voie Lactée), on parle d'archéologie galactique. Dans ce cadre, la migration radiale des étoiles, un phénomène dont l'importance avait été négligée jusqu'aux années 2000, apparaît comme un processus potentiellement clé, car le mélange des étoiles pourrait affecter une grande partie des traceurs

TABLE 1.1 – Propriété des populations stellaires des disque mince et épais[a].

			Mince	Épais
Densité volumique	$\rho_{0,\odot}$	($M_\odot$ pc^{-3})	4.5 10^{-2}	5.3 10^{-3}
Densité surfacique	$\Sigma_\odot$	($M_\odot$ pc^{-2})	28.5	7
Échelle de hauteur	$H_\odot$	(pc)	300	900
Échelle de longueur	$L_\odot$	(pc)	2600	3600
Masse en étoiles	M_D	(10^{10} $M_\odot$)	2.3	0.53
$\langle$Age$\rangle_\odot$	$\langle$A$\rangle_\odot$	(Gyr)	5	10
$\langle$Metallicite$\rangle_\odot$	$\langle$[Fe/H]$\rangle_\odot$	(dex)	-0.1	-0.7

a : L'indice $\odot$ indique ici des quantitées mesurées au rayon Galactique $R_\odot$=8 kpc. Les quantités moyennes sont indiquées par $\langle\ \rangle$.

utilisés pour étudier l'évolution des galaxies.

La partie 2, sera consacrée à la dynamique de la migration radiale des étoiles. Nous verrons d'abord des résultats analytiques sur les orbites stellaires, mettant en évidence l'origine de la migration radiale : l'interaction des étoiles avec les structures non-axisymétriques du disque (barre, spirales). Dans cette partie nous rappellerons également le processus de formation et d'évolution de la barre centrale et des spirales, nous montrerons que ces structures évoluent avec le temps, et que les outils analytiques ne sont plus suffisants pour étudier la migration radiale dans les disques qui se modifient avec le temps. Nous poursuivrons par un rappel des connaissances sur la migration radiale dans les potentiels gravitationnels variables avec le temps, ce qui nous amènera aux travaux que j'ai effectué sur la dynamique de la migration radiale pendant ma thèse. Les résultats de ces travaux sont regroupés dans un article donné à la fin de cette partie.

La partie 3 sera consacrée à l'étude des effets de la migration radiale des étoiles sur l'évolution chimique des disques et en particulier celle de la Voie Lactée. Cette étude sera basée sur l'analyse d'une simulation N-corps+gaz, et sur l'utilisation de modèles semi-analytiques d'évolution galactique. Nous commencerons par un rappel des travaux déjà effectués sur l'évolution des galaxies, incluant les effets de la migration radiale. Ensuite, nous verrons que la migration radiale peut être modélisée comme un processus de diffusion des étoiles dans les disques, et ainsi être incluse dans les modèles semi-analytiques. Puis, nous discuterons des travaux déjà réalisés dans ce domaine. Nous expliciterons comment la diffusion stellaire est modélisée dans ces travaux, ce qui nous amènera à présenter la méthode que nous avons développée pour construire un modèle de diffusion stellaire plus réaliste basé sur l'analyse d'une simulation N-corps+SPH. Cette méthode est explicitée dans un article publié dans MNRAS. Enfin, nous appliquerons notre modèle d'évolution galactique avec migration radiale à la Voie Lactée, et comparerons les résultats obtenus avec un grand nombre d'observations concernant le voisinage solaire, les disques minces et épais, et les profils d'abondances chimiques. Ces

résultats sont rassemblés dans deux articles soumis à A&A.

2 Éléments de dynamique

Dans ce chapitre nous allons rappeler les différents éléments de la dynamique galactique, qui amènent au phénomène de migration radiale des étoiles dans les disques, ainsi que les courants de gaz interstellaire. Nous allons donc commencer par décrire les orbites des étoiles dans différents potentiels gravitationnels en rotation qui n'évoluent pas avec le temps. Nous introduirons **l'approximation épicyclique**, la notion d'orbite guide, et d'épicycles. Nous définirons alors la **migration radiale** des étoiles, et les mouvements de ***churning*** et de ***blurring*** (dénomination introduite par Schönrich & Binney (2009)). Cette approximation nous permettra ensuite d'introduire les phénomènes de **résonances orbitales** avec une barre ou une spirale dans les disques, et nous verrons comment les étoiles peuvent être piégées par les résonances avec une barre faible. Par la suite, nous discuterons des différents modèles de formation et évolution des spirales et de la barre dans les disques galactiques. Nous verrons le rôle de ces structures pour **l'équilibre thermodynamique** des disques : les disques tendent vers l'équilibre thermodynamique en modifiant le moment angulaire des étoiles grâce à la barre et aux spirales, car elles permettent des **transferts de moment angulaire** entre les étoiles du disque et les particules du halo de matière noire qui sont en résonance. Ainsi la barre et les spirales changent avec le temps, et rendent le potentiel variable. Cette variabilité a des conséquences sur la migration radiale des étoiles, et de nouveaux phénomènes apparaissent, comme nous le verrons à la fin de cette partie, avec l'article (à soumettre) Kubryk, Athanassoula, Prantzos. Nous verrons dans cet article que l'évolution séculaire de la barre engendre un nouveau mécanisme de migration radiale des étoiles.

2.1 Orbites des étoiles dans les galaxies disques

Dans cette section nous allons résoudre les équations du mouvements afin de décrire les orbites suivies par les étoiles dans différents potentiels gravitationnels. Il existe de nombreux modèles de disques galactiques, comme par exemple les disques de Mestel (Mestel, 1963), de Kalnajs, de Kuzmin, les disques exponentiels, etc. Chacun de ces modèles est utile pour étudier des propriétés spécifiques de la dynamique dans les disques, toutefois, les observations ainsi que les simulations numériques montrent que les disques sont généralement bien décrits par

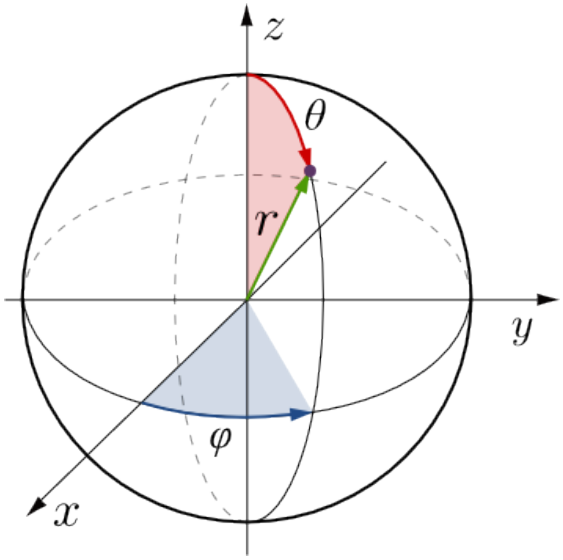

FIGURE 2.1 – Choix du système de coordonnées. La masse M reste immobile au centre du repère, car nous nous intéressons aux orbites de particules de masse négligeable devant M.

un profil exponentiel de densité surfacique d'étoiles.

Le potentiel créé par les disques, où toute autre distribution de matière est calculé grâce à l'équation de Poisson :

$$\Delta\Psi = 4\pi G\rho \tag{2.1}$$

où Ψ est le potentiel gravitationnel, G est la constante de gravitation et ρ est la densité volumique de matière.

Dans cette section, je rappellerai certains éléments de dynamique des étoiles dans les galaxies disques. Il sera question de résoudre les équations du mouvement dans des modèles simples de disques, afin de montrer d'où vient la migration radiale des étoiles. Cette section nous servira donc à définir ce qu'est la migration radiale.

2.1.1 Orbites dans les potentiels Newtoniens sphériques

Nous allons commencer par calculer les orbites dans le cas où le potentiel gravitationnel est créé par une masse ponctuelle M. Les particules dont nous voulons connaître la trajectoire ont une masse négligeable devant M, par conséquent nous pouvons considérer que M est immobile. Le potentiel créé est à symétrie sphérique, nous nous plaçons dans le repère illustrer en Fig. 2.1.

En se plaçant dans le cadre de la mécanique analytique, le Lagrangien s'écrit :

$$\mathscr{L} = T - \Psi = \frac{1}{2}(\dot{r}^2 + r^2\dot{\varphi}^2) + \frac{GM}{r} \tag{2.2}$$

où T et Ψ sont l'énergie cinétique et potentielle respectivement. L'énergie cinétique est exprimée dans le repère cylindrique, car du fait de la symétrie sphérique, nous pouvons choisir de décrire la trajectoire dans le plan $\theta = \frac{\pi}{2}$ (ou z =0) sans perdre en généralité. Enfin, G est la constante de gravitation, et M est la masse du corps central.

On peut alors calculer l'expression des variables conjuguées, qui nous servirons ensuite dans les équations de Hamilton, pour établir les équations du mouvement :

$$\frac{\partial \mathscr{L}}{\partial \dot{r}} = \dot{r} = p_r \qquad\qquad \frac{\partial \mathscr{L}}{\partial \dot{\varphi}} = r^2\dot{\varphi} = p_\varphi = L \tag{2.3}$$

où p_r et p_φ sont les variables conjuguées de r et φ. On reconnait pour p_φ l'expression du moment angulaire L de la particule. On peut alors exprimer l'hamiltonien du problème avec ces variables :

$$H = \frac{1}{2}(p_r^2 + \frac{p_\varphi^2}{r^2}) - \frac{GM}{r} \tag{2.4}$$

permettant d'écrire les équations de Hamilton :

$$\dot{r} = \frac{\partial H}{\partial p_r} = p_r \tag{2.5}$$

$$\dot{\varphi} = \frac{\partial H}{\partial p_\varphi} = \frac{1}{r^2}p_\varphi \tag{2.6}$$

$$\dot{p_r} = -\frac{\partial H}{\partial r} = -\frac{GM}{r^2} + \frac{p_\varphi^2}{r^3} \qquad \Longleftrightarrow \qquad \ddot{r} = -\frac{GM}{r^2} + \frac{p_\varphi^2}{r^3} \tag{2.7}$$

$$\dot{p_\varphi} = -\frac{\partial H}{\partial \varphi} = 0 \qquad \Longleftrightarrow \qquad \frac{dL}{dt} = 0 \tag{2.8}$$

Les équations 2.5 et 2.6 sont équivalentes aux équations 2.3, et ne nous apprennent donc pas grand chose. L'équation 2.7 est l'équation du mouvement que nous allons résoudre, et l'équation 2.8 montre que le moment angulaire est une constante du mouvement, et donc que la trajectoire de l'objet reste dans un plan, ce qui est cohérent avec le fait d'avoir choisi d'exprimer cette trajectoire dans le plan $z = 0$.

En multipliant à gauche et à droite par $\dot{r}$ dans l'Eq. 2.7, il devient possible d'intégrer une première fois l'équation :

$$\ddot{r}\dot{r} = -\frac{GM}{r^2}\dot{r} + \frac{L^2}{r^3}\dot{r} \qquad \xrightarrow{\text{intégration}} \qquad \frac{1}{2}\dot{r}^2 = \frac{GM}{r} - \frac{1}{2}\frac{L^2}{r^2} + \mathscr{E} \tag{2.9}$$

où la constante d'intégration $\mathscr{E}$ est l'énergie totale de la particule, qui est donc une constante du mouvement, comme le moment angulaire L.

En utilisant l'expression du moment angulaire $r^2\dot{\varphi} = L$, il vient $dt = \frac{r^2}{L}d\varphi$. Ainsi l'Eq. 2.9 se réécrit de la manière suivante :

$$\frac{1}{2}\left(\dot{r}^2 + \frac{L^2}{r^2}\right) - \frac{GM}{r} = \mathscr{E} \tag{2.10}$$

$$\Leftrightarrow \quad \frac{1}{2}\left(\left(\frac{dr}{d\varphi}\right)^2 + r^2\right)\frac{L^2}{r^4} - \frac{GM}{r} = \mathscr{E} \tag{2.11}$$

En faisant le changement de variable $u = \frac{1}{r} - \frac{GM}{L^2}$, on obtient après quelques lignes de calcul :

$$\left(\frac{du}{d\varphi}\right)^2 = \alpha - u^2 \qquad \text{avec} \qquad \alpha = \sqrt{\frac{G^2M^2}{L^4} + \frac{2\mathscr{E}}{L^2}} \tag{2.12}$$

En prenant la racine et en séparant les variables, on obtient alors :

$$\frac{du}{\alpha\sqrt{1 - \frac{u^2}{\alpha^2}}} = \pm d\varphi \tag{2.13}$$

Dans cette expression, le signe $\pm$ détermine le sens de parcours de l'orbite, et nous choisissons

le signe +. L'expression 2.13 s'intègre facilement et donne :

$$\arccos\left(\frac{u}{\alpha}\right) = \varphi - \omega \qquad \Longrightarrow \qquad \frac{u}{\alpha} = \cos\left(\varphi - \omega\right) \tag{2.14}$$

Alors, en remplaçant toutes les variables, on obtient l'expression finale

$$\frac{1}{r} = \frac{1 + e\cos(f)}{p} \tag{2.15}$$

avec

$$e = \sqrt{1 + \frac{2\mathscr{E}L^2}{G^2M^2}} \quad , \quad p = \frac{L^2}{GM} \quad \text{et} \quad f = \varphi - \omega \tag{2.16}$$

Les orbites dans le potentiel Newtonien sphérique sont donc des coniques dont un des foyers est l'objet central de masse M. Les paramètres de ces coniques sont l'excentricité e, le paramètre focal p, et l'angle f de la particule par rapport à un angle de référence ω, on appelle f l'anomalie vraie.

L'énergie $\mathscr{E}$ de la particule détermine l'excentricité de la conique, et détermine si la particule est liée gravitationnellement à l'objet central. En, effet si $e \geq 1$ la particule ne passe qu'une seule fois à proximité de l'objet central, il s'agit d'une particule libre : sa trajectoire est une parabole si e =1, ou bien une hyperbole si e >1. En revanche, pour $0 \leq e < 1$ la trajectoire est une ellipse, traduisant le fait que l'énergie de la particule est suffisamment faible pour qu'elle reste confinée autour de l'objet de masse M. La Fig. 2.2 illustre les différentes trajectoires autour de la masse M, indiquée au foyer des coniques. Notons que les trajectoires obtenues pour les particules liées à l'objet central sont fermées, mais qu'en générale, les trajectoires réelles sont des versions légèrement perturbées de ces orbites, qui ne bouclent pas parfaitement. Par exemple dans le système solaire, ces perturbations viennent de l'influence gravitationnelle des autres planètes, qui produisent un mouvement de précession des orbites qui est une rotation du grand axe des ellipses.

2.1.2 Orbites dans les potentiels de disques axisymétriques en rotation

Intéressons-nous maintenant au cas des orbites dans les disques galactiques. Pour l'instant, nous allons considérer que les disques sont axisymétriques. La première remarque que nous pouvons faire est que, dans le cas des galaxies disques, le problème n'est plus à symétrie sphérique. Nous utilisons toujours le repère illustré en Fig. 2.1, et nous choisissons de mettre

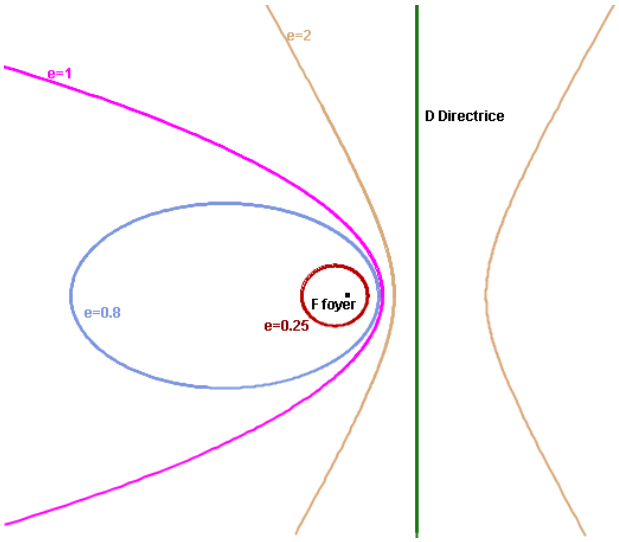

FIGURE 2.2 – Illustration des différentes trajectoires, selon l'excentricité de la particule, déterminant sont caractère lié ou libre. La masse M est au foyer F des coniques.

le disque dans le plan z =0. De par la symétrie du disque, nous perdons alors l'invariance par rapport à la coordonnée θ.

Considérons tout d'abord une particule dont la trajectoire reste dans le plan z =0. Cette particule n'a aucun moyen de savoir qu'elle se trouve dans un disque et non dans une répartition sphérique de matière. Par conséquent cette particule a une orbite ayant les mêmes caractéristiques que dans la section précédente : conservation du moment angulaire, et donc trajectoire qui reste confinée dans le plan z =0. La différence par rapport au cas précédent est l'expression du potentiel gravitationnel, qui n'assure plus forcément que la trajectoire soit fermée. Cette particule peut alors suivre une ellipse dont le grand-axe pourra être aussi en rotation, comme illustré en Fig. 2.3.

À présent, considérons une particule dont la trajectoire peut sortir du plan z =0. Dans ce cas la particule voit un potentiel $\Psi(r,z)$. La trajectoire d'une telle particule est alors constituée d'oscillations radiales entre l'apocentre et le péricentre (c'est aussi le cas des particules liées de la section précédente), mais aussi d'oscillations verticales, c'est-à-dire perpendiculaires au plan du disque z =0. Comme les équations décrivant de telles trajectoires sont en général non-intégrables, il est usuel d'utiliser l'approximation épicyclique (Binney & Tremaine, 1987), qui repose sur un développement au premier ordre des équations du mouvement, afin d'en déterminer des solutions approchées.

Pour décrire l'orbite d'une étoile, nous nous plaçons dans un référentiel en rotation, de sorte que si l'étoile avait une orbite circulaire, elle serait immobile dans ce référentiel. Nous devons donc prendre en compte les pseudo-forces d'inertie d'entraînement et de Coriolis, liées au caractère non-Galiléen du référentiel choisi. Dans les référentiels en rotation on remplace le

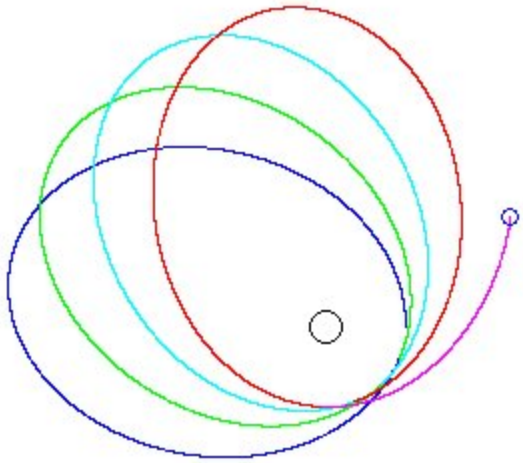

FIGURE 2.3 – Exemple de trajectoire d'une particule confinée au plan z =0 d'un disque galactique. Le centre galactique est indiqué par le grand cercle noir, et la particule est indiquée par le petit cercle noir.

potentiel Ψ par le potentiel effectif Ψ_{eff}, qui permet de décrire à la fois la force gravitationnelle et les pseudo-forces subies par l'étoile :

$$\Psi_{eff}(r,z) = \Psi(r,z) + \frac{L_z^2}{2r^2} \tag{2.17}$$

où $\Psi(r,z)$ est le potentiel gravitationnel du disque et L_z est le moment angulaire de l'étoile. Nous définissons la position R_g du minimum de ce potentiel, c'est-à-dire le rayon où les étoiles ayant le moment angulaire L_z sont en orbites circulaires :

$$\frac{\partial \Psi_{eff}}{\partial r}(R_g,0) = 0 \tag{2.18}$$

$$\Rightarrow \quad \frac{\partial \Psi}{\partial r}(R_g,0) - \frac{L_z^2}{R_g^3} = 0 \tag{2.19}$$

$$\Rightarrow \quad \frac{\partial \Psi}{\partial r}(R_g,0) = \frac{L_z^2}{R_g^3} \tag{2.20}$$

Considérons alors une étoile en orbite quasi-circulaire autour du rayon guide $r = R_g$ et dont les oscillations verticales sont centrées sur l'altitude z =0. Nous faisons le changement de variable $x = r - R_g$, afin de centrer les coordonnées radiales sur le rayon guide. Alors le potentiel effectif

se développe en séries de Taylor autour du point guide de l'étoile (x =0, z =0). Comme nous développons autour du minimum du potentiel selon la coordonnées r, les dérivées premières de la séries de Taylor sont nulles, et ne restent que les dérivées d'ordres supérieurs ou égaux à 2 :

$$\Psi_{eff}(x,z) = \Psi_{eff}(0,0) + \frac{1}{2}\left(\frac{\partial^2\Psi_{eff}}{\partial r^2}\right)_{(R_g,0)} x^2 + \frac{1}{2}\left(\frac{\partial^2\Psi_{eff}}{\partial z^2}\right)_{(R_g,0)} z^2 + o(xz^2) \tag{2.21}$$

Alors nous pouvons écrire les équations du mouvement approchées :

$$\ddot{x} = -\frac{\partial\Psi_{eff}}{\partial x} \iff \ddot{x} = -\left(\frac{\partial^2\Psi_{eff}}{\partial r^2}\right)_{(R_g,0)} x \iff \ddot{x} = -\kappa^2 x \tag{2.22}$$

$$\ddot{z} = -\frac{\partial\Psi_{eff}}{\partial z} \iff \ddot{z} = -\left(\frac{\partial^2\Psi_{eff}}{\partial z^2}\right)_{(R_g,0)} z \iff \ddot{z} = -\nu^2 z \tag{2.23}$$

où κ^2 et ν^2 sont les fréquences des mouvements épicycliques radiaux et verticaux respectivement. En première approximation, les mouvements épicycliques autour des orbites circulaires sont donc des oscillations harmoniques autour du point guide, dans le référentiel tournant avec ce dernier.

La solution générale des équations 2.23, est :

$$x(t) = X\cos(\kappa t + \psi) \tag{2.24}$$

$$z(t) = Z\cos(\nu t + \zeta) \tag{2.25}$$

où X et Z sont les amplitudes des épicycles radiaux et verticaux respectivement, ψ et ζ sont les phases des mouvements radiaux et verticaux.

Il est également possible de calculer les mouvements azimutaux (selon la coordonnées φ) des étoiles à partir de leur moment angulaire. En effet, la vitesse angulaire des étoiles en orbites

circulaires est $\Omega_g = \frac{L_z}{R_g^2}$. Or, comme L_z se conserve, il vient :

$$\dot{\varphi} = \frac{L_z}{r^2} = \frac{L_z}{R_g^2}\left(1+\frac{x}{R_g}\right)^{-2} \simeq \Omega_g\left(1-\frac{2x}{R_g}\right) \tag{2.26}$$

Alors, en remplaçant x par l'expression 2.24, nous pouvons intégrer l'équation, et obtenir l'expression des mouvements azimutaux :

$$\varphi(t) = \Omega_g t + \varphi_0 - \frac{2\Omega_g X}{\kappa R_g}\sin(\kappa t + \psi) \tag{2.27}$$

Pour mieux visualiser les résultats, exprimons cette équation dans un repère cartésien (x, y, z), centré sur le point guide (x =0,$\varphi = \Omega_g t + \varphi_0$), et en rotation avec celui-ci. Nous avons déjà défini les variables x et z, la variable y décrit la direction perpendiculaire à x et z. Dans ce repère, l'Eq. 2.27 devient :

$$y(t) = -\frac{2\Omega_g}{\kappa} X \sin(\kappa t + \psi) = -Y\sin(\kappa t + \psi) \tag{2.28}$$

Avec les équations 2.24, 2.28 et 2.25 sont avons la solution des équations du mouvement dans le cadre de l'approximation épicyclique. Cette approximation est valide tant que le potentiel effectif est bien approximé par un potentiel harmonique selon x, y et z.

Considérons un modèle de disque très peu étendu dans la direction z. Alors si le disque est suffisamment mince, l'expression de l'équation de Poisson 2.1 se simplifie, et permet de calculer la composante verticale du potentiel :

$$\frac{\partial^2\Psi(r,z)}{\partial z^2} = 4\pi G\rho(r,z) \tag{2.29}$$

Il est alors clair que pour avoir un potentiel de la forme $\Psi \propto z^2$, c'est-à-dire un potentiel harmonique, on doit avoir une densité ρ constante. Par conséquent l'approximation épicyclique pour les mouvements verticaux des étoiles, n'est valide que pour des étoiles restant très proches du plan z =0, où la densité de matière peut être considérée à peut près constante i.e. $|z| \lesssim 300$ pc. Or les disques galactiques peuvent avoir une échelle caractéristique de hauteur de ~1 kpc, par exemple pour le disque épais du voisinage solaire. L'approximation épicyclique n'est donc pas valide pour décrire les orbites ayant des oscillations verticales amples. En

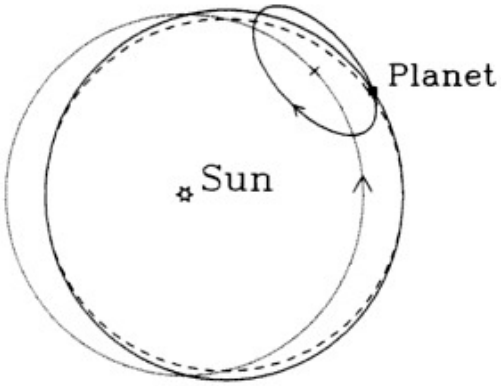

FIGURE 2.4 – Illustration de l'approximation épicyclique pour une orbite de planète autour du Soleil. La trajectoire elliptique vraie est en tirets, l'orbite guide est le cercle gris clair, les mouvements épicycliques sont indiqués par l'ellipse centrée sur le point guide (marqué par le symbole +). Et la trajectoire obtenue avec l'approximation épicyclique est la courbe noire en trait plein. (Extrait de (Binney & Tremaine, 1987)).

revanche, concernant les mouvements dans le plan du disque, la validité de l'approximation est plus étendue, jusqu'à des amplitudes de l'ordre du kpc.

Dans le plan z =0, d'après les équations 2.24 et 2.28, les epicycles sont donc des ellipses dont le rapport des axes vaut :

$$\frac{X}{Y} = \frac{\kappa}{2\Omega_g} \tag{2.30}$$

La valeur de ce rapport dépend du potentiel dans lequel l'objet se trouve. Par exemple, pour les potentiel Newtonien on a $\frac{X}{Y} = \frac{1}{2}$. La Fig. 2.4 compare la trajectoire d'une ellipse Képlerienne en tirets (correspondant aux calculs menés en Sec. 2.1.1) avec la trajectoire obtenue avec l'approximation épicyclique quand le rapport des axes vaut 1/2 (en trait plein). Les deux trajectoires sont proches l'une de l'autre, ce qui illustre la pertinence de l'approximation épicyclique.

En conclusion, nous avons vu que les disques galactique axisymétriques induisent des mouvements d'oscillation radiale des étoiles, qui sont décrits en approximant le mouvement des étoiles par la superposition d'une orbite guide circulaire et de mouvements épicycliques. Historiquement, il s'agit là de la première mise en évidence de la non-circularité des orbites stellaires. Cependant, les galaxies réelles ne présentent pratiquement jamais une symétrie axiale parfaite car des structures se forment spontanément dans les disques (nous discuterons plus en détails en section 2.3 de la barre et des spirales), c'est pourquoi nous allons voir

dans la suite comment les étoiles évoluent dans les disques non-axisymétriques, et quelle est l'influence des non-axisymétries sur les mouvements radiaux des étoiles.

Enfin, les orbites que nous avons étudié ici ont trois intégrales : L_z, E_r et E_z, qui sont respectivement le moment angulaire, l'énergie des mouvements épicycliques radiaux et verticaux. Ces intégrales s'expriment de la façon suivante (Binney & Tremaine, 1987) :

$$L_z = r^2\dot{\varphi} \tag{2.31}$$

$$E_r = \frac{1}{2}\kappa^2 X^2 = E \tag{2.32}$$

$$E_z = \frac{1}{2}\nu^2 Z^2 \tag{2.33}$$

où les variables sont les mêmes que dans les Eqs. 2.25 et 2.24. Notamment, nous verrons plus loin que la conservation du moment angulaire lors des mouvements épicycliques permet d'étudier la migration radiale en séparant les différents mécanismes dynamiques qui peuvent en être à l'origine.

2.1.3 Orbites dans les potentiels non-axisymétriques en rotation

Les potentiels sont non-axisymétriques notamment quand une barre et/ou des spirales se forment dans le disque (nous verrons en Sec. 2.3 la formation de telles structures). Les passages à proximité d'autres galaxies ou les galaxies satellites naines contribuent également à rendre le potentiel non-axisymétrique. Cependant, nous nous limiterons ici à la description des effets induits par une barre rigide en rotation à la vitesse angulaire Ω_b, qui nous permettra d'aborder les aspects de la dynamique dans les potentiels non-axisymétriques les plus fondamentaux pour la migration radiale des étoiles.

À l'aide de la figure 2.5, nous illustrons la forme du potentiel effectif créé par une barre en rotation. Nous travaillerons dans le référentiel en rotation avec la barre, qui est ici au centre de la figure, alignée verticalement. Le potentiel effectif est montré dans la moitié gauche de la figure et il est symétrique par rapport à l'axe vertical. Dans ce potentiel les points L1, L2, L3, L4 et L5 sont des points d'équilibre, c'est-à-dire qu'en ces points, on a $\nabla\Psi_{eff} = O$. La stabilité de ces points est examinée dans Kubryk, Athanassoula, Prantzos (à soumettre) donné en Sec. 2.4. Par analogie avec les points d'équilibre qui apparaissent dans le problème à trois corps, ces points sont appelés points de Lagrange. Nous montrons également dans la figure les orbites qui vivent dans ce potentiel, et que nous allons déterminer dans la suite. Par ailleurs, les points L1, L2, L4 et L5 ont presque le même rayon galacto-centrique, ils sont répartis autour du rayon de corotation (que nous expliciteront plus loin).

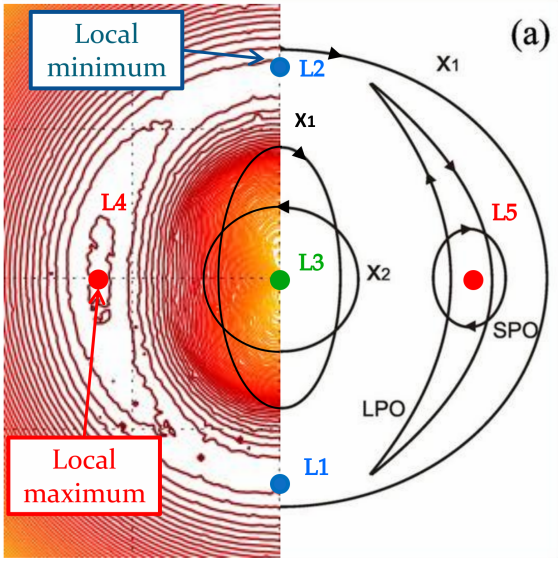

FIGURE 2.5 – La figure est divisée en deux. *Dans la moitié gauche*, est représenté le potentiel gravitationnel créé par une barre orientée verticalement et sans spirales. Le minimum du potentiel est au centre de la barre (disque vert), deux minima locaux sont alignés avec le grand axe de la barre (disques bleus), et deux maxima sont alignés avec le petit axe de la barre (disques rouges). *Dans la moitié droite*, sont indiquées les orbites qui vivent dans ce potentiel. Les familles d'orbites x1 et x2 au centre créent la forme de la barre, les orbites circulaires, hors de la barre sont aussi indiquées et appartiennent également à x1. Sont aussi indiquées les orbites en "fer à cheval" autour des maximas du potentiel, qui peuvent être soit LPO (pour Long Period Orbit), ou SPO (pour Short Period Orbits)

L'équation du mouvement dans ce potentiel est :

$$\ddot{\boldsymbol{r}} = -\vec{\nabla}\Psi - 2(\boldsymbol{\Omega_b} \times \dot{\boldsymbol{r}}) - \boldsymbol{\Omega_b} \times (\boldsymbol{\Omega_b} \times \boldsymbol{r}) \tag{2.34}$$

où les deux derniers termes de l'équation sont la force de Coriolis et la force centrifuge, qui sont ajoutées car nous travaillons dans un référentiel non-Galiléen. Et $\mathbf{r}$ est le vecteur (x,y) dans le référentiel en rotation avec la barre.

En prenant le produit scalaire de l'Eq. 2.34, avec $\dot{\mathbf{r}}$, il vient :

$$\frac{d}{dt}\left(\frac{1}{2}\dot{\mathbf{r}}^2 + \Psi - \frac{1}{2}\Omega_\mathbf{b} \times \mathbf{r}^2\right) = 0 \tag{2.35}$$

$$\iff \frac{dE_J}{dt} = 0 \tag{2.36}$$

où E_j est **l'énergie de Jacobi**, qui s'exprime également :

$$E_J = E - \Omega_\mathbf{b}.\mathbf{L_z} \tag{2.37}$$

Ainsi, E_J est une intégrale du mouvement dans les potentiels non-axisymétriques en rotation, et contrairement au cas axisymétrique, ni l'énergie E des mouvements épicycliques dans le plan, ni le moment angulaire $\mathbf{L_z}$ ne sont conservés, mais leurs variations sont reliées via l'Eq. 2.37.

2.1.3.1 Orbites stellaires à proximité des points de Lagrange

Pour étudier les orbites dans les potentiels non-axisymétriques en rotation, il est utile de commencer par les orbites très proches des points de Lagrange. Dans la suite, nous allons étudier les orbites autour du point L3, c'est-à-dire les orbites dans la barre. Toutefois, la méthode que nous allons appliquer est valide autour des autres points de Lagrange, et les résultats que nous allons trouver pour L3 sont valables pour L4 et L5 à condition de faire un changement de variable pour centrer les coordonnées en ces points, je donnerai plus de détails dans la suite. En revanche, autour de L1 et L2 nous verrons que le comportement des étoiles est différent de celui autour de L3, L4 et L5.

Suivant Binney & Tremaine (1987), pour déterminer les orbites stellaires au cœur de la barre,

c'est-à-dire autour du point L3 de coordonnées (0,0), nous allons développer le potentiel effectif en ce point. Alors, comme pour le cas axisymétrique, les dérivées premières sont nulles car on se trouve à un minimum du potentiel, et comme les axes de la barre sont alignés avec les axes x et y du repère tournant, les dérivées croisées sont nulles également. Cette méthode est aussi valable autour des autres points de Lagrange, et les équations sont les mêmes en faisant un changement de variable mettant le point étudié à l'origine des nouvelles coordonnées. Nous obtenons donc autour de L3 :

$$\Psi_{eff}(x,y) = \Psi_{eff}(0,0) + \frac{1}{2}\frac{\partial^2\Psi_{eff}}{\partial x^2}x^2 + \frac{1}{2}\frac{\partial^2\Psi_{eff}}{\partial y^2}y^2 + \dots \tag{2.38}$$

En posant $\psi_{xx} = \frac{\partial^2\Psi_{eff}}{\partial x^2}$ et $\Psi_{yy} = \frac{\partial^2\Psi_{eff}}{\partial y^2}$, et en introduisant 2.38 dans l'Eq. 2.34, on a les équations du mouvement suivantes :

$$\begin{cases} \ddot{x} = & 2\Omega_b\dot{y} - \Psi_{xx}x \\ \ddot{y} = - & 2\Omega_b\dot{x} - \Psi_{yy}y \end{cases} \tag{2.39}$$

Nous obtenons donc un système d'équations différentielles du second ordre à coefficients constants, dont les solutions générales sont de la forme

$$\begin{cases} x(t) & = X\exp(\lambda t) \\ y(t) & = Y\exp(\lambda t) \end{cases} \tag{2.40}$$

avec X et Y des constantes réelles, et λ une constante complexe que nous allons déterminer dans la suite. En remplaçant alors 2.40 dans 2.39 on obtient le système matriciel suivant :

$$\begin{cases} (\lambda^2 + \Psi_{xx})X - 2\lambda\Omega_b Y & = 0 \\ 2\lambda\Omega_b X + (\lambda^2 + \Psi_{yy})Y & = 0 \end{cases} \iff \begin{pmatrix} \lambda^2 + \Psi_{xx} & -2\lambda\Omega_b \\ 2\lambda\Omega_b & \lambda^2 + \Psi_{yy} \end{pmatrix}\begin{pmatrix} X \\ Y \end{pmatrix} = 0 \tag{2.41}$$

Alors, si le déterminant de la matrice est non-nul, la seule solution est $X = 0$ et $Y = 0$: les étoiles ne bougent pas de L3. Pour que les solutions soient non triviales, le déterminant doit

donc être nul, c'est-à-dire :

$$\lambda^4 + \lambda^2(\Psi_{xx} + \Psi_{yy} + 4\Omega_b^2) + \Psi_{xx}\Psi_{yy} = 0 \tag{2.42}$$

Nous obtenons ainsi, l'équation caractéristique du système, qui est du quatrième degrés, et donc, possède quatre racines complexes (opposées deux à deux) qui sont les valeurs possibles de λ dans 2.40. L'analyse des solutions de 2.42 permet de déduire la stabilité du point de Lagrange, ce qui a été discuté dans Pfenniger (1990). En effet, si λ possède une partie réelle non-nulle alors les expressions 2.40 divergent de façon exponentielle, l'étoile s'éloigne très rapidement du point de Lagrange : c'est un point d'équilibre instable. En revanche, si λ est imaginaire pur le mouvement est périodique autour du point de Lagrange : c'est un point d'équilibre stable. Il est alors possible de déterminer des conditions de stabilité, dépendant de la valeur des constantes dans 2.42. Dans l'article à soumettre Kubryk,Athanassoula,Prantzos (donné en Sec. 2.4), nous étudions ces conditions dans le cas un peu plus général où la barre n'est pas alignée avec les axes du repère.

La nature stable ou instable de l'équilibre aux points de Lagrange dépend de la forme du potentiel effectif en ces points via les coefficients Ψ_{xx} et Ψ_{yy}. Selon les conditions de stabilité obtenues par Pfenniger (1990) et dans notre article (Sec. 2.4), les points L1 et L2 sont toujours instable à cause de la forme en "selle de cheval" du potentiel effectif, et le point L3 est toujours stable car c'est le minimum absolu du potentiel effectif. En revanche, concernant les points L4 et L5, la stabilité est beaucoup plus sensible à la forme du potentiel et il n'est pas possible de généraliser leur nature en examinant l'expression des conditions de stabilité, il faut analyser les potentiels au cas par cas. Toutefois dans les simulations, il apparaît que L4 et L5 sont stables dans la plupart des cas parce que les potentiels galactiques simulés ont généralement les bonnes propriétés pour que ce soit le cas. On considère alors qu'il en est de même pour les potentiels réels.

Par conséquent, le fait que L3 soit stable, impose que λ soit un nombre imaginaire pur i.e. $\lambda = \pm i\alpha$ ou $\lambda = \pm i\beta$, car il doit y avoir quatre valeurs possibles, opposées deux à deux. Et on pose $0 < \alpha < \beta$. Dans ce cas les solutions des équations du mouvement 2.39 sont de la forme :

$$\begin{cases} x(t) &= X_1\cos(\alpha t + \phi_1) + X_2\cos(\beta t + \phi_2) \\ y(t) &= Y_1\sin(\alpha t + \phi_1) + Y_2\sin(\beta t + \phi_2) \end{cases} \tag{2.43}$$

Et en substituant ces expressions dans l'Eq. 2.39, on obtient les relations entre les constantes

X_1 et Y_1, ainsi que X_2 et Y_2 :

$$\begin{cases} Y_1 = \frac{\Psi_{xx}-\alpha^2}{2\Omega_b\alpha} X_1 = \frac{2\Omega_b\alpha}{\Psi_{yy}-\alpha^2} X_1 \\ Y_2 = \frac{\Psi_{xx}-\beta^2}{2\Omega_b\beta} X_2 = \frac{2\Omega_b\beta}{\Psi_{yy}-\beta^2} X_2 \end{cases} \tag{2.44}$$

Les orbites des étoiles composant la barre sont donc déterminées par les équations 2.43 et 2.44, qui décrivent une superposition de deux mouvements elliptiques, ayant chacun les fréquences α et β. Comme nous avons définit $0 < \alpha < \beta$, en utilisant l'Eq. 2.42 il vient :

$$\alpha^2 < \Psi_{yy} < \beta^2 \tag{2.45}$$

Alors, d'après les Eq. 2.44, on a $Y_1/X_1 > 0$ et $Y_2/X_2 < 0$, ce qui veut dire que les mouvements à la fréquence α se font dans le sens de rotation de la barre (on parle d'orbite prograde), et les mouvements à la fréquence β se font dans le sens opposé (on parle de mouvement rétrograde). Par conséquent, il existe deux classes d'orbites autour de L3 : les orbites progrades dont l'orbite guide est décrite par l'ellipse α et les epicycles décrits par l'ellipse β ; et les orbites rétrogrades où le rôle des ellipses α et β est inversé. Ce calcul repose sur un développement du potentiel autour du point L3, toutefois les résultats obtenus restent valides pour les orbites autour des points L4 et L5, qui sont également des points d'équilibre stables, à condition de centrer les variables sur L4 ou L5.

Par ailleurs, les orbites autour de L3 peuvent avoir leur grand axe orienté parallèlement au grand axe de la barre, ou bien perpendiculairement, formant les familles d'orbites "x1" et "x2" respectivement, selon la notation de Contopoulos & Papayannopoulos (1980).

Pour les trajectoires autour des points instables L1 et L2, des exponentielles croissantes en fonction du temps apparaissent dans l'expression des orbites. Une analyse détaillée des trajectoires d'étoiles en L1 et L2 est donnée par Romero-Gómez et al. (2006), où les auteurs montrent l'influence de ces points sur la formation d'anneaux d'étoiles autour de la barre.

2.1.3.2 Exemples d'orbites formant la barre

Ces orbites ont été étudiée dans différents potentiels gravitationnels constituant des modèles de barres rigides (sans évolution séculaire). Les travaux de Contopoulos & Papayannopoulos (1980), Athanassoula et al. (1983) et Contopoulos & Grosbol (1989) ont montré que la barre est supportée par une famille d'orbites nommée "x1". Les Figs. 2.6 et 2.7, illustrent les formes possibles de ces orbites, et comment elles dessinent la barre. Ces orbites sont fermées, traduisant le fait qu'elles sont en résonances (elles font un nombre entier d'oscillations pendant

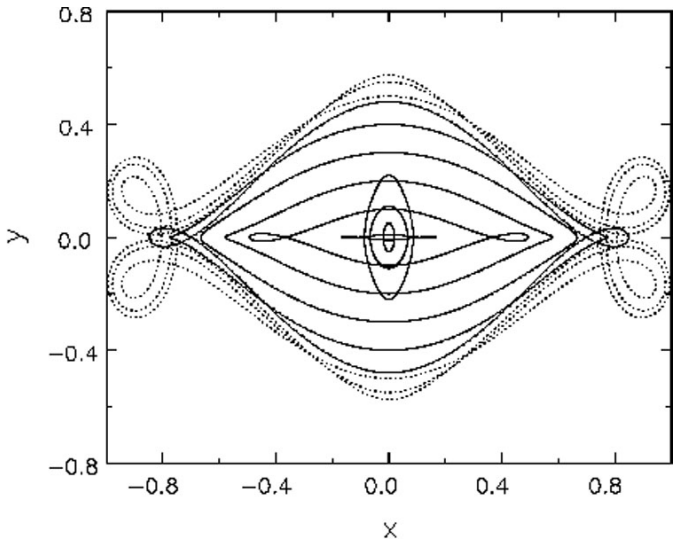

FIGURE 2.6 – Orbites supportant la forme d'une barre quelconque, dessinées dans le référentiel tournant avec la barre. Les orbites en traits pleins sont des membres de la famille x1, et sont en résonance 2 :1 avec la barre (c.f. Sec. 2.2) ces orbites sont alignées dans le sens de la barre. Les orbites perpendiculaires à la barre sont les orbites de la famille x2. Les orbites en pointillets sont en résonance 4 :1 (elles font 4 oscillations radiales, pendant 1 révolution dans la barre), et contribuent à la forme rectangulaire de la barre.

une révolution dans la barre). La plupart des étoiles constituant la barre sont en résonance 2 :1 (ILR) (panneau en haut à gauche de la Fig. 2.16), mais certaines étoiles sont sur d'autre résonances, et notamment la résonance 4 :1 qui contribuent alors à la forme rectangulaire que peuvent avoir les barres (voir Fig. 2.7).

Par ailleurs les orbites x1 sont fermées et stables, c'est-à-dire qu'une orbite proche d'une x1 mais légèrement perturbée (trajectoire non-fermée), ne s'en éloignera pas, par conséquent la famille x1 constitue la colonne vertébrale des barres, qui "piège" les orbites perturbées. Enfin, les étoiles réelles ne suivent pas exactement les orbites x1 car elles sont toujours perturbées par les petites irrégularités présentes dans les potentiels réels, mais elles s'enroulent autour des x1 et forment ainsi le corps de la barre. L'autre famille d'orbites est perpendiculaire à l'axe de la barre, c'est la famille "x2", qui est importante pour l'interaction de la barre avec le gaz.

2.1.4 Définition de la migration radiale : blurring et churning

Dans cette première section, nous avons décrit le mouvement des étoiles dans deux cas simples : le disque axisymétrique, et le disque comprenant une barre rigide en son centre. Nous avons résolu les équations de la dynamique, en faisant l'approximation que les orbites sont une superposition de deux mouvements, ce qui permet de trouver des solutions analytiques proches des orbites réelles. Ainsi, ces analyses permettent de mettre en évidence les deux

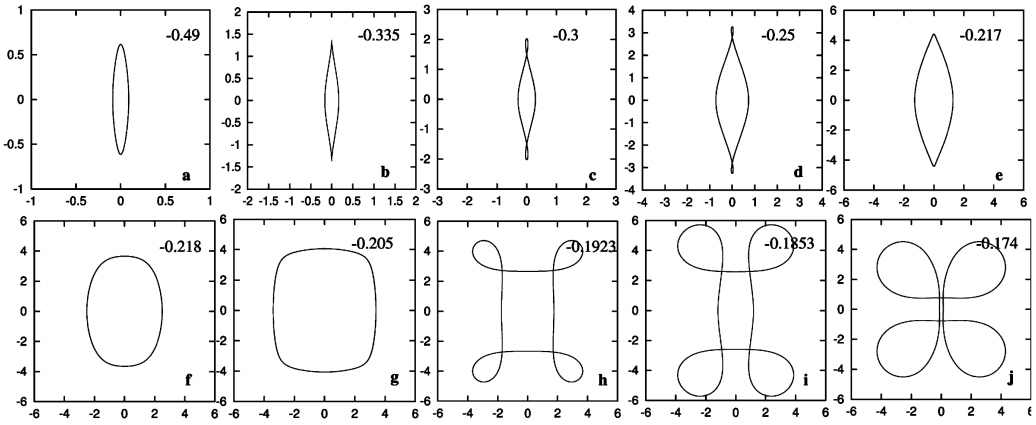

FIGURE 2.7 – Différents exemples d'orbites de la famille x1 supportant la forme de la barre. Figure extraite de Skokos, Patsis & Athanassoula (2002), où le nombre dans chaque panneau indique l'énergie de Jacobi de l'orbite, dans le potentiel étudié dans le papier.

phénomènes dynamiques principaux à l'origine de la migration radiale des étoiles, dans les disques galactiques

Dans un premier temps, nous avons vu le cas du disque axisymétrique, dans lequel les orbites sont bien décrites par la superposition de mouvements elliptiques rétrogrades, et de faible amplitude autour du point guide, et du mouvement du point guide lui-même, qui suit une orbite circulaire prograde autour du centre de la galaxie. Ces mouvements elliptiques sont appelés épicycles et leur amplitude dépend dépend de l'énergie de l'étoile. Dans ce cas la migration radiale vient de l'ellipticité des orbites, comme dans le potentiel Newtonien. En revanche elles ne sont généralement pas fermées, car le grand axe des ellipses tourne autour du centre galactique. C'est pourquoi nous avons vu deux fréquences apparaître : celle du point guide autour du centre galactique et celle de l'ellipse qui est donc la fréquence des mouvements radiaux. Notons au passage, que les épicycles décrits ici ne sont pas circulaires, contrairement à ceux intervenant dans la théorie développée par Hipparque (190 av. J.-C. - 120 av. J.-C.) puis Ptolémée (80 ap. J.-C. - 168 ap. J.-C.) dans l'*Almageste* (Ptolemaeus, 150 ap. J.-C.) au sujet des orbites planétaires dans le système solaire.

Dans un deuxième temps, nous avons vu le cas d'un disque avec une barre en son centre. Nous nous sommes intéressés aux orbites proches des points d'équilibre (ou points de Lagrange) qui apparaissent quand on se place dans le référentiel tournant avec la barre. Nous avons vu que le mouvement est là aussi bien décrit par la superposition de deux composantes : une orbite guide, autour de laquelle l'étoile oscille en suivant une ellipse. Cependant, à la différence du cas précédent, l'orbite guide n'est plus circulaire, elle est également elliptique. Dans ce cas, nous avons deux sources de migration radiale : d'une part, les épicycles comme dans le cas précédent, et d'autre part, les variations de l'orbite guide elle-même, qui apparaissent à cause de la barre au centre du disque. Nous précisons ici que, les bras spiraux génèrent eux aussi des

points de Lagrange, et que les résultats que nous avons rappelés dans le cas d'une barre, sont également valables dans le cas où la structure non-axisymétrique est une spirale. Enfin les mouvements radiaux, dans les disques non-axisymétriques peuvent être plus amples puisque, dépendant de la synchronisation des deux mouvements, les deux oscillations radiales peuvent se cumuler.

Ainsi, nous avons illustré deux choses : d'une part, que la migration radiale se sépare en deux composantes, qui sont souvent appelées ***churning*** (pour les mouvements de l'orbite guide) et ***blurring*** (pour les mouvements epicycliques) depuis Schönrich & Binney (2009) ; et d'autre part que les structures telles que la barre et les spirales peuvent augmenter les mouvements radiaux des étoiles.

Nous avons aussi, montré que l'une des différences entre le churning et le blurring, est la conservation du moment angulaire. En effet, nous avons montré qu'une trajectoire composée d'une orbite guide circulaire et d'épicycles, conserve son moment angulaire ; mais que ce n'est plus le cas lorsque l'orbite guide présente aussi des oscillations radiales.

Par ailleurs, nous verrons que cette séparation de la migration radiale en deux composantes est également utile lorsqu'il s'agit d'inclure la migration dans un modèle d'évolution galactique, comme nous le verrons au Chap. 3.

2.2 Résonances entre les étoiles et une barre faible dans le disque

Dans cette section nous allons, d'abord définir la notion de résonance, puis donner une description plus approfondie des orbites stellaires autour d'une barre, et nous intéresser plus spécifiquement aux étoiles en **corotation** avec la barre. Car la corotation tient un rôle prépondérant dans l'évolution des disques et des structures (barres, spirales), et est également au centre des travaux sur la migration radiale. Sur cette résonance, la vitesse de rotation des étoiles est la même que celle de la structure : $\Omega = \Omega_s$, où Ω est la vitesse angulaire des étoiles et Ω_s la vitesse angulaire de la structure. Comme la vitesse angulaire des étoiles dans les disque est une fonction décroissante du rayon (Fig. 2.8), et comme la vitesse angulaire de la structure est considérée fixe, alors il n'y a qu'un seul rayon où les étoiles et la structure tournent à la même vitesse. Ce rayon est appelé **rayon de corotation** que nous nommerons parfois Rc dans la suite. De plus, à cause de la décroissance de la vitesse angulaire des étoiles, si on se place dans le référentiel tournant avec la structure, les étoiles sous le Rc tournent dans le sens de la structure : $\Omega - \Omega_s > 0$; et les étoiles au-delà du Rc tournent dans le sens inverse : $\Omega - \Omega_s < 0$

Les autres résonances font intervenir, à la fois, la fréquence épicyclique κ (voir section précédente), et la différence de vitesse de rotation entre les étoiles et les structures non-axisymétriques $\Omega - \Omega_s$. On parle de résonance quand ces fréquences sont reliées via l'expres-

sion :

$$l\kappa + m(\Omega - \Omega_s) = 0 \tag{2.46}$$

où Ω_s est la fréquence angulaire de rotation de la structure (barre, spirales, etc), et l et m sont des entiers relatifs et naturels respectivement. Avec la corotation, les résonances dont nous parlerons dans la suite sont les résonances de Lindblad (qui ont été étudiées d'abord par Bertil Lindblad), car nous allons voir qu'elles affectent l'évolution de la barre et des spirales. Ces résonances sont définies par m =2 et $l = \pm 1$, où le signe + indique que $\Omega - \Omega_s$ <0, ces étoiles sont au-delà du Rc, c'est la résonance de Lindblad externe (ou OLR pour Outer Lindblad Resonance). Inversement, le signe − indique que $\Omega - \Omega_s$ >0, donc ces étoiles sont sous le Rc, c'est la résonance de Lindblad interne (ou ILR pour Intern Lindblad Resonance). On désigne également les résonances en utilisant la valeur absolue des entiers l et m, avec la notation $|m|$:$|l|$. Dans cette notation les résonances de Lindblad se notent 2 :1, ce qui signifie que pendant que le point guide fait un tour du centre galactique, il y a deux périodes épicycliques.

La Fig. 2.8, est un exemple de diagramme utilisé pour déterminer la position de la corotation et des résonances de Lindblad. Dans cette figure, on trace la vitesse angulaire des étoiles et les valeurs de $\Omega + \kappa/2$ et $\Omega - \kappa/2$ en fonction du rayon. La vitesse de rotation de la structure avec laquelle les étoiles peuvent entrer en résonance est indiquée par la ligne horizontale. Ici, les auteurs de ce diagramme (Yuan & Kuo, 1997), étudient les résonances avec une barre ayant la vitesse angulaire Ω_b =80 $\mathrm{km\,s^{-1}kpc^{-1}}$. Dans ce type de diagramme, les résonances sont aux intersections entre la ligne horizontale et les courbes de vitesses. On retrouve alors l'OLR au-delà de la corotation, et l'ILR sous la corotation, et selon la forme du potentiel, la courbe $\Omega - \kappa/2$ peut présenter un maximum local près du centre galactique, il est alors possible d'avoir trois intersections (et parfois plus) de la ligne horizontale avec cette courbe. Dans ce cas la résonance de Lindblad interne est divisée en deux : la résonance de Lindblad interne interne, la plus plus proche du centre (ou IILR) ; et la résonance de Lindblad interne externe (ou OILR). De ces deux résonances, la plus effective est l'OILR.

Nous allons maintenant décrire les comment se comportent les étoiles à la corotation dans le cas où la structure en rotation est une barre faible (nous expliciterons le terme "faible"). Suivant Binney & Tremaine (1987), nous réutilisons d'abord l'approximation épicycliques développées en Sec. 2.1.2 pour obtenir la solution générale des équations du mouvements, puis nous examinerons le cas des étoiles à la corotation, afin de montrer que la corotation "piège" les étoiles. Par ailleurs, les résonances de Lindblad peuvent piéger les étoiles (Goldreich & Tremaine, 1981), mais nous n'en parlerons pas ici.

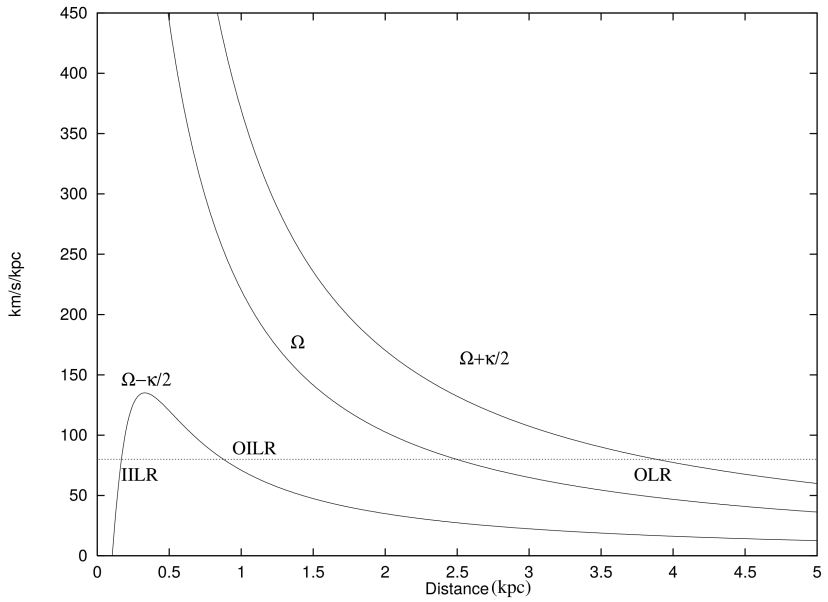

FIGURE 2.8 – Diagramme permettant de localiser les principales résonances entre les étoiles et une structure en rotation dans le disque. En fonction de la distance au centre de la galaxie, les courbes pleines indiquent la vitesse angulaire des étoiles Ω, et la valeur de $\Omega + \kappa/2$ et $\Omega - \kappa/2$. La ligne horizontale en pointillets indique la vitesse angulaire Ω_s de la structure. La corotation et les résonances de Lindblad sont alors localisées aux intersections entre la ligne horizontale et les courbes en traits pleins. (Extrait de Yuan & Kuo (1997))

2.2.1 Solutions générales des équations du mouvement

Nous repartons de l'équation du mouvement 2.34. On utilise l'expression du gradient en coordonnées cylindriques (r, φ, z), et l'expression de l'accélération dans ces coordonnées :

$$\ddot{\mathbf{r}} = (\ddot{r} - r\dot{\varphi}^2)\hat{\mathbf{e}}_r + (2\dot{r}\dot{\varphi} + r\ddot{\varphi})\hat{\mathbf{e}}_\varphi + \ddot{z}\hat{\mathbf{e}}_z \tag{2.47}$$

En posant φ =0 dans le grand axe de la barre, l'équation du mouvement dans le potentiel en rotation avec la barre à la vitesse Ω_b devient :

$$\ddot{r} - r\dot{\varphi}^2 = -\frac{\partial \Psi}{\partial r} + 2r\dot{\varphi}\Omega_b + \Omega_b^2 r \tag{2.48}$$

$$r\ddot{\varphi} + 2\dot{r}\dot{\varphi} = -\frac{1}{r}\frac{\partial \Psi}{\partial \varphi} - 2\dot{r}\Omega_b \tag{2.49}$$

Dans le cas étudié ici, on considère que la barre est faible, i.e. le potentiel gravitationnel créé par la barre est faible devant le potentiel créé par le disque. Ce qui permet de développer le potentiel :

$$\Psi(r,\varphi) = \Psi_0(r) + \Psi_1(r,\varphi) \tag{2.50}$$

où $\Psi_0(r)$ est le potentiel axisymétrique du disque (ordre 0 du développement), et $\Psi_1(r,\varphi)$ est la perturbation non-axisymétrique du potentiel du disque par la barre (ordre 1 du développement), avec $|\Psi_1/\Psi_0| \ll 1$. Nous pouvons également développer les coordonnées :

$$r(t) = r_0 + r_1(t) \quad ; \quad \varphi(t) = \varphi_0(t) + \varphi_1(t) \tag{2.51}$$

On retrouve ici l'idée de l'approximation épicyclique, où les mouvements sont décomposés en une orbite circulaire $(r_0,\varphi_0(t))$, autour de laquelle l'étoile peut effectuer des mouvements de faible amplitude $(r_1(t),\varphi_1(t))$. En remplaçant les termes 2.51 dans l'équation 2.48, on peut ensuite séparer les termes d'ordre 0 et d'ordre 1. Les termes d'ordre 0 à gauche et à droite

doivent se simplifier dans l'équation du mouvement, ce qui impose :

$$r_0 \dot{\varphi_0}^2 = \left(\frac{d\Psi_0}{dr}\right)_{r_0} - 2r_0\dot{\varphi}_0\Omega_b - \Omega_b^2 r_0 \tag{2.52}$$

qui se réécrit

$$r_0(\dot{\varphi}_0 + \Omega_b)^2 = \left(\frac{d\psi_0}{dr}\right)_{r_0} \tag{2.53}$$

On reconnaît dans cette expression la force centrifuge (membre de gauche) et la force issue du potentiel Ψ_0 (membre de droite), toute deux exprimées au rayon r_0 et dont on a simplifié les signes − qui apparaissent dans l'expression de ces deux forces. L'équation 2.53 est donc l'expression de l'équilibre entre la force centrifuge et l'attraction gravitationnelle. On définit $\Omega_0 \equiv \Omega(r_0)$ avec

$$\Omega(r) \equiv \pm\sqrt{\frac{1}{r}\frac{d\Psi_0}{dr}} \tag{2.54}$$

où 2.54 est l'expression de la vitesse circulaire des étoiles au rayon r dans le potentiel Ψ_0. On peut alors réécrire puis intégrer l'équation 2.53 :

$$\dot{\varphi}_0 = \Omega_0 - \Omega_b \quad \xrightarrow{\text{intégration}} \quad \varphi_0(t) = (\Omega_0 - \Omega_b)\,t \tag{2.55}$$

L'équation 2.55 décrit l'orbite guide circulaire, qui est prograde ($\Omega_0 - \Omega_b > 0$) pour $r_0 <$Rc, et rétrograde ($\Omega_0 - \Omega_b < 0$) pour $r_0 >$Rc.

Nous allons maintenant nous intéresser aux termes d'ordre 1 qui apparaissent dans les équations 2.48 et 2.49 :

$$\ddot{r_1} + \left(\frac{d^2\Psi_0}{dr^2} - \Omega^2\right)_{r_0} r_1 - 2r_0\Omega_0\dot{\varphi}_1 = -\left(\frac{\partial\Psi_1}{\partial r}\right)_{r_0} \tag{2.56}$$

$$\ddot{\varphi}_1 + 2\Omega_0\frac{\dot{r_1}}{r_0} = -\frac{1}{r_0^2}\left(\frac{\partial\Psi_1}{\partial\varphi}\right)_{r_0} \tag{2.57}$$

À présent, nous avons besoin de définir le potentiel Ψ_1 créé par la barre, et nous choisissons de l'exprimer de la façon suivante :

$$\Psi_1(r,\varphi) = \Psi_b(r)\cos(m\varphi) \tag{2.58}$$

où m =2 car nous nous intéressons au potentiel créé par une barre, et il faut Ψ_b <0 pour que φ =0 soit dans le grand axe de la barre, c'est-à-dire pour placer les maximas du potentiel effectif perpendiculairement à la barre, en $\varphi = \pm\frac{\pi}{2}$. Comme $\varphi_1 \ll \varphi_0$, nous faisons l'approximation $\varphi(t) \equiv \varphi_0(t)$ dans l'équation 2.58, avec φ_0 connu grâce à l'équation 2.55. En remplaçant dans les équations 2.56 et 2.57, il vient :

$$\ddot{r_1} + \left(\frac{d^2\Psi_0}{dr^2} - \Omega^2\right)_{r_0} r_1 - 2r_0\Omega_0\dot{\varphi_1} = -\left(\frac{d\Psi_b}{dr}\right)_{r_0} \cos[m(\Omega_0-\Omega_b)t] \tag{2.59}$$

$$\ddot{\varphi_1} + 2\Omega_0\frac{\dot{r_1}}{r_0} = \frac{m\Psi_b(r_0)}{r_0^2}\sin[m(\Omega_0-\Omega_b)t] \tag{2.60}$$

En intégrant l'équation 2.60, on obtient :

$$\dot{\varphi_1} = -2\Omega_0\frac{r_1}{r_0} - \frac{\Psi_b(r_0)}{r_0^2(\Omega_0-\Omega_b)}\cos[m(\Omega_0-\Omega_b)t] + Cste \tag{2.61}$$

ce qui permet de remplacer $\dot{\varphi_1}$ dans l'équation 2.59, ce qui donne :

$$\ddot{r_1} + \kappa_0^2 r_1 = -\left[\frac{d\Psi_b}{dr} + \frac{2\Omega\Psi_b}{r(\Omega-\Omega_b)}\right]_{r_0} \cos[m(\Omega_0-\Omega_b)t] + Cste \tag{2.62}$$

avec

$$\kappa_0^2 = \left(\frac{d^2\Psi_0}{dr^2} + 3\Omega^2\right)_{r_0} = \left(r\frac{d\Omega^2}{dr} + 4\Omega^2\right)_{r_0} \tag{2.63}$$

qui est la fréquence épicyclique (voir Sec. 2.1.2). La constante d'intégration qui apparaît peut être absorbée dans la valeur de r_1. L'équation du mouvement obtenue (2.62) est celle d'un

oscillateur harmonique de fréquence naturelle κ_0, qui est forcé à la fréquence $m(\Omega_0 - \Omega_b)$. La solution générale pour ce type d'équation est :

$$r_1(t) = C_1 \cos(\kappa_0 t + \psi) - \left[\frac{d\Psi_b}{dr} + \frac{2\Omega\Psi_b}{r(\Omega - \Omega_b)} \right]_{r_0} \frac{\cos[m(\Omega_0 - \Omega_b)t]}{\Delta} \tag{2.64}$$

Dans cette expression C_1 et ψ sont des constantes arbitraires, et nous avons définit :

$$\Delta \equiv \kappa_0^2 - m^2(\Omega_0 - \Omega_b)^2 \tag{2.65}$$

Finalement, on remplace la variable t par la variable φ_0 en utilisant l'expression 2.55. Il vient :

$$r_1(\varphi_0) = C_1 \cos\left(\frac{\kappa_0 \varphi_0}{\Omega_0 - \Omega_b} + \psi \right) + C_2 \cos(m\varphi_0) \tag{2.66}$$

avec

$$C_2 \equiv -\frac{1}{\Delta} \left[\frac{d\Psi_b}{dr} + \frac{2\Omega\Psi_b}{r(\Omega - \Omega_b)} \right]_{r_0} \tag{2.67}$$

L'équation 2.66, décrit les orbites stellaires de façon générale dans le potentiel créé par un disque perturbé par une barre faible. L'expression est valide partout, contrairement à l'analyse faite en section 2.1.3 qui ne concernait que le voisinage des points de Lagrange. On remarque cependant que l'équation 2.66 a une forme similaire à la composante x de l'équation 2.43, à ceci prêt qu'on a maintenant explicité toutes les constantes qui interviennent dans l'expression. Par ailleurs, cette expression permet de décrire aussi bien les orbites fermées (dans le cas où C_1 =0) que les orbites ouvertes, qui sont la superposition d'une orbite fermée et de petites perturbations (dans le cas où $C_1 \neq 0$, sauf si il y a résonance).

On remarque également que l'expression 2.66, suggère l'existence de cas particuliers, qui sont les résonances. En effet, l'expression diverge pour $\Omega_0 = \Omega_b$, c'est-à-dire pour la corotation, il est alors nécessaire de traiter ce cas de façon un peu plus détaillée, ce que nous ferons en Sec. 2.2.2. Aussi, si Ω et κ sont liés par l'expression 2.46, avec $l = \pm 1$ l'expression 2.65 est nulle, ce qui fait aussi diverger les équations. Dans ce cas, il s'agit des résonances de Lindblad puisque nous avons choisi m =2.

2.2.2 Étoiles piégées à la corotation

Les équations 2.66 et 2.67 divergent au rayon de corotation, quand $\Omega_0 = \Omega_b$. Par conséquent l'approche utilisée dans la section précédente doit être modifiée pour comprendre le comportement des étoiles au niveau de cette résonance. Nous réécrivons les équations du mouvement 2.56 et 2.57, en nous plaçant au point L5 i.e. $\Omega(r_0) = \Omega_b$ et $\varphi_0 = \frac{1}{2}\pi$, et en utilisant l'expression des fréquences épicycliques (Eq. 2.23) :

$$\ddot{r_1} + (\kappa_0^2 - 4\Omega_0^2) r_1 - 2 r_0 \Omega_0 \dot{\varphi_1} = -\frac{\partial \Psi_1}{\partial r} \tag{2.68}$$

$$\ddot{\varphi_1} + 2\Omega_0 \frac{\dot{r_1}}{r_0} = -\frac{1}{r_0^2}\frac{\partial \Psi_1}{\partial \varphi} \tag{2.69}$$

En utilisant l'analyse des orbites autour de L4 et L5 dans des potentiels analytiques de barre (voir Binney & Tremaine (1987)), on peut montrer : (i) que quand l'excentricité e des orbites tend vers 0, la composante non axisymétrique du potentiel (qui correspond à la barre) est proportionnelle à e^2 i.e. la barre est faible ; (ii) que les orbites à proximité des points de Lagrange stables (L3, L4, L5) sont une superposition de deux mouvements elliptiques aux fréquences α et β (conformément à l'analyse en Sec. 2.1.3) ; (iii) que lorsque $e \to 0$ les ellipses β sont des épicycles ; (iv) que les ellipses α sont très allongées dans la direction azimutale, avec $|Y_1/X_1| = e$; (v) que ces dernières ont une faible fréquence, avec $\alpha = e\Omega_b$.

Cette analyse permet de faire des hypothèses quant à l'ordre des termes dans l'expression 2.68. Lorsque la barre est faible ($e \ll 1$) : Ψ_1 est d'ordre e^2 d'après (i) ; r_1 est d'ordre e d'après (iv) ; φ_1 est d'ordre 1 d'après (iv) car les mouvements sont amples dans la direction azimutale ; $\dot{\varphi_1}$ est d'ordre e d'après (v) ; Par ailleurs, une dérivée temporelle revient à une multiplication par e. Ainsi, on ne conservant que les termes d'ordre e dans l'expression 2.68, il vient :

$$(\kappa_0^2 - 4\Omega_0^2) r_1 - 2 r_0 \Omega_0 \dot{\varphi_1} = 0 \tag{2.70}$$

Qui permet d'éliminer r_1 en substituant 2.70 dans 2.69 :

$$\ddot{\varphi_1}\left(\frac{\kappa_0^2}{\kappa_0^2 - 4\Omega_0^2}\right) = -\frac{1}{r_0^2}\left.\frac{\partial \Psi_1}{\partial \varphi}\right|_{(r_0, \varphi_0 + \varphi_1)} \tag{2.71}$$

Alors, en utilisant l'expression 2.58 pour remplacer Ψ_1, on obtient

$$\ddot{\varphi_1} = -\frac{2\Psi_b}{r_0^2}\left(\frac{4\Omega_0^2 - \kappa_0^2}{\kappa_0^2}\right)\sin[2(\varphi_0 + \varphi_1)] \tag{2.72}$$

L'expression 2.72, peut alors se réécrire ainsi :

$$\frac{d^2\psi}{dt^2} = -p^2 \sin\psi \tag{2.73}$$

avec

$$\psi \equiv 2\varphi_1 \qquad \text{et} \qquad p^2 \equiv \frac{4}{r_0^2}|\Psi_b(r_0)|\frac{4\Omega_0^2 - \kappa_0^2}{\kappa_0^2} \tag{2.74}$$

Précisons que la différence $4\Omega_0^2 - \kappa_0^2$ dans l'expression de p^2, est toujours positive (Binney & Tremaine, 1987), assurant la validité de l'équation obtenue. Par ailleurs, la singularité qui apparaissait dans l'équation 2.66 a disparue. L'expression 2.74 est l'équation d'un pendule pour la position azimutale φ_1 de l'étoile, avec φ_1 =0 quand l'étoile est à l'azimut du point L5.

Analysons maintenant le mouvement décrit par 2.74. Le point d'équilibre est en φ_1=0, c'est-à-dire au maximum du potentiel Ψ_1, et non au minimum. Dans le mouvement du pendule, il existe une énergie limite en dessous de laquelle le pendule oscille autour de la position d'équilibre, et si l'énergie est supérieure à cette limite, le pendule effectue des tours complets autour de son point d'attache. Le même phénomène se retrouve ici, l'énergie du pendule est donnée par :

$$E_p = \frac{1}{2}\dot{\psi}^2 - p^2\cos\psi \tag{2.75}$$

et si $E_p \leq p^2$ l'azimut de l'étoile oscille autour du point de Lagrange L5 (en $\varphi_0 = \frac{1}{2}\pi$), elle est donc piégée par le point de Lagrange. En revanche, si $E_p > p^2$, l'étoile effectue des tours complets autour du centre de la galaxie, elle n'est donc pas piégée par le point de Lagrange. Par symétrie, ces résultats sont également valables autour du point L4.

En injectant l'équation 2.75, dans 2.70, on obtient :

$$r_1 = -\frac{2r_0\Omega_0\dot{\varphi_1}}{4\Omega_0^2-\kappa_0^2} = \pm\left(\frac{r_0\Omega_0}{4\Omega_0^2-\kappa_0^2}\right)\sqrt{2[E_p + p^2\cos(2\varphi_1)]} \tag{2.76}$$

qui est alors l'expression du mouvement autour des points stables L4 et L5. Contrairement, aux expressions obtenues en section 2.1.3 qui ne sont valables qu'à proximité des points de Lagrange, l'expression 2.76 est valable quelque soit l'amplitude des mouvements autour de L4 ou L5, dans le cas où la perturbation du potentiel par la barre est faible. La forme de ces orbites est représentée dans la Fig. 2.5, leur aspect incurvé autour des points L4 ou L5 leur vaut le nom d'orbites en "fer à cheval". Comme les points L4 et L5 sont proches du rayon de corotation, les étoiles piégées autour de ces points oscillent d'un côté à l'autre de la corotation, avec des périodes différentes selon leur position initiale, ce qui a pour effet de *mélanger* les étoiles autour du rayon de corotation.

Dans cette section, nous avons donc montré comment les étoiles peuvent être piégées par la corotation avec la barre, autour des points de Lagrange L4 et L5. Toutefois, cette conclusion est obtenue pour une barre rigide, c'est-à-dire sans évolution. Dans l'article Kubryk, Athanassoula, Prantzos (à soumettre) donné en Sec. 2.4, nous examinons le cas où la barre évolue (le rayon de corotation se déplace), et étudions dans ce cas le piégeage des étoiles, et nous décrivons le lien de ce phénomène avec la migration radiale des étoiles.

2.3 Formation et évolution des structures non-axisymétriques dans les disques galactiques

Les études de l'Univers proche permettent d'estimer la fraction de galaxies elliptiques, disques, spirales et barrées. Aguerri, Méndez-Abreu & Corsini (2009) notamment, ont étudié un échantillon de 3060 galaxies issues du catalogue spectroscopique du SDSS-Data Release 5 (Adelman-McCarthy et al., 2007). Ces galaxies ont été sélectionnées en redshift, en magnitude absolue, en inclinaison et selon leur voisinage : dans l'intervalle de redshift 0.01<z<0.04 , avec une magnitude absolue M_r <-20, et avec b/a >0.5 pour éviter les effets de projection dus à l'inclinaison (où a et b sont le semi grand axe et le semi petit axe respectivement), et seules les galaxies n'étant pas à proximité d'autres objets ont été retenues. Le résultat de cette étude montre que 26% des galaxies de l'échantillon sont des galaxies elliptiques, 29% sont des galaxies lenticulaires, 20% sont des spirales de type précoce et 25% sont des spirales de type tardif. Autrement dit, environ 3/4 des galaxies de l'Univers proche sont des disques (étant soit lenticulaires, spirales précoces, ou spirales tardives). Enfin, parmi ces galaxies disques, la fraction de galaxies barrées est de 45%. La fraction de galaxies barrée dépend également du type de galaxie disque : 29% des lenticulaires ont une barre, 55% et 54% des spirales précoces et tardives respectivement ont une barre.

Dans les années 60 et 70 l'étude des galaxies et de leurs structures se faisait à l'aide d'outils analytiques basés essentiellement sur l'équation de Poisson, permettant de connaître le potentiel gravitationnel créé par un disque et ses structures ; et sur la distribution de Boltzmann qui permet de décrire la répartition des étoiles dans l'espace des phases ; et par des calculs d'orbites dans des potentiels spécifiques. Ces études analytiques considéraient des potentiels statiques, c'est-à-dire des galaxies dont les structures n'évoluent pas avec le temps, et ont permis de grandes avancées dans le domaine de la dynamique des galaxies, et sur la théorie des orbites (Binney & Tremaine, 1987). Au cœur de ces travaux, se retrouve souvent la friction dynamique, qui est un échange d'énergie cinétique entre une étoile et une structure massive lorsqu'elles passent à proximité l'une de l'autre. Dans les disques, où le mouvement de rotation des étoiles autour du centre galactique est décrit par son moment angulaire, la friction dynamique produit un échange de moment angulaire.

Toutefois, dès l'arrivée des premières simulations il est devenu clair que les disques galactiques et leurs structures changent avec le temps. Lorsque les changements sont lents (de l'ordre du milliard d'années ou plus) on parle "l'évolution séculaire" (Kormendy, 1979), par opposition aux processus d'évolution plus rapide (de l'ordre de la centaine de millions d'années). Et les travaux de Little & Carlberg (1991), ont montré que certaines approximations nécessaires pour mener les calculs analytiques ne permettent pas de décrire la réalité avec précision.

Nous avons vu dans les sections précédentes que les structures non-axisymétriques peuvent avoir une influence forte sur la migration radiale. Toutefois, les résultats analytiques sont obtenus dans le cas de structures rigides. Dans la section 2.4, je présenterai les résultats des travaux menés pendant ma thèse sur la migration radiale dans le cas où les structures évoluent. Mais avant d'aborder ce sujet, je vais rappeler dans cette section les mécanismes via lesquels les structures non-axisymétriques se forment. Je commencerai donc, par discuter des spirales, en abordant le modèle des modes spiraux, et le modèle des bras spiraux transitoires, puis je discuterai de la barre.

2.3.1 Les modes spiraux stationnaires

Les bras spiraux sont encore des structures dont les modèles de formation ne sont pas parfaitement établis. Les spirales ne peuvent pas être des structures matérielles, en effet, à cause de la diminution de la vitesse angulaire des étoiles en fonction du rayon galacto-centrique, les spirales s'étireraient et s'enrouleraient autour du centre galactique (Fig. 2.9). Ainsi elles présenteraient un aspect qui n'a jamais été observé dans les galaxies réelles, et auraient une durée de vie très courte, de seulement quelques rotations i.e. quelques centaines de millions d'années.

La Fig. 2.10 donne un exemple de spirale galactique. Il s'agit ici de la galaxie M51, qui présente deux bras spiraux très marqués et presque symétriques. Ce type de spirale est appelé "grand design", par opposition aux spirales floconneuses dont un exemple est donné en Fig. 2.12.

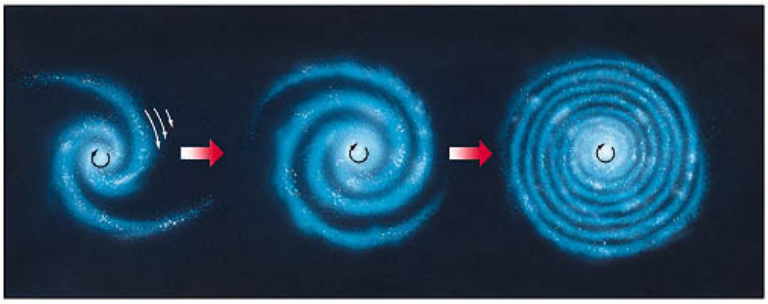

FIGURE 2.9 – Illustration des effets de la différence de vitesse angulaire sur des spirales considérées comme des objets matériels. (depuis ircamera.as.arizona.edu)

Dans le premier modèle viable de spirales, celles-ci sont vues comme des ondes de densité se propageant dans les disques galactiques. Ce modèle, présenté d'abord par Lindblad (1958), a été ensuite largement développé par Lin, Yuan & Shu (1969) et Shu (1970), jusqu'à ce que le modèle arrive finalement à maturité avec Lynden-Bell & Kalnajs (1972); Bertin et al. (1989a,b); Lowe et al. (1994), qui ont proposé un mécanisme pour la formation des ondes spirales permettant de comprendre pourquoi les disques forment de telles structures.

Dans ce modèle les bras ont une vitesse angulaire constante, ce qui n'est pas le cas des étoiles (qui ont une vitesse angulaire plus élevée vers le centre galactique) ainsi il existe un unique rayon auquel les étoiles tournent à la même vitesse que la spirale : c'est le rayon de corotation (Rc). Sous le Rc, les étoiles tournent plus vite que la spirale et la dépasse, tandis qu'au-delà du Rc, les étoiles tournent moins vite. Ainsi la spirale exerce sur les étoiles sous le Rc une force gravitationnelle qui tend à ralentir les étoiles (elles cèdent du moment angulaire à la spirale), à l'inverse les étoiles situées au-delà du Rc sont entraînées vers l'avant par la spirale (la spirale leur transmet du moment angulaire). Par conséquent, la spirale permet de transférer le moment angulaire des étoiles des parties internes du disque vers les parties externes. Nous allons maintenant voir en quoi ce transfert de moment angulaire joue un rôle fondamental, permettant aux disques galactiques de tendre vers l'équilibre thermodynamique.

Les disques galactiques sont des objets isolés, et composés de particules (les étoiles) auxquels s'appliquent donc la deuxième loi de la thermodynamique : les disques tendent à augmenter leur entropie jusqu'à atteindre l'équilibre thermodynamique. Pour un disque galactique, augmenter l'entropie revient à augmenter l'énergie des mouvements épicycliques de ses étoiles : c'est le "chauffage" du disque i.e. les étoiles passent d'orbites circulaires à des orbites présentant des oscillations radiales et verticales de plus en plus amples et rapides. L'énergie des épicycles étant décrite par les équations 2.32 et 2.33, cependant nous ne considérons ici que l'énergie E_r des mouvements dans le plan du disque.

Décrit en termes de position des étoiles dans l'espace des phases, un disque froid et mince est composé d'étoiles en orbites circulaires, qui occupent une faible portion de l'espace des phases, l'entropie du disque est donc faible. En revanche un disque chaud, est composé

FIGURE 2.10 – Observation de la galaxie M51, une spirale "grand design" typique, avec sa galaxie satellite en haut à droite. (Credit : NASA, Hubble Heritage Team, (STScI/AURA), ESA, S. Beckwith (STScI))

d'orbites présentant des oscillations épicycliques amples avec une distribution de vitesses plus large. Par conséquent les étoiles d'un disque "chaud" occupent une plus grande fraction de l'espace des phases, un tel disque possède alors une entropie supérieure.

Le mécanisme pour augmenter l'énergie des mouvements épicycliques fait intervenir l'énergie de Jacobi (Eq. 2.37), qui est une quantité conservée lors du mouvement. Par conséquent, les variations de l'énergie totale $E = E_c + E_r$ (avec E_c l'énergie de l'orbite circulaire) en fonction de la variation de moment angulaire L_z pour une étoile s'exprime :

$$\frac{dE}{d(L_z)} = \Omega_s \Longrightarrow E(L_z) = \Omega_s L_z \tag{2.77}$$

c'est-à-dire que lorsque le moment angulaire d'une étoile est modifié, elle se déplace linéairement dans le plan (E, L_z), suivant une droite de pente Ω_s, comme illustré en Fig. 2.11. Cette figure représente un diagramme de Lindblad qui permet de visualiser facilement où sont les orbites circulaires (sur la bordure de la zone grisée), et les orbites ayant une énergie épicyclique non-nulle (zone claire). La zone grisée dans cette figure indique les états inaccessibles pour les étoiles. Les flèches indiquent comment se déplacent les étoiles, dans le plan (E, L_z) lorsque leur moment angulaire est modifié, selon l'Eq. 2.77. Dans cette figure, est aussi indiquée la région où les étoiles tournent à la même vitesse que le mode spiral : au niveau du rayon de corotation (Rc). On constate alors, que les étoiles sur des orbites circulaires initialement sous le

Rc (et donc dans les régions internes du disque) ne peuvent que perdre du moment angulaire, et alors acquérir de l'énergie épicyclique (elles vont de la bordure de la zone grisée, vers la zone claire). À l'inverse, les étoiles en orbites circulaires au-delà du Rc (dans les régions externes du disque) ne peuvent qu'augmenter leur moment angulaire, et ce faisant, elles augmentent également leur énergie épicyclique (elles vont également dans la zone claire du diagramme).

En résumé, pour atteindre l'équilibre thermodynamique, un disque doit voir augmenter son entropie, ce qui se fait lorsque les étoiles passent des orbites circulaires à des orbites présentant des oscillations epicycliques, en augmentant l'énergie des mouvements épicycles. D'après l'Eq. 2.77 pour augmenter cette énergie, il faut faire varier le moment angulaire des étoiles. Lynden-Bell & Kalnajs (1972) ont montrer que des résonances entre les étoiles et la spirale permettent aux étoiles sous le Rc de céder leur moment angulaire aux bras spiraux, qui eux mêmes transmettent ce moment angulaire aux étoiles au-delà du Rc, produisant ainsi le chauffage du disque nécessaire pour atteindre l'équilibre thermodynamique.

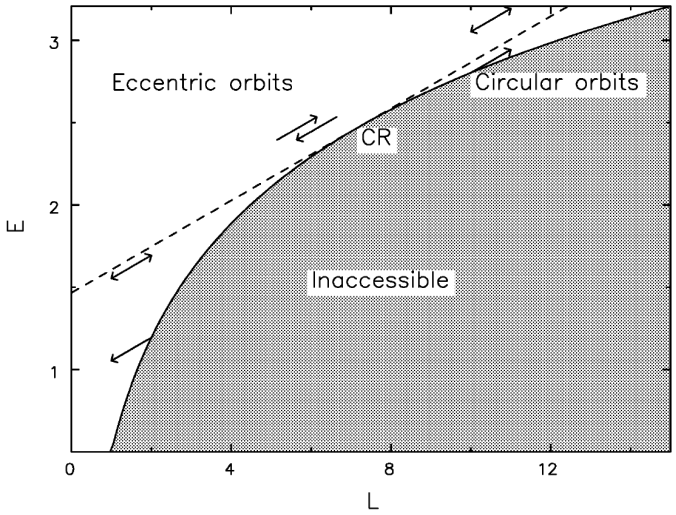

FIGURE 2.11 – Diagramme de Lindblad (extrait de Sellwood & Binney (2002)). La région grisée est inaccessible pour les étoiles, cette région est délimitée par la courbe indiquant l'énergie des étoiles en orbites circulaires, en fonction de leur moment angulaire. Par conséquent, toutes les étoiles de la région claire sont sur des orbites non-circulaires i.e. ces étoiles ont une énergie épicyclique non-nulle.

Toutefois, cette théorie de Lin, Shu, Lynden-Bell et Kalnajs (LSLBK) repose sur une approximation permettant de rendre l'influence des bras spiraux plus locale. En effet, l'action d'un bras spiral se propage par interaction gravitationnelle dans tout le disque, affectant alors toutes les étoiles. L'approximation qui a permis d'écrire la théorie de la propagation des spirales dans les disques, consiste à travailler avec des spirales étroitement enroulées. Ainsi, un bras spiral (qui est une surdensité) est immédiatement suivi par une sous-densité d'étoiles, elles même suivi de près par un nouveau bras spiral, etc. Il en résulte qu'à suffisamment grande

échelle (dépendant de l'étroitesse choisie entre les spirales) les surdensités et sous-densités s'annulent vis à vis de la gravitation. Cette approximation permet donc de mettre en équation la propagation de proche en proche de l'onde de surdensité, ce qui est mathématiquement plus "facile" dans le sens où les équations sont alors linéaires. Cependant, les solutions fournies dans le formalisme de LSLBK ne forment pas une base complète de solutions, c'est-à-dire que toutes les solutions ne peuvent pas être exprimées dans ce cadre.

Certaines équations provenant initialement de la physique des plasmas, fournissent une meilleure description de la propagation des spirales. En effet, un plasma est un fluide composé de particules chargées électriquement, qui interagissent alors à la fois par collision, mais aussi par le biais de l'interaction électromagnétique qui, comme la gravitation, est une interaction à longue distance. Par conséquent, dans les plasmas, une surdensité de particules chargées peut avoir des effets non-locaux, de la même manière qu'une surdensité d'étoiles peut influencer toutes les étoiles du disque galactique.

Les équations en question sont celles de Van Kampen (1955), et concernent les ondes stationnaires dans les plasmas au sein desquels les collisions sont négligeables, et seule l'interaction à longue distance est considérée, ce qui constitue un comportement similaire à celui des étoiles dans les galaxies. Les modes stationnaires issus de ces équations forment une base complète de solutions, ce qui n'est pas le cas de la théorie de LSLBK. Mais ces modes n'ont pas d'équation de dispersion pour lier le vecteur d'onde à la pulsation de chaque mode, par conséquent toutes les pulsations sont des solutions acceptables i.e. il n'y a pas de nombre de bras privilégié. Il est alors nécessaire de faire intervenir des paramètres supplémentaires pour expliquer le nombre de bras dans chaque galaxie.

Ces paramètres viennent par exemple de l'environnement de la galaxie. En effet, les spirales "grand design" dont les exemples typiques sont M51, M81 ou NGC 5364, ont toujours une galaxie voisine, comme l'illustre par exemple la Fig. 2.10. Ce qui implique une asymétrie du potentiel gravitationnel. Les disques galactiques semblent donc répondre à cette perturbation par la formation de deux bras spiraux très marqués et approximativement symétriques l'un de l'autre. Cependant rien n'indique que les bras ainsi formés persisteront si la galaxie voisine fini par s'éloigner de la galaxie étudiée.

Cependant, ces travaux ont permis de mettre en évidence un mécanisme pour la croissance des spirales. Ils ont montré que la résonance de Lindblad interne et la corotation se comportent vis à vis des ondes de densité comme des barrières réflectives et semi-réflectives respectivement, formant ainsi une cavité résonante dont les spirales sont des modes propres.

2.3.2 Les bras spiraux transitoires

Le modèle alternatif aux modes stationnaires des disques stellaires, est celui des "feuilles en cisaillement", c'est-à-dire des disques infiniment minces, dans lesquels il existe un différentiel de vitesse. Comparé au modèle de la section précédente, le modèle de la feuille en cisaillement

FIGURE 2.12 – Observation de la galaxie NGC 4414, un exemple de spirale "floconneuse", i.e. une organisation complexe de spirales. (Crédit : NASA et ESA)

ne considère qu'une petite région du disque devant la taille du disque total.

Ce modèle est développé indépendamment par Goldreich & Lynden-Bell (1965), Julian & Toomre (1966) et plus récemment Fuchs (2001), et montre que les disques en rotation différentielle sont instables et que de petites perturbations dans la répartition du gaz (comme les nuages), sont les graines induisant la formation de bras spiraux. Le mécanisme d'amplification des instabilités est appelé "amplification par balancement", c'est un phénomène non-linéaire permettant de très fortes amplifications des instabilités.

Aussi, dans ce modèle de multiples bras spiraux peuvent se former puis disparaître de façon continue, se qui peut laisser apparaître une organisation complexe des bras spiraux. La Fig. 2.12 illustre une spirale dont le schéma est complexe, par opposition aux spirales "grand design". Il s'agit ici de la galaxie NGC 4414.

La première étape de ce mécanisme est la formation d'un bras précurseur, qui pointe vers l'avant (dans le sens de la rotation des étoiles). Du fait de la rotation différentielle du disque, se bras se retourne pour devenir un bras "traînant", qui pointe dans le sens opposé de la rotation des étoiles. Lors de la phase de retournement, la densité d'étoiles dans le bras augmente et forme le bras final : c'est l'amplification par balancement.

Comme on peut le voir dans la Fig. 2.14, extraite de Julian & Toomre (1966), les bras spiraux sont liés aux mouvements épicycliques des étoiles. En effet, l'étoile considérée a un mouvement circulaire au départ (sans oscillations radiales). Quand la graine rattrape l'étoile (qui

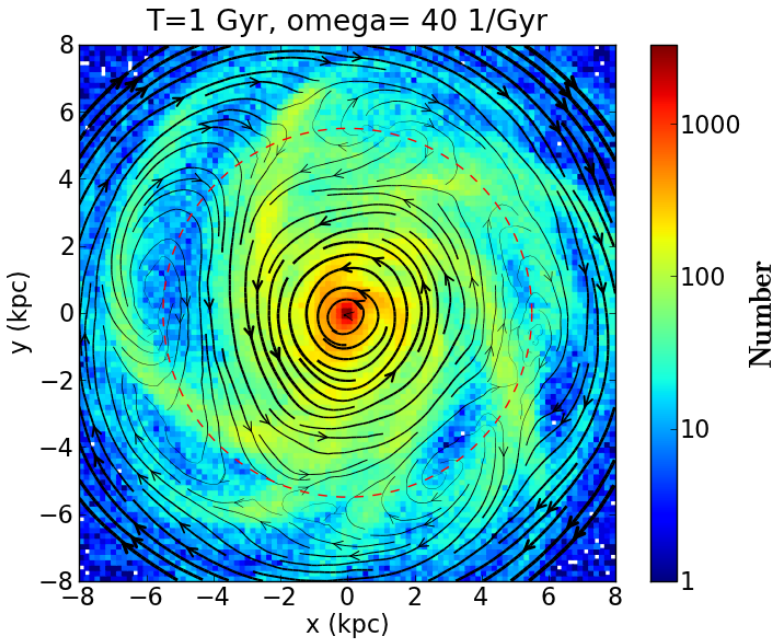

[p]

FIGURE 2.13 – Dans une simulation N-corps+SPH (Gadget3) à 1 Gyr, représentation de la trajectoire des étoiles dans un référentiel tournant à 40 Gyr^{-1}. L'échelle de couleur indique la densité d'étoiles, les courbes noires la vitesse moyenne des étoiles dans chaque pixel. Plus ces courbes sont épaisses, plus les étoiles vont vite, et les flèches indiquent le sens de rotation. Le cercle rouge en tirets, indique le rayon auquel les étoiles tournent à la même vitesse que le référentiel.

va moins vite parce que plus éloignée du centre galactique), elle cède du moment angulaire à l'étoile, qui amorce alors des mouvements épicycliques d'oscillations radiales. Les cercles sur la trajectoire de l'étoile indiquent des durées égales, on constate alors que l'étoile va plus lentement après avoir dépassé la graine, quand elle est plus proche du centre (les cercles sont plus rapprochés les uns des autres). Or les régions où les étoiles se déplacent plus lentement sont nécessairement plus dense en étoiles. Et ces régions sont agencées en bras spiraux. Une fois la spirale formée, la densité de la région est augmentée, ce qui permet de renforcer les effets de la perturbation du moment angulaire des étoiles et donc de précipiter encore d'avantage les étoiles dans les bras spiraux. Par ailleurs, la ligne horizontale en tirets longs et courts alternativement, indique le rayon moyen de l'étoile, après le passage de l'étoile à proximité de la graine, c'est le rayon de l'orbite guide. On observe que cette ligne se prolonge un peu au-dessus du rayon initial de l'étoile, cette étoile a donc vécu un épisode de churning vers l'extérieur, bien que cette migration soit ici de très faible amplitude.

Quant aux étoiles plus proches du centre galactique, qui tournent plus rapidement que la graine, elles perdent du moment angulaire lorsqu'elles dépassent la graine. Il en résulte également un mouvement épicyclique et une régions où les étoiles deviennent plus lentes.

Le phénomène décrit ci-dessus, est également en accord avec les considérations évoquées dans la section précédente sur l'équilibre thermodynamique des disques galactiques. En effet, dans ce modèle la variation du moment angulaire des étoiles se fait grâce aux spirales, ce qui a pour effet de chauffé le disque, et donc de le faire tendre vers son équilibre thermodynamique.

Enfin, comme ce mécanisme chauffe les étoiles du disque, il ne produit que des bras spiraux transitoires. En effet, si les étoiles acquièrent de trop larges mouvements épicycliques, leurs orbites finissent par être trop désorganisées, et n'arrivent plus à se synchroniser pour former un bras spiral : le chauffage du disque permet de le rendre stable vis à vis de la formation de bras spiraux.

D'après Toomre (1981), le mécanisme de l'amplification par balancement est le mécanisme principal de formation des bras spiraux, ce qui implique que les bras observés dans les galaxies sont transitoires.

À l'aide de simulations à très haute résolution D'Onghia, Vogelsberger & Hernquist (2013), ont confirmé que lorsque le bruit est faible dans la densité du disque, aucun bras spiral n'apparaît dans la simulation pendant au moins les trois premières rotations du disque. En revanche, dans ces mêmes simulations, des spirales transitoires apparaissent en moins d'une année galactique lorsque sont ajoutées dans le gaz des particules plus denses que les autres, et comparables à des nuages de gaz moléculaires géants. La conclusion est que ces particules servent de graines pour la formation des bras spiraux. Il est intéressant de noter qu'actuellement seules des spirales transitoires ont été produites dans les simulations N-corps. Baba, Saitoh & Wada (2013) ont également montré que le mécanisme de l'amplification par balancement est à l'origine des bras spiraux transitoires et récurrents observés dans leurs simulations N-corps.

Les simulations N-corps ont également permis de vérifier que les bras transitoires sont différents des modes stationnaires évoqués dans la section précédente. En effet, les modes stationnaires ont une vitesse de rotation unique, ils tournent de façon rigide. En revanche, les bras transitoires ont une vitesse angulaire qui diminue vers l'extérieur du disque, de la même façon que les étoiles (Grand, Kawata & Cropper, 2012, 2014; Baba, Saitoh & Wada, 2013). Les bras transitoires sont donc en corotation avec les étoiles quelque soit le rayon considéré. Par ailleurs, ce comportement des bras spiraux à été confirmé dans les observations des galaxies proches M51, NGC 1068, M101, IC 342, NGC 3938 et NGC 3344 (Merrifield, Rand & Meidt, 2006; Meidt et al., 2008; Meidt, Rand & Merrifield, 2009).

2.3.3 La barre centrale

Comme nous l'avons déjà dit, les observations montrent qu'un peu plus de la moitié des galaxies spirales forment une barre en leur centre. Nous donnons un exemple de ce type de galaxie dans la Fig. 2.15 montrant la galaxie UGC 12158. Dans les simulations, les disques forment spontanément une barre car ils sont initialement hors de l'équilibre thermodynamique. En

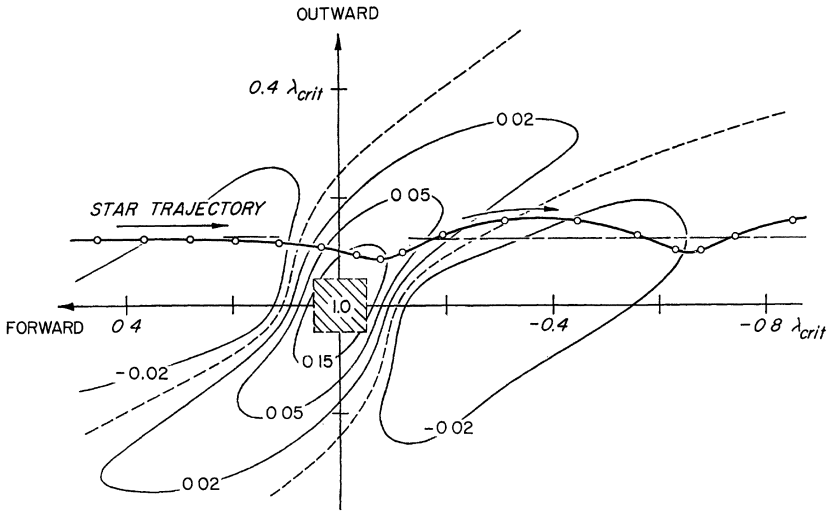

[p]

FIGURE 2.14 – Exemple d'une trajectoire d'étoile passant à proximité d'une surdensité (la graine du bras spiral est indiquée par le carré hachuré). Les courbes pleines sont les courbes d'égales sur-densité d'étoiles. Les courbes en tirets sont les courbes d'égales sous-densité d'étoiles. (extrait de Julian & Toomre (1966)). Le mouvement de l'étoile est montré dans le référentiel en rotation avec la surdensité constituant la graine du bras (le carré hachuré). L'étoile considérée est à un rayon galactocentrique plus grand que la graine, par conséquent elle tourne moins vite que la graine.

effet, nous avons mentionné au sujet des spirales que les structures non-axisymétriques permettent aux disques de tendre vers l'équilibre thermodynamique, c'est donc aussi le cas des barres.

Les travaux de Little & Carlberg (1991), ont montré comment la friction dynamique entre le barre et les étoiles contribue aux échanges de moment angulaires. Toutefois, ces travaux ont été menés dans le cadre de barres rigides, or les simulations numériques montrent que les barres évoluent avec le temps : leur taille et leur vitesse de rotation peuvent changer. Différentes études ont montré que les échanges de moment angulaire, sont le moteur de l'évolution des structures dans les disques galactiques. Nous avons déjà mentionné Lynden-Bell & Kalnajs (1972) à propos de la formation des spirales. Mark (1976) a montré qu'un moyen d'amplifier une onde spirale est de faire diminuer le moment angulaire du disque, en le transférant au halo de matière noire, via les résonances entre la spirale les étoiles et le halo. Kormendy (1979) puis Sellwood (1980) sont les premiers à proposer que ces mêmes échanges soient le moteur de l'évolution séculaire de la barre. D'autres travaux sur les simulations N-corps sont ensuite venu approfondir ces résultats, en particulier L. Athanassoula (avec Athanassoula (2002) ;Athanassoula & Misiriotis (2002) et Athanassoula (2003)) sur l'étude de l'échange du moment angulaire entre la barre, le disque et le halo.

Par ailleurs, les travaux de Little & Carlberg (1991) portant à la fois sur les aspects analytiques et

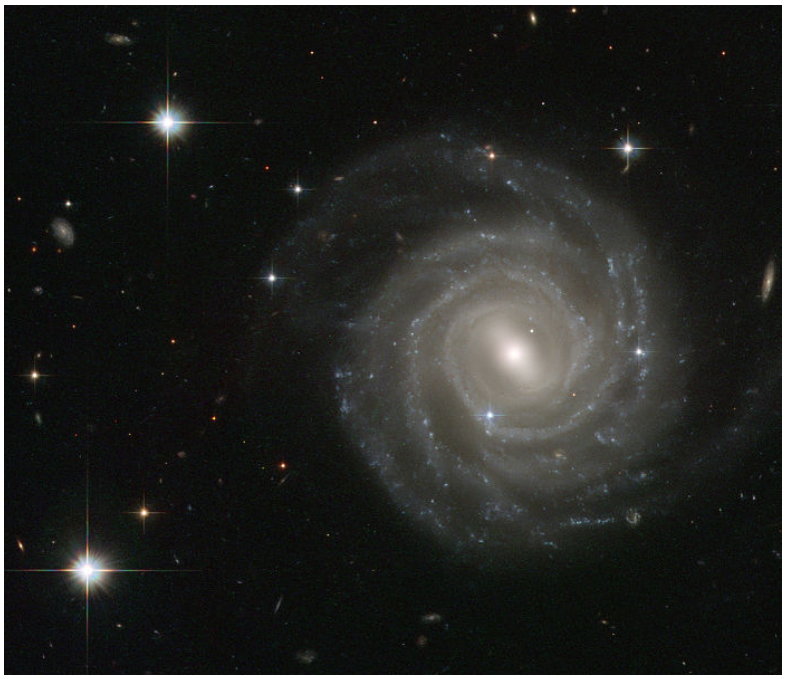

FIGURE 2.15 – Observation de la galaxie UGC 12158, un exemple de spirale barrée. (Crédit :ESA/Hubble & NASA)

sur les simulations N-corps ont permis de montrer les limitation des travaux analytiques qui ne prennent pas en compte l'auto-gravitation des disques dans l'étude de la friction dynamique. En effet, les auteurs expriment les variations de moment angulaire des étoiles causées par la friction dynamique avec une barre, puis ils comparent les variations analytiques obtenues aux variations observées dans des simulations N-corps. Ils trouvent alors, que l'évolution de la rotation de la barre est différente (étant soit plus lente soit plus rapide que les prédictions analytique selon la nature de la barre). C'est pourquoi aujourd'hui les travaux sur la dynamique galactique se font essentiellement à l'aide de simulations N-corps ou N-corps+gaz.

Dans la Fig. 2.16 extraite de Athanassoula (2002), nous voyons pour une simulation de disque barré, la distribution de la masse du disque et du halo en fonction du rapport de fréquence $(\Omega-\Omega_p)/\kappa$ (panneaux du haut). Et la variation de moment angulaire pour les étoiles en fonction du même rapport de fréquence (panneaux du bas). Nous pouvons voir que les étoiles sur l'ILR perdent 0.06 unités de moment angulaire, et que les étoiles à la corotation avec la barre gagnent une faible quantité de moment angulaire (0.01 unités). En revanche, les particules de matière noire, en corotation avec la barre gagnent 0.045 unités de moment angulaire. Ainsi, les étoiles de la barre perdent du moment angulaire, en le cédant majoritairement aux particules de matière noire.

Cette perte de moment angulaire a pour première conséquence le ralentissement de la rotation de la barre, en conséquence de quoi les résonances avec la barre se déplacent vers l'extérieur.

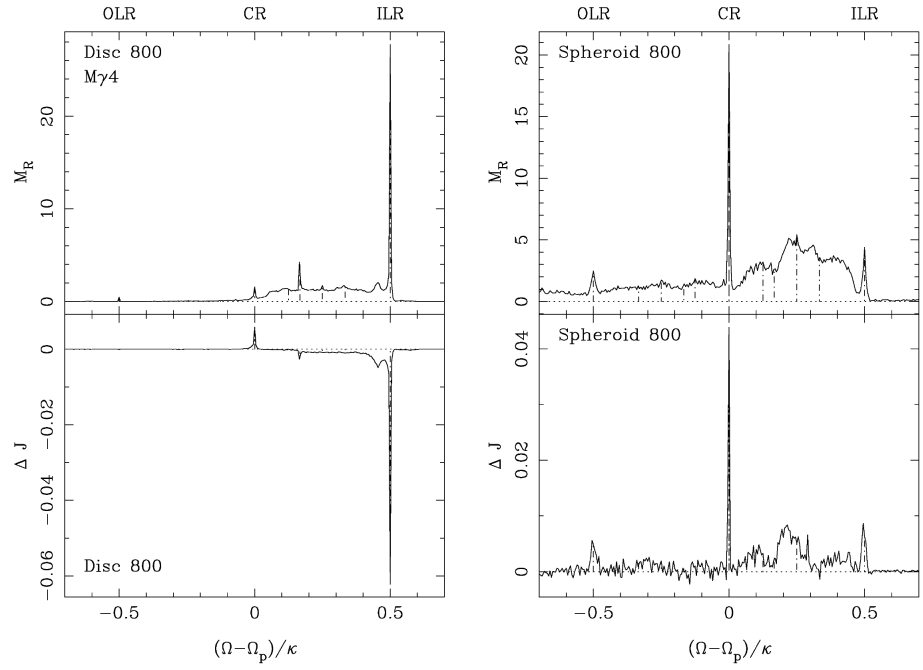

FIGURE 2.16 – Les panneaux du haut indiquent la masse en fonction du rapport des fréquences, pour les particules du disque et celles du halo. Les panneaux du bas indiquent les variations de moment angulaire du disque et du halo en fonction du rapport des fréquences. Extrait de Athanassoula (2002)

En effet la vitesse angulaire des étoiles est une fonction décroissante du rayon, donc si la barre tourne moins vite, les étoiles en corotation avec elle sont alors plus vers l'extérieur du disque. Et il en va de même pour les autres résonances et en particulier l'ILR, et donc la barre s'allonge en même temps que sa rotation ralentie, vérifiant alors l'hypothèse que les échanges de moment angulaire amplifient la barre.

Ces études montrent également qu'il est important de considérer des halos non-rigides. En effet dans le cas de halo rigides, il ne peut pas y avoir de transfert de moment angulaire, et les simulations produisent en générale des barres peu développées.

Par ailleurs, les barres vivent généralement dans des disques présentant des structures spirales, qui affectent le potentiel gravitationnel. Dans ce cas, Patsis, Kalapotharakos & Grosbøl (2010) ont montré que la barre est presque seulement supportée par des orbites chaotiques.

2.4 Migration radiale des étoiles dans les potentiels variables

Nous avons vu dans les sections précédentes que les mouvements radiaux des étoiles sont influencés par les structures non-axisymétriques et en particulier la barre et les bras spiraux qui peuvent se former dans les disques. Dans les sections 2.1 et 2.2, nous avons rappelé des

éléments de dynamique galactique qui décrivent le mouvement des étoiles dans les galaxies disques, dans le cas où les structures sont rigides.

Par la suite, nous avons discuter de la formation et de l'évolution de la barre et des spirales dans les disques galactiques. Nous avons vu que ces structures se forment spontanément dans les disques dynamiquement froids, car ils sont loin de l'équilibre thermodynamique. Et nous avons rappelé le mécanisme permettant à la barre et aux spirales de chauffer le disque, et ainsi de le faire tendre vers l'équilibre. Nous avons vu différents modèles de spirales, montrant que les spirales ne sont pas des structures fixes une fois formées, de même pour la barre. Nous avons rappelé que les échanges de moment angulaire entre la barre, le disque et le halo de matière noire, sont le moteur de l'évolution séculaire des barres galactiques.

Cette discussion permet de mettre en évidence que les calculs analytiques obtenus pour des structures rigides, ainsi que les conclusions qui en sont tirées, ne sont pas nécessairement valides dans les galaxies réelles ou dans les simulations N-corps. Malheureusement, inclure l'évolution séculaire des galaxies dans la dynamique stellaire, empêche de résoudre analytiquement les équations du problème. La meilleure méthode est donc d'étudier le comportement des étoiles dans des simulations N-corps (ou N-corps+gaz) pour comprendre les mécanismes couplant l'évolution séculaire et la migration radiale des étoiles, et étudier son impact sur la formation et l'évolution des galaxies réelles.

2.4.1 Contexte

Comme nous l'avons dit, l'étude de la dynamique galactique avec des potentiels gravitationnels changeant avec le temps, nécessite l'utilisation de simulations N-corps.

Sellwood & Binney (2002), dans un article fondateur pour l'étude de la migration radiale dans les potentiels variables, ont étudié la migration radiale causée par une spirale transitoire à deux bras, de courte durée de vie, et qui apparaît spontanément. Dans leur simulation, c'est la seule structure non-axisymétrique qui se forme, permettant alors d'étudier spécifiquement les effets d'une spirale transitoire : les auteurs montrent que le churning a majoritairement lieu autour du rayon de corotation de la spirale, par échange de moment angulaire ; que les étoiles en orbites quasi-circulaire sont les plus susceptibles de migrer à la corotation ; et que ce mécanisme de migration n'augmente pas la dispersion de vitesses des étoiles i.e. les étoiles ayant migré restent sur des orbites quasi circulaires. Ils élaborent aussi un cadre théorique pour expliquer le phénomène, basé sur la conservation de l'énergie de Jacobi, et sur le diagramme donné en Fig. 2.11. Leur analyse repose sur les orbites en "fer à cheval", que nous avons détaillé en Sec. 2.2. Toujours en utilisant les orbites en fer à cheval, les auteurs montrent que la durée de vie de la spirale permet aux étoiles de n'effectuer qu'un seul passage d'un côté à l'autre du rayon de corotation. Par conséquent, la spirale entraîne un échange de position radiale, entre les étoiles de chaque côté de la corotation. Cet effet est plus conséquent que le mélange engendré par les orbites en fer à cheval dans un potentiel fixe (Sec. 2.2.2), car dans ce cas les orbites sont permanentes, ce qui permet éventuellement aux étoiles de retourner

à leur point de départ. En revanche, le potentiel variable créé par la spirale transitoire, fait que ces orbites n'existent que lorsque la spirale est présente. Ainsi, les étoiles échangent leurs places autour de la corotation, et aucune ne revient à sont point de départ. Cet article explore également les conséquences de la migration radiale sur les observables liées à l'évolution chimique des galaxies, dont nous reparlerons dans le chapitre 3.

D'autres travaux utilisant les simulations N-corps sont venus ensuite explorer plus en détails le mécanisme de diffusion stellaire proposé par Sellwood & Binney (2002) autour de la corotation avec les bras spiraux, ainsi que les conséquences de la migration sur différentes observables de la Voie Lactée ou des galaxies externes (nous y reviendrons en partie 3). Et d'autres mécanismes de migration radiale ont été suggérés, ce que nous allons voir dans la suite.

Les différentes études menées par R. Roskar (Roškar et al., 2008b,a, 2012), ont confirmé les différents points présentés dans Sellwood & Binney (2002), et étudié les effets de spirales transitoires récurrentes. En effet, leurs simulations forment spontanément des spirales, qui se forment puis disparaissent, laissant la place à de nouvelles spirales dont la vitesse angulaire est différente. Ainsi, de multiples rayons de corotation apparaîssent et disparaissent, permettant aux étoiles migrante de passer d'un rayon de corotation à l'autre, grâce à la conservation de la circularité des orbites lorsque les étoiles migrent à un rayon de corotation. La récurrence des spirales transitoires produit alors une migration radiale bien plus importante, puisque les étoiles ne sont plus contraintes de migrer en restant autour d'un seul rayon de corotation, mais ont la possibilité d'explorer tout le disque, générant alors une **diffusion des étoiles** dans les disques. Par ailleurs, ces travaux se penchent aussi sur les effets de la migration sur l'évolution galactique, et en particulier, montrent que son impact est de plus en plus fort vers les régions de plus en plus loin du centre galactique, car la formation stellaire locale va en diminuant, permettant aux étoiles venant d'autres régions de représenter une fraction de plus en plus importante de la totalité des étoiles locales. Leur étude porte également sur l'impact de la migration sur differents marqueurs observationnels de l'évolution chimique, ce que nous verrons plus en détails en partie 3.

La question de l'influence de la migration radiale sur la formation du disque épais est encore débattue. Certains travaux (Schönrich & Binney, 2009; Sales et al., 2009; Loebman et al., 2011) ont suggéré que la migration pourrait expliquer la formation du disque épais observé dans les galaxies disques, en faisant migrer vers l'extérieur du disque des étoiles venant des régions centrales de la galaxies. Ces étoiles venant du centre, elles sont en moyenne plus vieilles, et ont une forte dispersion de vitesses verticales. En allant vers l'extérieur, la densité surfacique de matière diminue, donc la force gravitationnelle de rappel des étoiles vers le plan du disque diminue également. Par conséquent, du fait de leur forte dispersion de vitesses verticale, les étoiles venant du centre qui se retrouve plus loin dans le disque pourraient avoir des oscillations verticales plus amples, formant ainsi un disque épais. Cependant, les travaux de Minchev et al. (2012) montrent que ce mécanisme ne serait pas valide. En effet, lors du déplacement vers l'extérieur, l'action verticale $J_z = E_z/\nu$ (où ν et E_z définissent les epicycles verticaux - voir Sec. 2.1.2) se conserve, et ν décroit à cause de la diminution de la

densité surfacique de matière. Il en résulte que E_z diminue également pour les étoiles des régions centrales, migrant vers l'extérieur, c'est-à-dire que leur dispersion de vitesses verticales diminue. Par conséquent ces étoiles ne contribueraient pas à la formation du disque épais. Par ailleurs, Minchev et al. (2012) confirment leur conclusion en analysant le comportement des étoiles migrantes dans des simulations N-corps.

En plus de la corotation avec des spirales transitoires, d'autres mécanismes de migration ont été mis en évidence dans les simulations N-corps :

- Un processus voisin de celui décrit précédemment avec les spirales transitoires, fait intervenir les surdensités qui peuvent se former lorsque différentes spirales de longue durée de vie, ayant des vitesses angulaires différentes, sont en interférence constructive. Ce mécanisme décrit par Comparetta & Quillen (2012), produit également une diffusion stellaire dans le disque, grâce aux multiples rayons de corotations avec les surdensités qui se forment, mais le mécanisme agirait sur les échelles de temps plus courtes.
- Minchev & Famaey (2010),Minchev et al. (2011) ont montré que dans les galaxies spirales barrées, où les spirales et la barre n'ont pas nécessairement la même vitesse angulaire, des superposition de résonances peuvent se produire, induisant une réponse non-linéaire des étoiles. Ce mécanisme est, lui aussi, plus rapide que la corotation avec des spirales transitoires, et les auteurs montre qu'il est un ordre de grandeur plus efficace que les spirales transitoires.
- Le cas des spirales barrées a également été étudié de façon phénoménologique par Brunetti, Chiappini & Pfenniger (2011), à l'aide de simulations N-corps. Dans cette étude, la migration radiale est décrite par des coefficients de diffusion radiale des étoiles. Ces travaux soulignent l'importance jouée par la barre dans de telles galaxies, en montrant le lien entre la force de la barre (évaluée grâce au mode m=2 de la décomposition de la densité stellaire en série de Fourier) et la diffusion des étoiles dans le disque. Ces travaux montrent également que les coefficients de diffusion varie fortement en fonction du rayon galacto-centrique et du temps : autour de la corotation avec la barre on trouve une région de forte migration dans les disques dynamiquement froids, et cette région suit la corotation quand elle se déplace à cause de l'évolution séculaire de la barre ; au-delà de la barre, là où les spirales se développent, on trouve une région étendue jusqu'au bord externe du disque, dans laquelle le coefficient de diffusion est élevé mais qui diminue également lorsque le disque est dynamiquement plus froid.
- Les effets de marées causés par une galaxie satellite naine produisent une forte migration radiale dans les régions externes du disque (Quillen et al., 2009). Cette étude se concentre sur la simulation de la migration radiale dans la Voie Lactée, et montre qu'un satellite peut induire des courants d'étoiles, visibles dans les distributions de vitesses. Les courants mis en évidence vont de l'extérieur vers l'intérieur, en particulier, le voisinage solaire serait alors peuplé d'étoiles venant des régions externes du disque, brouillant les observables concernant l'évolution chimique. Par ailleurs, ces courants pourraient correspondre à ceux observés dans le voisinage solaire, suggérant ainsi le

passage récent d'une galaxie satellite.

- Enfin, Bird, Kazantzidis & Weinberg (2012) ont examiné l'influence d'une succession de fusions mineures : un bombardement de satellites. Ce phénomène intervient dans le scénario de la formation des galaxies par fusions successives de galaxies. L'analyse de simulations menée pour cette étude, montre que la migration radiale est plus forte dans les disques perturbés par les fusions mineures, et affecte surtout les régions externes du disque, car les étoiles y sont moins contraintes gravitationnellement.

2.4.2 Travaux de dynamique effectués durant la thèse

Dans l'article Kubryk,Athanassoula,Prantzos, (soumis ou qui sera soumis prochainement), nous étudions le churning dans une simulation N-corps+gaz (*Gadget3*). La galaxie simulée présente des spirales, et une barre. Les bras transitoires sont de moins en moins forts au fur et à mesure que le disque est chauffé, et la force de la barre augmente avec le temps, et devient rapidement (après 2 Gyr) la structure non-axisymétrique dominante dans le disque. L'évolution séculaire de la barre se traduit par sa croissance et la diminution de sa vitesse de rotation, ce qui déplace sont rayon de corotation de ~4 kpc à 2 Gyr, jusqu'à ~14 kpc à 10 Gyr. C'est une simulation à haute résolution, comportant 2 millions de particules réparties entre le gaz, les étoiles primordiales (présentes dès t=0), les étoiles nouvelles (qui se forment à partir du gaz), et le halo de matière noire. La durée totale de cette simulation est de 10 Gyr.

Afin d'analyser cette simulation, j'ai développé une bibliothèque complète de routines d'analyse de données et de visualisation en Python, utilisant le module *py_unsio* (http ://projets.lam.fr/projects/unsio/wiki/PythonReadData) développé au LAM. Ainsi les routines élaborées sont utilisables sur n'importe quelle simulation *Gadget*, mais aussi sur les simulations *Ramses* et toute simulation dont les fichiers de sortie sont dans un format connu par *UNSio*.

Afin d'étudier l'évolution des spirales et de la barre présent dans cette simulation, nous avons réalisé des spectrogrammes du disque galactique pour chaque rayon (Fig. 4 de l'article en Sec. 2.4.3), permettant d'analyser les structures du disque en terme de modes de Fourier, de suivre l'évolution de leur vitesse angulaire, de leur amplitude (i.e. de leur force). Les spectrogrammes permettent également de déterminer le lieu des résonances avec les différents modes de Fourier présent dans le disque, en particulier le rayon de corotation (RC) de chacun des modes (Fig. 6 de l'article en Sec. 2.4.3) et les résonances de plus haute multiplicité comme les résonances de Lindblad internes et externes. Par ailleurs, nous avons utilisé une seconde méthode de détermination du rayon de corotation, en déterminant l'évolution de la vitesse de rotation de la barre, et la vitesse circulaire des étoiles en fonction du rayon. Nous trouvons heureusement, que les deux méthodes donnent les même résultats.

Nous nous sommes intéressé à divers aspects de la migration radiale ayant lieu dans cette simulation. Nous avons d'abord vérifié que le moment angulaire des étoiles est bien un indicateur valide du rayon de l'orbite guide des étoiles, ce qui nous permet de séparer les mouvements de churning et de blurring (Fig. 8, 9 et 10 de l'article en Sec. 2.4.3). Puis, nous

avons déterminé les lieux où la migration est la plus forte (Fig. 11 et 12 de l'article en Sec. 2.4.3) (en terme de fraction d'étoiles migrantes), en analysant l'évolution du moment angulaire des étoiles sur des intervalles successifs de 1 Gyr. Nous sélectionnons les étoiles présentant une migration significative sur ces intervalles, en fixant un seuil pour les variations de moment angulaire sur les intervalles de temps. Ce seuil est fixé à 400 kpc^2Gyr^{-1}, correspondant à une variation de ~1.8 kpc pour le rayon guide. Ainsi, entre ~3 Gyr et ~8 Gyr, nous trouvons une bonne corrélation entre la position du rayon de corotation avec la barre (qui se déplace vers l'extérieur avec l'évolution séculaire de la barre) et les régions de forte migration, ce qui indique que la région de corotation avec la barre induit la plus forte migration radiale (avec une fraction forts migrateurs à environ ~35 % : Fig. 14 de l'article en sec. 2.4.3), sur cet intervalle de temps. Avant 3 Gyr, nous ne trouvons pas cette corrélation bien que la barre soit déjà formée (à environ 2 Gyr), et l'analyse des spectrogrammes du disque révèle que les modes m=3, m=4 et m=5 de Fourier sont plus forts que la barre à cette époque (Fig. 5 de l'article), et que ces modes ont des RC répartis dans presque tout le disque (Fig. 6 de l'article), qui induisent une forte migration radiale dans tout le disque. Et sur l'intervalle entre 8 et 9 Gyr, la corrélation se perd parce que le rayon de corotation de la barre est presque hors du disque stellaire, dans des régions très peu peuplées en étoiles.

Nous nous sommes intéressés au piégeage des étoiles autour des points de Lagrange, afin de mettre en évidence un nouveau mécanisme de migration radiale. En effet, nous avons vu en Sec. 2.2, que les maxima du potentiel effectif créés par une barre sont des points d'équilibre stables, qui peuvent piéger les étoiles si elles ont une énergie de Jacobi suffisamment basse. Mais la vitesse de rotation des barre à tendance à diminuer, à cause de l'échange de moment angulaire avec le halo. Dans ce cas, les points de Lagrange se déplacent vers l'extérieur du disque, avec le rayon de corotation de la barre. Si les étoiles restent piégées lors de ce mouvement, elles suivent le déplacement des points de Lagrange, et sont entraînées vers l'extérieur. Ce mécanisme de migration n'ayant jamais été étudié, nous avons dû développer de nouveaux outils pour analyser la dynamique stellaire dans un potentiel très variable (comprenant simultanément l'évolution séculaire de la barre, et la formation récurrente de bras spiraux transitoires). En effet, le potentiel créé par la galaxie simulée est très influencé par les bras transitoires, qui créent des points de Lagrange également transitoires. La difficulté est donc que les points d'équilibre stables se déplacent vers l'extérieur, et que leur nombre et position sont influencés par les bras transitoires.

Pour analyser le potentiel, nous avons utiliser le fait que le temps caractéristique du déplacement de la barre est plus long que celui de la durée de vie des bras transitoires. Nous avons donc supposé que l'effet d'un seul bras spiral est négligeable dans notre problème. Cependant, comme les bras spiraux se forment de façon continue dans cette simulation, les effets cumulés de plusieurs bras transitoires ne sont sans doute pas négligeables. Alors, pour analyser le potentiel effectif et déterminer la position des points d'équilibre pertinents pour notre étude, nous avons lissé spatialement le potentiel effectif à l'aide d'un filtre de Fourier. Nous n'avons gardé que les modes m=1 et m=2 dans la décomposition du potentiel en modes de Fourier (Fig. 20 et 21 de l'article). Nous avons montré que les points de Lagrange du potentiel lissé

restent stables en nombre et en position, mis à part leur mouvement vers l'extérieur (Fig. 23 de l'article), et qu'ils piègent les étoiles. Nous avons montré qu'une partie des étoiles piégées autour de ces points est entraînée vers l'extérieur. Et nous avons étudié les conditions pour que les étoiles restent piégées pendant que les points de Lagrange se déplacent : nous avons montré que l'énergie cinétique de l'étoile doit être suffisamment élevée au moment où elle entre dans la région de corotation de la barre, pour compenser le fait que cette énergie diminue lorsqu'elle migre vers l'extérieur (car les fréquences épicycliques diminuent). En effet, la condition pour rester sur une orbite en fer à cheval autour d'un point de Lagrange de type L4 ou L5, est d'avoir une énergie totale (ou énergie de Jacobi avec $E_J = E_{cin} + E_{pot}$) suffisamment grande pour pouvoir franchir les points de Lagrange de type L1 ou L2.

Résultats importants : notre étude indique clairement que notre nouveau mécanisme de migration radiale est bien valide (Fig. 16 de l'article), et qu'il peut entraîner les étoiles sur de très longues distances : certaines étoiles initialement à 2 kpc, peuvent se retrouver à 14 kpc. Et, bien qu'un nombre limité d'étoiles soient concerné (environ 15% des étoiles prises dans la résonance de corotation restent piégées plus de 2 Gyr : Fig. 27 de l'article), l'impact peut être important sur les régions les plus externes du disque là où la formation stellaire est faible. Ainsi, ce phénomène peut avoir des conséquences sur les profiles photométriques radiaux des disques galactiques et contribuer au "coude" qui y est parfois observé dans les régions externes des disques Bakos et al. (2011), à la forme en "U" des profiles de couleur, ainsi qu'à l'augmentation de l'échelle de longueur du disque.

Par ailleurs, nous avons montré que le déplacement des points de Lagrange et du rayon de corotation produit les mêmes effets qu'un bras transitoire, tel que décrit par Sellwood & Binney (2002). En effet nous avons montré que la plupart des étoiles ne sont pas entraînées vers l'extérieur par les points de Lagrange, elle tournent autour des points de Lagrange tant qu'ils sont à proximité, et lorsqu'ils s'éloignent les étoiles cessent leur migration radiale. Il en résulte un mélange des étoiles de la région de corotation, qui échange leurs places de façon symétrique par rapport au rayon de corotation, comme dans les travaux de Sellwood & Binney (2002).

2.4.3 Article : un nouveau mécanisme de migration radiale

Mon. Not. R. Astron. Soc. **000**, 000–000 (0000) Printed 15 July 2014 (MN LATEX style file v2.2)

Radial migration in a bar-dominated disk galaxy II : Dynamical aspects

M. Kubryk, E. Athanassoula, N. Prantzos

15 July 2014

ABSTRACT

In this paper, we analyse the dynamics of stars in the simulation already used in a companion paper (Kubryk, Prantzos & Athanassoula 2013). We explore in more details the mechanisms of radial displacement (*churning*) experienced by the stars and we show that the corotation region of the bar is the most effective churning inducer. We also find a new churning mechanism induced by the outward displacement of the bar's corotation resonance. We call this mechanism *bar-induced churning*. We show that the instantaneous effective potential does not describe accurately the churning occurring in the bar's corotation region, because it contains information about structures that are short-lived (up to few hundred million years), in comparison to the characteristic period of horseshoe orbits (at least 1 Gyr). We show that a more appropriate method to work with non-steady potentials, is to smooth the effective potential, to keep only the effects of the largest structures that live longer than the small structures. Then we define the *n-Lagrangian points* found in the smoothed effective potential, that live long enough to affect the stellar orbits in the corotation region of the bar, and that can be interpreted as a representation of the combined effects of multiple Lagrangian points, both short-lived and long-lived. Finally we use this method to analyse a new migration mechanism, that we call *bar-induced churning*. We show that stars experiencing this phenomenon are trapped around maximum-type 2-Lagrangian points, and that such stars with high Jacobi energy are more likely to remain trapped while the corotation moves outward. Finally, we show the fraction of stars remaining in the corotation region, and show that only 11% of the coldest stars (low Jacobi energy) and 17% of the warmest stars remain in the corotation region for more than 3 Gyr while it moves outward. In any case, the fraction stars concerned by the *bar-induced churning* reveals that this mechanism does not concern a lot of stars, therefore, most of the corotating stars only experience a local mixing around the corotation radius, they swap their places as if the bar were a local transient feature, as in the mechanism of Sellwood & Binney (2002), for transient spiral arms. The mechanism of *bar-induced churning* can be important for studies of the outer regions of disc galaxies: if the bar's corotation reaches this regions where few stars are formed locally, the number of stars brought by *bar-induced churning* can constitute a large fraction of the local stars, and affect the luminosity and color profiles.

1 INTRODUCTION

In a companion paper (Kubryk, Prantzos & Athanassoula 2013), we investigated the consequences of radial migration (both churning *and* blurring – as defined in Schönrich & Binney (2009)) on chemical evolution in an N-body+SPH simulation, concerning an isolated, early type, barred galaxy. Do to so, we analysed the simulation to get an empirical model of radial migration described as a diffusion process, as in Brunetti, Chiappini & Pfenniger (2011). In the present paper, we analyse more precisely the dynamics of radial migration in this simulation, focussing on the churning mechanisms.

Being able to account for many observations of chemical composition of the local stars and for photometry profiles of disk galaxies, radial migration or radial mixing of stars seems to play an important role in galactic evolution. This is, for example, the case of the age-metallicity relation of the stars in the Solar neighbourhood (Casagrande et al. 2011), or of the "U-shape" in radial photometry profiles (Roediger et al. 2012). Radial migration has also been proposed as a possible mechanism for the thick disk formation (Schönrich & Binney 2009), but this issue is still under debate (e.g. Minchev et al. 2012a). See also Kubryk, Prantzos & Athanassoula (2013) and references there-in for other observational evidence radial migration.

Schönrich & Binney (2009) distinguished two components in the radial movement: the *churning* and the *blurring*, that are associated respectively to the change of guiding radius, and to the epicyclic movements of the stars around it. Few direct observations of stars moving radially due to churning have been made. In the solar neighbourhood, the Hercules stream could be explained by stars affected by the outer Lindblad resonance of the central bar (Dehnen 2000); and the Hyades stream could be the result of an inner Lindblad resonance with a spiral pattern (Sellwood 2010). Sev-

eral physical phenomenons, supported by numerical simulations analysis and theoretical arguments, are able to induce radial displacement of stars through churning.

Episodic churning was identified in N-body simulations by Sellwood & Binney (2002). It happens to stars having low orbital eccentricities that are trapped in a corotation resonance with a transient spiral structure. These stars follow horseshoe orbits i.e. they have periodic oscillations around the corotation radius, they periodically gain and lose the same amount of angular momentum (and preserve their Jacobi constant). In their paper, Sellwood & Binney (2002), have shown that the life-time of the spiral is approximately half the period of the horseshoe orbits, meaning that the stars cross only once the corotation radius, so they swap their places symmetrically, with respect to the corotation radius. They have also shown that this movement preserves the angular momentum distribution. Notice that that the horseshoe orbits are not a libration due to epicyclic motion, the stars following this type of orbits have an oscillating guiding center following horseshoe orbits, plus epicyclic movements around the guiding center. In addition, the authors have shown that stars on nearly circular orbits are more sensitive to the corotation resonance: by experiencing larger guiding radius variations. They have also shown that this mechanism do not heat the stars experiencing radial migration which remain on quasi circular orbits. Following Sellwood & Binney (2002), numerous studies with N-body simulations have focused on the origin of radial migration in galactic disks.

The works of Roškar et al. (2008b), Roškar et al. (2008a), Roškar et al. (2012), confirmed the aforementioned effects, and also described the effects of recurrent transient spiral arms which are rotating rigidly. They have found multiple transient spiral patterns in their N-body simulations resulting in multiple corotation radii which evolve with time. As a result, the stars can experience successive churning episodes, being repeatedly trapped in corotation resonances with different transient arms. Due to this mechanism, the stars can explore a large part of the disk, or even the whole disk, being scattered by the multiple corotations. A key aspect of this phenomenon is the conservation of the quasi-circularity of orbits experiencing a churning episode. As we already mentioned, Sellwood & Binney (2002) have shown that stars having low eccentricity undergo larger radial migration around the corotation radius. Therefore, if stars were heated while migrating, they would not be able to experience successive episodes of churning.

Comparetta & Quillen (2012), have described a similar churning mechanism experienced by stars in corotation resonance with short lived density peaks. The physics of the stars at corotation is the same, but in this study the authors focused on the short lived density peaks created by constructive interferences of transient spiral patterns (rigidly rotating). When transient spiral patterns rotating at different angular speeds are interfering constructively, they create short lived density peaks at a variety of radii and angular speeds, and each one has a specific corotation radius. As a result, the stars can be transported from a corotation radius to an other, and undergo large displacements in the disk. They have shown that this churning mechanism is more pervasive in the disk, and happens on shorter time scales.

Minchev & Famaey (2010), Minchev et al. (2011), Minchev et al. (2012b), have found another mechanism involving the interaction of a bar with spiral patterns. They have shown that when resonances from the bar and the spiral pattern overlap, due to the different rotation speeds of these structures, the response of the stars is stronger i.e. the angular momentum variations are larger around the corotation. Minchev et al. (2012b) notice that the corotation with the bar induces a churning that appears similar to the churning induced in Sellwood & Binney (2002), by a transient spiral pattern. This behaviour is surprising since the bar is not transient but only slowly evolving. We discuss briefly this issue in Sec. 7.4 of this work.

All the previous migration mechanisms involve a corotation resonance with a bar or a spiral. But other resonances can induce migration, namely the Lindblad resonances. As in the case of corotation, the Lindblad resonance can induce changes in the angular momentum of stars, but these stars are radially heated, in contrast to the case of corotation. However, this mechanism does not appear to be efficient at the Lindblad resonances with a transient spiral (Sellwood & Binney 2002), inducing only low angular momentum variations. In studies of galactic bars (Athanassoula 2003) the Inner Lindblad Resonance (ILR) appears to be the locus where the stars in the disc lose the largest amount of angular momentum. However, the stars on the ILR are on elongated orbits constituting the bar and they are not concerned by the radial migration, because their decreasing angular momentum results in a decreasing rotation speed of the bar and not in guiding radius variations. On the other hand, the stars in corotation with the bar, gain a small amount of angular momentum (most of the angular momentum lost at the ILR is transferred to the dark matter particles corotating with the bar).

Other studies revealed that recurrent transient arms do not rotate rigidly, but follow the differential rotation speed of the disk. Grand, Kawata & Cropper (2012b,a, 2014), have studied the radial migration around this type of transient arms, and showed that the stars experience churning episodes at various radii around the arm. Indeed, if an arm follows the differential rotation speed of the disk, each point of the arm is a corotation radius. Therefore, the mechanism highlighted in Sellwood & Binney (2002) occurs all along the arm. This behaviour of transient arms has also been found in simulations by Baba, Saitoh & Wada (2013). The comparison between the migration induced by recurrent rigid arms or recurrent winding arms is not easy since each type of arms has been found in hardly comparable simulations, having different initial conditions. Nevertheless, it seems that each of these two phenomena have similar qualitative impacts: the stars can explore the entire disk, as in the stellar diffusion described in Brunetti, Chiappini & Pfenniger (2011). In addition, the fact that different behaviours of the arms are found in the simulations is a problem itself and it should be determined whether this comes from different analysis methods and interpretations of the results, or whether the simulations truly exhibit different types of transient arms.

Finally, it has been shown that churning can be induced by an orbiting dwarf satellite galaxy. Quillen et al. (2009) described the churning coming from tidal effects of a dwarf satellite orbiting around the galaxy. This mechanism concerns the stars of the outer disk; for instance, in the Milky Way it could involves stars of the solar neighbourhood and larger radii. Sánchez-Blázquez et al. (2009) have shown that the merger-driven gas inflows causes the potential to deepen, resulting in a redistribution of the angular momentum towards the external parts of the disk and inducing an outward movement of the stars.

In this paper we identify and analyse a new migration mechanism: the *bar-induced churning*. This mechanism occurs when a bar appears in a disk galaxy. During the secular evolution of the bar, its rotation speed decreases and the corotation radius moves outwards. A fraction of the stars in the bar's corotation region, remains trapped in the corotation resonance thus they follow the displacement of the corotation radius, and are driven outwards. We

will give further details, and describe the dynamics of this migration mechanism, in the next sections of this paper.

Our analysis revealed that, in the numerical simulation we used, the region where stars corotate with the bar is the most churning-inducing. Therefore, in this paper, we study the *churning* of stars corotating with a bar, in a disk perturbed also by transient spiral arms. We will show the dynamical origin of churning in this region, and describe what are its consequences on the position of stars in the disk.

It is likely that all these types of churning occur in real disk galaxies, at different periods and radii during their evolution and in different proportions, depending on the individual history of each galaxy. In this paper we will study the churning in one peculiar simulated galaxy, which is isolated and forms a strong bar and recurring transient spiral arms (details about the morphology of this galaxy will be given later). We shall try to identify and disentangle the various migration mechanisms.

In Sec. 2, we describe the simulation, and we give some characteristics of the simulated galaxy. In Sec. 3, we show different behaviours of stars at the corotation resonance, we define what we will consider as *bar-induced churning*, and see how stars experiencing churning can be separated from the ones moving radially because of the epicyclic oscillations. In Sec. 4, we show that the region where stars corotate with the bar is the most churning-inducing. In Sec. 5, we will describe the stellar movements found in this simulation. In sec. 6, we start investigating the dynamic of stars corotating with the bar in a disk perturbed by recurrent transient spiral arms, and show that the Lagrange points found in the instantaneous effective potential do not describe accurately the churning and we analyse the stability of the Lagrangian points in the corotation region. In Sec. 7, we show that churning is better described by 2-Lagrangian points (that we will define in that section). We study statistically the behaviour of stars in the corotation region to show that the local radial mixing (around the bar's corotation radius) is the most effective churning mechanism in this simulation, and that *bar-induced churning* due to stars following the corotation region as it moves outward, concerns only a few stars. Finally, we summarize our results in Sec. 8.

2 THE NUMERICAL SIMULATION

2.1 The set-up

The simulation we use is performed using the GADGET-3 code (Springel, Yoshida & White 2001; Springel & Hernquist 2002, 2003; Springel 2005), with a softening length of 50 pc. In this code, the matter constituting a galaxy is represented by different components: the GAS, the HALO, the DISK (stars already existing at t=0, i.e. the oldest stars in the galaxy) and the STARS (new stars that are formed from the GAS component at t>0). The initial composition of the used simulation is: 83.2% of total mass in the HALO component (1 000 000 particles), 12.6% in the GAZ component (initially 750 000 particles) and 4.2% in the DISK component (200 000 particles). So the initial galaxy is made of a dark matter halo, a gaseous disk, and an old stellar disk.

The dark matter halo has a core in its inner region. It is described by the density function

$$\rho_h(r) = \frac{M_h}{2\pi^{3/2}} \frac{\alpha}{r_c} \frac{\exp(-r^2/r_c^2)}{r^2+\gamma^2} , \quad (1)$$

where M_h is the total mass of the halo,γ is the core radius and r_c is the cut-off radius. The constant α normalizes the density, and is defined as

$$\alpha = [1 - \sqrt{\pi}\exp(q^2)(1-\mathrm{erf}(q))]^{-1} , \quad (2)$$

where $q = \gamma/r_c$ (Hernquist 1993). The values chosen for this simulation are $M_h = 2.5\times10^{11}$ M$_\odot$, rc = 30 kpc, γ = 1.5 kpc. So, each dark matter particle has a mass of 2.5×10^5 M$_\odot$.

The initial gas (GAS) and old stars (DISK) form the initial disc of the galaxy, that is described by the following density:

$$\rho_d(R,z) = \frac{M_d}{4\pi h^2 z_0} \exp\left(-\frac{R}{h}\right) \mathrm{sech}^2\left(\frac{z}{z_0}\right) , \quad (3)$$

with R the cylindrical radius, h the disc scale-length, z_0 the disc sclae-height, and M_d the total mass of the disc. The initial radial velocity dispersion of the disk particles:

$$\sigma_R(R) = 100\exp\left(-\frac{R}{3h}\right) \text{ km s}^{-1} . \quad (4)$$

For the DISK component, h = 3 kpc, z_0 =0.6 kpc, and the mass of each particle is 2.5×10^5 M$_\odot$.

The GAS component is described by the same projected density distribution, with a smaller scale-height, set by the hydrodynamical equilibrium that is computed during the iterative calculation of the initial conditions (Rodionov & Athanassoula 2011).

The simulated galaxy is isolated, meaning that it evolves in a closed box, without interaction with neighbouring galaxies, and no gas accretion during the simulation. As a result, the gas (GAS component) is rapidly depleted by stellar formation, augmenting the number of stellar particles (STARS component). Thus, the gas fraction comes to levels in good agreement with observations at z =0 and at intermediate z.

For more information on the initial conditions and the simulation see Athanassoula, Machado & Rodionov (2013), and references therein.

2.2 Global properties and radial profiles of the simulated galaxy

Some snapshots of the simulation are displayed in Fig. 1, where we show gas in the upper panels, and stars in the lower panels, at different times of the evolution. Most of the stars are formed during the first ∼2 Gyr when the gas density is the highest. In that period, the non-axisymmetric structures of the disk are dominated by the presence of transient spiral structures. By ∼2 Gyr, a bar is formed in the center of the galaxy and grows steadily until the end of the simulation, when it extends to almost half the size of the stellar disk. The bar torques push the particles within corotation inwards towards the innermost region, where they form a disky, circular-like, strong inner concentration. This inwards motion is particularly important for the gas due to the shocks along the leading edges of the bar (Athanassoula 1992). Due to its high gaseous density, this innermost part becomes a region of intense star formation. This inner region – often referred to as discy-bulge, pseudo-bulge, or discy pseudo-bulge (Kormendy & Kennicutt 2004; Athanassoula 2005; Nowak et al. 2010) – has a strong concentration of mainly gas and young stars, as well as older stars. Due to this inwards motion, the annulus beyond the discy pseudo-bulge and within corotation is depleted of gas. This morphology has been already observed both in previous simulations (Athanassoula 1992; Athanassoula, Machado & Rodionov 2013) and in observations (Jorsater & van Moorsel 1995; Lindblad et al. 1997).

Fig. 2 displays the evolution of the azimuthally averaged radial

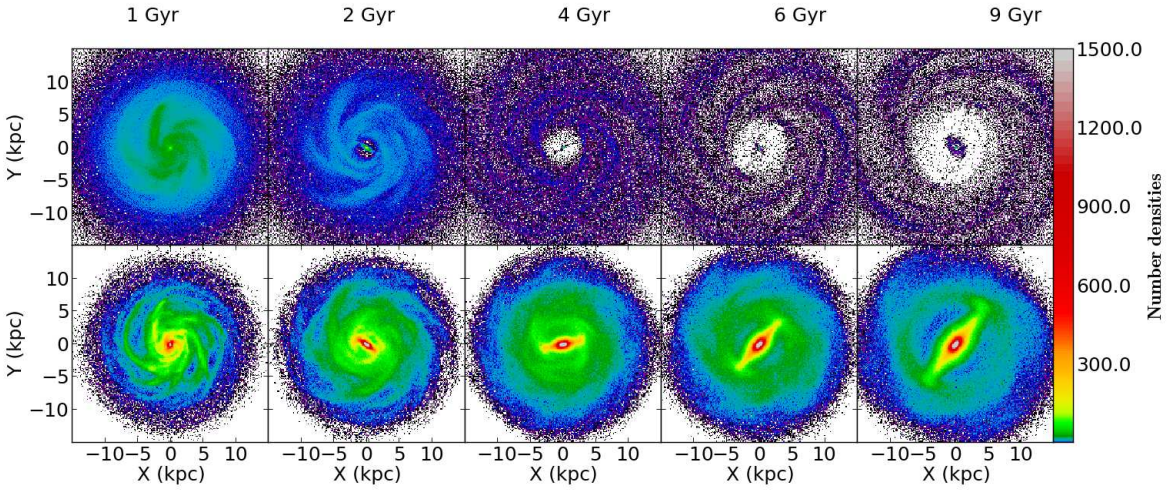

Figure 1. Face-on view of the simulated galaxy at 1, 2, 4, 6 and 9 Gyr. Gas-particles are displayed in the upper row and star-particles in the lower one. The color scale (see on-line version) on the right shows the number of particles per pixel, with size 75×75 pc.

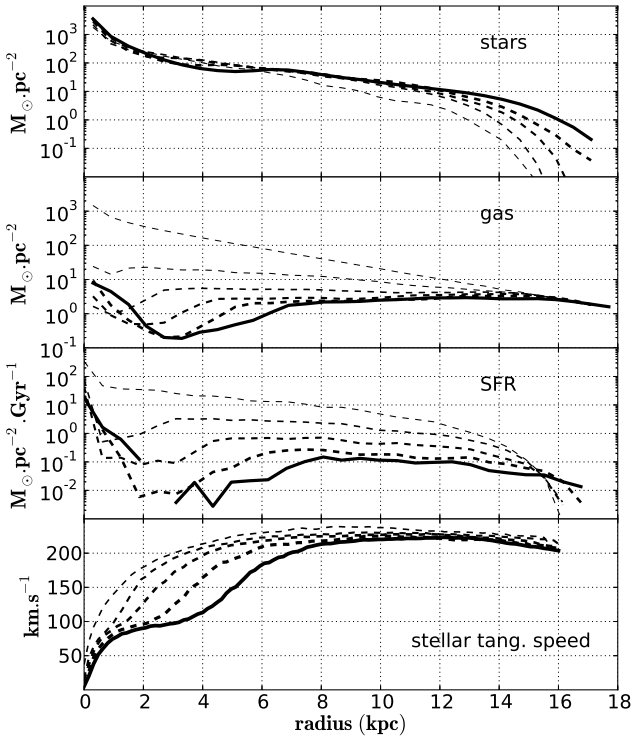

Figure 2. From top to bottom: azimuthally averaged radial profiles of the stellar surface density, gas surface density, star formation rate, and tangential velocity curves. Curves correspond to snapshots taken every 2 Gyr, with the thickness of the line increasing with time and the *thick solid* ones corresponding to the final (10 Gyr) result. The missing part of the thick solid curve of the SFR, indicates that their is no stellar formation between 2 and 3 kpc during the last 2 Gyr, because of the lack of gas.

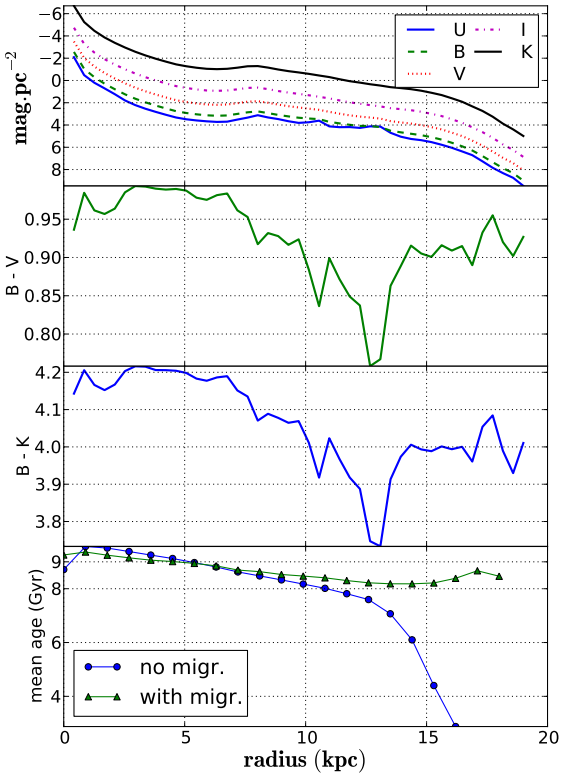

Figure 3. Azimuthally averaged photometric radial profiles of the galaxy at the final time of 10 Gyr. The upper panel shows the absolute magnitude per parsec square, without extinction, for the U,B,V,I and K bands (see legend in the figure). The two middle panels show the final B-V and B-K profiles, respectively. The bottom panel shows the average stellar age of all stars born in radius *R* (filled circles) and of all stars found in radius *R* (triangles) at the end of the simulation.

profiles of the surface densities of stars and gas, the star formation rate, as well as of the average stellar tangential velocity. It should be emphasized that the average surface density profiles provide little information for the inner disk, which is dominated by the bar. They, however, clearly reflect the inside-out formation of the disk, as they extend outwards and become flatter with time. The gaseous profile is mostly depleted in an annulus encompassing the bar, due to the action of the bar, which gradually produces a "spoon-shaped" profile; the latter effect is also responsible for the late depletion of stars in the 2-6 kpc ring, which also produces a shallow hole in the stellar profile. The SFR profile displays similar features as the gaseous profile. The small values of the SFR outside 14 kpc result in a steep stellar profile beyond that radius. In the absence of infall, the gas is substantially depleted, only ∼8% of the initial quantity remaining at the end of the simulation.

We get photometric information on the simulated galaxy by post-processing the photometric evolution of the stellar populations. To do so we adopt the latest version of the PEGASE-HR code (Le Borgne et al. 2004), which includes metallicity-dependent stellar tracks, and we ignore the extinction effects. In the upper panel of Fig. 3, we present photometric profiles of the galaxy at the end of the simulation (10 Gyr). The obtained light emission is more and more intense when looking from U-band to K-band, because most of the stars are formed in the first 2 Gyr, so they are old and emitting in longer wavelengths. All photometric bands display the same "spoon shape", as the stellar surface density profile.

In the two middle panels of Fig. 3, we display the B-V and B-K color profiles. In those two profiles, the values decrease monotonically from ∼2 to 12 kpc, but then increase again from 13 to 18 kpc, so that from the center to outer edge, the disk becomes first "bluer" and then "redder". This result is hard to understand in the framework of a pure inside-out formation scenario, where the younger (bluer) stars have to be found at the larger radii and the older (redder) stars in the inner regions. Such effects have been found both in observations of real disk galaxies (see Bakos et al. 2011, and references therein) and in simulations (Roškar et al. 2008a). They are interpreted in terms of radial migration occurring in disk galaxies, although the nature of that migration has not been clearly established yet.

The lower panel of Fig. 3 presents the average stellar age as a function of galactic radius for two cases: i) if no migration had occurred (that can be done since we know the birth radius of all the stars formed from gas, so we can rebuild the stellar disk as if no migration occurred), ii) if migration occurs (that is the real stellar disk found at 10 Gyr, in which stars have experienced radial migration). Case i) displays a sharp decrease at ∼13 kpc, as expected from the radial profiles of the SFR presented in Fig. 2: the few stars *born* in the outer disk are young, because of the inside-out formation of the galaxy. In case (ii), no such down-trend is observed, because the outer regions are populated by a dominant old stellar component coming from inner radii, which increases substantially the corresponding average stellar age. Taking into account that the average metallicity profile of the stellar disk is flat at 10 Gyr (Fig. 2 in Kubryk, Prantzos & Athanassoula (2013)) one concludes that it is simply the larger age of the migrated stars and not their metallicity that is at the origin of the up-turn of the B-V and B-K colors in the outer disk.

2.3 Transient spiral arms

In the simulation we observe transient spiral arms (Fig. 1). To analyse their properties, namely their multiplicity (number of arms), pattern speed, and strength (power), we perform at each radius a Fourier analysis of the azimuthal density variations, followed by a Fourier transform along the temporal coordinate (Sellwood & Athanassoula 1986; Masset & Tagger 1997). With this method, the arm multiplicity n, corresponds to the Fourier mode m=n. For example, the bar is described by the mode m=2, and a 3-arm spiral is described by the mode m=3 of the Fourier decomposition. The Fourier transform along the time coordinate is expressed using the conjugate coordinate which is the frequency. We obtain maps of the power in a given Fourier mode in the radius-angular speed plane (see Fig. 4), for a given time interval. In these maps, a pattern is indicated by an horizontal structure. The length of the structure indicates the radial extent of the pattern, and its position on the y-axis, indicates the angular speed of the pattern. For one Fourier mode, it is possible to have multiple horizontal structures, if there are various spirals having the same multiplicity, rotating at different angular speeds (see Fig. 4). Note that the strength of each of these spirals of same multiplicity, changes with time.

By summing the power associated to each pixel of the maps, we obtain the total power of the given arm multiplicity in the given time interval. By evaluating the total power on successive time intervals, we get the evolution of the power with respect to time. We display graphically the results of this method in Fig. 5. All the modes grow roughly at the same pace between 0 and 1 Gyr. Then, the modes m=3 and m=5 decrease until the end of the simulation. The mode m=4 grows until 2 Gyr approximately, and then experiences a fast decrease followed by a slow increase until 10 Gyr. Finally, the mode m=2 grows as quickly as m=4 until 2 Gyr, but contrary to the other modes, it keeps growing until 10 Gyr, faster than the m=4 mode. For the m=2 mode, the behaviour between 0 and 2 Gyr is due to the formation of the bar, while after 2 Gyr, it is due to the secular evolution of the bar (Athanassoula 2013). The evolution of the m=4 mode after 2 Gyr is also related to the secular evolution of the bar, but before this time, it is related to 4-arms spiral patterns. Note also that the m=3 and 5 modes have almost the same evolution after 2 Gyr.

These different modes are representative of the structures' evolution in the disk: the mode m=2 is associated with a bar, m=3 and m=5 result from the presence of any spiral patterns having 3 or 5 arms, and m=4 is associated both with the bar and with any spiral pattern made of 4 arms. Therefore, Fig. 5 shows that before 2 Gyr, the disk is dominated by multiple pattern spirals (see also Fig. 1 left-most panel) although a bar starts to grow (see next subsection). After 2 Gyr the spirals become gradually weaker, while the bar keeps growing. All this was also verified by viewing the individual snapshots of the simulation.

We also use the data coming from the Fourier analysis of the stellar densities, to determine the angular speed of the patterns and their corotation radii. We know the angular speed of stars, which is indicated by the red dashed curve in Fig. 4. And we can identify the angular speed where the maximum power of the pattern is, therefore, we find which radius along the curve of stellar angular speed corresponds to the speed of the identified maximum; which gives the corotation radius (CR) of the stars with the pattern. For example, using Fig. 4, in the interval 1-2 Gyr the maximum power is found at $\Omega \simeq 44$ km/s/kpc, corresponding to a corotation radius of 4.8 kpc. And in the interval 2-3 Gyr, the maximum power is found at $\Omega \simeq 35$ km/s/kpc, corresponding to a corotation radius of 6 kpc. We repeat this for patterns m=1 to m=5, on 1 Gyr time intervals, so we obtain the evolution of the corotation radius of each pattern between 0 and 9 Gyr. These results are summed-up in Fig. 6, where

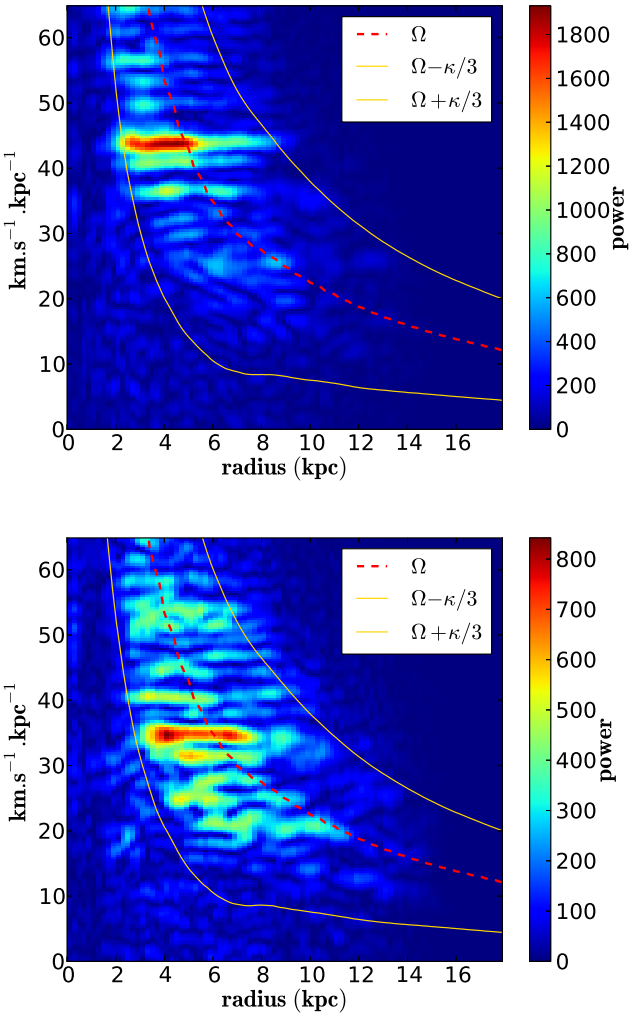

Figure 4. Power-spectrum of the m=3 mode. These maps are obtained through Fourier analysis (see text). *Upper panel:* power-spectrum in the interval 1-2 Gyr. *Lower panel:* power-spectrum in the interval 2-3 Gyr. The red dashed curve indicates the rotation frequency of stars at 1 Gyr (in the upper panel) and 3 Gyr (in the lower panel). The yellow curves indicate $\Omega-\kappa/3$ (lower curves) and $\Omega+\kappa/3$ (upper curves).

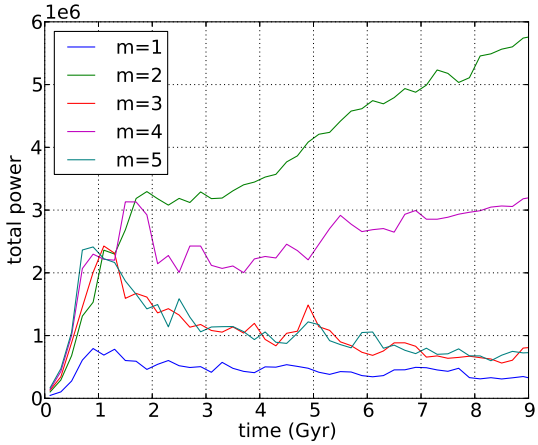

Figure 5. Total power over the whole disk of the Fourier components m=1, 2, 3, 4 and 5 (see legend), over the whole disk and the whole simulation time.

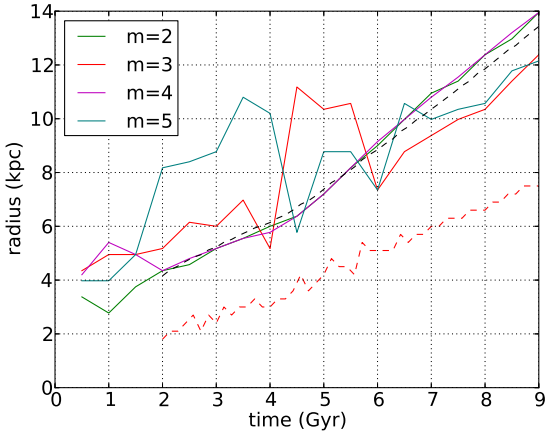

Figure 6. Evolution of the corotation radii of patterns from m=2 to m=5 (see legend) on 1 Gyr time intervals from 0 to 9 Gyr, every 0.5 Gyr. Each data point is plotted at the center of the interval it represents. The black dashed curve indicates the corotation resonance of the bar, and the red dashed curve indicates the bar radius.

we find that corotations with patterns occur at multiple radii over the disk.

We notice in Fig. 6, that the m=4 mode follows closely the m=2 mode after 2 Gyr. This behaviour indicates that, once the bar is formed, the m=4 mode represents only the first harmonic of the m=2 mode i.e. the bar. So, there are almost no spiral patterns having four arms after 2 Gyr. We also notice that these two modes remain close to the corotation radius calculated with an other method, where we determine the angle of the bar at each time step, and deduce its angular speed (see next subsection). The results obtained using this second method are indicated by the black dashed curve in the figure. Finally, we observe strong jumps between 4 and 4.5 Gyr for the components m=3 and m=5, and a jump between 5.5 and 6 Gyr for the component m=3. This comes from the multiple patterns existing in each mode. To determine the corotation radius with a mode, we use the maximum found in the power maps (e.g. Fig. 4). Because the strength of each pattern do not remain constant with time (the spirals are transient), the maximum in the power maps can jump from one pattern to an other, when the dominant one fades out. As a result, the angular speed that we determine can display discontinuities, that affect the value of the corotation radius of the Fourier mode.

2.4 Bar evolution

In this simulation, the central bar is the most significant non-axisymmetric structure in the galaxy, reducing the relative importance of spiral arms as it grows (Fig. 1). Therefore, it is expected that various dynamical phenomena linked to asymmetries in the gravitational potential (e.g. disk heating, radial migration, chaos, resonances), will increasingly be consequences of the action of the bar, rather than of other structures (such as transient spiral arms). In view of the discussion in the next sections, we analyze the bar by computing m=2 Fourier mode in the angular distribution of the stellar particles (Athanassoula & Misiriotis 2002). From these results we deduce the bar strength, its angular speed and the length of

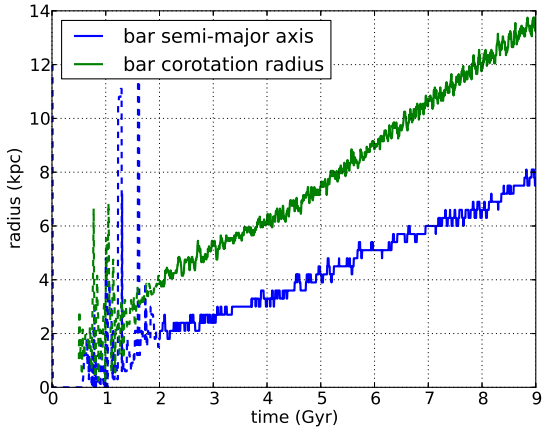

Figure 7. Length of the bar semi-major axis (blue curve) and bar corotation radius (green curve). Values before 2 Gyr show strong variations because the bar is not yet completely formed and the Fourier results in the mode m=2 are not reliable (dashed part of the curves).

its semi-major axis (which will sometimes be called "radius" in the following), as well as the corotation radius (results are displayed in Fig. 7). The determination of the bar length is done using the determination of the amplitude of the azimuthal m=2 Fourier mode $A_2(R) = \sqrt{a_2^2(R) + b_2^2(R)}$ at each radius, where $a_2(R)$ and $b_2(R)$ are the coefficients of the second harmonic in the Fourier decomposition of the azimuthal surface density of stars at radius R,and $a_0(R)$ is the coefficient in the mode m=0 at radius R. We define that the radius where the value of $A_2(R)/a_0(R)$ becomes lower than 0.20 marks the bar's major-axis length.

The bar becomes longer with time, its outer edge moving from 2 kpc at 2 Gyr to 8 kpc at 10 Gyr. And it slows down as it transfers its angular momentum to the halo (Athanassoula 2003). The decreasing angular speed of the bar with time, combined with the decreasing angular speed of the disk as a function of radius, creates the outward displacement of the corotation radius, which reaches the outer rim of the stellar disk at the end of the simulation. In this simulation, the bar starts its formation between 1 Gyr and 2 Gyr, where its strength grows quickly, although we do not have a safe estimation of the parameters describing bar evolution before 2 Gyr, because it is too small. After 2 Gyr, its mass increases, it becomes more and more elongated, its strength increases until the end of the simulation. Knowing the length of the semi-major axis of the bar, we can separate the bar region from the disk region, and compute the average tangential velocity of the star particles in the disk (R > bar radius). For times below 2 Gyr, the bar is not yet formed so we take stars at radii bigger than the radius of the bar at 2 Gyr (~1.8 kpc). We find that the average tangential speed of stars on the disk is very slowly decreasing with time: it is around 225 km/s at the beginning, and around 217 km/s at the end of the simulation. Therefore, we will sometime consider that the rotation speed of the disk is constant at 220 km/s over the whole simulation time.

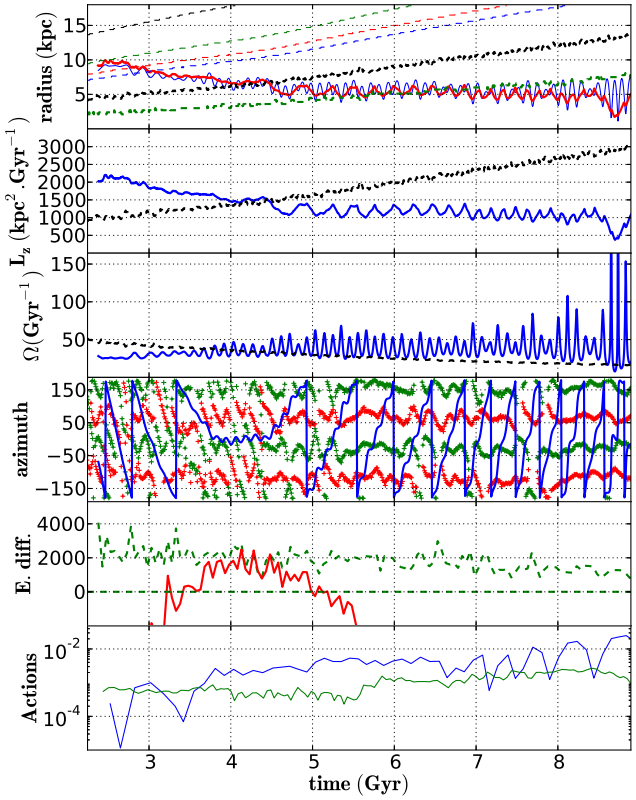

Figure 8. Temporal evolution of relevant quantities for a star corotating with the bar between 3.8 and 4.5 Gyr, around an unstable *2-Lagrangian point* (defined in Sec. 7). In the different panels we display, from top to bottom: ***panel 1***, radius of the stellar particle(thin blue curve), vertical angular momentum divided by the average stellar tangential speed in the disk at each time step (thick curve red), corotation radius (thick dashed black curve), locus of the outer resonances defined by $\Omega = \kappa/m$, where Ω is the angular speed of the star in the frame rotating with the bar. We indicate various resonances: m=1 (thin black dashed), m=2 (thin green dashed), m=3 (thin red dashed), m=4 (thin blue dashed), and the length of the bar's major axis (thick dashed green curve). ***Panel 2***, the vertical angular momentum of the star (blue curve) and the vertical angular momentum corresponding to the corotation with the bar (black dashed curve). ***Panel 3***, the angular speed of the star (full blue curve), and of the angular speed of the bar (dashed black curve). ***Panel 4***,the azimuth of the star in the frame rotating with the bar (0 degrees is set on the major axis of the bar), and the azimuth of the "averaged" Lagrangian points we show in green the unstable points (minima of the effective potential) and in red the stable points (maxima of the effective potential). ***Panel 5***, the Jacobi energy of the star (solid red), the difference between the maximum and minimum values of the effective potential at corotation (dashed green). ***Panel 6***, the radial and vertical actions, blue and green curve respectively.

3 MOTIONS OF INDIVIDUAL PARTICLES

3.1 Definitions and examples

The orbit of a star in the potential of a galactic disk is commonly described as the superposition of a main circular motion (defining the guiding radius), and harmonic oscillations called epicycles (Binney & Tremaine 1987). Sellwood & Binney (2002) called *blurring* the radial oscillations around the guiding radius and *churning* the modifications of the guiding radius. A star can experience churning (or angular momentum variations), when it is in a resonant interaction with non-axisymmetric structures of the gravitational potential (spirals, bar) (Lynden-Bell & Kalnajs 1972). We listed in the introduction all the known physical processes able to induce churning.

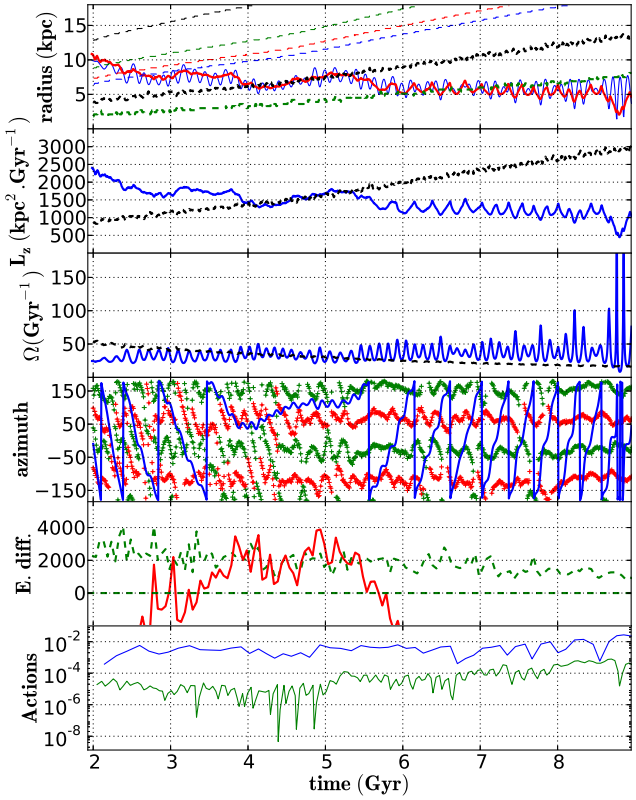

Figure 9. A star corotating with the bar between 4 and 5.5 Gyr, around a stable major Lagrangian point. This is an example of short bar-induced churning. See Fig. 8 for a description of the panels.

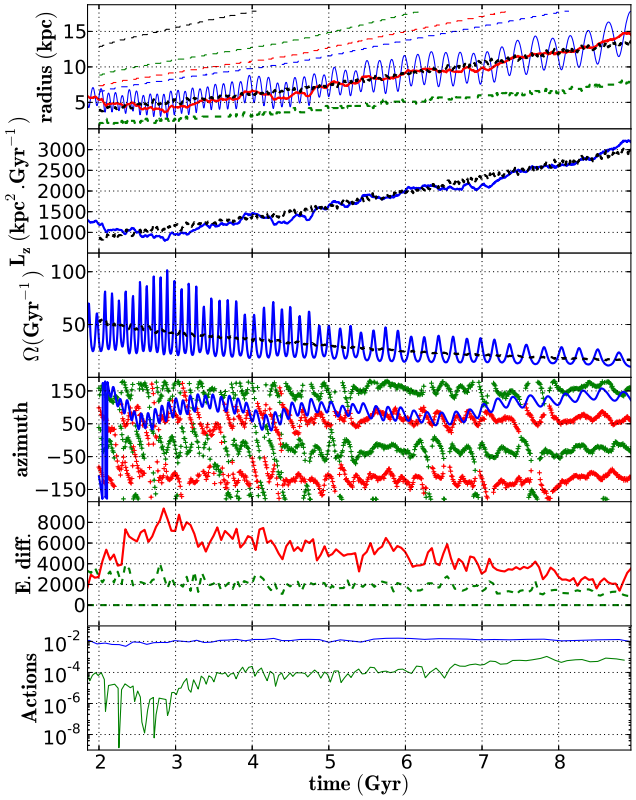

Figure 10. A star corotating with the bar since 2.5 Gyr until 9 Gyr. This star is also moving around a stable major Lagrangian point. This is an example of long bar-induced churning. See Fig. 8 for a description of the panels.

Figs. 8, 9 and 10 show three typical stellar orbits interacting with the bar through its corotation resonance. In the upper panel of these figures, the thin solid blue curve is the galactocentric radius of the stellar particle, where the epicyclic oscillations are visible. The thick black dashed curve is the corotation radius of the bar. The thick red solid curve is an estimation of the guiding radius, computed as $R_g(t) = \frac{L_z(t)}{V_{tang}(t)}$, where $V_{tang}(t)$ is the average tangential speed of the stars in the disk at each time step (see previous section). We see that it remains close to the average galactocentric radius of the star, showing that L_z can be used as a proxy for guiding radius, thus allowing one to disentangle the effects of blurring and churning. The other panels are fully described in the legend of Fig. 8, and will be analysed throughout this article.

In Fig. 8, the star enters the corotation at time 3.8 Gyr and leaves the resonance at time 4.5 Gyr approximately. This is a very short interaction that hardly affects the radial position of the star as its guiding radius only moves from 6 kpc to 7 kpc approximately. After its interaction with the corotation, we have identified by plotting its orbit in the frame rotating with the bar that the star follows a succession of resonances with the bar: the 5:1 between 5 and 6 Gyr, the 4:1 between 6 and 6.5 Gyr, the 3:1 between 7 and 7.5 Gyr, and the 2:1 between 8.7 and 9 Gyr (the times are approximates). During these resonances, we observe that the angular momentum (and guiding radius) of this star displays oscillations, and that it decreases when the star enters in a new resonance. Ultimately, this star is in a 2:1 resonance with the bar, meaning it follows an elongated orbit constituting the bar.

In Fig. 9, the star enters the corotation region at 4 Gyr and leaves it at 5.5 Gyr approximately. This interaction holds for a longer time, and affects much more the orbit of the star than the previous example: it moves its guiding radius from 6 to 8 kpc approximately. As the previous star, this one follows a succession a resonances with the bar: the 4:1 between 6 and 7 Gyr, the 3:1 between 7.2 and 8 Gyr, and the 2:1 between 8.7 and 9 Gyr. Again, the star loses angular momentum when entering a new corotation, and is ultimately captured by the bar, on the 2:1 resonance. Although the behaviour at corotation of these two stars seems similar, we will see in the next sections of this paper that they have different dynamical origins. This star is an example of short bar-induced churning.

In Fig. 10, we have an example of a star experiencing a large bar-induced churning. The star enters the corotation around 2.5 Gyr, and remains trapped until the end of the simulation: its guiding radius follows closely the corotation radius. The orbit of this star is therefore strongly affected, we see that it is driven from 5 to almost 14 kpc by the corotation resonance. The third panel, allows to verify that it remains corotating with the bar: the angular frequency of the star follows closely (on average) that of the bar since 2.5 Gyr approximately. This argues that corotation with a bar having steadily decreasing angular velocity can cause a large out-

ward radial displacement in the disk, resulting in a phenomenon that we will call *bar-induced churning*. That is a newly identified phenomenon inducing guiding radius variations. The proportion of stars concerned by this phenomenon will be investigated in Sec. 6. In addition, we have computed the epicyclic frequency $\kappa(r)$ in the disk, that is estimated using the circular speed of stars in the galaxy (Binney & Tremaine 1987). The frequency $\kappa(r)$ decreases when the radius r increases. We have checked that the frequency of radial and azimuthal oscillations (panels 1 and 3 of the figure), follows closely the value of $\kappa(r)$, meaning that the decreasing frequency of the oscillations, is due to the outward movement of the star.

At this point of the paper, the important information to take from these figures are:

- L_z/V_{tang} is a good proxy for the guiding radius (red curve in panel 1) because the angular momentum L_z is not affected by epicyclic motion
- When a star enters the corotation region of the bar, it experiences episodes of churning.
- Stars can be trapped in the corotation resonance for various durations, leading to various guiding radius variations.
- Other phenomenons occur when stars are outside corotation radius that also affect their guiding radius (angular momentum).

In the following, we will identify the main sources of churning, and investigate the causes for the large disparity in the times stars remain in corotation with the bar. This study will be done at times larger than 2 Gyr, because prior to this period the bar is in the process of forming, so that its amplitude varies strongly with time. The behaviour at early times (< 2Gyr, when the bar is not yet in place) is ruled by transient spiral arms, and should be the same as in (Grand, Kawata & Cropper 2012b).

3.2 Finding the *churned* star particles

Although instructive, the study of the galactocentric radius of a star does not allow one to establish unambiguously the occurrence of churning. That is due to the epicyclic oscillations in the motion of particles (Fig. 8 to Fig. 10 show some examples). As discussed previously, it is more appropriate to use the variation of the vertical angular momentum L_Z to that effect. However, to detect only significant churning episodes, a threshold of ΔL_Z has to be adopted, otherwise almost 100% of the stars would be found to undergo churning because of minor variations of their guiding radius. Our results suggest a "reasonable" threshold value of 400 kpc^2 Gyr^{-1}: much smaller values lead to false identifications of churned stars, while much larger ones lead to missing episodes of significant churning.

The value of the threshold for ΔL_Z can be linked to an approximate guiding radius variation ΔR_g via the tangential speed of the stars: $\Delta R_g \simeq \frac{\Delta L_Z}{V_{tang}}$. This is an approximation because we use the mean tangential speed, so we estimate a mean ΔR_g value for a given ΔL_Z. In the simulation, the average tangential speed of the stars in the disk is approximately constant at 220 kpc Gyr^{-1} ,thus, our threshold for the churned stars corresponds then to $\Delta R_g \simeq$1.8 kpc.

4 SOURCES OF CHURNING

To investigate the origin of stellar churning, we will determine and analyse the fraction of stars that were churned, as a function of radius and time, on different time intervals of 1 Gyr, covering in total the range from 1 to 9 Gyr. We chose to work on 1 Gyr time intervals, because it approximately corresponds to 5 characteristic dynamical time (or 5 bar rotations), so this is a long enough period to observe the dynamical effects induced by the bar or the spirals on the stars.

As mentioned in the previous section, the angular momentum variations of individual stars are a proxy for guiding radius variations. Therefore, in each of our time intervals, we select the churned stars using the threshold ΔL_Z >400 kpc^{2}Gyr^{-1} for angular momentum variations. Once the churned stars are found, we record their first churning time (that is, the first time a star crosses the chosen angular momentum threshold in a time interval) and their *initial* galactocentric radius (i.e. the radius at the beginning of the time interval). Then, we bin the churned stars in the plane *initial galactocentric radius vs. first churning time*. And we normalize the number obtained in each radial bin with the total number of stars in each bin at the beginning of the time interval. Thus, we get the fraction of stars that were churned, from each initial radius as a function of time, on the defined time intervals.

The results are displayed in Fig. 11. Before 2 Gyr, the bar is not yet fully formed and churning occurs almost everywhere in the disk, due to the corotation of stars with transient spiral arms that form at almost all radii (see also Grand, Kawata & Cropper 2012b). In the interval 1-2 Gyr, we see that the region where the fraction of migrating stars is the highest (within the 1-sigma contours, between 3 and 7 kpc) is where we find the corotation radii of the m=3, 4 and 5 Fourier modes. In the interval 2-3 Gyr, the corotation radii are more spread in the disk, the m=5 mode being around 8 kpc, and the m=3 around 6 kpc. And we find stars migrating around the corotation of the bar (m=2 and 4 modes), but the correlation do not appear clearly. In this interval, the highest migrating fraction appears correlated with the m=3 and m=5 modes (corresponding to spiral patterns). From 3 to 8 Gyr, the churned fraction of stars appears more concentrated around the bar corotation radius, highlighting a tight correlation between radial churning and corotation with the bar. After 6 Gyr the corotation radii of all the modes remain close to one another, and near the region of high migrating fraction. However, due to the weakness of the modes 3 and 5 at that times (see Fig. 5) compared to the modes 2 and 4, we conclude that radial migration is induced by the corotation with the bar after 3 Gyr. The transient spiral arms probably become weaker because the effectiveness of their formation decreases due to the disk heating (by the bar and the spirals) that makes it more and more stable against arms formation. Finally, in the last interval from 8 to 9 Gyr, the bar corotation radius is almost outside the stellar disk so the stars affected by the resonance are mostly at radii lower than the corotation radius because their are almost not stars at larger radii.

We repeated the previous analysis using each churned star's *final* galactocentric radius (i.e. the radial position of the stars at the end of the time interval), to investigate where the churned stars go once they started to experience guiding radius variations. Again, the number of star we obtain in each radial bin is normalized by the total number of stars at the beginning of the time interval, in this bin. We display the results in Fig. 12. In the first time interval, from 1 to 2 Gyr, we see the effect of the transient arms: stars tend to spread over the whole disk, contributing to its extension toward larger radii. In the second time interval, from 2 to 3 Gyr, we see that churned stars also tend to spread in the disk. That is due to the fact that transient arms corotate with stars at many radii in the disk, so the guiding radius variation of stars trapped in corotations can be larger. On the next intervals, from 3 to 8 Gyr, the final radius of the churned stars remains roughly symetrical around corotation radius and almost no spreading away from that radius is observed.

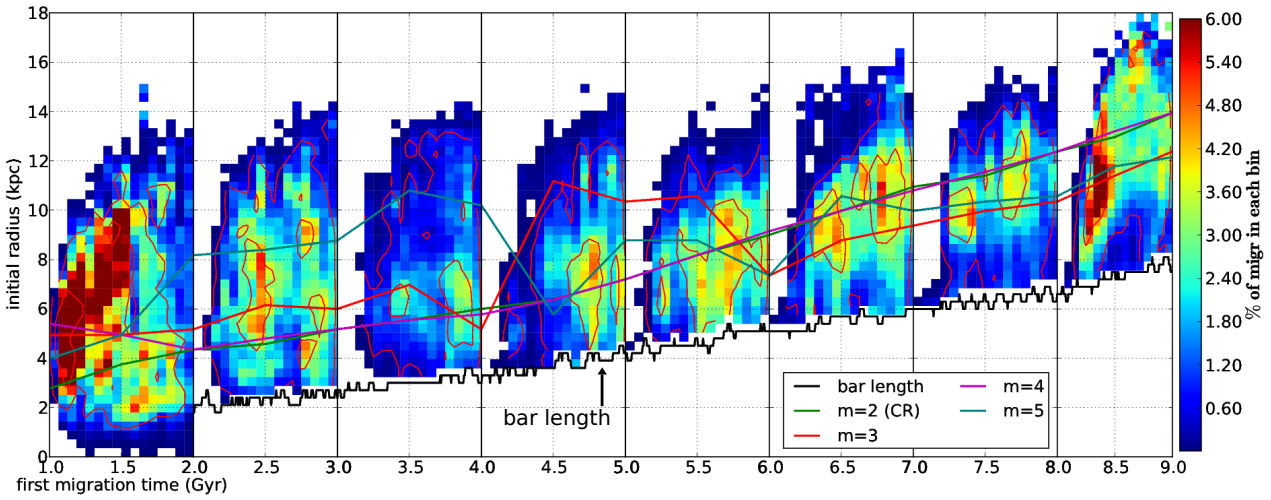

Figure 11. Initial radius and first churning time for all the churned stars (selected using the thresholdΔL_z >400 kpc^{2}Gyr^{-1}) born before the beginning of each time interval. Each panel displays the result on one time interval: [1,2Gyr] for the first panel, [2,3Gyr] for second panel, etc. First churning time is recorded when angular momentum change of the star crosses the threshold for the first time in each interval. The color scale indicates the fraction of churned stars. The color scale indicates the fraction of migrating particle in each bin, from 0 (white) to 6% (red). Some values can be higher than 6% (in the first and last intervals), but are still indicated red, in order to improve the color contrast. The thick black curve is the bar radius. We did not plot the results below the bar radius to focus on churning in the disk. The other thick coloured curves indicate the corotation radius of patterns from m=2 to m=5 (see legend). The patterns m=2 and m=4 are related to the bar. The patterns m=3 and m=5 are spirals. The strength of the various patterns is indicated in Fig. 5. The thin red contours are 1 σ and 2 σ density isocontours for the churned fraction. See on-line version for a full color figure. In each temporal interval, our temporal bins are 0.13 Gyr wide and our radial bins are 0.0625 kpc wide.

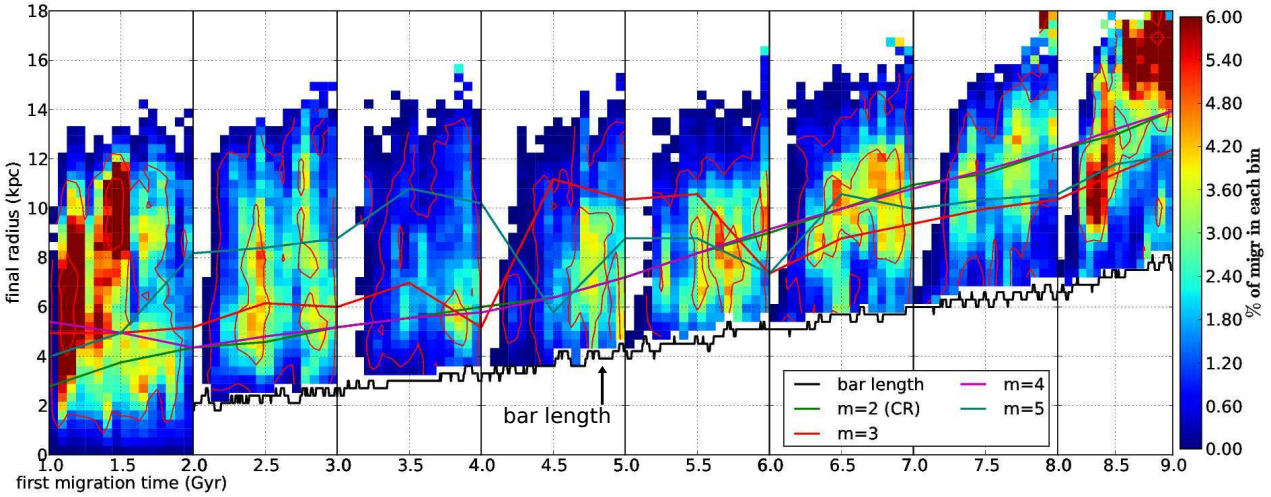

Figure 12. Same work as in Fig. 12, but using the *final* radius of the stars on each time intervals.

This is in agreement with the fact that the churning induced by the bar, makes stars swap their places around the corotation radius, as suggested in Fig. 13. In that figure, we show the variations, for all star particles, of their L_Z on three time intervals (1-2 Gyr, 4-5 Gyr and 9-10 Gyr), as a function of their final L_Z (at the end of the corresponding interval). It can be seen that stars remain close to the bar corotation radius, because stars below L_{corot} gain the amount of angular momentum to reach the symmetrical position with respect to L_{corot}; and the same happens to the stars above L_{corot}, except that they lose angular momentum. These results were already discussed in (Sellwood & Binney 2002). This effect will be call *mixing* in the following, because the stars are mixed radially through churning in a 4 kpc wide region around the corotation radius. This behavior is very different from the *bar-induced churning*, and we will compare the later to the former in Sec. 7. Finally in the interval from 8 to 9 Gyr in Fig. 12, we see that the stars that started to experience a churning episode within the corotation radius, are now outside corotation: they have gain angular momentum through the same mechanism as explain before, and moved to region where very few stars are initially present. This contributes to a late extension of the disk, beginning roughly at 7.5 Gyr, which is visible in the stellar surface density of Fig. 2.

By integrating the fraction of churned stars from Fig. 11 over time in each interval, we obtain Fig. 14. Where we display i) the fraction of stars that are churned (i.e. the number of churned stars divided by the total star number), and ii) the fraction of churned

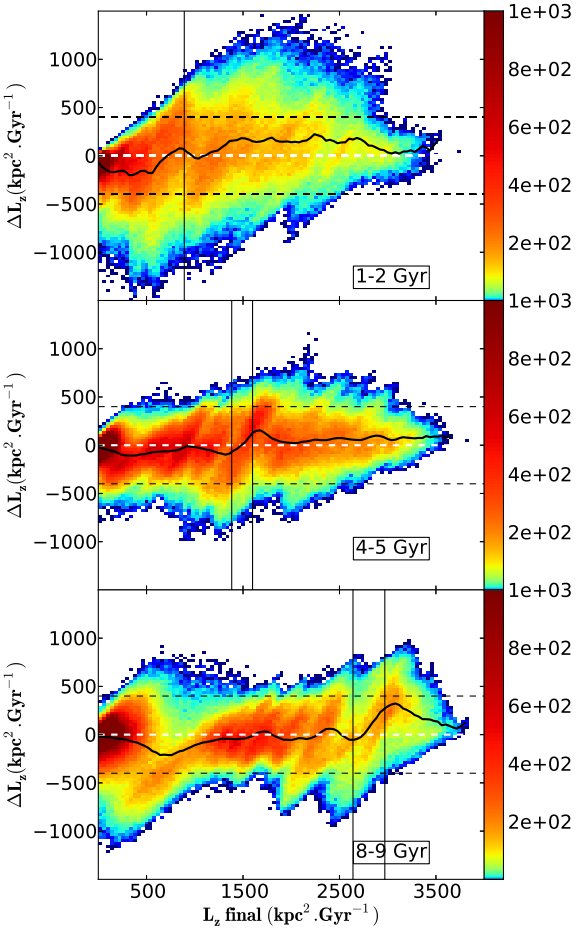

Figure 13. Angular momentum variation (ΔL_z) for all stars versus final angular momentum $L_z\,final$, at different times of the galaxy evolution: between 1-2 Gyr (*upper panel*), 4-5 Gyr (*middle panel*) and 8-9 Gyr (*lower panel*). In all panels, the horizontal white dashed line corresponds to no variation in L_z and the two horizontal black dashed lines correspond to $\Delta L_z = \pm 400$ kpc^{2}Gyr^{-1}, which is the threshold value we adopted to identify the migrating stars (Sec. 3.3). The thick full black curve in all panels is the average ΔL_z for each $L_z\,final$ and the thin black vertical lines are the values of $L_{corot} = R^2_{corot}\Omega_{bar}$ of the bar at the beginning and the end of the time interval, respectively. The color scale indicates the number of stars in each bin of the plane ($\Delta L_z, L_z\,final$). See on-line version for full color figure.

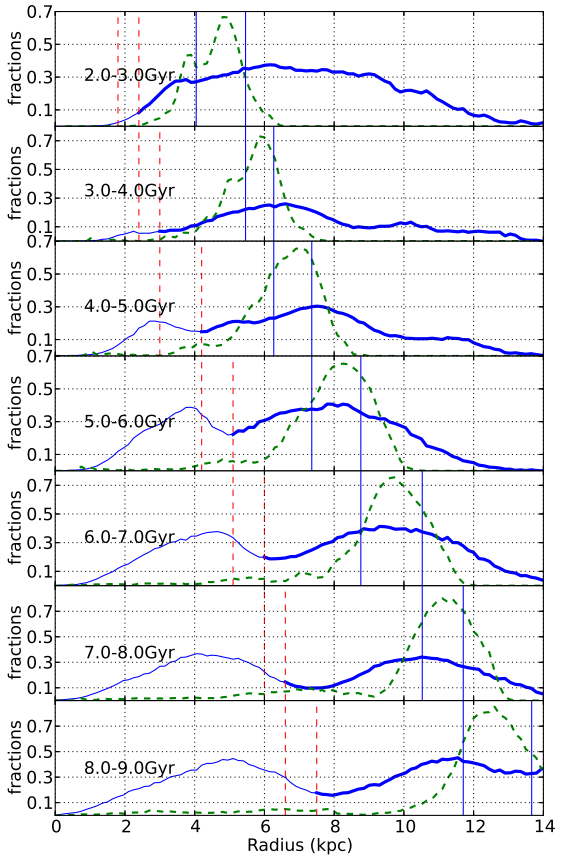

Figure 14. In all panels: fraction of all churned stars (full blue on-line curve) and fraction of churned stars at corotation (dashed green on-line curve), as a function of the radius of stars at the beginning of each time interval. The (blue on-line) full vertical lines indicate the corotation radius at the beginning and end of each time interval and the (red on-line) vertical dashed lines the corresponding length of the bar's semi-major axis. The corresponding time intervals are indicated on each panel.

stars at corotation with the bar (i.e. the number of churned stars at corotation divided by the number of all the detected migrating stars, using the threshold in angular momentum variation), both results are function of the initial radius of stars on each time interval. In our 1 Gyr temporal bins, we define stars at corotation as the ones lying in the angular speed interval $[0.9\Omega_{bar}(t_c); 1.1\Omega_{bar}(t_c)]$, where t_c is the center of a given time interval. This selection criterion relies on the fact that, in this simulation, the angular speed of the bar decreases by approximately 10% every 1 Gyr. In each panel, we indicate by vertical lines the radius of the bar (dashed; red on-line) and the corotation radius (solid; blue on-line) at the beginning and at the end of the corresponding time interval. We remind that this paper focus on the churning occurring in the disk, so we will only analyze the fraction outside the bar radius (indicated by the thick part of the blue curve). However, we know that the orbits constituting the bar are elongated along the bar's major axis, and that stars on these orbits, periodically gain and lose angular momentum between apocenter and pericenter. As a result, these stars are detected as churned ones by our method, and the fraction of churned stars is enhanced below the length of the bar's semi-major axis.

In Fig. 14, we reduce the amount of churned stars detected in the bar region by rejecting the stars whose first churning time is shorter than the characteristic dynamical time of the disk, that is one rotation of the bar. The angular momentum variation of the stars on elongated orbit in the bar occur on much shorter time scales than this characteristic time, because the angular speed of stars is higher in the central region of galaxies. Therefore, with that method, we reduce the number of churned stars detected in the bar, while conserving this number in the disk.

In the 2-3 Gyr time interval, the fraction of churned stars is around 35% over most of the disk, and this fraction holds even several kpc away from bar corotation (solid blue on-line curve, from 3 to 9 kpc). In the 4-5 kpc region, corotation is responsible for ~2/3

of those churned stars (dashed green on-line curve), but in the rest of the disk, churning is due to other physical processes. In the 4-5 Gyr interval, the fraction of churned stars has dropped to ∼20% (or lower) over most of the disk and remains around 30% in the corotation radius (∼6-7 kpc); again, almost 2/3 of the latter are due to bar corotation. Finally, in the 7-8 Gyr interval, the fraction of churned stars remains at ∼30% around corotation radius, and the corotating stars represent about 2/3 of the total churned stars in this region; elsewhere in the disk, the fraction drops to ∼10%.

Our results show that at all times there are stars experiencing churning all over the disk. Before 3 Gyr, transient spirals are obviously at the origin of that churning. Once the bar is strong enough compared to the spiral patterns, it enhances churning at the bar's corotation, which produces then systematically about 2/3 of churned stars around corotation radius. However, churning persists at those times all over the disk, even away from the corotation with the bar, albeit at lower levels (churned fractions around 10-20%).

We will see in the next section, that the churning of those stars is due to various dynamical effects involving the corotation radii of the spiral patterns, and resonances of higher multiplicity with the bar.

5 GLOBAL STELLAR MOVEMENTS

In a companion paper (Kubryk, Prantzos & Athanassoula 2013), we analysed the effects of radial migration on the chemical evolution by post-processing the chemical results using a semi-analytical code. To do so, we had to insert radial migration in the latter code, using a probabilistic model for the amount of stellar mass exchange between the radial zones at each time step. In this model, we have free parameters and we analysed the simulation present paper to obtain numerical values for the free parameters.

In this section, we will describe more precisely the stellar movements induced by the resonances of higher multiplicity with the bar, by the corotation resonances of the spiral arms and the bar, and by the bar-induced churning. We will explain how these migration mechanisms combine with cumulative effects over time, leading to the strong radial migration observed in this simulation.

5.1 Bar's resonances of higher multiplicity

The resonances of higher multiplicity affecting stars at radii larger than CR (corotation radius) are defined as:

$$\Omega = -\frac{\kappa}{m}, \tag{5}$$

where Ω is the angular speed of stars in the frame rotating with the bar, κ is radial epicycles frequency, and m is the order of the resonance.

In Fig. 15, we display the initial vs. final angular momentum of stars, on successive 1 Gyr intervals: 1-2 Gyr, 3-4 Gyr, 5-6 Gyr and 8-9 Gyr. Using the circular velocity, we determine the L_z value corresponding the radii where we find the resonances. The L_z where the stars are on some resonance are indicated with vertical lines in the figure: the magenta thick dashed line, marks the position of the bar's corotation at the central time of each interval, and the black dashed lines indicate the resonances of higher multiplicity of the bar. The orange dashed line marks the OLR (defined by $\Omega = -\kappa/2$) at the central time of each interval. The coloured solid lines indicates the corotation resonances of the spiral patterns (lee legend of the figure). Finally, the red thick curve is the average initial angular momentum as a function of the final angular momentum.

In the left-most panel of Fig. 15, the stars having $L_{z\,initial} \geq 1000\ kpc^2 Gyr^{-1}$ approximately, gain angular momentum on the interval 1-2 Gyr. Because this occurs before the time where the bar is fully formed (2 Gyr), we can say that the stars have gained angular momentum because of the transient spiral arms, that are the strongest on this time interval. The stars below $L_{z\,initial} \sim 700\ kpc^2 Gyr^{-1}$ (within the bar's corotation radius) lose angular momentum because they start forming the bar, and once in the bar, they are on the ILR (inner resonance of order 2 with the bar), so they transfer their angular momentum to the dark matter halo (Athanassoula 2002). In this panel, the resonance of order 4 and the corotations with spirals are superposed, which is a remarkable resonance overlap, but it don't appear to create a particularly strong migration episode as it would be expected (Minchev et al. 2011) probably because the overlap do not last for enough time.

On the two middle panels of Fig. 15 (intervals 3-4 Gyr, 5-6 Gyr), we see mainly the effects of the bar, because the strength of the spiral patterns has decreased while that of the bar has increased, so that, on average, the bar is the dominant non-axisymmetric structure. We see that the inner part of the disk lose angular momentum (again, because of the ILR). The stars around the bar's corotation have lost angular momentum if the are below the corotation at the end of the time interval, while they have gain angular momentum if they are above the corotation at the end of the interval, and the value are almost symmetric with respect to the CR. This indicates that the stars around the corotation radius have swapped their places, in agreement with the results of Sellwood & Binney (2002), about the effects of a transient spiral patterns (we will come back on this behaviour in Sec. 7). Finally, the stars located around the OLR of the bar (the resonance of order m=2) have gain angular momentum, according to Athanassoula & Misiriotis (2002), this is due to transfer of angular momentum between the ILR and the OLR: the angular momentum of stars at the ILR is mostly transfered to the dark matter particles at the OLR, but a few amount of angular momentum is also transferred to the stars at the OLR. On these panels, the other resonances of higher multiplicity with the bar and the corotations with spiral patterns have almost no effects. And the angular momentum exchange around the CR, increases at latter times, because the bar gain strength.

On the right-most panel of Fig. 15 (interval 8-9 Gyr), the outer resonances of higher multiplicity are out of the disk, and we see only the effects of the ILR, and the stellar movements around the CR which almost out of the disk.

Therefore on 1 Gyr intervals, the spiral rules the stellar movements at t≤2 Gyr, and the bar's corotation becomes the most effective churning inducer after 2 Gyr outside the bar region. And, on 1 Gyr intervals, we cannot see the bar-induced churning because the bar's CR do not move enough: according to Fig. 7, the CR have an outward displacement of 1.25 kpc approximately, so the stars following the CR do not come from radii far from the final position of CR. As a result they have small impact on the average initial angular momentum in Fig. 15.

In Fig. 16, we display the initial vs. final angular momentum of the stars on the time intervals 1-3 Gyr, 1-5 Gyr, 1-7 Gyr and 1-9 Gyr. The magenta dashed line marks the position of the bar's corotation at the end of the interval, the red curve is the average initial angular momentum as a function of the final angular momentum, and the orange dashed line marks the OLR (the outer resonance of order 2) at the final time of each interval. The purpose of this figure is to investigate the cumulative effects over time of the migration mechanisms.

We can see that in the inner parts of the disk, in the region of

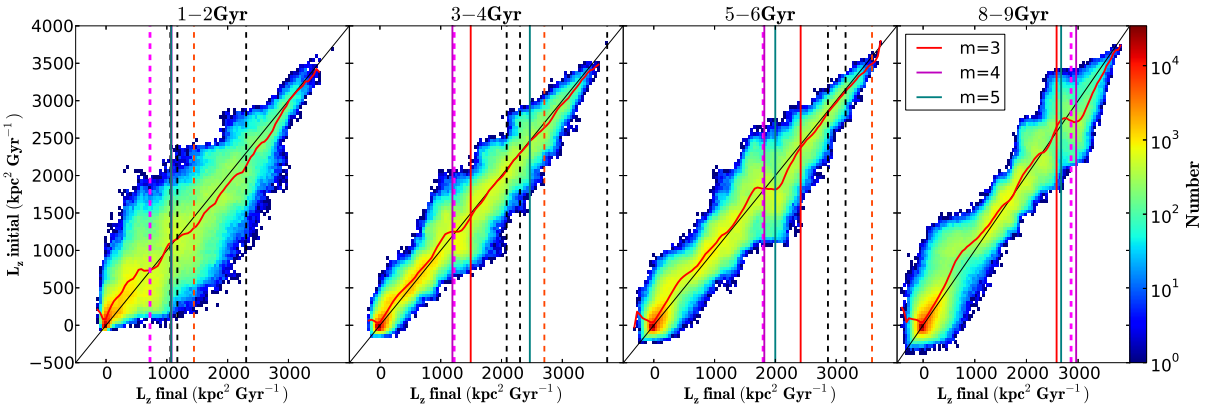

Figure 15. On the time intervals 1-2 Gyr, 3-4 Gyr, 5-6 Gyr and and 8-9 Gyr (from left to right panels), we display the initial versus final angular momentum for all the stars (formed from the gas in the simulation: the STAR component of the disk) existing at the beginning of each time interval. The color scale indicates the number of stars in each pixel, the black solid line indicates the locus of the diagonal $L_{z\,final} = L_{z\,initial}$. Using the radius of a given resonance and the circular velocity at this radius, we determine the corresponding value of L_z. The thick magenta dashed line marks the place of the bar's corotation at the end of the time interval. The orange dashed vertical line, marks the OLR (outer Lindblad resonance) of the bar. The black dashed vertical lines mark the resonances of multiplicity m=4, m=3 and m=1 (from left to right) with the bar, defined by Eq. 5. And the coloured solid vertical lines indicates the position of the corotation resonances with the Fourier modes in the disk, from m=3 to m=5 (see legend).

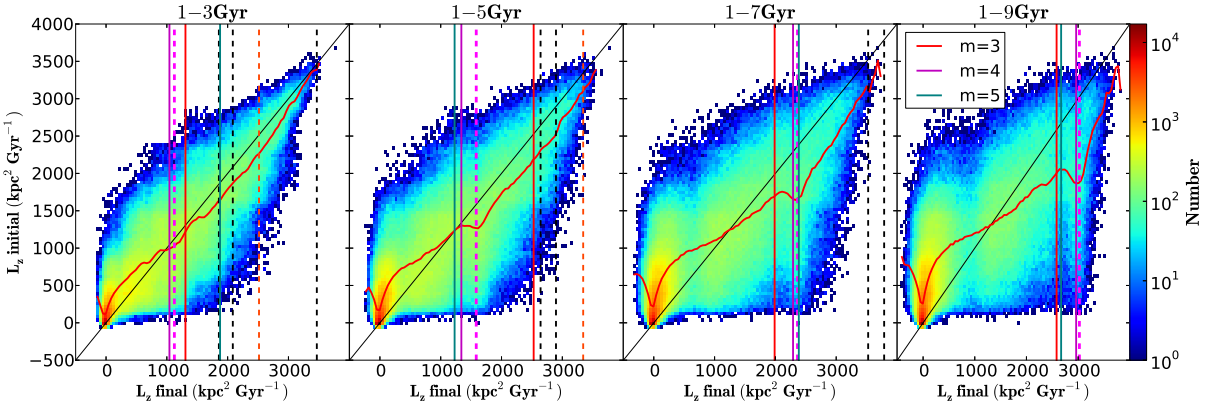

Figure 16. On the time intervals 1-3 Gyr, 1-5 Gyr, 1-7 Gyr and 1-9 Gyr (from left to right panels), we display the initial versus final angular momentum for all the stars (formed from the gas: the STAR component of the disk) existing at the beginning of each time interval. The color scale indicates the number of stars in each pixel, the black solid line indicates the locus of the diagonal $L_z final = L_z initial$. The thick magenta dashed line marks the place of the bar's corotation at the end of the time interval. The orange dashed vertical line marks the OLR, the thin black dashed vertical lines mark the resonances of order 4, 3 and 1 (from left to right) with the bar, defined by Eq. 5, at the end of each time interval. And the coloured solid vertical lines indicates the position of the corotation resonances with the Fourier modes in the disk, from m=3 to m=5 (see legend).

the bar, the initial angular momentum is larger than the final angular momentum in average. That is due to the fact that stars traped in the bar are on the ILR, as already exposed about the previous figure. Here, we see the cumulative effects of the ILR over time: the stars in this region lose more and more angular momentum, as a consequence, the rotation speed of the bar decreases.

Outside the bar's corotation region, the stars come in average from inner radii when comparing their state at 1 Gyr with later times. The average initial angular momentum (red solid curve) is below the diagonal, and the curve displays a hollow around the CR. To explain the behaviour of the average initial angular momentum, we have to combine the effects of the early spiral arms (at t<3 Gyr), with the resonances of higher multiplicity with the bar, and the bar-induced churning (stars trapped in the corotation region moving outward).

On the left-most panel (1-3 Gyr), the early spirals induce an outward movement of the stars having $L_z \geq 1500\ kpc^2Gyr^{-1}$ between 1 and 2 Gyr (see Fig. 15) and the OLR can also have appreciable affects. For example, the stars at $L_{z\,final} = 2000\ kpc^2Gyr^{-1}$, have an average initial angular momentum of $1770\ kpc^2Gyr^{-1}$. The difference is $230\ kpc^2Gyr^{-1}$, corresponding to an average initial guiding radius approximately 1 kpc inward (because the circular speed is approximately 220 km/s). This value is roughly the same between $1500\ kpc^2Gyr^{-1}$ and the OLR (at $L_{z\,final} \approx 2500\ kpc^2Gyr^{-1}$). For stars having their final angular momentum above the OLR, the average gain of angular momentum decreases. This is because, on that time interval, the OLR has moved outward, (from $1450\ kpc^2Gyr^{-1}$ in the left-most panel of Fig. 15 to $2500\ kpc^2Gyr^{-1}$ in the left-most panel of Fig. 16) so the stars in that L_z interval have gain angular momentum, while stars at radii larger than OLR have not yet felt its effects.

On the following interval (1-5 Gyr), The OLR is now around

3400 kpc^2Gyr^{-1}, so the stars that were at radii larger than the OLR on the interval 1-3 Gyr, have now gained roughly the same amount of angular momentum than the stars that were between 1500 and 2500 kpc^2Gyr^{-1} on the interval 1-3 Gyr. Around the bar's corotation radius (magenta dashed line), we see the effects of the position swapping already described: the stars below the CR have larger initial angular momentum, and stars above the CR have lower initial angular momentum. The difference, when compared to Fig. 15, is that the changes around the CR are not symmetric, because we start seeing the effects of the bar-induced churning: the trapped stars can come from very low radii, even from the initial position of the corotation (which is around 2 kpc at 2 Gyr), therefore they lower the average initial angular momentum of the stars in the corotation region.

On the next time intervals (1-7 Gyr and 1-9 Gyr), we observe mainly the effects of the ILR and the bar's corotation. On these intervals we observe a stronger impact of the bar-induced churning, that lower the average initial angular momentum around the CR. This effect of the bar-induced churning appears to increase when the bar's corotation reaches the outer regions of the disk. For example, when the corotation corresponds to $L_{z\ final} \approx 1575\ kpc^2Gyr^{-1}$ at 5 Gyr, we have an average initial angular momentum of 1250 kpc^2Gyr^{-1}, corresponding to an average outward movement of 1.5 kpc for the guiding radius of the stars corotating with the bar at 5 Gyr. While when the bar's corotation corresponds to $L_{z\ final} \approx 3000$ kpc^2Gyr^{-1} at 9 Gyr, the average initial angular momentum is at corotation is approximately 1900 kpc^2Gyr^{-1}, corresponding to an average outward movement of 5 kpc approximately for the stars in the corotation region at 9 Gyr. In sec. 7, we will analyse the dynamics of the bar-induced churning, and the fraction of stars concerned by this phenomenon.

In the end, we have shown that to understand the radial migration we had to combine the effects of the transient arms prior to the bar formation, the effects of the various resonances with the bar outside the corotation radius (mainly the ILR and OLR and their cumulative effects over time), the bar's corotation and the bar-induced churning.

5.2 Effects of the corotations with spirals

In Figs. 9 and 8, we have examples of stars that undergo radial displacements before entering the corotation region of the bar. The star in the first figure is born at 10 kpc at 2.5 Gyr, and its radial position decreases steadily to 7.5 kpc between 2.5 and 3.5 Gyr, then its guiding radius remains roughly constant until the star starts corotating with the bar. In the second figure, the star starts at 11 kpc and moves steadily inward between 2 and 3 Gyr, ending at 7 kpc, then its guiding radius experiences small variations (that can be due to small perturbations in the galactic disk), until it also starts corotating with the bar. These movements occur far from the corotation resonance with the bar, so it can not be involved. Therefore, we suspect other resonances to be responsible for this radial migration.

In Fig. 17, we display the angular momentum of the stars as a function of their initial angular momentum, on the interval 2-3 Gyr. Using our analysis of the corotations with patterns, we convert our corotation radii to angular momentum: $L_{z,corot} = R_{corot} * V_{tang}$ where R_{corot} is one identified corotation radius and V_{tang} is the tangential speed of stars, which is approximately 220 km/s. Therefore, we are able to indicate the location of the corotation in the figure (vertical lines), and the location of the stars that have influenced by each corotation on the time interval (tilted dashed lines). Stars that migrate because of the corotation resonance should swap their

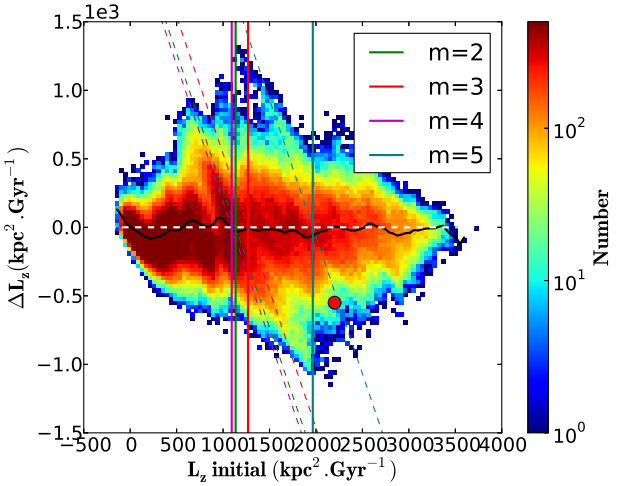

Figure 17. Angular momentum variation for all stars versus initial angular momentum between 2 and 3 Gyr. The color scale indicates the number of star in each bin. The black curve indicates the average experienced by the stars as a function of their initial angular momentum. The vertical lines indicate the position of the different corotations (see legend), and the tilted dashed lines indicate the position of the stars influenced by each corotation and have the corresponding color. These lines have the slope -2, because stars influenced by corotation resonances swap their places around the corotation radius. The red dot indicates where the star in Fig. 8 is.

places around the corotation radius (Sellwood & Binney 2002), as a result, the dashed lines have a slope -2. The star in Fig. 8, is indicated by the red dot: its radius at 2 Gyr is 11 kpc and its guiding radius variation is -4 kpc, that gives an initial angular momentum of 2420 $kpc^2.Gyr^{-1}$ and an angular momentum variation of -880 $kpc^2.Gyr^{-1}$. So, this star is close to the purple dashed line, meaning that it is in the region where the stars have most likely been influenced by the corotation with the m=5 pattern, between 2 and 3 Gyr. This star loses angular momentum and migrate inward, crossing the corotation radius of the m=5 pattern.

In Fig. 18, we do the same work between 2.5 and 3.5 Gyr, and the red dot indicate the position of the star in Fig. 9. This star is at 10 kpc at 2.5 Gyr and at 7.5 kpc at 3.5 Gyr, thefore its initial angular momentum is 2200 $kpc^2.Gyr^{-1}$ and its angular momentum variation is -550 $kpc^2.Gyr^{-1}$. As the previous example, this star is also close to the region of influence of the m=5 pattern, that make it lose angular momentum, resulting in an inward radial migration.

This analysis gives an illustration of the churning induced by corotations with spiral patterns. In our two examples, we have only two stars migrating inward, but a deeper analysis of their effects should have brought results similar to Sellwood & Binney (2002). But, since the bar is the dominant non-axisymmetric structure for most of our simulation time, we focused on the migration induced by the interactions with the bar.

We highlighted in this section that the corotation with the bar is very effective in inducing stellar churning, and that stars churned from the corotation region tend to remain in that region. In the next section, we will investigate the dynamical effects supporting this phenomenon. To do so, we will analyse the effective potential and examine the correlation between the existence of Lagrangian points and the radial churning of stars around the corotation radius.

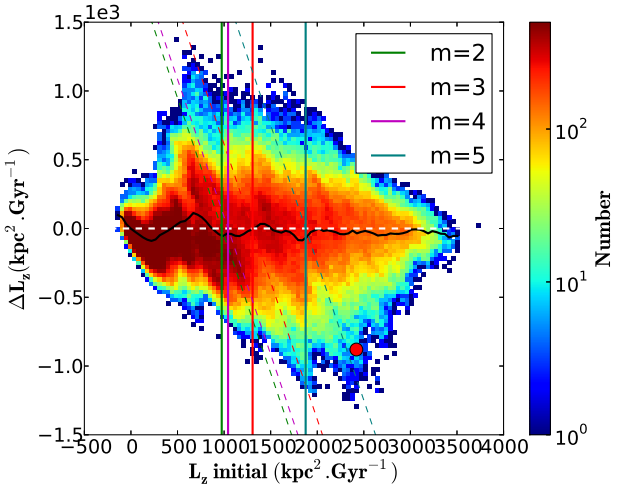

Figure 18. Angular momentum variation for all stars versus initial angular momentum between 2.5 and 3.5 Gyr. The color scale indicates the number of star in each bin. The black curve indicates the average experienced by the stars as a function of their initial angular momentum. The vertical lines indicate the position of the different corotations (see legend), and the tilted dashed lines indicate the position of the stars influenced by each corotation and have the corresponding color. These lines have the slope -2, because stars influenced by corotation resonances swap their places around the corotation radius. The red dot indicates where the star in Fig. 9 is.

6 DYNAMICS AROUND THE LAGRANGIAN POINTS

6.1 In the simplified case

The Lagrangian points are the equilibrium points of the effective potential, that is defined as:

$$\Phi_{eff}(r,\theta) = \Phi(r,\theta) - \frac{1}{2}\Omega_b^2 r^2, \quad (6)$$

where Φ is the potential in a Galilean reference frame, Ω_b is the angular speed of the bar, and (r,θ) are the polar coordinates.

The dynamics of stars around Lagrange points have been well studied in the case where the potential do not evolve with time, and more specifically, in the simple case where the only non-axisymmetric component of the potential is a bar with constant rotation speed and no secular evolution (see for example Binney & Tremaine (1987), or papers by Athanassoula *et al.*). In this case, the Lagrangian points are aligned with the bar major and minor axis: two maximum-type points, usually called L4 and L5, aligned with the minor axis; two saddle-type points, L1 and L2, aligned with the major axis; plus the minimum of the potential at the center of the galaxy, called L3. The points L1, L2, L4 and L5 are near the corotation radius, and are fixed in space and time.

The stellar movement around the Lagrangian points can be quasi-periodic or unstable. The equations ruling the quasi-periodic motion are given in Binney & Tremaine (1987), and the ones ruling the unstable motion are given in (Romero-Gómez et al. 2006). To understand of which type is the stellar motion at corotation with the bar in this simulation, we investigate the stability of the Lagrangian points.

Following (Binney & Tremaine 1987), but without assuming the 4-fold symmetry of the potential, we obtain the following results :

$$\begin{cases} \Phi_{xx} + \Phi_{yy} + 4\Omega_b^2 \geqslant 2\sqrt{\Phi_{xx}\Phi_{yy} - \Phi_{xy}^2} & (a) \\ \Phi_{xx}\Phi_{yy} - \Phi_{xy}^2 \geqslant 0 & (b) \end{cases} \quad (7)$$

where the Φ_{xx}, Φ_{yy} and Φ_{xy} are the second derivatives of the effective potential with respect to variables x, y, and cross derivative respectively, and Ω_b is the rotation speed of the bar. This result is equivalent to that of Pfenniger (Pfenniger 1990), who however kept these inequalities written in an other form, to distinguish between different types of unstability.

The analysis of the stability conditions shows that the saddle-points L1 and L2 are always unstable, meaning that stars around them can reach these points, but they will not stay (Romero-Gómez et al. 2006); and the maximum-type Lagrangian points L4 and L5 are stable, meaning that stars rotating around these points (following horseshoe orbits Binney & Tremaine (1987)) will not be driven away from the Lagrangian points by small perturbations of there orbit.

6.2 In our simulation

We computed the effective potential in our simulation a 10 pc softening length. The left panels of Fig. 19 display the effective potential maps at times 2 and 4.5 Gyr. As expected, the effective potential decreases when moving to radii far from corotation radius (which is marked by a blue dashed circle), and shows local maxima and minima near the corotation radius. In our simulation, the Lagrangian points are also close to corotation, but they are not aligned with the bar axis, and their number and location are varying with time. We observe that the spiral arms or over-densities crossing the corotation radius, have a strong influence on these characteristics: where they cross the corotation, the potential reaches a minimum and has the shape of a saddle point, and between these points the effective potential reaches a maximum value.

We found that the stability condition (a) in Eq. 7 for the Lagrangian points, is always verified in our N-body simulation, so their stability depends only on condition (b). We obtain always negative values of the stability condition (b) for the saddle-type Lagrangian points. The maximum-type Lagrange points are clearly stable at early times, but the analysis is more difficult at later times because we want to compute derivatives of the effective potential, which is more noisy. Nevertheless, we can consider that the maximum-type Lagrangian points of the effective potential are stable since we always get roughly $\Phi_{xx}\Phi_{yy} - \Phi_{xy}^2 \geqslant 0$ (condition (b)) around them. Therefore, we expect the motion of the stars around the maximum-type Lagrangian points to be quasi-periodic: they should rotate around the local maxima of the effective potential. And the motion of the stars around the saddle-type Lagrangian points should be as described in (Romero-Gómez et al. 2006).

We check the previous analysis with a visualization of the stellar orbits around the maxima of the instantaneous effective potential. In Fig. 19 the right column displays the average star particle velocity vectors in each pixel of the disk, in the frame rotating with the bar, at 2 Gyr (upper panel) and 4.5 Gyr (lower panel). Here we assume that epicyclic motions have negligible influence on these figures, because they introduce blurring without changing the average speed value, so, when there is only one family of orbit passing through a pixel, the average speed-vector of the stars in that pixel is the speed-vector that would have a star following the guiding orbit in that pixel i.e. without blurring. It reveals that the stars in

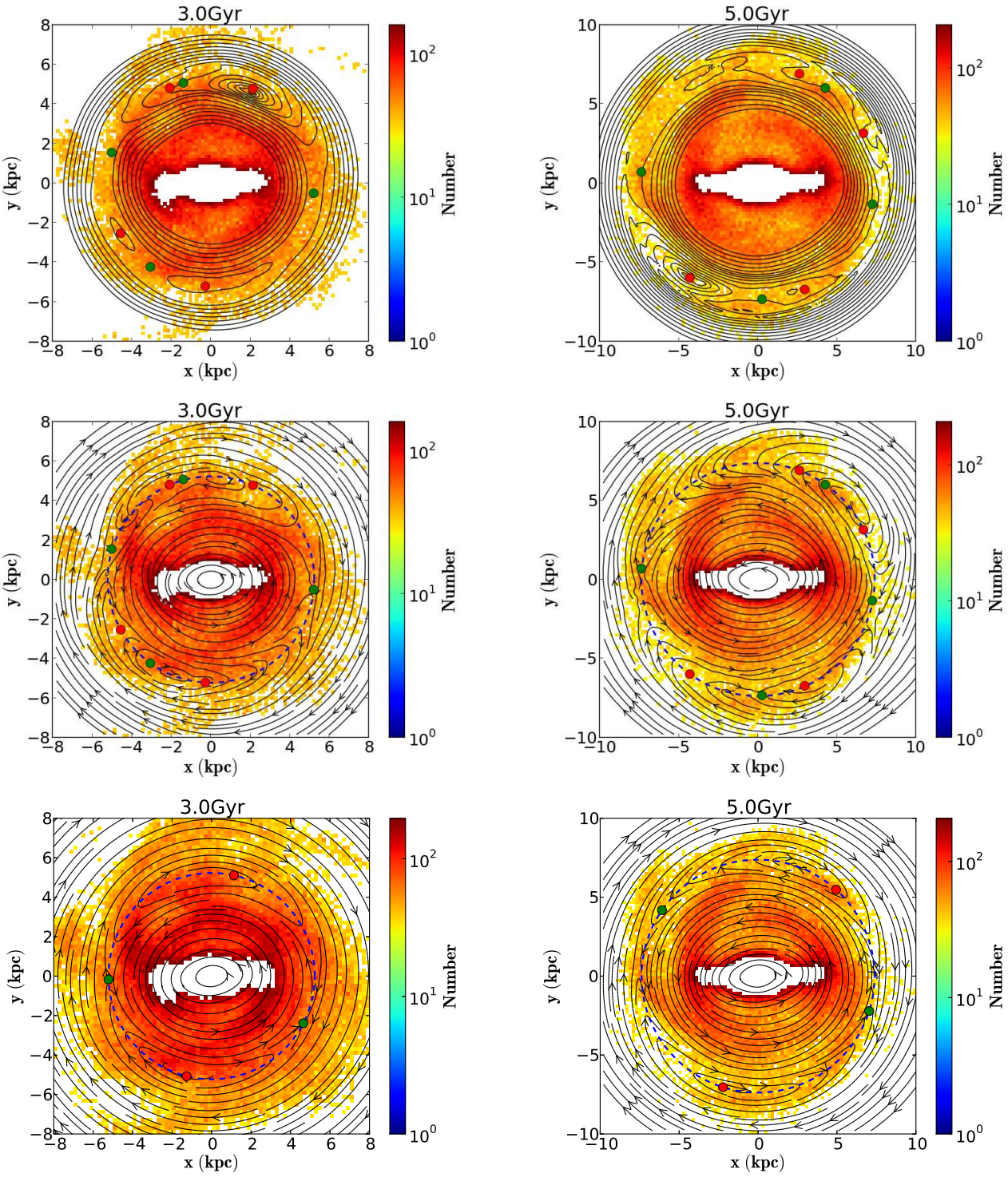

Figure 19. *Upper row*: the left and right panels, show the isocontours of the effective potential (black lines), and a density map of the stars at 2 and 4.5 Gyr. The dashed-blue circle represent the corotation radius at the time of each panel. *Middle row*: The left and right panels, show average velocity maps (black lines with arrows indicating the direction of average speed vectors) in the reference frame rotating with the bar, and the density map of the stars at 2 and 4.5 Gyr. The color scale in all panels represents the number of stellar particle in each pixel. The blue dashed circle represents the corotation radius at the time of each panel. The central region (in white) has been removed to improve the density contrast. (See on-line version for coloured figure). *Lower row*: Addition of snapshots (previously aligned with the axis of the bar) in the time interval $2.9 < 3.0 < 3.1$ Gyr (left panel) and $4.9 < 5.0 < 5.1$ Gyr (right panel). We display the average velocity maps (black lines) in the reference frame rotating with the bar, and the density map of the stars. The color scale in both panels represents the number of stellar particle in each bins. The blue dashed circle represents the corotation radius at the time of each panel. In the first two rows, the green/red dots mark the locus of minimum-type/maximum-type 8-Lagrangian points at 3 Gyr and 5 Gyr. While in the last row, these dots mark the locus of the 2-Lagrangian points. The notion of n-Lagrangian point will be explained in Sec. 7.

the corotation region rotate around different points located on the corotation radius.

Following the the previous analysis of the Lagrangian points in our simulation, we should see in the right panels of Fig. 19 the stars following horseshoe orbits around stable maximum-type Lagrangian points. But when comparing the stream maps (right panels) with the effective potential at the same times (left panels in the figure), we notice a discrepancy: the center of the cells and the points of transition from one cell to an other in our stellar-streams maps, do not match the place of the Lagrangian points that can be identified by eye in the effective potential maps.

This drawback can be explained by the fact that transient arms have very short typical life-time (< 0.1 Gyr) compared to the characteristic dynamical time of the galaxy (which approximately increases from 0.2 to 0.4 Gyr on 8 Gyr). The same behavior for the transient arms is observed in other simulations (Grand, Kawata & Cropper 2013). Therefore, a single arm, and its effects on the Lagrangian points, may not have time to influence the guiding orbit of stars, and only the time average gravitational forces exerted by successive arms, may be relevant to understand the stellar churning. We will investigate that hypothesis in the next section.

7 COROTATING STARS IN A NON-STEADY POTENTIAL

We have seen in the previous section that the instantaneous effective potential fails to fully explain the velocity maps, because the typical life-time of transient arms is short compared to dynamical characteristic time, thus a single arm hardly affects the guiding radius of stellar orbits. We found that the position of Lagrangian points in the instantaneous potential do not match the position of the "vortices" found in the velocity maps, created by the stars following horseshoe orbits around the maximum-type Lagrangian points. This is because we were using tools developed for steady potentials. Therefore, to understand the dynamics of stars in potentials evolving with time, with many recurrent transient spiral arms, we have to find other methods.

One method is to work with smoothed potentials, assuming that the smallest structures are too short-lived to have an appreciable impact on the stellar orbits. Therefore, smoothing the potential allow to consider the effects of the largest non-axisymmetric structures only, that live long enough compared to the dynamical time scale of stellar orbits (about 0.3 Gyr for one revolution around the galactic center). As a result, we expect the smoothed effective potential to evolve more slowly with time, giving sense to Lagrangian points at least on time intervals commensurable with the dynamical time scale of stellar orbits.

In addition, with the panel 4 in Fig. 10, we can estimate that the period of the horseshoe orbit can be about 2 Gyr or longer. In the previous subsection, we estimated that the minimal period of horseshoe orbits is approximately 1 Gyr, which in agreement with the estimated period of 2 Gyr for the particle in Fig. 10. This time scale is long compared to the life-time of transient spirals, therefore it brings further justification to the smoothing of the effective potential.

In the following, we will smooth the effective potential, using low-pass Fourier filter, and introduce the notion of n-Lagrangian points. They we will argue that we need to use the 2-Lagrangian points to describe the movement of stars corotating with the bar, and we will follow the evolution of these points. Then we will check that the 2-Lagrangian points describe more accurately the guiding orbit of stars in the frame rotating with the bar. Finally, we will do statistics on the stars trapped in the corotation region, in order to characterize the proportion of stars concerned by the different motions that can be induced in the corotation region.

7.1 Introducing the n-Lagrangian points

We smooth the effective potential at the corotation radius using Fourier filters: we perform a Fourier analysis of the azimuthal variations of the effective potential at the corotation radius, and reconstruct a smoothed potential by summing Fourier modes from m=0 to m=n. The high frequency variations are described by higher modes, therefore, the lower is n the smoother is the potential. We will call the equilibrium points found in such a smoothed potential *n-Lagrangian points*, where n is the maximum Fourier mode that is used. With this method, when $n \rightarrow \infty$, we get the instantaneous potential, and the ∞-Lagrangian points are the Lagrangian points.

Our hypothesis is that the variations of the effective potential described by the first modes of the Fourier decomposition are spatially large, and persistent in time, because created by larger structures in the disk, that should evolve on larger time-scale than the small perturbations. Therefore, applying a low-pass Fourier filter on the effective potential will give spatially smoother potential, and it should also produce smoother temporal variations of the potential. The obtained smoothed potential can be interpreted as the potential ruling the phenomenons occurring on large time scales. In the following, by adjusting the value of n, we want find the potential describing phenomenons ruled by the bar, which is a structure having a longer life-time than the transient spiral arms.

In Figs. 21 and 22, we give examples of smoothed effective potential in the corotation region of the bar. We display the 8-Lagrangian points (upper panel) and 2-Lagrangian points (lower panel) at 3 and 5 Gyr of the simulation. It is visible that a lower value of n leads to less equilibrium points, because the small variations are smoothed. In addition, the 8-Lagrangian points are very close to the Lagrangian points. We used them in Fig. 19, to mark the position of the Lagrangian points found in the effective potential. But we have seen that these points are created by transient arms, so they do not describe the stellar movements having large dynamical time-scale.

7.2 Fourier analysis of the effective potential at corotation

As already said, Lagrangian points are places where the first derivatives of the effective potential are null. Based solely on this definition, we catch all the small perturbations of the potential created by low amplitude short-lived local overdensities. Most likely, the stellar orbits are not influenced by these minor Lagrangian points. Therefore, we want to find the Lagrangian points created by more significant structures (e.g. the bar), that live long enough to affect the stellar orbits.

We analysed the trajectory of stars experiencing *bar-induced churning*, trapped in the corotation region between 2 and 9 Gyr. The results are displayed every 1 Gyr in Fig. 20 for 564 star particles, where we see the radial movements of the trapped stars following the corotation radius (white curve) of the bar (upper panel). In addition, we clearly see that these stars tend to stay roughly on the axis perpendicular to the long axis of the bar (lower panel) after ~4.5 Gyr. Apparently, the stars remaining trapped around the corotation of the bar behave as if they were trapped around the Lagrangian points L4 and L5 found in the simple model, suggest-

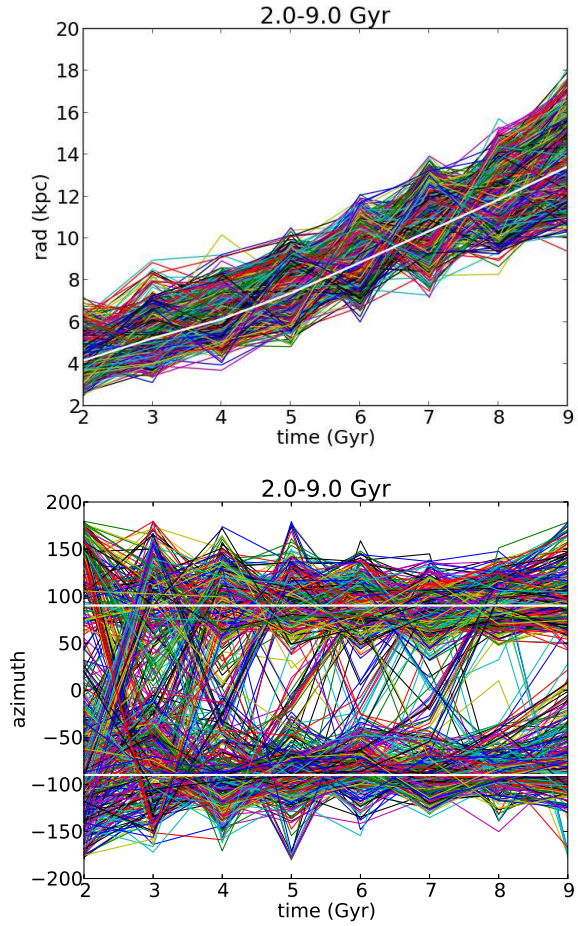

Figure 20. We identified 564 star particles trapped in the corotation region between 2 and 9 Gyr (experiencing *bar-induced churning*), and we display here the evolution of their position in the frame corotating with the bar every Gyr. *Upper panel*: galacto-centric radius of these stars, the thick white curve indicates the corotation radius of the bar. *Lower panel*: azimuth of these stars in the frame corotating with the bar (the long axis of the bar is a 0° here), the thick white lines indicates the -90° and 90° angles (axis perpendicular to the bar)

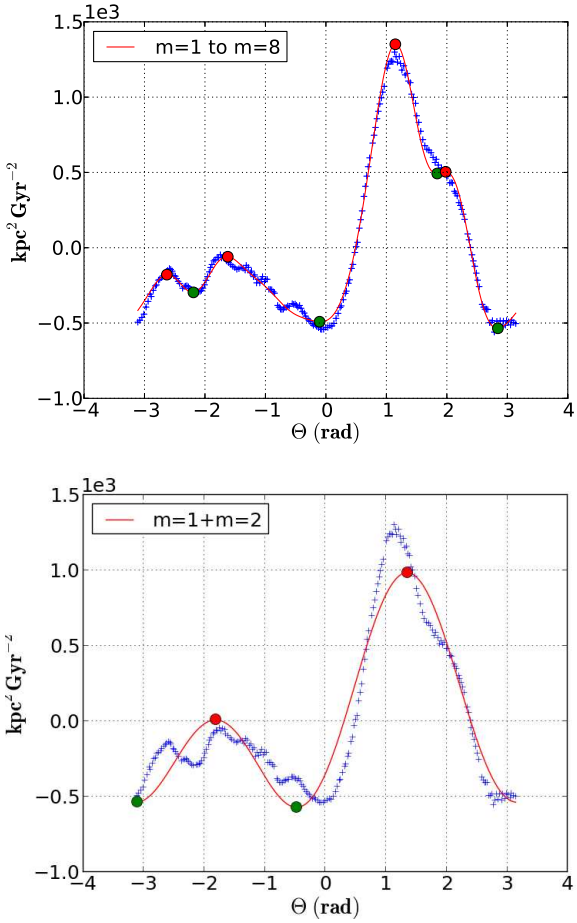

Figure 21. Effective potential minus mean value, in the corotation region at 3 Gyr. Θ =0 marks the bar major axis. The blue crosses indicate the value of the effective potential minus the mean value at each time, the red line is the superposition of the modes m=1 to m=8 (upper panel), m=1 and m=2 (lower panel) of the Fourier spectrum. The red and green filed circles mark the maximum-type and minimum-type n-Lagrangian points respectively, with n=8 in the upper panel and n=2 in the lower panel.

ing that the 2-Lagrangian points may explain their movement. Before ∼4.5 Gyr, this trend do not appear clearly yet because of the lower bar's strength allowing stars to escape a Lagrangian points and being captured by the other: there are lot of exchanges between the Lagrangian points. After ∼4.5 Gyr, the stars seem more tightly trapped around the Lagrangian points.

Indeed, since these stars interact with the bar, which is a strong m=2 Fourier mode of the stellar density in the disk, it appears natural to consider that the 2-Lagrangian points may play a role in this movement. As a result, we smooth the effective potential at corotation by keeping only the m=1 and m=2 modes of the Fourier decomposition of the effective potential at corotation, expressed as function of azimuthal angle (the mode m=0 is always null in our analysis, because we remove the mean value).

The results of this analysis at times 3 and 5 Gyr are provided in Figs. 21 and 22, where the azimuth zero corresponds to the major-axis of the bar. The amplitude of the modes m=1, 2 and 3 in the effective potential at corotation for the times between 2 and 9 Gyr are displayed in Fig. 23. In the latter figure the modes m=1 and m=2 have larger amplitudes than the mode m=3 (and than higher modes that are not shown here) at almost all times, meaning that the effect of the most prominent structures in the disk can be catch by considering only the two first modes. As a consequence of our choice to keep only the m=1 and m=2 modes, we always find two maximum-type and two minimum-type 2-Lagrangian points in the smoothed effective potential of the corotation region.

7.3 The 2-Lagrangian points

In Fig. 24 we display the azimuthal position of the obtained 2-Lagrangian points, and their position on the disk, in the reference frame rotating with the bar. We find that the points remain at constant azimuthal position while moving outward with the corotation radius. These results are also used in the panel 4 in Figs. 8, 9 and 10.

We compare the evolution of the azimuth of stars trapped in the corotation with the maximum-type 2-Lagrangian points in Fig. 25. The position of the 2-Lagrangian points coincide quite well with the azimuth of the stars. Before ∼4.5 Gyr the 2-Lagrangian points are not well defined because the strength of the bar is not

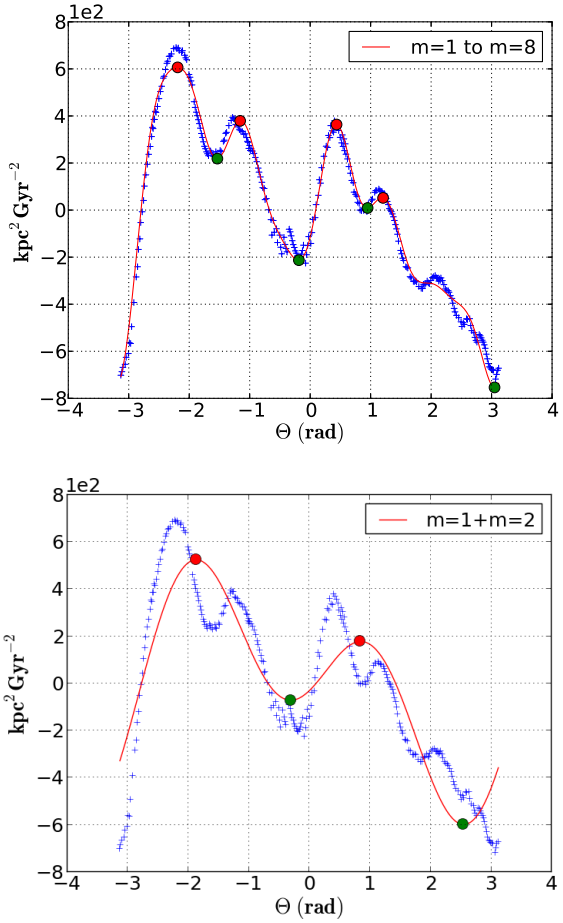

Figure 22. Effective potential minus mean value, in the corotation region at 5 Gyr. Θ =0 marks the bar major axis. The blue crosses indicate the value of the effective potential minus the mean value at each time, the red line is the superposition of the modes m=1 to m=8 (upper panel), m=1 and m=2 (lower panel) of the Fourier spectrum. The red and green filed circles mark the maximum-type and minimum-type n-Lagrangian points respectively, with n=8 in the upper panel and n=2 in the lower panel.

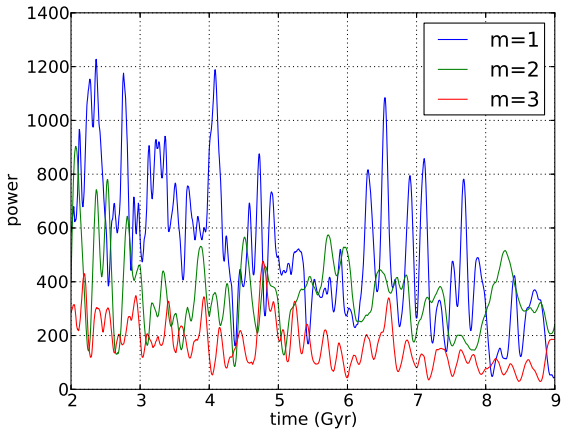

Figure 23. Power of the Fourier modes m=1, 2 and 3 (see legend) found in the effective potential at corotation radius. The Fourier analysis is made along the azimuthal coordinate at each time between 2 and 9 Gyr. The curves displayed in this figure are smoothed using a Savitzky-Golay algorithm.

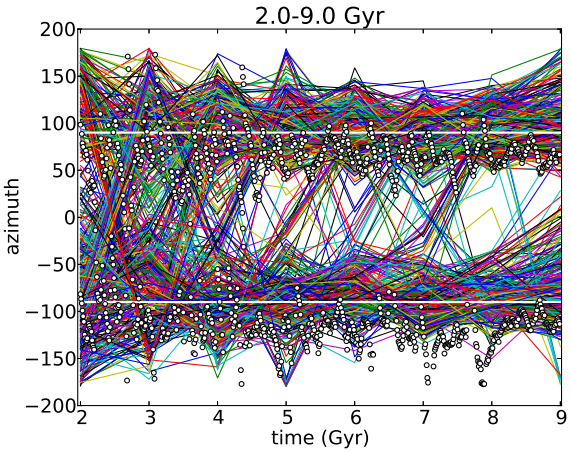

Figure 25. Same as Fig. 20, but we added the position of the maximum-type 2-Lagrangian points (white circles) found in the effective potential.

large enough compared to that of the spirals, resulting in larger dispersion in the position of the 2-Lagrangian points. This explains the behaviour of the trapped stars before ~4.5 Gyr. Notice, that the the azimuth of the 2-Lagrangian points appear with a tilt angle compared to the axis perpendicular to the bar. However, our analysis show that the 2-Lagrangian points may well help to understand the behaviour of stars experiencing *bar-induced churning*.

We checked that when adding modes higher than m=2 we find more equilibrium points, that spread around the preferred azimuthal positions that were found with modes up to m=2, resulting in a progressive blurring of Fig. 24.

Using our knowledge about Lagrangian points, we have a better understanding of why the stars that corotate with the bar can be trapped for many different times in the context of evolving potentials:

- we know that the saddle points of the steady effective potential (L_1, L_2 Lagrangian points) are always unstable (Sec. 6.1). Their homologue 2-Lagrangian points are also saddle points (green filled circles in Fig. 21) and they are moving outward, as the corotation radius. Therefore, they are also unstable: the stars that corotate with the bar and that are located on such a point will not remain trapped in the corotation. This behaviour is illustrated in Fig. 8, where we see in panel 4 that when this star is in corotation (between 3.5 and 4.5 Gyr approximately), it is located around an unstable 2-Lagrangian point (Green crosses).
- in steady potentials, we expect the maximum Lagrangian points (L_4, L_5) to be stable (Sec. 6.1). But the notion of stability of the equilibrium points is valid only in steady potentials, so, when dealing with evolving potentials, it has to be taken with caution. Nevertheless, we will consider here that the maximum 2-Lagrangian points (red filled circles in Fig. 21) are "stable". More precisely, we mean that, under the assumption that these points move slowly enough (adiabatic evolution), the stars trapped on horseshoe orbits around them can stay around these "stable" 2-Lagrangian points while they move, under some conditions that will be described in the next subsection. This behaviour is illustrated in Figs. 9 and 10. In Fig. 9, we see a star that is corotating with the bar and that is trapped around a stable 2-Lagrangian point,

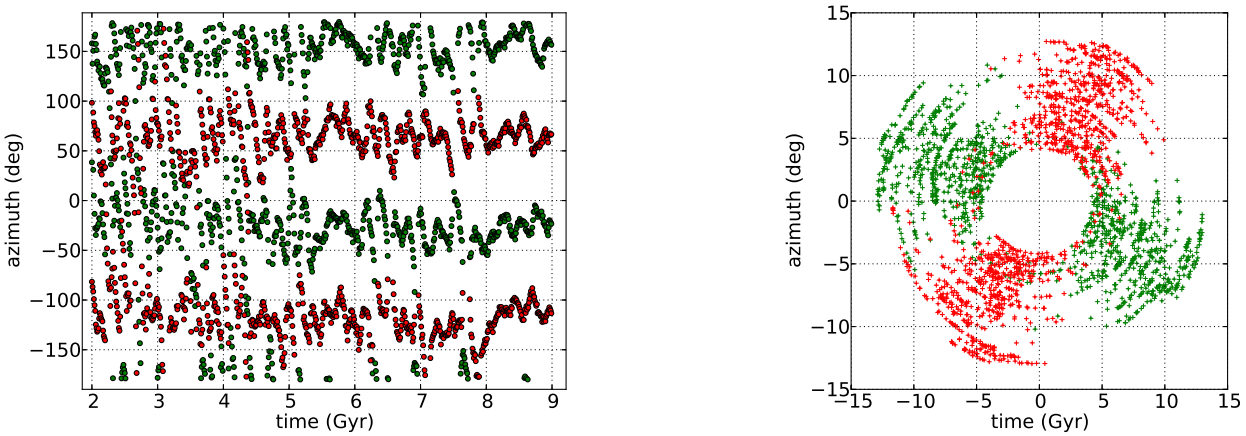

Figure 24. *Left panel*: azimuthal position of the 2-Lagrangian points as a function of time, in the frame rotating with the bar (the major axis of the bar is on the axis (theta=0°, theta=180°). Red and green filled circles mark the maximum-type and minimum-type Lagrangian points respectively. *Right panel*: position of the Lagrangian points in a face-on view of the disk, at same times as in the left panel. The bar is aligned with the x axis.

albeit for a short time. And in Fig. 10, we see a star remaining trapped around the 2-Lagrangian point for a long time. This difference of behaviour for stars trapped round stable 2-Lagrangian points is the object of the following subsection.

To check that the 2-Lagrangian points found in the low Fourier modes allow a better description of the churning of stars at corotation, we plot the lower panels of Fig. 19. On these panels, we added the snapshots on time intervals 2.45-2.55 Gyr, centred on 2.5 Gyr (left panel) and 4.4-4.6 Gyr, centred on 4.5 Gyr (right panel). The snapshots are aligned with the bar axis, and the velocity are expressed in the frame rotating with the bar at each time of the time intervals. Then we build spatial bins and in each bin, we compute the average velocity vector of the stars, thus allowing to trace stellar-streams maps, as in the middle row of the same figure. Then we mark the locus of the minimum-type and maximum-type 2-Lagrangian points that we found in the smoothed effective potential.

Now we have better agreement between the stellar stream maps and the effective potential: the maximum-type 2-Lagrangian points are close to the center of the vortices of stars on horseshoe orbits, and the minimum-type 2-Lagrangian points are close the frontier between two adjacent vortices.

7.4 The Jacobi energy

We have shown that the time a star remains trapped in the corotation resonance depends first on its location: namely whether it is orbiting around a stable or unstable 2-Lagrangian point, but it appeared that this criterion is not enough to understand why some stars trapped around "stable" 2-Lagrangian points do not remain trapped.

To investigate further the behaviour of the particles in the simulation, we look at the Jacobi energy of a star, which is computed as:

$$E_J = \frac{1}{2}|\dot{r}|^2 + \Phi_{eff} \qquad (8)$$

where $\dot{r}$ is the velocity of the star in the reference frame corotating with the bar, and Φ_{eff} is the effective potential given by Eq. 6.

In Figs. 8, 9 and 10, the panel 5 displays the Jacobi energy E_J

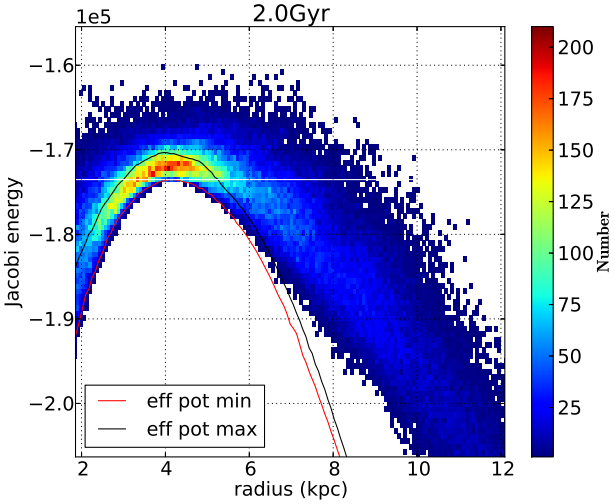

Figure 26. Distribution of the stars in the radius vs. Jacobi energy plane, at time 2 Gyr. The color scale represents the number of stars in each bin. The red line is the minimum value of effective potential at each radius, and the black line is its maximum value at each radius. The white line separates the stars that can cross the corotation radius (above the line), and the ones which can not (below the line). In this figure, the horseshoe orbit region is above the white line and below the black curve.

of the star (red curve) and the maximum and minimum values of the effective potential on the corotation radius (green dashed curves), that we denote as $\Phi_{eff}(R_{corot}, \Theta_{max})$ and $\Phi_{eff}(R_{corot}, \Theta_{min})$ respectively. In these plots, we subtracted $\Phi_{eff}(R_{corot}, \Theta_{min})$ from the three energy above, because the minimum value of E_J to cross the corotation is $\Phi_{eff}(R_{corot}, \Theta_{min})$. This is illustrated in Fig. 26, where we have the repartition of the stars, at 2 Gyr, in the plane Jacobi energy *vs.* radial position. Stars rotating around a maximum of the effective potential have to cross the corotation radius, this means that their Jacobi energy must be above the minimal value of the potential at corotation radius (this value corresponds the lowest saddle-type Lagrangian point): these stars have to be above the

white line in Fig. 26. So the first criterion to experience migration due to the corotation is

$$E_J(R) \geq \Phi_{eff}(R_{corot}, \Theta_{min}) \quad (9)$$

We can see in Figs. 8 to 10 that, while the stars are corotating with the bar, they satisfy Eq. 9.

To understand how a star's Jacobi energy evolves when it migrates outward, we can rewrite Eq. 8 using the actions J_R and J_z:

$$E_J(R) = \kappa(R)J_R + \nu(R)J_z + \Phi_{eff}(R) \quad (10)$$

because in the epicycles approximation (Binney & Tremaine 1987), we have $E_J = E_R + E_z + \Phi_{eff}$ for planar movements, and $E_R = 1/2\kappa^2 X^2$, $E_z = 1/2\nu^2 Y^2$ for the kinetic energies; and $J_R = 1/2\kappa X^2$, $J_z = 1/2\nu Y^2$ for the actions, where X and Y are the amplitudes of the radial and azimuthal epicycles respectively; κ and ν are the radial and vertical epicyclic frequencies respectively.

From the panel 6 in Fig. 10, we see that the actions of stars have only small variations while they remain in the disk, that are not enough to explain the decreasing value of E_J, so we will consider the actions to be conserved quantities. The remaining variables are the epicyclic frequencies κ and ν, that are functions of the effective potential (Binney & Tremaine 1987), that decreases when radius increases. This is observed in panels 1 and 4 in Fig. 10. Therefore when a star moves outward its kinetic energy decreases because of the decreasing frequencies κ and ν in Eq. 10.

As a result, we expect that the conditions for a star to be trapped for a long time in corotation with the bar, is to rotate around a maximum type 2-Lagrangian point, and to have a high initial (i.e. at the moment the star enters corotation region) Jacobi energy, to compensate the decreasing kinetic energy while moving outward, and still verify Eq. 9. Given the expression 10, this condition is equivalent to require high values of the actions. The panel 6 of the Figs. 10, 9 and 8 gives an illustration, where the radial action in 10 is approximately constant at 0.015 kpc^2Gyr^{-1}, while it has the value 0.003 kpc^2Gyr^{-1} in Figs. 9 and 8, i.e. the long trapped star have a radial action roughly 5 times larger than the two other cases which are trapped for short times.

To test the previous hypothesis, we select two different groups of stars: one with low initial Jacobi energies (but with enough energy to cross the corotation radius: Eq. 9), and one with higher initial Jacobi energies. Both groups have their guiding radii (angular momentum over tangential speed) in the corotation region.

Using Fig. 26 we illustrate the above selection criteria. We define as the corotation region, the region comprised in-between the two points of intersection between the white line and the black curve. As the potential evolve with time, the corotation region also changes, as displayed in the lower panel of Fig. 27. The stars having low Jacobi energy are above the white line and below the black curve. And the stars having higher Jacobi energy are above the maximum of the effective potential, that is above the maximum of the black line in Fig. 26.

Once the stars belonging to these groups are identified at a given time, we follow how many of them remain in the corotation region (that is moving with time) every 0.5 Gyr. In Figs. 27 and 28, we display the evolution of the fraction of stars belonging to each group (number of remaining stars from one group over the initial number of stars in the group), for different initial times t_0, from 2 to 8.5 Gyr, every 0.5 Gyr. In the upper panel of these two figures, the fractions are displayed as a function of absolute time, meaning that the first point of each curve is the fraction at t_0+0.5 Gyr. In

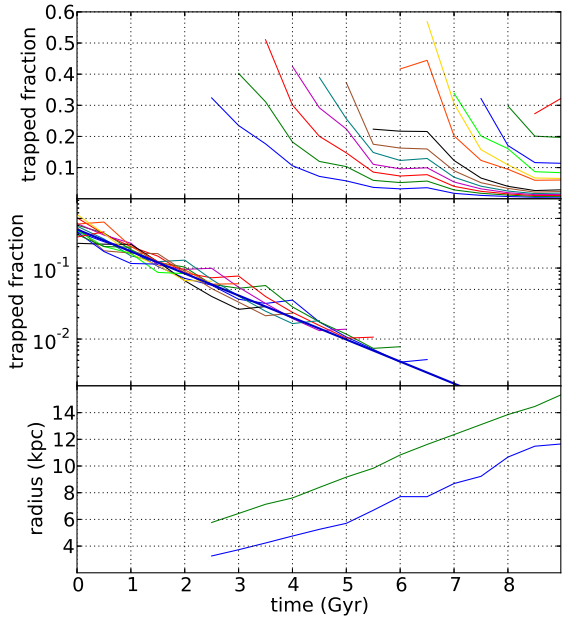

Figure 27. Evolution of the fraction of stars in the horseshoe orbit region (which is defined in the Ej-R plane), for successive initial times t_0 between 2 and 9 Gyr, every 0.5 Gyr. At each t_0, the number of stars in the horseshoe orbit region is obtained, then we follow how many of these initial stars remain in the horseshoe orbit region and we compute the fraction of remaining stars over initial number of stars. *upper panel*: evolution of the fraction of stars as a function of time. The different colors indicate different t_0. *Middle panel*: evolution of the fraction of stars as a function of the relative times $t' = t - t_0$. The thick blue line is a fit having equation $f(t') = 0.35\exp(-t'/1.4)$. *Lower panel*: evolution of the corotation region, as defined in the text.

the middle panel, the fractions are displayed in a relative time defined as $t' = t - t_0$, so that the time evolution of the fractions can be compared. We observe that the initial time do not have a strong influence on the evolution of the fraction of remaining stars, only the time elapsed since the initial time appears relevant to describe the fraction of remaining stars in the corotation region. And the lower panel display the evolution of the corotation region, as defined in the previous paragraph.

In Fig. 27, we show the results for the low energy stars. In the middle panel, the red thicker line have equation $f(t') = 0.35\exp(-t'/1.4)$ to fit the data. In Fig. 28, we have the results for the higher energy stars. In the middle panel of this figure, the ticker red line is the same as in Fig. 27, and the black thicker line have equation $g(t') = 0.5\exp(-t'/1.7)$. Therefore we have a characteristic time $t_{1/2}$ that is the time necessary to reduce by 50% the number of stars, from each group, in the coration region. For the low energy stars we have $t^L_{1/2} = 1.4\ln(2) \approx 0.97\ Gyr$ while for the higher energy stars we find $t^H_{1/2} = 1.7\ln(2) \approx 1.18\ Gyr$. So we have a verification of our initial hypothesis: the stars in the corotation region with higher initial Jacobi energy are likely to follow the corotation region for a longer time, than the stars with low initial Jacobi energy.

In addition, this analysis gives a hint about a question raised by Minchev et al. (2012b) in the discussions of their paper. In the theory developed by Sellwood & Binney (2002) the most significant migration is observed when the non-axisymmetric structure is transient and have a life-time roughly equal to half the period of

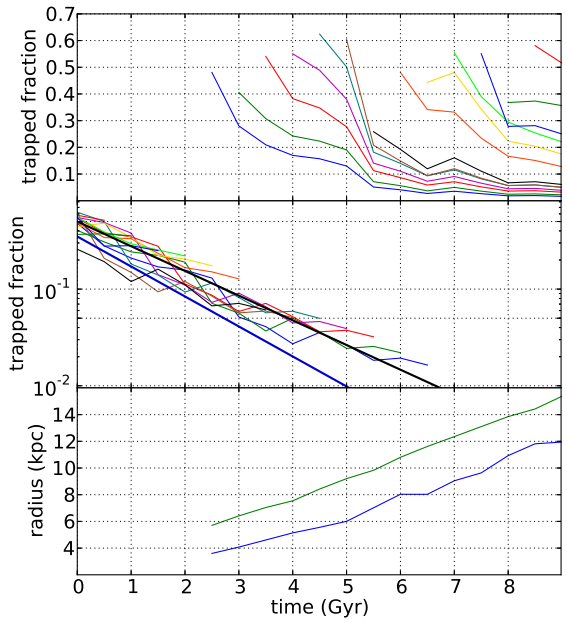

Figure 28. Same process as in Fig. 27, except that the stars are selected with higher energies. In the middle panel, the thick blue curve is the same as in Fig. 27. The thick black line is a fit having equation $g(t') = 0.5\exp(-t'/1.7)$.

horseshoe orbits. However, the bar appears to be the most effective driver of radial migration in our simulation, although it is not a transient feature. In our analysis, the stars having higher Jacobi energy are more likely to follow the corotation with the bar when it moves outward. In the same time, it has been shown that the stars with small eccentricity (low Jacobi energy) are more likely to be trapped on horseshoe orbits around Lagrangian points. Therefore, the stars trapped on horseshoe orbits have lower probability to follow the corotation. As a result, because of the outward movement of the corotation radius, the bar is seen as a transient feature for the low energy stars, and is felt during a time T_{on}.

The Oort constants A and -B are equal in the epicyclic approximation, if the galaxy have a flat rotation curve (Binney & Tremaine 1987). Therefore, using Eq. 11 from Sellwood & Binney (2002), we can estimate the minimal period of the horseshoe orbits:

$$T_{min} = \pi R_0 \sqrt{\frac{-B}{A|\Psi_0|}} \qquad (11)$$

where Ψ_0 is the amplitude of the azimuthal variations of the effective potential at the corotation radius. At 4.5 Gyr, $\Psi_0 \simeq 0.5\times10^3$ kpc^2Gyr^{-2} (Fig. 21) and the corotation radius $R_{co} \simeq 7$ kpc. Therefore, we have $T_{min} \simeq 0.9$ Gyr. From Fig. 7, we deduce that the speed of the corotation radius is approximately $V_{cr} \simeq 1.5$ $kpc.Gyr^{-1}$. Then, assuming that the efficiency of the bar is maximal i.e. $T_{on} = 0.5T_{min}$, we can estimate the displacement of the corotation radius $d = T_{on}V_{cr} \simeq 0.7$ kpc. Therefore, to keep the low energy stars on horseshoe orbits, the corotation radius have to move less than 0.7 kpc approximately. And the value of Ψ_0 at 4.5 Gyr, is fairly representative of the amplitude of the varitations found in the effective potential over the whole simulation (it varies from $\sim 1\times10^3$ to $\sim 0.2\times10^3$ kpc^2Gyr^{-2} between 2 and 9 Gyr).

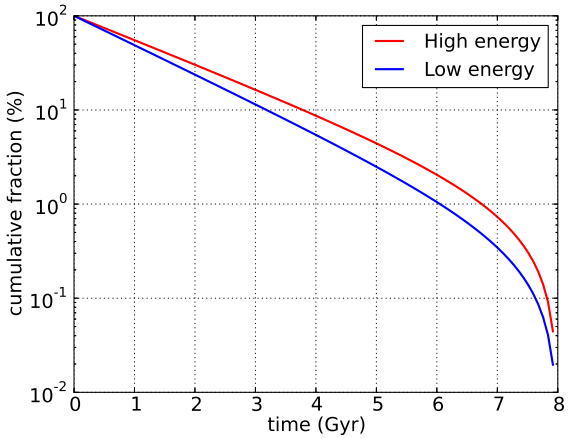

Figure 29. Cumulative fraction of stars that remain in the corotation region for the low energy groups (blue curve) and the higher energy group (red curve),as defined in Sec 7.4. This curves are obtained using the fitting functions obtained using Figs. 27 and 28.

7.5 Statistics on corotating stars (at t⩾2Gyr)

Using our analysis of the stars remaining in the corotation region (Sec. 7.4), we can describe statistically the behaviour of stars in the corotation region. Doing so, we can compare the impact of stellar migration due to the mixing of stars around the corotation radius of the bar, to the impact of the bar-induced churning (defined in Sec. 3.1).

Given the speed of the outward displacement of the corotation region (lower panel of Fig. 27), 3 Gyr is approximately the minimum duration ensuring that there is no overlap between the initial and final position of the corotation region. Therefore the stars trapped at least for 3 Gyr, in this simulation, have moved radially and followed the corotation region. These are stars experiencing bar-induced churning.

In Fig. 29, we display the cumulative fraction of star trapped in the corotation region for smaller and smaller times. These results are obtained using the fitting functions $f^L(t') = 0.3\exp(-t'/1.4)$ for the low energy stars, and $f^H(t') = 0.3\exp(-t'/1.8)$ for the higher energy stars. For the low energy stars (red curve), we get that 11% of these stars initially in the corotation region, are trapped for more than 3 Gyr, while 17% of the higher energy stars remain trapped for more 3 Gyr. The higher energy stars spend more times in the corotation, however, the fraction of these stars among the total number of stars in the corotation region is low compared to the fraction of low energy stars. As a result, the absolute number of stars remaining in the corotation region, while it moves outward, is dominated by low energy stars.

Our analysis shows that the fraction of stars experiencing bar-induced churning is low, as a result the impact of this migration mechanism is more appreciable on the outer edge of the disk where only a few stars are formed locally. So this mechanism could have strong impact on the study linked to the external parts of the disks, such as the breaks found in the luminosity and color profiles (Fig. 3).

We also get from Fig. 29, that most of the stars in the corotation region are trapped for short times: about 50% (for any energy) of them are trapped for less than 1 Gyr. This is lower than the period of horseshoe orbits, so the main effect of the corotation resonance is to mix stars around the corotation radius. Then, because of the

exponentially decreasing stellar surface density of the disk, the average effect of this mixing is to drive stars outward. Indeed, stars on the inner side of the corotation will reach the outer side, and vice-versa the stars initially on the outer side. But since the stars initially on the inner side, outnumber the ones initially on the outer side, in average we get that the corotation induce an outward movement of the stars, as shown in a previous paper using the same N-body +SPH simulation (Kubryk, Prantzos & Athanassoula 2013).

8 SUMMARY

In this work, we studied radial migration defined as a guiding radius variation of the stellar orbit. We have checked that the vertical angular momentum, combined with the tangential speed of stars, allows to estimate the guiding radius of stars. It allows to study specifically the churning, because the angular momentum is not affected by the epicyclic oscillations.

We studied specific aspects of stellar radial migration in a bar-dominated disk galaxy, by analyzing a N-body+SPH simulation (with *gadget-3*). In this simulated galaxy, the bar is formed around 2 Gyr and then evolves secularly until the end of the simulation (9 Gyr). During the secular evolution period, the bar grows, its rotation speed decreases and its strength increases until 9 Gyr. As a result the corotation radius, and the other resonances with the bar move outward with time. We also find transient spiral arms in the simulation, whose strength increases until 1 Gyr approximately, and then, decreases slowly until the end of the simulation. We have shown that the transient arms (m=3 and m=5 Fourier modes) rule the radial migration before approximately 3 Gyr, passed that time, the bar has gained enough strength relatively to the arms, so it becomes the main driver of radial migration in the disk.

We have found that since the bar formation, the corotation region with the bar is the dominant place where stars start to be churned. We selected the migrating stars, with a threshold in angular momentum variations on 1 Gyr time intervals, in order to to get a quantitative description of the phenomenon. This analysis holds for strong migrators, since we set our threshold on a relatively high value (we select stars experiencing $\Delta R \gtrsim 1.8 kpc$), therefore, it gives a lower limit for the fraction of migrating stars. This work on strong migrators shows that the corotation region of the bar is where the fraction of migrating stars is the highest, with values around 35% in this simulation at all time since the bar is formed (at 2 Gyr). We also found that, amongst the migrating stars, around 70% of them are in corotation with the bar, in the corotation region. This value drop to 0% at radii far from corotation, so the migration occurring at other radii, is not due to velocity dispersion, allowing stars far from corotation radius, to have the same angular speed as the bar. This analysis also exhibit that radial migration occurs before the bar formation, at times lower than 2 Gyr, over the whole disk. This is due to transient spiral arms, that have a decreasing angular speed over their length, and that corotate with the stars at all radii (**?**). We also shown that migration at these early times contribute to the radial extension of the disk: some of the stars that where starting to migrate below 10 kpc at 1 Gyr, are found around 14 kpc at 2 Gyr.

We have analyse the churning of stars by comparing the initial and final angular momentum of the stars on various time intervals. On successive 1 Gyr intervals, we have described the effects of the ILR in the bar region, the effects of the bar's corotation and the OLR. And observed that the effects of the bar are roughly symmetric around the CR. On larger time intervals, always starting at 1 Gyr, we analysed the cumulative effects over time of the migration mechanisms, thus allowing to describe the impact of the bar-induced churning on the average initial angular momentum of stars.

We have shown that the instantaneous effective potential do not describe accurately the movement of stars corotating with the bar, because it is shaped by transient arms or small overdensities, that have short life-time compared to the characteristic period (~ 1 Gyr) of stars on horseshoe orbits around Lagrangian points. The problem is that Lagrangian points are used to study steady potentials, in this context the Lagrangian points do not change with time. While in our case, the Lagrangian points change quickly, because of the influence of local short-lived overdensities on the potential near the corotation with the bar. As a result, we defined the *n-Lagrangian points*, that are found in the smoothed effective potential, and represent the combined effects of large structures (that live long enough) and of multiple short-lived Lagrangian points.

We described how we can find n-Lagrangian points, that also correspond to a time and spatial average of the effective potential, using a Fourier low-pass filter to smooth the effective potential. We tested that the 2-Lagrangian points manage to describe how the stars move in the disk around the corotation region. This can be seen on maps of the average velocity (in each pixels) of the stars (in space and time), in the frame rotating with the bar. These maps display some vortices created by stars on horseshoe orbits, centred on maximum-type 2-Lagrangian points, and extending azimuthally from a minimum-type 2-Lagrangian points to the next one.

We studied how stars can be trapped in horseshoe orbits around the maximum-type 2-Lagrangian points for long periods so they can be driven outward with the the corotation resonance. We call this migration mechanism the *bar-induced churning*. We shown that the type (local maximum or saddle point) of 2-Lagrangian points, is a first criterion to determine whether a star can be trapped for a long time. And we found a second criterion, which is the initial value of the Jacobi energy when the star starts corotating. We have shown that the stars having higher initial Jacobi energy are more likely to be trapped for a long time in the corotation region while the corotation radius moves outward. We also studied the amount of stars affected by this migration mechanism, and found that only a small fraction are trapped for a long time. As a result, this phenomenon mostly have appreciable effects on the outer parts of the disk where few stars are formed locally, on the condition that the corotation radius reaches these regions.

We have also shown that because of its secular evolution (that is responsible for the outward movement of the bar corotation region), the bar acts on the coldest (low Jacobi energy) corotating stars as a transient structure having a life-time approximately equal to half a horseshoe orbit period. Explaining why it is so effective to induce radial migration, therefore, secularly evolving bars are also in the scope of the theory developed by Sellwood & Binney (2002) about transient arms.

The result of our analysis is that, in this simulation, the main radial migration inducer is the corotation resonance with the bar, that makes the coldest corotating stars swap their places around the corotation radius, as if the bar was a transient structure. Because of the exponential stellar surface density profile of the disk, this exchange of stars results in an average outward movement of the stars of a few kpc, as already exposed in a companion paper (Kubryk, Prantzos & Athanassoula 2013). And the other migration mechanisms (bar-induced churning, corotations with spirals, resonances of higher multiplicity with the bar) are less effective, except at early times where the corotations with spiral arms are the main migration inducers.

ACKNOWLEDGEMENTS

It is a pleasure to thank Albert Bosma for many discussions and encouragement, Volker Springel for making available to us the version of GADGET used here and Jean-Charles Lambert for his computing assistance. EA acknowledges financial support to the DAGAL network from the People Programme (Marie Curie Actions) of the European Union's Seventh Framework Programme FP7/2007-2013/ under REA grant agreement number PITN-GA-2011-289313. EA also acknowledges financial support from the CNES (Centre National d'Etudes Spatiales - France).

REFERENCES

Athanassoula E., 1992, MNRAS, 259, 345
Athanassoula E., 2002, ApJLett, 569, L83
Athanassoula E., 2003, MNRAS, 341, 1179
Athanassoula E., 2005, MNRAS, 358, 1477
Athanassoula E., 2013, Bars and secular evolution in disk galaxies: Theoretical input, Falcón-Barroso J., Knapen J. H., eds., p. 305
Athanassoula E., Machado R. E. G., Rodionov S. A., 2013, MNRAS, 429, 1949
Athanassoula E., Misiriotis A., 2002, MNRAS, 330, 35
Baba J., Saitoh T. R., Wada K., 2013, ApJ, 763, 46
Bakos J., Trujillo I., Azzollini R., Beckman J. E., Pohlen M., 2011, Memorie della Societa Astronomica Italiana Supplementi, 18, 113
Binney J., Tremaine S., 1987, Galactic dynamics
Brunetti M., Chiappini C., Pfenniger D., 2011, A&A, 534, A75
Casagrande L., Schoenrich R., Asplund M., Cassisi S., Ramirez I., Melendez J., Bensby T., Feltzing S., 2011, Arxiv preprint arXiv:1103.4651
Comparetta J., Quillen A., 2012, Arxiv preprint arXiv:1207.5753
Dehnen W., 2000, AJ, 119, 800
Grand R. J. J., Kawata D., Cropper M., 2012a, MNRAS, 426, 167
Grand R. J. J., Kawata D., Cropper M., 2012b, MNRAS, 421, 1529
Grand R. J. J., Kawata D., Cropper M., 2013, ArXiv e-prints
Grand R. J. J., Kawata D., Cropper M., 2014, MNRAS, 439, 623
Hernquist L., 1993, ApJS, 86, 389
Jorsater S., van Moorsel G. A., 1995, AJ, 110, 2037
Kormendy J., Kennicutt, Jr. R. C., 2004, ARA&A, 42, 603
Kubryk M., Prantzos N., Athanassoula E., 2013, MNRAS, 436, 1479
Le Borgne D., Rocca-Volmerange B., Prugniel P., Lançon A., Fioc M., Soubiran C., 2004, A&A, 425, 881
Lindblad P. A. B., Kristen H., Joersaeter S., Hoegbom J., 1997, A&A, 317, 36
Lynden-Bell D., Kalnajs A. J., 1972, MNRAS, 157, 1
Masset F., Tagger M., 1997, A&A, 322, 442
Minchev I., Famaey B., 2010, ApJ, 722, 112
Minchev I., Famaey B., Combes F., Di Matteo P., Mouhcine M., Wozniak H., 2011, A&A, 527, A147
Minchev I., Famaey B., Quillen A. C., Dehnen W., Martig M., Siebert A., 2012a, A&A, 548, A127
Minchev I., Famaey B., Quillen A. C., Di Matteo P., Combes F., Vlajić M., Erwin P., Bland-Hawthorn J., 2012b, A&A, 548, A126
Nowak N., Thomas J., Erwin P., Saglia R. P., Bender R., Davies R. I., 2010, MNRAS, 403, 646
Pfenniger D., 1990, A&A, 230, 55
Quillen A., Minchev I., Bland-Hawthorn J., Haywood M., 2009, MNRAS, 397, 1599
Rodionov S. A., Athanassoula E., 2011, A&A, 529, A98
Roediger J. C., Courteau S., Sánchez-Blázquez P., McDonald M., 2012, ApJ, 758, 41
Romero-Gómez M., Masdemont J. J., Athanassoula E., García-Gómez C., 2006, A&A, 453, 39
Roškar R., Debattista V. P., Quinn T. R., Stinson G. S., Wadsley J., 2008a, ApJLett, 684, L79
Roškar R., Debattista V. P., Quinn T. R., Wadsley J., 2012, MNRAS, 426, 2089
Roškar R., Debattista V. P., Stinson G. S., Quinn T. R., Kaufmann T., Wadsley J., 2008b, ApJLett, 675, L65
Sánchez-Blázquez P., Courty S., Gibson B. K., Brook C. B., 2009, MNRAS, 398, 591
Schönrich R., Binney J., 2009, MNRAS, 396, 203
Sellwood J., 2010, MNRAS, 409, 145
Sellwood J., Binney J., 2002, MNRAS, 336, 785
Sellwood J. A., Athanassoula E., 1986, MNRAS, 221, 195
Springel V., 2005, MNRAS, 364, 1105
Springel V., Hernquist L., 2002, MNRAS, 333, 649
Springel V., Hernquist L., 2003, MNRAS, 339, 289
Springel V., Yoshida N., White S. D. M., 2001, NewA, 6, 79

3 Impact de la migration radiale sur l'évolution chimique des galaxies

Ces vingt dernières années, des études observationnelles et théoriques ont suggéré que la migration radiale des étoiles pourrait influencer les propriétés des disques galactiques. Déjà dans les années 90, il avait été réalisé que la dispersion observée dans la relation âge-métallicité des étoiles du voisinage solaire (panneau du haut de la Fig. 3.1 extrait de (Edvardsson et al., 1993)) était manifestement trop grande pour être expliquée uniquement par la diffusion hors du rayon de naissance due aux mouvements épicycliques. Par ailleurs, l'analyse des données du Geneva-Copenhagen Survey (Casagrande et al., 2011) montre que la distribution en métallicité des étoiles du voisinage solaire contient à la fois des étoiles jeunes et vieilles à des métallicités aussi faibles qu'élevées (Fig. 3.1 panneau du bas). Ces observations sont impossibles à reproduire avec les modèles d'évolution classiques (en anneaux indépendants, donc sans migration radiale), qui produisent une relation unique, sans dispersion, entre âge et métallicité au voisinage solaire.

De plus, Wielen, Fuchs & Dettbarn (1996) ont montré que le Soleil devrait être né ~2 kpc plus à l'intérieur de sa position actuelle pour expliquer sa métallicité élevée, comparée à celle du milieu interstellaire local, et à celle des étoiles voisines. Cette valeur est proche de l'excursion radiale maximale autorisée par les épicycles $\Delta R \sim \sqrt{2}\sigma_R/\kappa$ ~2 kpc (en considérant les valeurs locales observées de la dispersion radiale des vitesses σ_R ~50 km/s (Holmberg, Nordström & Andersen, 2009) et la fréquence épicyclique $\kappa \sim 37$ kms^{-1}kpc^{-1} (Binney & Tremaine, 1987)). Depuis, la métallicité solaire a été revue à la baisse (Asplund et al., 2009), si bien qu'elle est maintenant compatible avec celle des jeunes étoiles du voisinage solaire, ainsi qu'avec le milieu interstellaire local. Toutefois, des incertitudes persistent au sujet de la nécessité d'un mélange radial important afin d'expliquer les observations (see e.g. Haywood, 2012; Nieva & Przybilla, 2012).

Selon les modèles "classiques" de l'évolution du voisinage solaire, la métallicité du voisinage solaire ne doit pas avoir augmenté significativement depuis la formation du Soleil (il y 4-5 Gyr). Ceci est expliqué par les effets combinés de la faible efficacité de la formation stellaire, et de l'infall continu de gaz intergalactique pendant cette période. Ainsi, sans migration radiale stellaire, il devrait être impossible de trouver des étoiles beaucoup plus métalliques que le

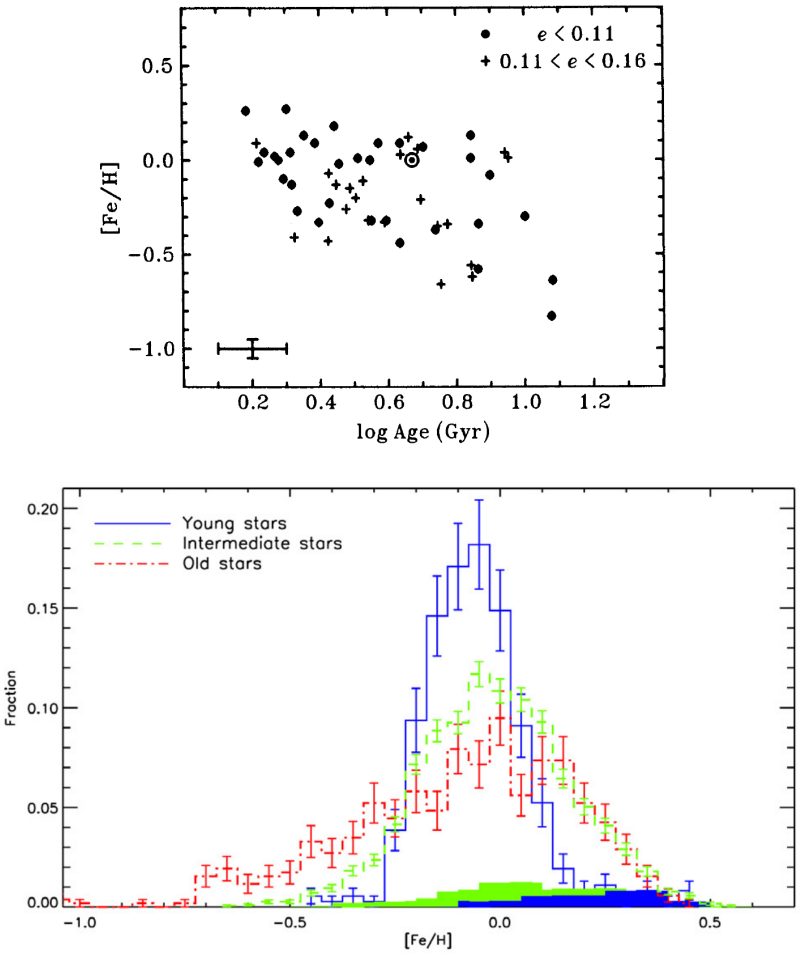

FIGURE 3.1 – **Panneau haut** : âge et métallicité des étoiles observées au voisinage solaire (Extrait de Edvardsson et al. (1993)). **Panneau bas** : distribution en métallicité des étoiles observées au voisinage solaire, selon différentes tranches d'âges (Extrait de Casagrande et al. (2011)

Soleil, mais les observations montrent que les étoiles du voisinage solaire peuvent atteindre des métallicités de ~0.4 dex. Or, la migration radiale pourrait permettre aux étoiles des régions internes (plus métalliques) de se déplacer jusqu'au voisinage solaire, ce qui en ferrait un bon candidat pour expliquer les distributions de métallicité observées (Chiappini, 2009), ainsi que la dispersion dans la relation âge-métallicité des étoiles au voisinage solaire.

Sellwood & Binney (2002) (SB02) ont montré que, en présence d'un bras spiral transitoire, les étoiles d'un disque galactique peuvent se déplacer bien plus loin que la limite maximale autorisée par les épicycles : les étoiles en corotation avec une telle spirale transitoire peuvent être déplacées à des rayons galacto-centriques différents vers l'intérieur ou l'extérieur, leur rayon final étant approximativement le symétrique de leur rayon initial par rapport à rayon de corotation avec la spirale. Ils ont également montré que, lors de ce processus, la distribution en moment angulaire des étoiles n'est pas modifiée, et que les étoiles migrantes ne sont pas chauffées cinématiquement. Puis, en utilisant un modèle semi-analytique simple, ils ont montré comment la migration peut augmenter la dispersion dans la relation âge-métallicité locale, de façon bien plus significatives qu'avec les seuls mouvements épicycliques. Cette étude a ensuite inspiré un grand nombre de travaux théoriques sur la migration radiale tant à l'aide de simulations N-corps (e.g. Roškar et al., 2008a; Sánchez-Blázquez et al., 2009; Martínez-Serrano et al., 2009; Sales et al., 2009; Roskar, 2010; Minchev & Famaey, 2010; Minchev et al., 2011; Brunetti, Chiappini & Pfenniger, 2011; Minchev et al., 2012; Grand, Kawata & Cropper, 2012; Baba, Saitoh & Wada, 2013; Bird et al., 2013; Di Matteo et al., 2013; Kubryk, Prantzos & Athanassoula, 2013; Grand, Kawata & Cropper, 2014), que de simulations semi-analytiques Lépine, Acharova & Mishurov (2003); Prantzos (2009); Schönrich & Binney (2009); Minchev, Chiappini & Martig (2013); Wang & Zhao (2013); Minchev, Chiappini & Martig (2014). À cause de la difficulté qu'il y a à reproduire un disque similaire à celui de la Voie Lactée avec les simulations N-corps+SPH, celles-ci se concentrent sur l'étude de la dynamique de la migration radiale et de son impact général sur l'évolution chimique ; les modèles semi-analytiques, quant à eux, se concentrent sur les propriétés de la Voie Lactée.

Lépine, Acharova & Mishurov (2003) a considéré un modèle-jouet de disque avec une résonance de corotation fixe, déplaçant les étoiles à la corotation vers l'intérieur ou l'extérieur. Ils ont montré que, dans le cas de la Voie Lactée, les profils d'abondance (supposés exponentiels au départ) s'aplatissent entre 8 et 10 kpc (autour de leur rayon de corotation), mais les données actuelles ne permettent pas de conclure à ce sujet (Luck & Lambert, 2011). En analysant des simulations N-corps+SPH Roškar et al. (2008b) a présenté une étude systématique des implications de la migration radiale (façon SB02) sur l'évolution chimique des disques ; ils ont discuté la dispersion dans la relation âge-métallicité locale, l'élargissement de la distribution en métallicité des étoiles locales, l'aplatissement des profils d'abondance, ainsi que l'aplatissement de l'histoire de la formation stellaire. Certains de ces effets avaient déjà été analysés plus en détail à l'aide d'un modèle semi-analytique simple par Prantzos (2009), qui a trouvé que le mécanisme de migration de SB02 produit une dispersion de la relation âge-métallicité qui dépend de l'âge des étoiles (parce que les étoiles jeunes ont moins de temps pour migrer loin de leur rayon de formation, vers des régions de métallicité très différente de leur région

d'origine) et a montré comment les extrémités de la distribution en métallicité des étoiles locales peuvent être affectées par la migration.

Schönrich & Binney (2009) ont couplé un code complet d'évolution chimique à une prescription paramétrée de la migration radiale, dans laquelle les mouvements épicycliques (le blurring) et les varitations de l'orbite guide dues aux bras spiraux (le churning) sont considérés séparément. Ils une très bonne concordance entre leur modèle et les données observationnelles du voisinage solaire. Par ailleurs, ils ont suggéré que la migration radiale pourrait expliquer la formation du disque épais de la Galaxie, en amenant dans le voisinage solaire des étoiles plus "chaudes" cinématiquement. Cette hypothèse a ensuite été examinée à l'aide de simulations N-corps, mais des résultats différents ont été obtenus aucun résultats permettant de trancher définitivement cette question n'a encore été obtenus. Par exemple, Loebman et al. (2011) trouvent que les processus séculaires (i.e. la migration radiale) sont suffisant pour expliquer les propriétés cinématiques du disque épais local ; alors que Minchev et al. (2012) trouvent que la migration radiale affecte très peu l'épaisseur du disque et suggèrent que la formation du disque épais nécessite des fusions galactiques dans la jeunesse de la Voie Lactée. Cette question est donc encore sujet à débat aujourd'hui, entre les partisans d'une formation du disque épais par des processus d'évolution séculaire internes au disque, et les partisans d'une formation par des fusions galactiques à une époque reculée (e.g. Bournaud, Elmegreen & Martig, 2009; Brook et al., 2012; Forbes, Krumholz & Burkert, 2012; Steinmetz, 2012; Bekki & Tsujimoto, 2011), tandis que Bovy et al. (2012), en séparant les populations stellaires en fonction de leurs abondances chimiques (i.e. dans le plan [O/Fe] vs [Fe/H]), ont suggéré que le disque épais n'est pas une composante distincte du disque de la Voie Lactée.

3.0.4 La migration radiale vue comme un processus de diffusion des étoiles

Comme nous l'avons vu dans la partie 2, derrière le terme "migration radiale" se cache en fait plusieurs phénomènes. Nous nous sommes focalisés sur la migration produite par l'évolution séculaire de la barre, qui entraîne les étoiles piégées à la corotation vers l'extérieur du disque. Dans l'article présenté en Sec. 2.4.2, nous avons montré que la migration radiale causée par ce mécanisme concerne une fraction limitée des étoiles, et que notre nouveau mécanisme est surtout intéressant pour l'étude des régions externes des disques galactiques.

Nous avons aussi rappelé en Sec. 2.4 les autres mécanismes induisant de la migration stellaire, qui ont été étudiés jusqu'à aujourd'hui. En particulier, nous rappelé les travaux de Roskar (Roškar et al., 2008b,a, 2012), qui montrent comment une succession de phénomènes transitoires, créant une succession de rayons de corotation différents, induisent des processus de diffusion des étoiles. Nous illustrons ces effets dans la Fig. 3.2 (issue de l'analyse d'une simulation N-corps+SPH dans Kubryk, Prantzos & Athanassoula (2013)), où nous montrons l'évolution de la distribution radiale d'une unique population stellaire née entre 0 et 1 Gyr, à 8 kpc. Sur cette figure, les différentes courbes indiquent la distribution à un temps t différent (voir légende), ainsi, on voit que ces distributions sont approximativement gaussiennes, ce

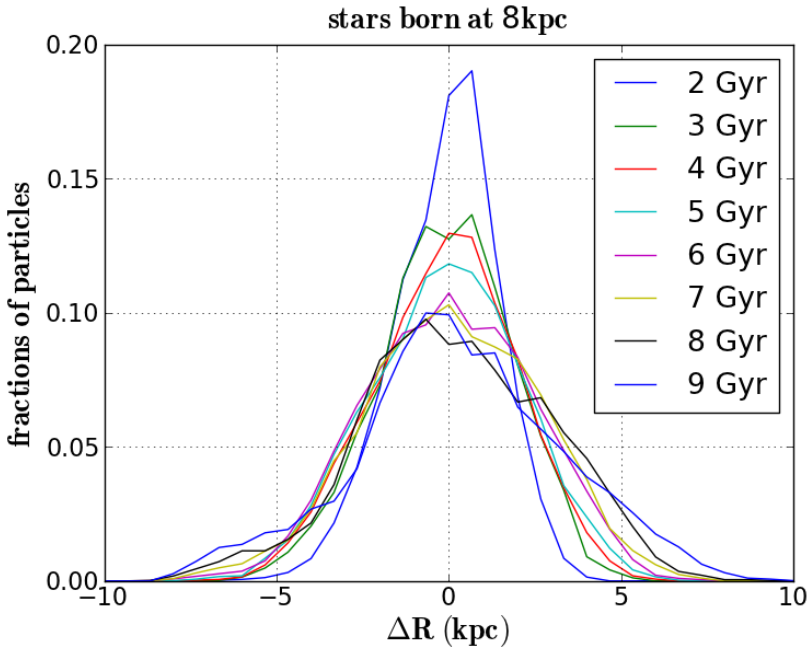

FIGURE 3.2 – Évolution de la distribution radiale des particules stellaires nées à 8 kpc entre 0 et 1 Gyr dans une simulation N-corps+SPH. Chaque courbe correspond à la distribution radiale de ces étoiles à un temps t indiqué dans la légende. Les distributions sont centrées sur le rayon d'origine. (Extrait de Kubryk, Prantzos & Athanassoula (2013))

qui est cohérent avec un processus de diffusion, qu'elles s'élargissent avec le temps, et qu'elles restent centrées sur le rayon d'origine.

Cette idée a été avancée par Brunetti, Chiappini & Pfenniger (2011), qui montrent dans leurs travaux que la migration radiale peut être considérée comme un processus de diffusion. Ils établissent l'expression des coefficients de diffusion, qui dépendent du temps et de la position radiale, et montrent que la diffusion des étoiles dépend aussi de la "température" du disque. Les travaux de Shevchenko (2011), ont également montré que la diffusion stellaire peut se faire grâce au chaos généré par les superpositions de résonances mises en évidence par Minchev & Famaey (2010). Et dans Kubryk, Prantzos & Athanassoula (2013), nous avons comparé les résultats d'une simulation N-corps+SPH avec les résultats d'une simulation semi-analytique (dans laquelle les paramètres de la diffusion stellaire sont obtenus grâce à l'analyse de la même simulation N-corps+SPH). Il ressort de cette comparaison que la migration radiale vue comme un processus de diffusion, permet de capturer les effets principaux de la migration radiale, et ainsi, de retrouver dans la simulation semi-analytique les propriétés de la galaxie simulée en N-corps+SPH.

D'une manière générale, modéliser la migration radiale par un processus de diffusion ne permet de représenter que les mouvements moyens des étoiles du disque, et donc les mouve-

ments les plus significatifs. En revanche, les mouvements concernant peu d'étoiles, et étant très asymétriques par rapport au rayon d'origine ne sont pas ou mal représentés. C'est par exemple le cas du nouveau mécanisme de migration que nous avons étudié dans la partie 2. Ne pas représenter ce mécanisme à essentiellement des conséquences sur la modélisation des régions les plus externes du disques, et donc sur la modélisation des "cassures" observées dans les profils radiaux de densité surfacique d'étoiles, et dans les profils de couleurs (Bakos et al., 2011). Cependant, pour que ce mécanisme affecte les régions externes, il faut que le corotation de la barre ait atteint cette région (Sec. 2.4.2). Les estimations de la taille de la barre dans la Voie Lactée donnent des valeurs entre 2.5 et 3 kpc (Babusiaux & Gilmore, 2005; Bobylev et al., 2014), d'après de nombreux travaux (e.g. Athanassoula, 1992) $R_c \simeq 1.2\ R_B$, d'où un rayon de corotation à environ 3.6 kpc, ce qui est loin du bord extérieur de la Voie Lactée (à environ 15 kpc). Par conséquent, le nouveau mécanisme de migration radiale mis en évidence dans notre article en Sec. 2.4.2, est négligeable dans l'étude de la Voie Lactée.

3.1 Modèle de migration basé sur l'analyse d'une simulation N-corps

Nous avons étudié les effets de la migration radiale sur l'évolution chimique d'une galaxie disque dominée par une barre, en analysant une simulation N-corps+SPH. Puis nous avons construit un modèle de migration radiale sous forme de diffusion stellaire, paramétré par des coefficients de diffusion issus de l'analyse de la simulation N-corps+SPH. Puis, nous avons montré qu'un modèle semi-analytique paramétré de manière adéquate, dans lequel nous avons inclus le modèle de diffusion radiale des étoiles, peut reproduire les propriétés de la galaxie N-corps+SPH et permet d'étudier son évolution chimique de façon plus complète.

3.1.1 Analyse de la simulation N-corps+SPH

Résultat important : en analysant la simulation N-corps+SPH, nous avons trouvé que le fluide non-dissipatif constitué par les étoiles se comporte différemment du fluide dissipatif qu'est le gaz, vis à vis de la migration radiale : les étoiles migrent loin et dans de fortes proportions dans tout le disque, alors qu'en moyenne le gaz reste proche de son rayon initial dans le disque (Fig. 4 et 5 de l'article en Sec. 3.1.3). Cependant, dans les régions internes de la galaxie, la barre transfert une grande quantité de gaz vers le centre, affectant considérablement l'évolution du bulbe/barre. Nous montrons donc clairement que le gaz et les étoiles ne doivent être traités de la même façon dans les modèles d'évolution chimiques incluant la migration radiale. Ce résultat est important dans la mesure où certains modèles d'évolution, notamment Schönrich & Binney (2009), font migrer le gaz comme les étoiles.

Ici, nous nous concentrons sur la migration des étoiles dans la partie du disque au-delà de la barre, laissant l'évolution du bulbe pour de futurs travaux. Par "migration radiale", nous désignons ici tout type de déplacement radial des étoiles, les éloignant de leur rayon de formation. Nous avons étudié l'impact de la migration radiale sur divers aspects de l'évolution

chimique du disque, bien que l'utilisation de l'Approximation du Recyclage Instantané [1], ainsi que la représentation de la chimie par un seul "métal" (l'oxygène) dans la simulation N-corps+SPH n'offrent pas des conditions idéales d'analyse.

La migration radiale augmente la dispersion en métallicité des étoiles dans toutes les zones radiales et à tous les âges stellaires (Fig. 8 de l'article en Sec. 3.1.3), mais d'autres facteurs contribuent à cette dispersion : les variations de la métallicité du gaz, causé par un mélange incomplet. À cause de l'évolution rapide dans toutes les zones radiales du modèle, les distributions en métallicité diffèrent peu d'une zone à l'autre (leur pic étant proche du rendement stellaire), et la migration radiale ne change pas ce résultat. D'un autre coté, la migration radiale aplati les profiles radiaux de métallicité (Fig. 12 de l'article en Sec. 3.1.3), en amenant des étoiles pauvres en métaux des régions externes vers les régions internes (riches en métaux), et des riches en métaux des régions internes vers les régions externes (pauvres en métaux). À cause de ce mélange, les profiles d'abondance des populations d'étoiles à un âge donné élevé, apparaissent plus plats que ce qu'ils étaient au moment de la naissance de ces étoiles. En conséquence, leur observation ne peut pas être utilisée pour en déduire la véritable évolution des profiles d'abondance. Toutefois, l'importance de cet effet dépend beaucoup du profile de métallicité du disque : si il est relativement plat au moment de la naissance des étoiles, les effets seront négligeables, mais s'il est assez pentu, la migration radiale pourrait complètement effacé cette signature. Les variations azimutales de métallicité du gaz et des étoiles sont affectées de la même manière. Nous montrons que de ces variations ne constituent pas un outil de diagnostic fiable pour la migration radiale, car ils pourraient avoir d'autres origines (infall local de gaz peu métallique ou fusion avec une galaxie pauvre en métaux). Enfin, nous obtenons une forme en "U" pour les profils de couleur, du fait des étoiles vieilles et plus rouges qui se sont déplacées des régions internes vers les régions externes (ce qui a déjà été trouvé par Roškar et al. (2008a)).

3.1.2 Modèle semi-analytique d'évolution chimique avec migration radiale

À cause des limitations sur l'évolution chimique imposées par l'Approximation de Recyclage Instantané dans la simulation N-corps+SPH, nous avons également étudié les effets de la migration radiale en adoptant une autre stratégie. Nous avons montré que ces effets peuvent étudiés avec une bonne précision en post-traitant les résultats de la simulation N-corps+SPH avec un modèle semi-analytique d'évolution chimique, incluant une chimie détaillée et une description paramétrée de la migration radiale. Dans ce travail, nous avons donc introduit la migration radiale dans un code d'évolution chimique semi-analytique. Il est à noté, qu'ici, nous avons traité la migration radiale sans séparer les deux composantes (le churning et le blurring). Pour cela, nous avons choisis de modéliser la migration radiale comme un processus de diffusion, en utilisant un formalisme similaire à celui de Sellwood & Binney (2002), étant donné que leur paramétrisation est validée par l'analyse de simulation N-corps par

1. dans cette approximation les étoiles massives se forment et meurent instantanément en libérant du matériel gazeux enrichi en éléments chimiques, les progéniteurs de SNIa sont notamment concernés

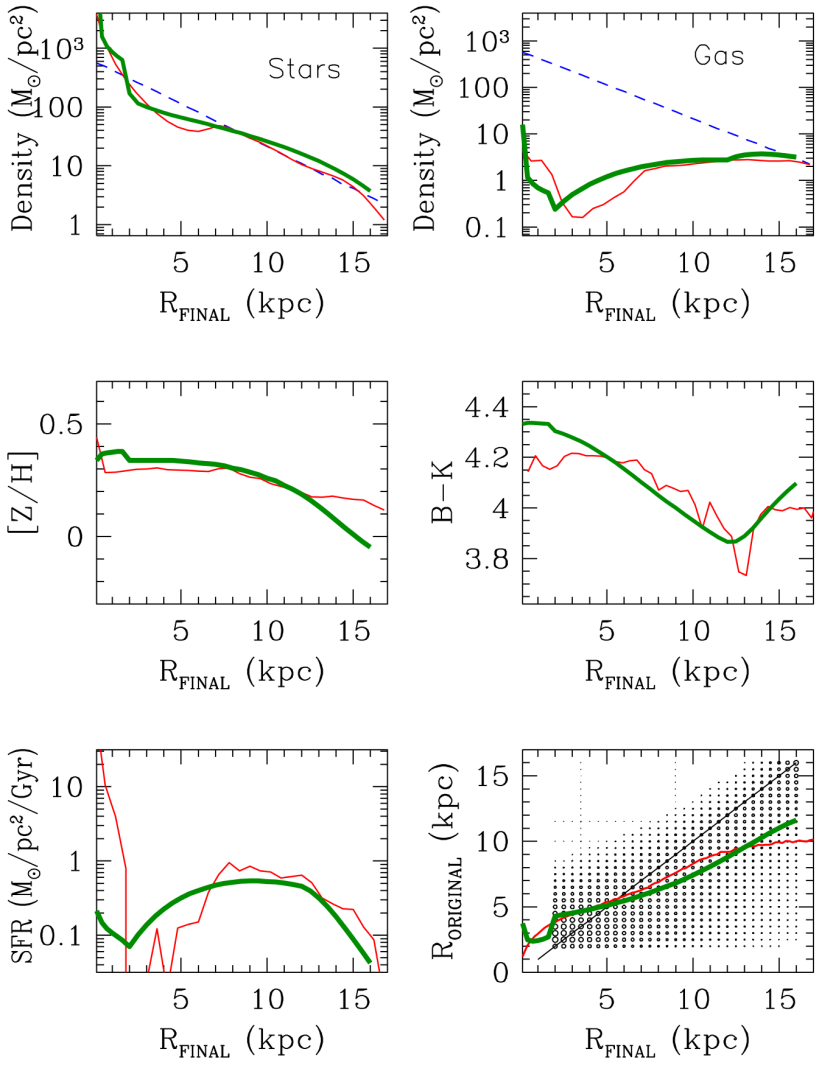

FIGURE 3.3 – Comparaison des résultats du modèle semi-analytique avec la simulation N-corps+SPH. Dans tout les panneaux, les *courbes rouges* représentent les résultats du modèle N-corps+SPH à la fin de la simulation (10 Gyr), et les *courbes vertes* indiquent les résultats obtenus avec notre modèle semi-analytique. **En haut à gauche** : densité surfacique d'étoiles et en **haut à droite** : densité surfacique du gaz ; dans ces deux panneaux la *courbe en tirets bleus* correspond au profil initial du gaz. **Milieu à gauche** : profil de métallicité. **Milieu à droite** : profil de couleur B-K. En **bas à gauche** : profil du taux de formation stellaire. En **bas à droite** : rayon de naissance vs. rayon final de toute les étoiles.

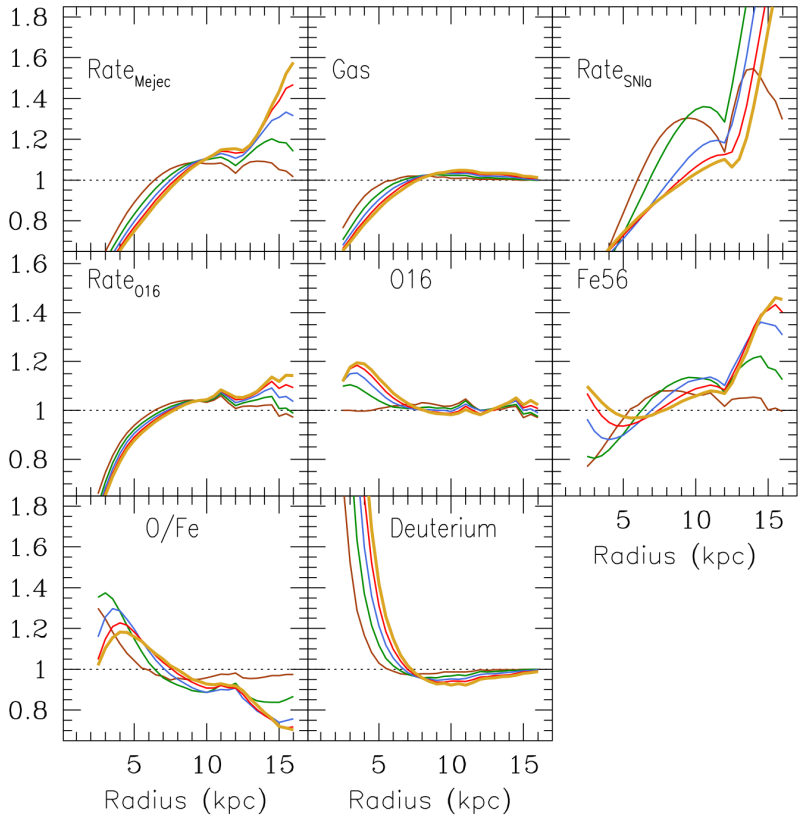

FIGURE 3.4 – Profils radiaux issus de notre modèle, pour divers quantités obtenues avec la migration *divisés par* les profils correspondants obtenus sans migration. Ces résultats sont obtenus sans l'Approximation du recyclage instantané, et nous donnons les résultats tous les 2 Gyr, la courbe dorée représentant les résultats finaux à 10 Gyr. **Première ligne** : taux de masse éjectée par les étoiles, densité surfacique du gaz, et taux de SNIa. **Deuxième ligne** : taux de masse de O-16 éjectée, et profils d'abondance en O-16 et Fe-56 dans le gaz. **Troisième ligne** : profils du rapport O/Fe dans le gaz, et profils du Deutérium.

Brunetti, Chiappini & Pfenniger (2011). Pour déterminer la valeur des paramètres du modèle de migration, nous avons analysé les déplacements stellaires dans la simulation N-corps+SPH, en ajustant par des gaussiennes les distributions de populations stellaires (par exemple Fig. 3.2) autour de leur rayon de formation. Un couplage différent par certains aspects entre un code N-corps+SPH et un code semi-analytique a été réalisé par Minchev, Chiappini & Martig (2013), pour l'étude de la Voie Lactée.

Dans la Fig. 3.3 nous comparons les profils principaux issus de notre modèle semi-analytique avec ceux du modèle N-corps+SPH à la fin de la simulation (10 Gyr). Nous obtenons une concordance satisfaisante entre les deux simulations, ce qui illustre le fait que notre méthode d'implémentation de la migration radiale en tant que diffusion des étoiles, permet de saisir les effets les plus significatifs de la migration sur l'évolution galactique.

Les résultats principaux de notre étude :

- Nous avons développé une méthode de post-traitement des simulations N-corps+SPH, afin l'évolution chimique à la migration radiale. L'intérêt du couplage entre simulations N-corps et semi-analytique est de profiter des avantages de ces deux types de simulations : l'analyse de simulations N-corps permet une description réaliste de la diffusion stellaire, et les simulations semi-analytiques permettent une description plus détaillée de l'évolution chimique (avec plus d'éléments chimiques, les effets de l'infall, et sans l'Approximation de Recyclage Instantané).
- Nous trouvons que la migration radiale affecte l'évolution chimique à la fois indirectement (en affectant les relations âge-métallicité et les distributions en métallicité des étoiles déplacées dans le disque) et directement, en déplaçant les sources de nucléosynthèse de longue durée de vie (SNIa ou les étoiles de la Branche Asymptotique des Géantes (AGB) de masse 1.5 $M_{\odot}$) altérant ainsi les profils d'abondance dans le gaz. Ce qui est illustré dans le panneau en haut à droite de la Fig. 3.4 où on voit que la migration diminue le taux de SNIa dans les régions internes, et l'augmente dans les régions externes, ce qui affecte le profil du Fe56 et, par conséquent, le profil de O/Fe.
- Nous avons montré comment les profils radiaux des éléments O, Fe et D sont affectés par la migration dans le cas de notre simulation (Fig. 3.4), mais d'autres éléments (e.g. les éléments formés par le Processus lent (s-process) dans les étoiles AGB) pourraient aussi être concernés.
- Nos résultats du post-traitement montrent clairement que l'ensemble des conséquences de la migration radiale sur l'évolution chimique ne peut pas être évalué avec des simulations utilisant l'Approximation de Recyclage Instantané.

Nous insistons cependant, sur le fait que l'impact de la migration radiale sur l'évolution chimique dépend du système étudié. Trois facteurs ont été identifiés pour l'instant : la force des inhomogénéités dans le potentiel gravitationnel, e.g. la barre ou les bras spiraux (en considérant que les perturbations les plus fortes engendrent les effets les plus significatifs) ; la durée de la migration radiale (plus la barre agit longtemps, plus les effets sont importants) ; et la pente des profils d'abondance au moment où la plupart des étoiles se forment. Ces facteurs peuvent s'annuler les uns les autres et masquer les effets de la migration radiale sur l'évolution chimique : par exemple, une barre forte attirant du gaz peu métallique vers les régions internes va aplatir les profils de métallicité ; les étoiles formées à partir du gaz ainsi altéré auront quasiment les mêmes abondances chimiques partout dans le disque, même si la migration radiale est très forte. C'est ce qui arrive dans la simulation étudiée ici, bien que la platitude des profils de métallicité observée dès les premiers temps de la simulation, s'explique par l'évolution en boîte fermée avec une formation stellaire rapide et précoce. Dans le cas d'une galaxie évoluant plus lentement de l'intérieur vers l'extérieur, des profils de métallicité plus pentus seraient attendus ; toutefois, dans ce cas, une étoile aurait moins de temps pour migrer, alors l'impact de la migration sur l'évolution chimique ne serait pas forcément plus significatif.

Il est à noter qu'un infall continu de gaz pauvre en métaux, ce qui est attendu pour la Voie Lactée, devrait aussi atténuer l'impact de la migration radiale sur la composition chimique du gaz, en diluant les variations radiales des abondances.

3.1.3 Article : Migration radiale, impact sur l'évolution chimique

Monthly Notices of the ROYAL ASTRONOMICAL SOCIETY

MNRAS **436,** 1479–1491 (2013) doi:10.1093/mnras/stt1667
Advance Access publication 2013 October 3

Radial migration in a bar-dominated disc galaxy – I. Impact on chemical evolution

M. Kubryk,[1]★ N. Prantzos[1] and E. Athanassoula[2]

[1]*UPMC-CNRS, UMR7095, Institut d' Astrophysique de Paris, F-75014 Paris, France*
[2]*OAMP, LAM, 2, place Le Verrier, F-13248 Marseille cedex 04, France*

Accepted 2013 September 3. Received 2013 September 2; in original form 2013 April 16

ABSTRACT

We study radial migration and chemical evolution in a bar-dominated disc galaxy, by analysing the results of a fully self-consistent, high-resolution *N*-body+smoothed particle hydrodynamics (SPH) simulation. We find different behaviours for gas and star particles. Gas within corotation is driven in the central regions by the bar, where it forms a pseudo-bulge (discy-bulge), but it undergoes negligible radial displacement outside the bar region. Stars undergo substantial radial migration at all times, caused first by transient spiral arms and later by the bar. Despite the important amount of radial migration occurring in our model, its impact on the chemical properties is limited. The reason is the relatively flat abundance profile, due to the rapid early evolution of the whole disc. We show that the implications of radial migration on chemical evolution can be studied to a good accuracy by post-processing the results of the *N*-body+SPH calculation with a simple chemical evolution model having detailed chemistry and a parametrized description of radial migration. We find that radial migration impacts on chemical evolution both directly (by moving around the long-lived agents of nucleosynthesis, like e.g. SNIa or asymptotic giant branch stars, and thus altering the abundance profiles of the gas) and indirectly (by moving around the long-lived tracers of chemical evolution and thus affecting stellar metallicity profiles, local age–metallicity relations and metallicity distributions of stars, etc.).

Key words: galaxies: abundances – galaxies: evolution – galaxies: ISM – galaxies: kinematics and dynamics.

1 INTRODUCTION

In the past decade, observational and theoretical studies suggested that radial migration of stars may play an important role in shaping the properties of galactic discs. Already in the 1990s, it was realized that the observed dispersion in the age–metallicity relation of the solar neighbourhood (Edvardsson et al. 1993) was apparently too large to be explained solely by orbital diffusion due to epicyclic motions (i.e. by stars born in the inner Galaxy, in regions of metallicity higher than the local one). Moreover, Wielen, Fuchs & Dettbarn (1996) argued that the Sun should have originated ∼2 kpc inwards from its current Galactocentric radius, in order to explain its high metallicity with respect to the one of the local interstellar medium (ISM) and of nearby stars; that value was close to the maximum radial epicyclic excursion $\Delta R \sim \sqrt{2}\sigma_R/\kappa \sim 2$ kpc (in view of the observed local values of radial velocity dispersion $\sigma_R \sim 50\,\mathrm{km\,s^{-1}}$ (Holmberg, Nordström & Andersen 2009) and epicyclic frequency $\kappa \sim 37\,\mathrm{km\,s^{-1}\,kpc^{-1}}$ Binney & Tremaine 2008). Since then, the solar metallicity has been revised downwards (Asplund et al. 2009) and it is compatible with the one of nearby young stars and of the local ISM; still, it is unclear whether observations require important radial mixing, i.e. beyond the one implied by epicyclic motions; see e.g. Haywood 2012; Nieva & Przybilla 2012).

Sellwood & Binney (2002) (hereafter SB02) showed that, in the presence of recurring transient spirals, stars in a galactic disc could undergo radial displacements much larger than envisioned before: stars found at corotation with a spiral arm may be scattered to different galactocentric radii (inwards or outwards,) a process which preserves overall angular momentum distribution and does not contribute to the radial heating of the stellar disc. This development paved the way for a large number of theoretical studies on radial migration, both with numerical *N*-body codes and with semi-analytical models.

Lépine, Acharova & Mishurov (2003) considered a toy-model disc with corotation at a fixed galactocentric radius, removing stars locally and 'kicking' them inwards and outwards. They find that in the case of the Milky Way disc, the abundance profile (assumed

★E-mail: kubryk@iap.fr

to be initially exponential) flattens in the 8–10 kpc region, but current data are inconclusive in that respect (Luck & Lambert 2011). Analysing *N*-body+smoothed particle hydrodynamics (SPH) simulations, Roškar et al. (2008b) presented a systematic investigation of the implications of radial migration (*à la* SB02) for the chemical evolution of galactic discs; they discussed dispersion in the age–metallicity relation, broadening of the metallicity distribution, flattening of observed past abundance profiles and flattening of the observed past star formation history. Some of those effects were analysed in more detail with a simple toy model by Prantzos (2009), who found that the SBO2 mechanism produces an age-dependent dispersion in the age–metallicity relation (because young stars have insufficient time to migrate from far-away regions with different metallicities) and showed how the tails of the local metallicity distribution can be affected by that process.

Schönrich & Binney (2009) coupled a full chemical evolution code with a parametrized prescription of radial migration, distinguishing epicyclic motions ('blurring') from migration ('churning') due to transient spirals. They found excellent agreement between the results of their model and observations of the solar neighbourhood and they suggested that radial mixing could also explain the formation of the Galaxy's thick disc, by bringing to the solar neighbourhood a kinematically 'hot' stellar population from the inner disc. That possibility was subsequently investigated with *N*-body models, but controversial results are obtained up to now (compare e.g. Loebman et al. 2011 to Minchev et al. 2012). The issue is still under debate and it is unclear whether the Galaxy's thick disc is due to secular evolution or to the effects of past mergers (e.g. Bournaud, Elmegreen & Martig 2009; Brook et al. 2012; Forbes, Krumholz & Burkert 2012; Steinmetz 2012; Bekki & Tsujimoto 2011), while Bovy, Rix & Hogg (2012) suggest that the thick disc is not a distinct component of the Milky Way.

Minchev & Famaey (2010) suggested a different mechanism for radial migration than transient recurring spirals, namely resonance overlap of the bar and spiral structure; this strongly non-linear coupling leads to a more efficient redistribution of angular momentum in the disc and produces a stellar velocity dispersion increasing with time, in broad agreement with local observations. This bar–spiral coupling was studied in detail by Shevchenko (2011) and Brunetti, Chiappini & Pfenniger (2011); the latter found that the extent of radial migration depends also on the kinematic state of the disc, being reduced in the case of kinematically hot discs. The radial motion of stars in discs was analysed with *N*-body+SPH models for both non-barred (Grand, Kawata & Cropper 2012a) and barred (Grand, Kawata & Cropper 2012b) disc galaxies. By tracing particle motion around the spiral arms they showed that particles move along the arms in the radial direction, migrating towards the outer (inner) radii on the trailing (leading) side of the arm. On the other hand, Comparetta & Quillen (2012) found that radial migration may also be induced by short-lived transient density peaks (produced by interfering spiral patterns) and it may be more pervasive than that mediated by the growth and decay of long-lived individual spiral patterns. Migration due to short-lived, recurrent grand design spirals is also found in the simulations of Athanassoula (2012). Finally, the observed diversity of photometric disc profiles and, in particular, the properties of their outskirts (see Bakos et al. 2011, and references therein) have been interpreted in terms of radial migration, either fully (Roškar et al. 2008a), or partially (Sánchez-Blázquez et al. 2009).

In this work, we study the implications of radial migration on the chemical evolution of a barred disc galaxy. We use an *N*-body+SPH simulation to study the evolution of a disc galaxy embedded in (and interacting with) a live dark matter halo of $10^{12}\,\mathrm{M}_\odot$, for 10 Gyr; an early-type disc galaxy with a strong bar is formed (Section 2). We quantify the extent of radial migration for stars and gas (Section 3) and we study its implications for the chemical evolution of the disc in Section 4. We find that, despite the important amount of radial migration occurring in our model, its impact on the chemical properties is limited. The reason is the rather flat abundance profile which is established early on in our model, due to the rapid early evolution across the whole disc.

The analysis of the results allows us to describe the radial displacement of stars in the disc in a parametrized way. We implement this parametrized description in a 'traditional' detailed chemical evolution model (including long-lived sources and sinks of elements). This strategy allows us to overcome the limitations of the Instantaneous Recycling Approximation (IRA) adopted in the *N*-body+SPH simulation and to investigate in detail the true impact of radial migration. We find (Section 5) that radial migration impacts on chemical evolution both directly (by affecting the age–metallicity relations, abundance profiles and metallicity distributions of stars across the disc) and indirectly, by moving around the long-lived nucleosynthesis sources and thus altering the abundance profiles of the gas; we show, in particular, how the radial profiles of O, Fe and D are affected. Our post-processing results show clearly that the full impact of radial migration on chemical evolution cannot be evaluated with numerical codes using IRA.

2 THE NUMERICAL SIMULATION

The simulation used in this paper was done with the GADGET3 code and it is very similar to simulation 116 described and analysed in Athanassoula, Machado & Rodionov (2013), except that here we describe the old disc component (disc in the standard GADGET notation) by 200 000 particles and that the softening of the halo and disc is 100 pc (instead of 50 pc in simulation 116).

The adopted simulation has four components (HALO, DISC, GAS, STARS), having the following initial settings.

(i) A disc made of two initial components that are a gaseous disc (component GAS), and an old stellar disc (component DISC) having the same initial azimuthally averaged density distribution. Therefore, the density distribution of the initial total disc is

$$\rho_\mathrm{d}(R,z) = \frac{M_\mathrm{d}}{4\pi h^2 z_0}\exp\left(-\frac{R}{h}\right)\mathrm{sech}^2\left(\frac{z}{z_0}\right), \quad (1)$$

where $M_\mathrm{d} = 5\times10^{10}\,\mathrm{M}_\odot$ is the total mass of the disc (gas and old stars), the initial gas fraction is 0.75, $h = 3$ kpc is the disc scalelength and $z_0 = 0.6$ kpc is the disc scaleheight. The DISC component is made of 2.5×10^5 particles having mass $2.5\times10^5\,\mathrm{M}_\odot$, and has an imposed initial radial velocity dispersion of $\sigma(R) = 100\exp(-R/3h)\,\mathrm{km\,s^{-1}}$. The number of particles in this component remains constant during the simulation. The GAS component features 7.5×10^5particles having mass $5\times10^4\,\mathrm{M}_\odot$, which can be partially converted into new-formed stars belonging to the component STARS (this one is empty at the beginning of the simulation). So the number of particles in the components GAS and STARS can change.

(ii) A live spherical halo (component HALO) having the initial density distribution:

$$\rho_h(r) = \frac{M_h}{2\pi^{\frac{3}{2}}}\frac{\alpha}{r_c}\frac{\exp\left(-r^2/r_c^2\right)}{r^2+\gamma^2}, \quad (2)$$

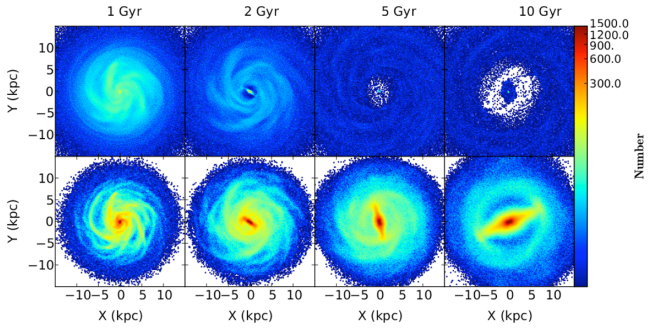

Figure 1. Face-on view of the simulated galaxy at 1, 2, 5 and 10 Gyr. Gas-particles are displayed in the upper row and star particles in the lower one. The colour scale on the right shows the number of particles in each pixel.

where $M_h = 2.5 \times 10^{11}\,M_\odot$ is the halo mass, $\gamma = 1.5$ kpc is the core radius, $r_c = 30$ kpc is the cut-off radius. And $\alpha = [1 - \sqrt{\pi}\exp(\gamma^2/r_c^2)(1 - \mathrm{erf}(\gamma/r_c))]^{-1}$ is a normalization factor. There are 10^6 particles having mass $2.5 \times 10^5\,M_\odot$ in the HALO component.

(iii) The softening length is 50 pc for all components, and the opening angle for the tree-code is 0.5.

The particles in the component GAS are converted into stars with the prescriptions (including a threshold on gas volume density) given in the paper of Springel & Hernquist (2003), hereafter SH03 (see Section 2 and, in particular, equations (2) and (23) of that paper), which lead to a satisfactory agreement with the Schmidt–Kennicutt law. Thermal feedback is also introduced as in SH03, and the IRA is used for the chemical enrichment of the gas particles, implemented as described in section 5.3 of SH03. Metal diffusion between neighbouring gas particles is not taken into account. No gas infall is considered in this simulation, i.e. the galaxy evolves as a closed box for 10 Gyr.

Some snapshots of the evolution are shown in Fig. 1. Most of the stars are formed during the first ∼2 Gyr; in that period, the gas is depleted and the disc is dominated by the presence of spiral transient structures. After 2 Gyr, a bar is formed in the centre of the galaxy and grows steadily until the end of the simulation, when it extends to almost half the size of the stellar disc. The bar drives gas from the inner Lindblad resonance radius inwards. Evolving locally as in a closed box (i.e. without being replenished by infall), the gas is steadily depleted all over the disc, but more rapidly in the inner regions. Towards the end of the simulation, due to the combined action of the bar and star formation, the remaining gas is found mostly in a ring outside the bar which is separated by the central gaseous concentration by a low-density annulus. The same holds for the stellar disc, which forms an inner ring (see Buta 1995 for a definition and description of inner rings).

The central bar appears to be the most significant asymmetric structure in the potential, reducing the importance of spiral arms as it grows (Fig. 1). Therefore, it is expected that various dynamical phenomena linked to asymmetries in the gravitational potential (e.g. disc warming, radial migration, chaos, resonances, etc.), will increasingly be consequences of the action of the bar, rather than of other structures (such as transient spiral arms).

Fig. 2 displays the evolution of the azimuthally averaged radial profiles of the surface densities of stars, gas and star formation rate, as well as of the average stellar and gas metallicities and the one of stellar tangential velocity. It should be emphasized that the average surface density profiles provide little information for the inner disc, which is dominated by the bar. The aforementioned profiles clearly

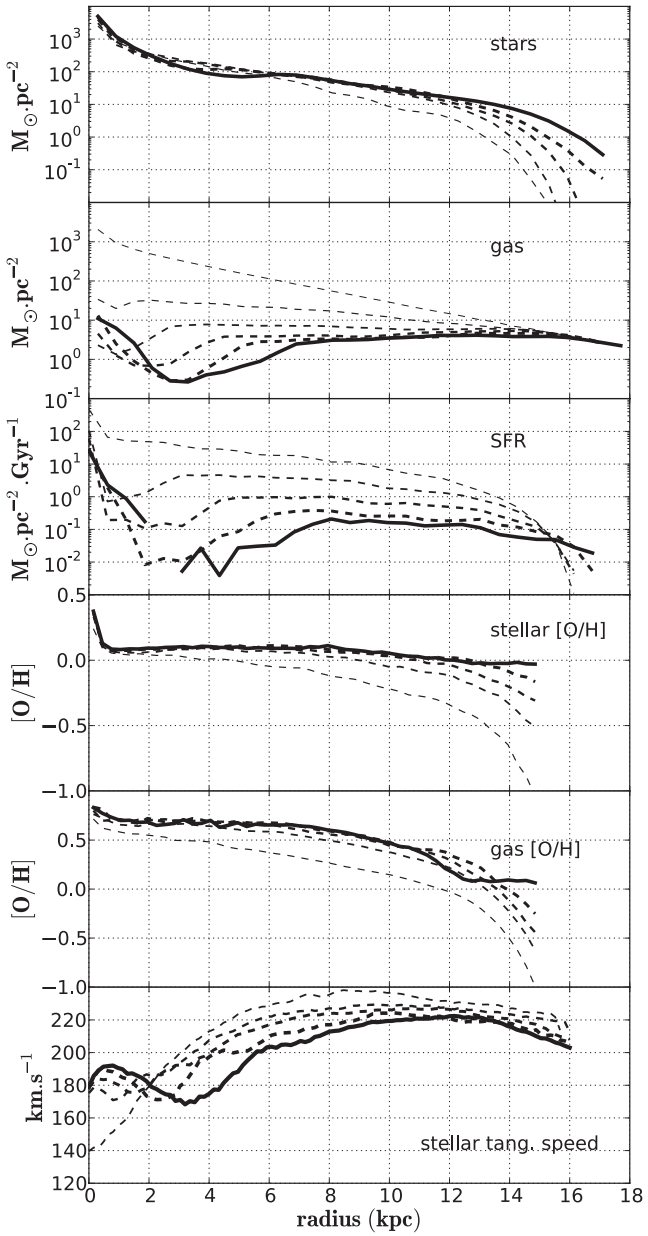

Figure 2. From top to bottom: azimuthally averaged radial profiles of the stellar surface density, gas surface density, star formation rate, average stellar and gas metallicities and rotation velocity curves. Curves correspond to snapshots taken every 2 Gyr, with the *thick solid* ones corresponding to the final (10 Gyr) result.

reflect the inside-out formation of the disc, with the gas profiles being much more rapidly depleted in the inner disc than in the outer one, resulting in oxygen profiles becoming flatter with time. The gaseous profile is mostly depleted in the inner disc, due to both the adopted SFR law and the action of the bar which gradually produces a spoon-shaped profile. The stars at the edge of the bar can switch from almost circular orbits to elongated ones (aligned with the bar axis), thus contributing to the bar growth. Once on an elongated orbit, a star oscillates between central region and the radius of its former circular orbit. As a result, the stellar profile acquire the same spoon-shape, and it evolves with time as the bar grows longer. The SFR profile displays similar features as the gaseous profile, as expected. The small values of the SFR outside 14 kpc result in

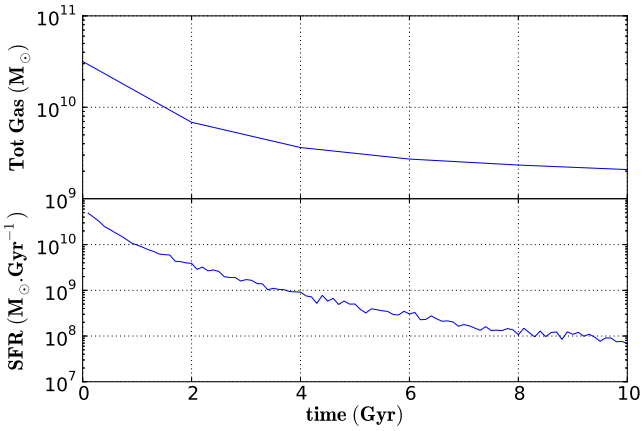

Figure 3. Evolution of the total gas amount (top) and of the total star formation rate (bottom) in the simulation.

a steep stellar profile beyond that radius. In the absence of infall, the gas is substantially depleted, only ∼8 per cent of the initial quantity remaining at the end of the simulation in the whole galaxy and ∼13 per cent in the disc region (outside the bar). One should notice that the final gas metallicity in the outer disc is lower than at previous epochs. This is a consequence of low-metallicity gas from the region of bar corotation region driven inwards (see also Section 4.1) since bar corotation is located at $R \sim 15$ kpc towards the end of the simulation.

Fig. 3 displays the evolution of the total amount of gas (top) and of the star formation rate (bottom). Due to the adopted criteria for star formation, more than 65 per cent of the stellar population of the galaxy is formed in the first Gyr of the evolution and approximately 85 per cent is formed *in* the first 2 Gyr.

3 GLOBAL BEHAVIOUR OF STAR AND GAS PARTICLES

The orbit of a test particle (star) in the potential of a galactic disc is commonly described, to first-order approximation, as the superposition of a main circular motion (defining the *guiding radius*), and harmonic oscillations called epicycles. Following SB02, we call *blurring* the radial oscillations around the guiding radius and *churning* the modifications of the guiding radius. Churning may occur through resonant interactions of the star with non-axisymmetric structures of the gravitational potential (spirals, bar), causing changes in the angular momentum of the stars. SB02 showed that stars near corotation of a spiral perturbation may gain (lose) energy and angular momentum as they fall in the potential well of that perturbation from the leading (trailing) edge, while conserving the value of their Jacobi constant. Those changes in angular momentum make them move towards the outer (inner) disc, where they are deposited in a new quasi-circular orbit. The process conserves the overall distribution of angular momentum and does not add random motion, i.e. it does not heat the disc radially. In contrast, blurring conserves the angular momentum of individual stars but it heats radially the disc (the epicyclic radius increases with time).

In a companion paper (Kubryk, Athanassoula & Prantzos, in preparation), we analyse in some detail the behaviour of star particles undergoing churning and, in particular, the role of bar corotation and its interaction with spiral arms, in that behaviour. Here, we study the impact of both churning and blurring on the chemical evolution of the disc. It is instructive to consider first the global behaviour of star and gas particles in the simulation, by plotting their initial

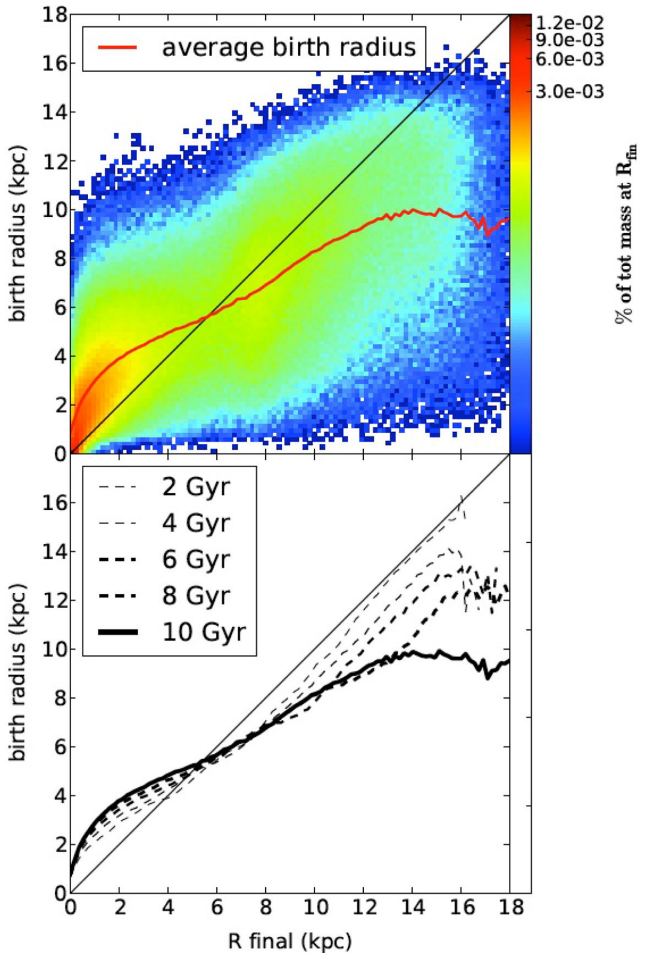

Figure 4. Upper panel: birth radius (at any time) versus final radius (at 10 Gyr) of all star particles; the colour scale represent the percentage of total stellar mass at final radius, while the red curve displays the mean birth radius of the stars at each final radius (in bins 100 pc wide). Lower panel: evolution of the mean birth radius of the stars at each final radius with snapshots taken every 2 Gyr and with the thickest full curve corresponding to the final time of 10 Gyr. Non-migrating stars are located on the diagonal black line (birth radius = final radius).

versus final radius (for star particles, the initial radius is their birth radius).

The results for the star particles appear in Fig. 4. Stars at a given final radius R_f originate from a large range of birth radii R_i. The distribution of R_i versus R_f is not symmetrical with respect to the diagonal implying that it is not solely due to blurring (=epicyclic motion). The average ratio R_f/R_i differs significantly across the galaxy: it is smaller than 1 in the inner zones($R_f < 5.5$ kpc) and larger than 1 in the outer ones. Stars in the inner galaxy were born on average a couple of kpc outwards, whereas stars lying in the outer zone were born several kpc inwards. The secular evolution of the bar is responsible for the inwards movements of the stars lying inwards of 5.5 kpc at the end, because stars on initially near-circular orbits can be captured on elongated orbits at the edge of the bar, implying a mean displacement towards small radii. The steady increase of the ratio with R_f is due to the fact that there are smaller and smaller amounts of native stars as one moves to the outer disc: the corresponding average birth radius of the stellar population at R_f is then more and more affected by the population which migrated from the inner zones.

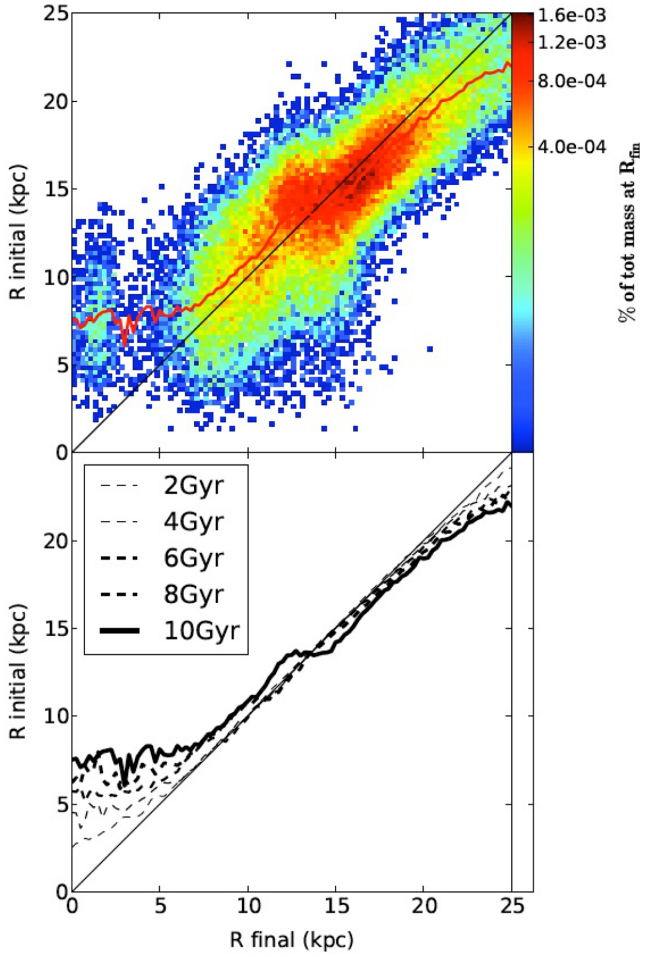

Figure 5. Same as in the previous figure, but for gas particles. Except that here we consider the initial radius (at $t = 0$ Gyr), since no new gas particle appear during the simulation time.

The results for gas-particles, appear in Fig. 5 (upper panel), where the birth radius of the previous figure is replaced by the initial radius since all the gas particles are present at the beginning of the simulation. In the upper panel, we distinguish two regions: inner ($\leq$8 kpc) and outer ($\geq$8 kpc) one.

In the inner region, almost all gas particles come from larger radii (there is practically no particle which has kept its original radius since the beginning). As for the stars, the inward movement of the gas particles lying in the inner zones is due to the bar (Roberts, Huntley & van Albada 1979; Athanassoula 1992); this gas falls to the innermost regions following orbits with an important radial component. As a result, since the gas forms a continuous fluid (contrary to the stars), the stream of falling gas creates a shock at each leading edge of the bar. The gas at radii smaller than the corotation radius, initially on circular orbits, loses energy and angular momentum each time it passes through the shock, thus it also falls towards the inner galaxy. The inflowing gas forms a small central gaseous disc (Figs 1 and 2), where the gas density remains high enough to trigger star formation even at late times (Fig. 2). The inner galaxy is then constantly depleted of its gas by star formation and fed by the action of the bar, which brings gas from more and more large radii as the corotation moves outwards (because of the slowing down of the bar). As a result, the area between the central gaseous disc and the corotation of the bar is almost devoid of gas in the end.

In the outer regions ($R > 6$ kpc), the gas particles are only slightly affected by the bar corotation radius: particles at radii smaller than corotation move slightly inwards ($\leq$1 kpc) while the ones at larger radii move slightly outwards. But the average initial radius remains close to the diagonal, around which the distribution of initial radii stays roughly symmetric.

Comparing Figs 4 and 5, we see that both stars and gas display strong evolution in the inner regions, while only the stars display such evolution in the outer galaxy. The average displacement of gas particles in response to gravitational potential asymmetries is smaller than the one of stellar particles, because gas is a continuous dissipative fluid while stars form a non-dissipative, discrete, one. The bar affects the gas mainly by driving large amounts of it to the inner regions, where they fuel star formation. Its role on the behaviour of the stellar fluid is more diverse, as will be discussed in the next sections.

4 CHEMICAL EVOLUTION

One of the major applications of the work of SB02 concerned the age–metallicity relation in the solar neighbourhood. Using a toy model for the evolution of the metallicity profile of the Milky Way disc and a probabilistic description of the radial migration, the authors showed that a large dispersion can be obtained in the local age versus [Fe/H] relation. They found that this dispersion can be substantially larger than the corresponding observational scatter and compatible with the results of the survey of (Edvardsson et al. 1993). The seminal paper of Roškar et al. (2008b) revealed other implications of radial migration, concerning the metallicity distribution and the stellar metallicity gradients in the disc.

In this section, we explore the aforementioned consequences of radial migration in our bared disc model. Our investigation is limited by the use of just one metal in the numerical simulation, and by the fact that the IRA has been adopted. For those reasons, standard monitors of chemical evolution like e.g. abundance ratios (O/Fe etc.) cannot be used and the results are inaccurate at late times and low gas fractions (where IRA fails to account for the late return of metal-poor gas from long-lived low-mass stars). Still, it is instructive to explore some of the implications of that approximate treatment in order to get some insight into the effects of radial migration on chemical evolution.

4.1 The age–metallicity relation

We assume in the following that the unique metal in the simulation represents oxygen, because it constitutes almost half of the solar metallicity and because its evolution is described by IRA in a satisfactory manner in many cases, being a product of short-lived massive stars. We are fully aware that at late times IRA may overpredict oxygen abundances, but we are interested mostly in relative, not absolute, values of the abundance.

Fig. 6 (upper panel) displays the evolution of the azimuthally averaged metallicity in three different galactocentric radii, located at 4, 8 and 12 kpc, respectively. Metallicity increases rapidly in the first couple of Gyr and more slowly (less than a factor of 2 or 0.3 dex) in the remaining evolution. This applies to all radii, albeit with a small delay in the early stages, due to the inside-out formation of the disc (see fifth panel from the top in Fig. 2). The most conspicuous feature in Fig. 6 is the decline of the metallicity at 12 kpc in the last 2 Gyr of the evolution which is, in principle, unexpected. The origin of that feature is understood after inspection

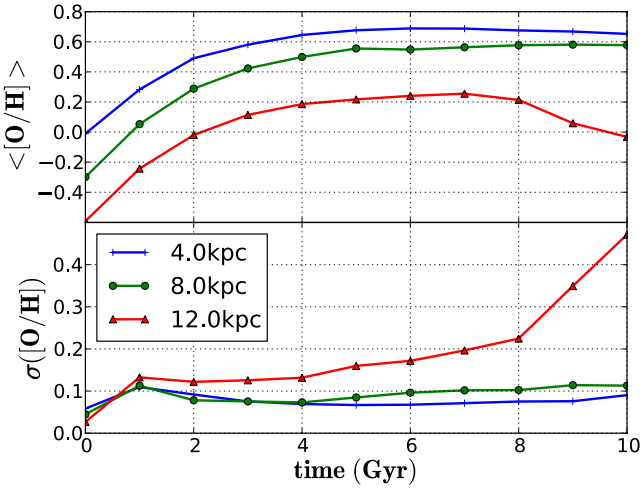

Figure 6. Evolution of the azimuthally averaged gas metallicity [O/H] (upper panel) and of the corresponding dispersion (in dex, lower panel) at three different galactocentric zones of width $\Delta R =$ 1 kpc: 4 (solid blue), 8 (green circles) and 12 (red triangles) kpc.

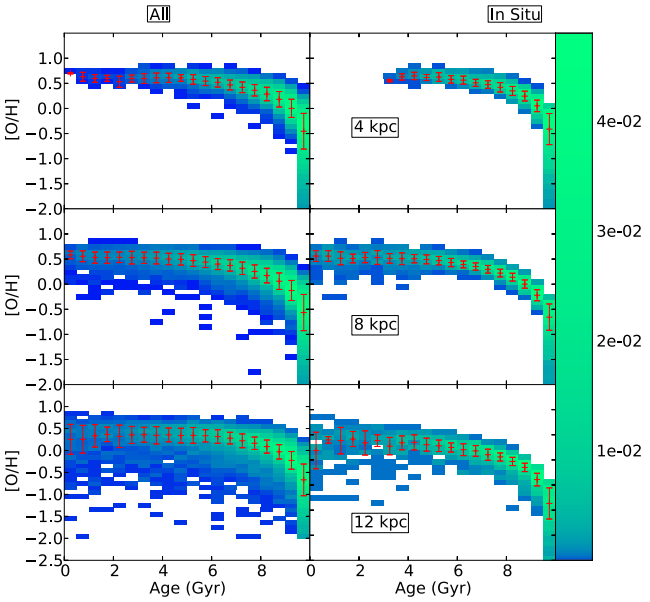

Figure 7. Stellar age–metallicity relation for three zones at galactocentric radii $R =$ 4, 8 and 12 kpc, respectively (from top to bottom) and width $\Delta R = \pm 1$ kpc. Results are displayed for all stars present in the zone at 10 Gyr (left-hand panels) and for stars which were formed in that zone and are still there at 10 Gyr (*in situ* stars, right-hand panels). In all panels, at each age bin (Δ(Age) = 1 Gyr) the metallicity distribution is fitted by a Gaussian function, and its peak and standard deviation are displayed with (red) dots and error bars, respectively.

of Fig. 2: in the last 2 Gyr of the evolution, bar corotation is located at ∼12 kpc and drives inwards gas from the outer regions; that gas is metal poor because the metallicity profile declines rapidly outside 12 kpc (due to weak stellar activity at $R > 12$ kpc), and dilutes the oxygen abundance at that radius while at the same time flattens the abundance profile in the region between 12 and 16 kpc.

The lower panel of Fig. 6 shows the dispersion in the gas metallicity in those same zones. Dispersion is fairly small (less than ∼0.1 dex) during the whole evolution in the 4 and 8 kpc zones. In contrast, it becomes important in the 12 kpc zone in the last couple of Gyr, for the same reason as the decline in metallicity of that zone, namely the dilution with metal-poor gas from the outer disc. This gas is driven inwards by the bar corotation and does not exchange metals with local gas, because of the simplified treatment of metals in the adopted version of the GADGET code. Thus, although the effect of the declining metallicity discussed in the previous paragraph is real (at least in the framework of our model), the effect of a late increasing dispersion is a numerical artefact, which impacts also on the results of the stellar metallicity dispersion as we shall see in the next paragraph.[1]

The stellar age–metallicity relation at 4, 8 and 12 kpc is displayed in Fig. 7, for all the stars found at 10 Gyr in those zones (left-hand panels) and for those stars only that have been formed in those same zones (right-hand panels). In all zones, metallicity remains flat for stars younger than 6 Gyr, as expected, because of insignificant star formation during that period. For stars born *in situ*, dispersion is small and follows the corresponding gaseous dispersion (see Fig. 6), except in the first couple of Gyr where the gas metallicity increases rapidly: since our stellar age bins have a width of 1 Gyr, we obtain a large range of metallicity values in the first bins (and consequently a large dispersion) even though the corresponding 'instantaneous' dispersion in the gas is small. It should be noticed here that the term 'dispersion' has not exactly the same meaning in the case of gas and stars: for the gas, it means *instantaneous dispersion* (at any given time), but for the stars it always concerns a given *age-interval* (here taken to be of 1 Gyr); as a result, independently of any radial migration, the latter is always larger than the former: stars of age 4(±0.5) Gyr have a larger metallicity dispersion than the gas had 4 Gyr ago.

At late times, metallicity evolves little and *in situ* formed stars present smaller dispersion. Radial mixing, either through churning or blurring, increases that dispersion, albeit by modest amounts. We confirm the trend originally found in SB02 of smaller dispersion with decreasing age: it is due to the fact that younger stars have less time to migrate from far away regions. However, the overall effect is smaller in our case because the metallicity gradients we obtain are substantially flatter than in SB02 at all ages. At very late times, dispersion increases in the outer regions (see panels for 8 and 12 kc), for a reason independent of radial migration: The bar corotation progressively moves outwards, driving inwards metal-poor gas from the outer disc which is mixed (but not completely) with metal richer gas in the regions from 8 to 12 kpc. This is seen in Fig. 2 (the gas metallicity profile of the outer disc flattens at 10 Gyr from metal-poor gas driven inwards) and in Fig. 13 (bottom-left panel, with important azimuthal variations of gas metallicity at 12 kpc). It is these variations in gas metallicity (from incomplete gas mixing from outer regions) that drive the large dispersion in stellar metallicity in the outer regions at late times.

Those results are quantitatively illustrated in Fig. 8, which shows that dispersions generally decrease with time and that the fractional dispersion difference between all the stars and the *in situ* formed ones is also a decreasing function of time (except in the case of stars at 8 and 12 kpc, due to the aforementioned reasons).

[1] We are currently implementing a considerably improved module of chemical evolution in the GADGET code, which contains elements from short-lived and long-lived sources – including Fe from SNIa –, and accounts for mixing of gas phases.

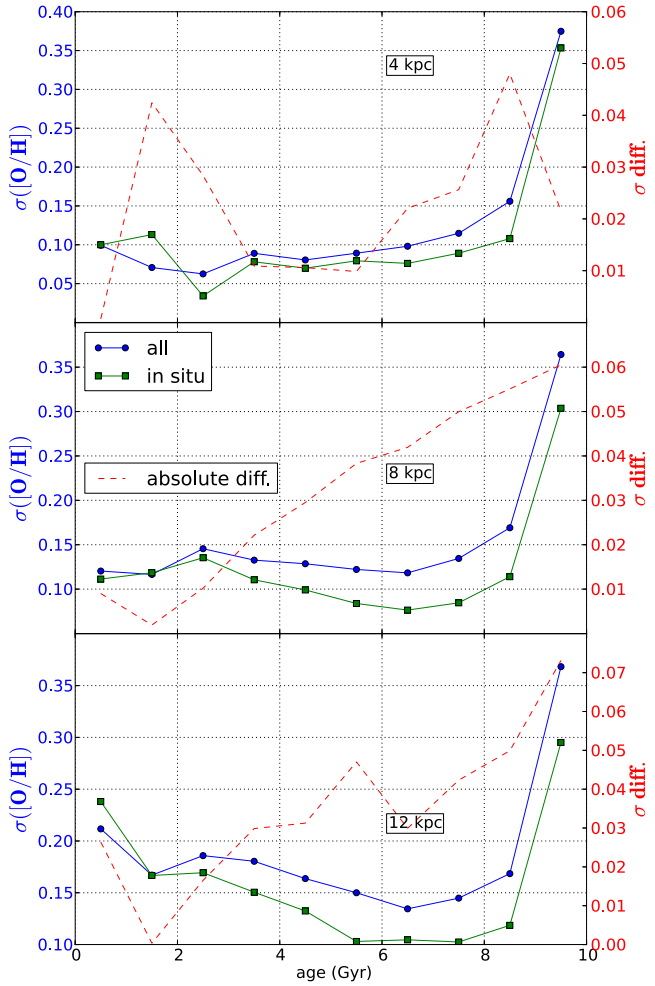

Figure 8. Evolution of the stellar metallicity dispersion in three zones of galactocentric radius $R = 4$, 8 and 12 kpc and width $\Delta R = \pm 1$ kpc. The dispersion is calculated as one standard deviation σ([O/H]) around the mean value. The blue curves (circles) correspond to all stars present in the zone and the green curves (squares) to stars formed within the zones; both curves read on scales on the left. The red (dashed) curve represents the difference of the two others $\sigma_{\rm dif} = |\sigma_{\rm all} - \sigma_{\rm insitu}|$ and is read on the right-hand axis.

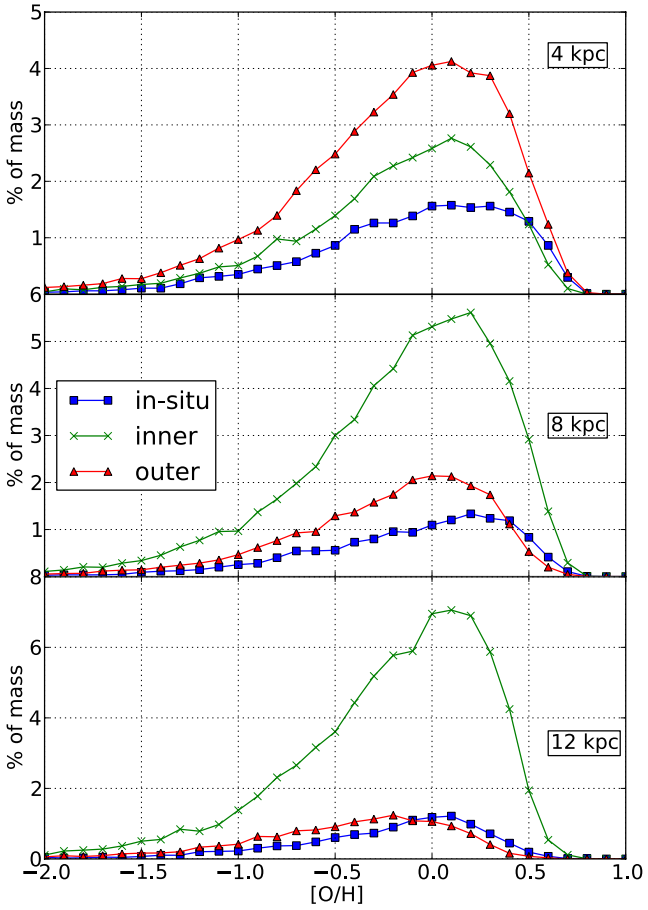

Figure 9. Contributions to the metallicity distributions of three radial zones ($R = 4$, 8 and 12 kpc, from top to bottom, and width $\Delta R = \pm 1$ kpc) from stars born in situ (squares and blue curves), coming from the inner galaxy (crosses and green curves) and from the outer galaxy (triangles and red curves). The width of the metallicity bins is 0.1 dex.

4.2 Metallicity distributions

As discussed in Roškar et al. (2008b), radial mixing reshuffles the metallicity distributions of stars across the disc. Our simulation shows clearly this effect, as can be seen in Fig. 9. In each one of the $\Delta R = 1$ kpc wide zones centred on 4, 8 and 12 kpc, respectively, stars born in situ constitute a minority at all metallicities. The stellar population at 4 kpc is dominated by stars from outer zones while those at 8 and 12 kpc are dominated by stars from the inner disc.

Due to the rapid metallicity evolution, stars originating in different regions and ending in the same zone cover the whole metallicity range but *differ little in their average metallicity*. The small differences in the peak metallicities are explained by the fact that all zones in our model evolve practically as closed boxes, since gas particles do not suffer significant radial displacement and there is no gaseous infall. In that case, the peak of the metallicity distribution corresponds to the stellar yield, which is fixed in the model. The largest differences occur in the zones at 8 and 12 kpc, where stars originating in the inner and the outer zones differ, on average, by 0.1 dex in metallicity. Combined to the fact that most of those stars are formed quite early (first 2 Gyr) and have enough time to migrate all over the disc, this produces a negligible change in the peak of the metallicity distribution.

For that same reason, the width of the metallicity distributions is barely modified between stars born in situ and all the stars found in a given zone, as can be seen by comparing the black solid curves between left- and right-hand panels in Fig. 10. On the other hand, radial mixing does change the ratio between young and old stars in a given region, as can be seen in that same figure: as one moves outwards, from 4 to 12 kpc, the fraction of 'young' stars (here defined as those younger than 7 Gyr) born in situ becomes more and more important with respect to the one of 'old stars' (older than 9 Gyr), because of the inside-out star formation; however, if all stars are considered, then 'young' stars are always a minority, even at 12 kpc (right-hand panels in Fig. 10), because most of star formation occurs in the first couple of Gyr in our model.

4.3 Evolution of abundance profiles

The shape of the abundance profiles of disc galaxies constitutes a key diagnostic tool of their evolution. It has been realized long ago, with simple (independent-ring) models, that the inside-out formation of discs produces generically profiles in the gas and young stars which flatten with time (Matteucci & Francois 1989; Prantzos & Aubert

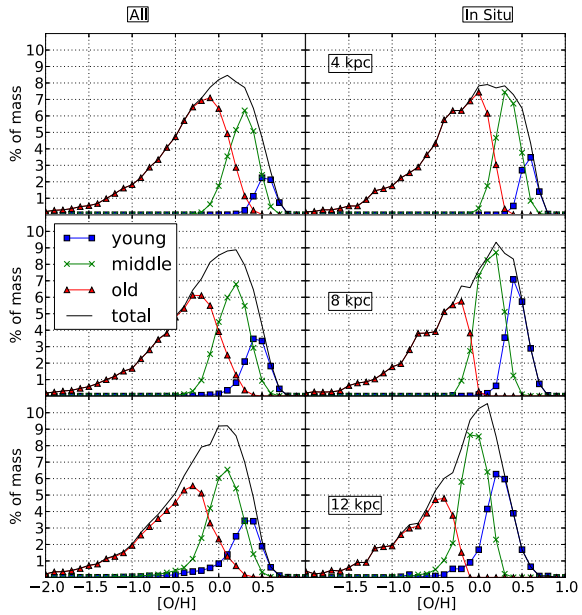

Figure 10. Metallicity distributions in three regions (of radius $R = 4, 8$ and 12 kpc, from top to bottom), for all the stars found in those zones (left) and for the stars born in situ (right). In each panel, three classes of stellar ages are displayed: 'young' (<7 Gyr, squares and blue curves), 'middle-aged' (7–9 Gyr, crosses and green curves) and 'old' (>9 Gyr, triangles and red curves); their sum (total metallicity distribution) is indicated by the black curves. The width of the metallicity bins is 0.1 dex.

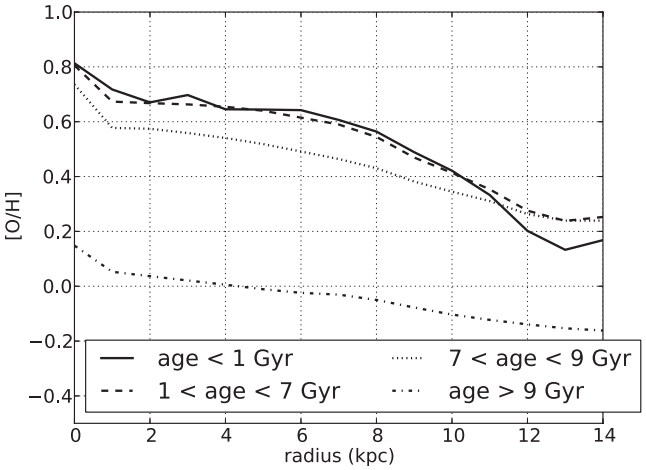

Figure 11. Abundance profiles of stars in various age bins. After radial mixing, profiles appear to be flatter for old stars, in contrast to what happens with the gaseous profiles.

1995; Boissier & Prantzos 1999; Hou, Prantzos & Boissier 2000). This was confirmed by chemo-dynamical simulations, e.g. Samland & Gerhard (2003). In a recent study comparing various codes of disc evolution for Milky Way type discs, Pilkington et al. 2012) find that (i) the gradient of oxygen may vary widely from one simulation to another, but in most cases it is substantially larger than observed in the Galaxy and (ii) in most cases, the oxygen profile flattens with time.

On the basis of such considerations, it was expected that observations of stars of various ages across the disc of the MW could reveal the shape of the abundance profile as a function of time allowing one to probe the evolution of that profile and thus to draw conclusions about the local history of star formation rate versus infall and/or radial inflows of gas. Although most studies of disc chemical evolution agree that profiles flatten with time, some models (e.g. Chiappini, Matteucci & Romano 2001) based on a different assumptions conclude that profiles steepen with time.

Such observations have been conducted over the years, using mostly planetary nebulae to trace the past evolution of abundance profiles. In particular, Maciel & Costa (2009) find that the abundance profile of oxygen flattens with time, thus supporting quantitatively the findings of Hou et al. (2000). However, Stanghellini & Haywood (2010) find the opposite trend, namely a steepening of oxygen profiles with time. It appears that the systematic uncertainties in ages and distances of those sources are so large at present that they do not allow for a robust evaluation of past abundance gradients. The situation may change in the future, with improvement in distance estimates and the use of proxies for the age, e.g. the [α/Fe] ratio (Cheng et al. 2012).

Roškar et al. (2008b) realized that one of the consequences of radial migration is to reduce and even inverse the abundance gradient of a stellar population across the galactic disc: an early steep gradient may be subsequently erased by migration of old stars towards the outer regions. Thus, even in the absence of any systematic uncertainties, abundance determinations in planetary nebulae would be of little help in revealing the past abundance profile of the disc.

We present in Fig. 11 our profiles in stars of various age bins. It can be seen that, contrary to Fig. 2, where the gas abundance profile systematically flattens with time, the stellar average abundance profile appears to be flatter for older stars. This confirms the finding of Roškar et al. (2008b) and implies that even accurate observations of present days abundance profiles of stars of various ages cannot reveal the past history of the true abundance profile of the disc.

We notice, however, that the implications of this finding are not totally negative because, *in the case of a monotonic evolution of the profile,* the true abundance gradient of a stellar population at the time of its formation *should have been steeper than observed today* (since radial migration always flattens it). If the presently observed abundance profile of old stars is steeper than the one of the gas (as claimed by e.g. Maciel & Costa 2009), then it can be safely inferred that the disc evolved from a steeper to a flatter profile. This is by itself an important conclusion, albeit in a qualitative level.

The strong early star formation of our disc galaxy leads to small early-abundance gradients and thus minimizes the effects of radial migration, despite the fact that the stars have time enough (8 Gyr, on average) to migrate. Thus, the average metallicity profile of stars after the first 2 Gyr (which constitute about 90 per cent of all stars) in our simulation has a slope of $\mathrm{d}\log Z/\mathrm{d}R = -0.03$ dex kpc^{-1}. At the end of the simulation (10 Gyr), those same stars display a slope of -0.02 dex kpc^{-1}, i.e. radial migration has modified the slope of the abundance profile by only -0.01 dex kpc^{-1}.

In order to evaluate the effect of a steep initial metallicity profile (while keeping the same dynamical evolution), we imposed an artificial gradient of -0.08 dex kpc^{-1} to all stars formed in the first 2 Gyr and we assumed that the disc evolved exactly as in our simulation. The results appear in Fig. 12 (top panel) and are compared to those of the original simulation (bottom panel). It can be seen that the slope of the final abundance profile is of -0.04 dex kpc^{-1}, i.e. the same amount of radial migration modified the slope by -0.04 dex kpc^{-1}, instead of -0.01 dex kpc^{-1} in the original simulation. We conclude that the effect of radial migration on the final abundance profile of stars depends not only on the strength of the

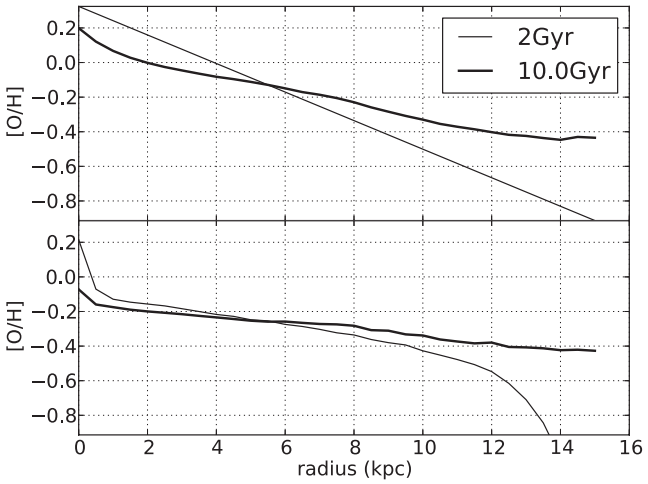

Figure 12. Evolution of the stellar metallicity gradient in the case of our simulation (bottom) and of the same simulation with an imposed initial gradient of -0.08 dex kpc^{-1} (top). The stellar population after time $t = 2$ Gyr is displayed with thin curves in both panels; that same population, at the end of the simulation (i.e. aged of 8 Gyr) appears in thick curves.

various churning mechanisms, but also on the overall history of the disc (star formation versus infall and resulting chemical evolution).

4.4 Azimuthal variations of metallicity

The question of azimuthal variations in either the gaseous or stellar metallicity of a disc galaxy has been addressed by various authors either from the observational (Li, Bresolin & Kennicutt 2013, and references therein) or from the theoretical point of view, e.g. Di Matteo et al. (2013) and references therein. In particular, Di Matteo et al. (2013) explored the possibility of azimuthal variations in old star composition as signatures of radial migration, in the case of a barred galaxy. In their controlled experiment (*N*-body with the SPH part switched off, i.e. no star formation) they imposed initial metallicity profiles and studied the azimuthal distribution of star particles after 4 Gyr. They found azimuthal metallicity variations depending on the initial metallicity profile and persisting during the whole period of bar activity.

Our results concerning the azimuthal metallicity of gas and stars are displayed in Fig. 13. It can be seen that in early times azimuthal variations are small in both gas and stars (0.1 dex at maximum). At late times, as the bar corotation moves outwards, metal poor gas is driven inwards from the outer disc, creating local azimuthal variations of up to 0.3 dex (a factor of 2) in the gas metallicity at 12 kpc. As already discussed for Fig. 2, this important gas inflow reduces the average radial metallicity of gas in the outer disc. However, the bulk of the stellar population in all radii is formed in early times and despite substantial radial migration it shows no significant azimuthal variations in its metallicity, because the metallicity gradient is always small. If a steep metallicity profile is imposed (as in Fig. 12) stronger azimuthal variations in the stellar population are obtained, but they never exceed the corresponding variations in the gas metallicity.

We notice that important azimuthal variations in the gas metallicity can also be obtained in the case of local infall of metal-poor gas (infall is not included in our simulation). In an analogous way, a merger with a metal-poor satellite could also create azimuthal variations in the stellar metallicity. For those reasons, it appears

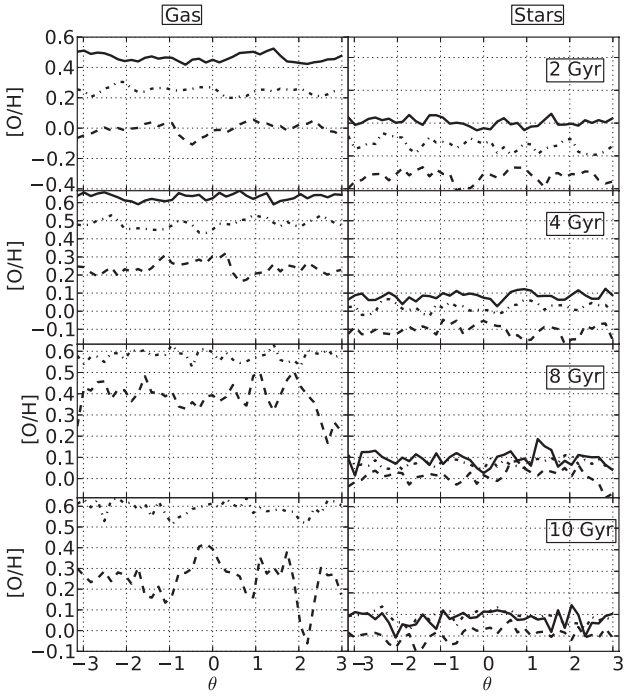

Figure 13. Azimuthal variations of metallicity in four different times (2, 4, 8 and 10 Gyr, from top to bottom) and in three different galactocentric distances: 4, 8 and 12 kpc (solid, dotted, dashed, respectively), for the gas (left) and for the stars (right).

that azimuthal variations of metallicity in either gas or stars do not provide unambiguous information about radial migration.

5 CHEMICAL POST-PROCESSING AND THE IMPLICATIONS OF NON-IRA

As discussed in Section 4, the analysis of the chemical evolution part of our simulation is limited by the use of IRA and of a single metal. Here, we show that it is possible to overcome this limit and gain considerable more insight, by post-processing the evolution of the simulated disc with a simple, classical model of galactic chemical evolution including a much more elaborated chemistry. In this section, we first establish a parametrized description of the churning+blurring processes in the disc of our simulation. We then implement it in a classical chemical evolution model for that same galaxy, first with IRA, in order to check whether the results of the numerical simulation – which uses IRA – are satisfactorily reproduced. We show that this is indeed the case. We drop then the IRA and run the same model by introducing more chemical elements and, in particular, Fe from SNIa. This procedure allows one to exploit in detail the chemical evolution of the system (by introducing more metal sources or different prescriptions for the rates for e.g. SNIa), once the successful description of churning+blurring through a parametrized scheme is established.

5.1 Parametrization of churning+blurring

Up to now, two different types of parametrization of radial mixing have been introduced in the literature. SB02 adopted a global mixing scheme, in which one assumes that a star born at radius R_0 at time t may be found at time t_0 (i.e. after time $\tau = t_0 - t$) in radius R_f with

a probability $P(R_0, R_i, \tau)$ given by a Gaussian function

$$P(R_\mathrm{f}, R_O, \tau) = \left(2\pi\sigma_\tau^2\right)^{-1/2} \exp\left(-\frac{(R_\mathrm{f} - R_0)^2}{2\sigma_\tau^2}\right), \quad (3)$$

where σ_τ is the 1σ dispersion in the radial displacement of the particles from their birth place R_0 after time τ. SB02 adopt, for illustration purposes an expression for σ_τ which includes two terms accounting for churning and blurring, respectively; notice that their term for churning is not symmetric with respect to particle exchange (i.e. it depends explicitly on R_0) but this does not have to be generically the case.

On the other hand, Schönrich & Binney (2009) treat separately blurring and churning. For the former, they make some assumptions about the radial dependence of the radial velocity dispersion of stars. For the latter, they adopt a local scheme, in which only stars from second-nearest neighbouring zones can exchange places during a time-step, with a probability adjusted to reproduce some observables in the solar neighbourhood, such as the metallicity distribution. According to their scheme, not only stars but also cold gas (molecular) is affected by churning. However, it seems improbable that gas – which is dissipative – behaves as the collisionless fluid of stars. Furthermore, molecular gas is bound in molecular clouds with lifetimes of only 10^7 yr, i.e. too short for any appreciable radial displacement. The results of our numerical simulations support these considerations, as discussed in Section 3 (see also Fig. 5), so we shall ignore here any radial migration of gas particles; we shall see that this approximation is valid for most of the disc, but not inside the bar, which drives rapidly gas towards the central regions.

In this work, we adopt an approach similar to the one of SB02, since their parametrization is supported by the analysis of numerical simulations by Brunetti et al. (2011) who analysed a star-only controlled simulation performed with the GADGET-2 code. Although they had no gas or star formation in their simulation, their conditions are not very different from ours, since in our case star formation occurs essentially in the first couple of Gyr. Brunetti et al. (2011) found that the radial displacement of stars in their simulation can be described by Gaussian functions simulating a diffusion process. They caution that modelling the stellar migration as a diffusion process is valid only for time intervals less than the diffusion time-scale, which they estimate from the simulation results to be of the same order as the rotation period. In other terms, radial migration can be described as a diffusion process with diffusion coefficients depending both on time and (original) position.

We first follow the positions of all the stars of the numerical simulation born at a given radius R_0 as a function of time. As displayed in Fig. 14 those stars are found at later times t at various positions R_t. The distributions of particles as a function of the position can be approximated by Gaussians with widths generally increasing as a function of time. Similar behaviour characterizes the radial positions of stars born in that same radius R_0 at later times or at different original radii. By constructing a sufficiently dense grid in R_0 and t, we find that the evolution of the radial dispersion of stars can be described by expressions similar to the one of equation (3), where the widths are given by

$$\sigma_\tau(R_0) = a(R_0)\tau^N + b(R_0). \quad (4)$$

Our fitting procedure produces values of N in a narrow range $N = 0.4$–0.5 at all radii and we fixed here $N = 0.5$. Using a least square method, we get the values of $a(R_0)$ and $b(R_0)$ at each radius R_0:

$$a(R_0) = -6.67e^{-2}R_0 + 2.75, \quad (5)$$

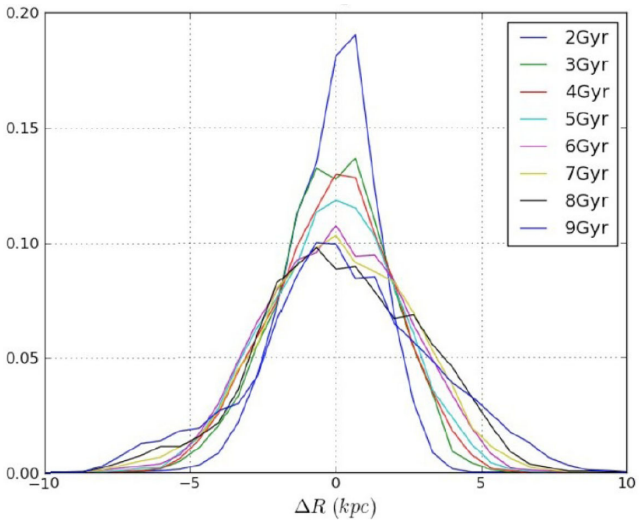

Figure 14. Radial positions of particles born at radius $R_0 = 8$ kpc between 0 and 1 Gyr after times τ spanning the range of 2 to 9 Gyr.

$$b(R_0) = -2.26e^{-1}R_0 + 2.71. \quad (6)$$

We implement this description of radial migration in a 1D code of chemical evolution with independently evolving annuli (Boissier & Prantzos 1999). The initial configuration contains a dark matter halo of 10^{12} M$_\odot$ with an NFW profile and a gaseous disc of 5×10^{10} M$_\odot$ with an exponential scalelength of 2.7 kpc, i.e. the same initial conditions as the N-body+SPH simulation. The disc annuli evolve as closed boxes, assuming azimuthal symmetry and IRA. The local star formation rate is assumed to be $\Psi(R, t) = \nu \frac{V}{R} \Sigma_\mathrm{Gas}^{1.5}$, with ν adjusted as to reproduce the final gas profile of the simulation. During a time-step dt a mass of stars $m_S(R_0, t) = \Psi(R_0, t)\,\mathrm{d}t$ is created at radius R_0. In subsequent time-steps, that mass undergoes radial migration to other zones R according to the adopted probabilistic description of equations 3 and 4. Obviously, if the final profiles of gas, gas metallicity and SFR of the 1D simulation match the corresponding final profiles of the N-body+SPH simulation, the chemical evolution part of the former simulation can be considered as a successful description of the latter. And if the final profiles of stars and stellar metallicity *as well as* the initial versus final radii of the two simulations match each other, then the adopted probabilistic description scheme can be considered as a successful description of the radial migration obtained by the N-body code.

The results of our 1D calculation appear in Fig. 15, where they are compared with those of the N-body+SPH simulation. It can be seen that, the final profiles of gas and star formation are reasonably well reproduced by the parametrized simulation, albeit with a sizeable difference in the bar region (from 2 to 6 kpc). The reason for that discrepancy is that we do not consider any radial motion of the gas, an approximation which accounts well for the relation of R_0 versus R_f of gas particles in most of the disc (see Fig. 5), but not in the region of the bar, which drives gas inwards. This also accounts for the small discrepancy of the final SFR observed in that same region. The metallicity of the gas is well reproduced over the whole disc.

The aforementioned features are obtained in the independent ring approximation adopted for the gas. The results for the final profiles of stars, stellar metallicity and colour depend also on the adopted prescription for radial migration. In Fig. 15, it is seen that over a 12 kpc region (from 3 to 15 kpc) the curves of the average initial

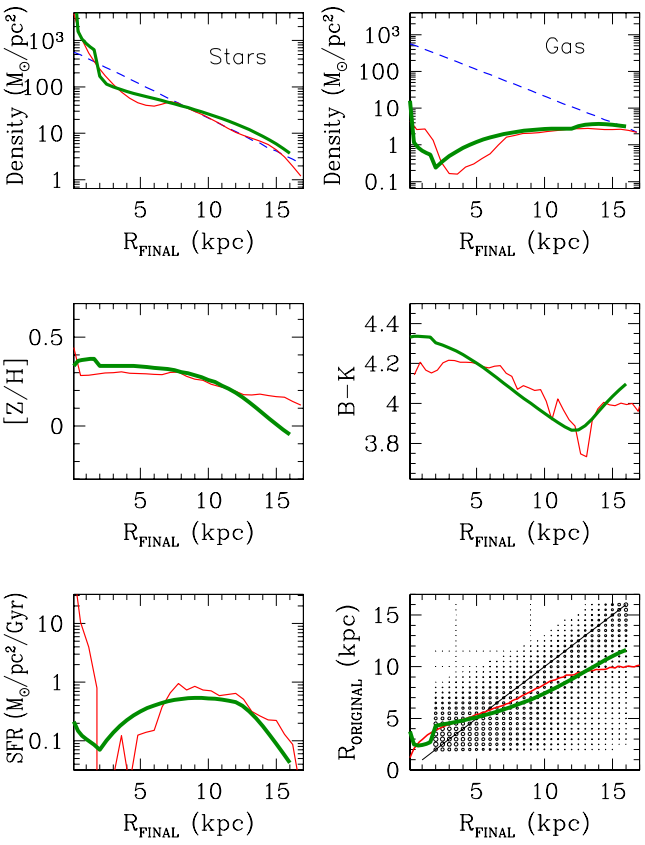

Figure 15. Results of the 1D chemical evolution model with IRA and parametrized description of the radial migration, as developed in Section 5.1, compared to those of the *N*-body+SPH calculation. In all panels, *thin curves* correspond to final profiles (at 10 Gyr) obtained with GADGET and *thick curves* to corresponding profiles obtained with the parametrized description and the semi-analytical model. Top left: stellar surface density and top right: gas surface density; in both panels the *dashed curve* corresponds to the initial gaseous profile of the disc. Middle left: metallicity profile; middle right: $B-K$ colour profile. Bottom left: star formation rate profile. Bottom right: birth radius versus final radius for all star particles (to compare with Fig. 3).

R_0 versus final R_f radius of the stars between the two simulations differ by an amount smaller than the difference between R_0 and R_f in the *N*-body+SPH simulation (a difference which reaches almost 5 kpc in the outer disc). This suggests that the adopted description of radial migration manages to reproduce reasonably well the effect. Furthermore, the final profiles of average stellar metallicity and $B-K$ colour are also well reproduced; in particular, we obtain the upturn of $B-K$ around 13 kpc, as in the *N*-body+SPH simulation. Taking into account the extreme simplicity of our formula (using Gaussian functions with a regular time dependence, while the true situation is more complicated), we consider the overall result as fairly successful.

In summary, we have shown that a simple model of galactic chemical evolution, augmented with a simplified description of radial migration a la SB02, can reproduce fairly satisfactorily the results of a full *N*-body+SPH calculation, once the diffusion coefficients have been determined from the latter simulation. This opens the way for realistic post-processing of *N*-body simulations, with simple chemical evolution models including many more chemical elements and nucleosynthetic sources (that were neglected in the *N*-body simulation). For instance, one may consider other elements than the single case of oxygen considered here, like e.g. Fe from both core collapse and thermonuclear supernovae; it is also possible to study the evolution of the system dropping IRA and considering the finite lifetimes of stars, allowing one to consider the evolution of s-elements or deuterium. We illustrate some of those possibilities in the next section.

5.2 Implications for chemical evolution

We run the same model as in the previous section, considering the finite lifetimes of stars as well as Fe from SNIa. We adopt the stellar lifetimes of Schaller et al. (1992), the stellar yields Woosley & Weaver (1995) and the prescription of Greggio (2005) for the rate of SNIa, which accounts for single degenerate dwarves as progenitors of those objects; each SNIa is assumed to eject 0.7 $M_\odot$ of Fe. We run the model twice: a first time without radial migration (i.e. assuming independent annuli) and a second time with radial migration.

The results of the two simulations are compared in Fig. 16, which displays the final radial profiles of various quantities obtained with radial migration *divided by* the corresponding profiles obtained without radial migration.

A first effect concerns the rate of mass ejection from long-lived sources (top-right panel). Radial migration depopulates the inner disc and populates the outer one with long-lived (low-mass) stars. In the absence of radial migration the long-lived stars return lately a considerable amount of gas in the inner disc, where little gas is left and; with radial migration, a fraction of them does not return that mass in their birth place, but in the outer disc, where they migrate. However, the impact is not the same in the final gaseous profile of the inner and outer disc (top-middle panel): in the inner disc, almost the totality of the gas is depleted early on from star formation, and

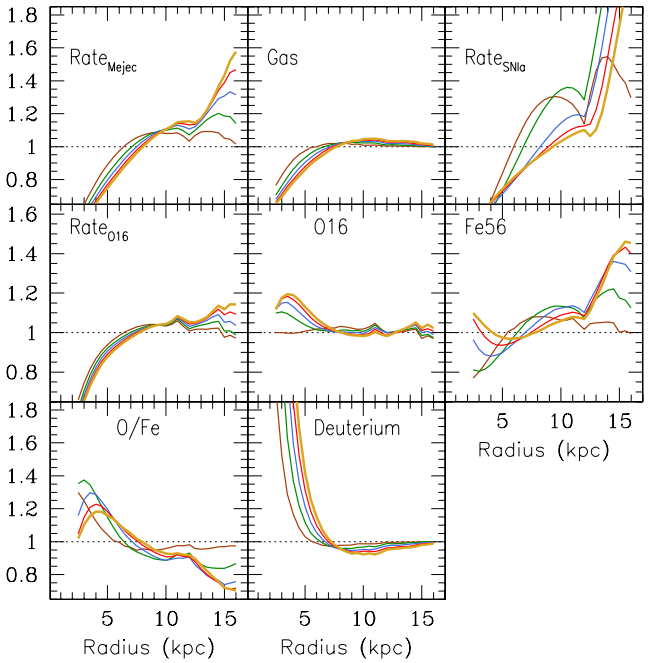

Figure 16. Radial profiles of various quantities obtained with radial migration *divided by* the corresponding profiles obtained without radial migration. Calculations are performed without IRA and results are displayed every two Gyr, the thickest curves corresponding to the final profiles at 10 Gyr. First row: rate of mass ejection by stars, gas surface density and rate of SNIa. Second row: rate of mass ejection of O-16 and gas abundance profiles of O-16 and Fe-56. Third row: gas profiles of O/Fe ratio and deuterium.

the gas non-returned from the migrated stars is a large fraction of it; radial migration reduces the surface density of gas in the inner disc. In contrast, in the outer disc, little of the initial gas is consumed. The supplementary gas brought by the ejecta of migrated stars barely changes the overall surface density there.

The rate of oxygen ejection (middle-left panel) behaves in a similar way to the rate of gas ejection (upper-left panel), albeit for a non-intuitive reason: in the case of a strong early star formation (as in this simulation), most of oxygen is released at late times not by massive stars but by the numerous intermediate and low-mass stars formed early on, which simply release their initial oxygen (their net yield being zero, there is no chemical enrichment). In the inner regions, some of those stars are missing because of radial migration, hence less oxygen is released lately. The opposite holds for the outer regions. However, those considerations do not impact on the oxygen profile, because only the massive stars (which do not have time to migrate) enrich the local ISM with oxygen: in the inner disc radial migration reduces the local gas amount (see top middle panel and previous paragraph), and the dilution of the same oxygen mass in a smaller gas amount results in a larger oxygen abundance, by ∼20 per cent. The effect is negligible in the outer disc.

SNIa produce a large fraction of iron in a galaxy, from one to two thirds, depending on the assumed prescription for their rate. In our case, radial migration removes a large fraction of SNIa from the inner disc and brings them in the outer disc (top right). The effect on the Fe abundance profile is straightforward in the outer disc, where Fe mass fraction is found to be ∼40 per cent larger with radial migration. In the inner disc it is negligible: the missing Fe from migrated SNIa is compensated in those regions by the effect of the Fe ejected from massive star explosions being diluted in less gas (see previous paragraph for oxygen).

The effects analysed in the previous paragraphs are summarized in the bottom-left panel, displaying the O/Fe ratio: radial migration of long-lived stars (including SNIa) makes the O/Fe ratio larger in the inner disc (by up to 20 per cent) and smaller in the outer one (by 30 per cent). Overall, it introduces a ∼50 per cent difference between the O/Fe ratios at 5 and 15 kpc; this corresponds to an increase of $\sim 0.02\,\mathrm{dex\,kpc^{-1}}$ in the radial gradient of [O/Fe] in the gaseous phase.

Finally, in the bottom-middle panel we display an interesting effect concerning the abundance of deuterium. Deuterium is produced only in the big bang, it is only destroyed when passing in stellar interiors (a process called astration) and most of it is astrated in the numerous low and intermediate-mass stars; as a result, its abundance is steadily reduced in chemical evolution. Radial migration removes a fraction of those stars from the inner disc, hence the abundance of D in the gas of those regions is not depleted as much as in the case of no migration but remains much higher, by up to 80 per cent. In the outer disc, the D-free gas released by the migrators has little effect, because there are considerable amounts of the initial gas, which has not been consumed by star formation. We then find that, overall, radial migration introduces an increase in the absolute value of the D gradient of $\sim 0.025\,\mathrm{dex\,kpc^{-1}}$.

6 SUMMARY

In this work, we study the effect of radial migration on the chemical evolution of a bar-dominated disc galaxy, by analysing an *N*-body+SPH simulation and using appropriately tuned semi-analytical models.

We find that the non-dissipative fluid of stars behaves differently from the dissipative fluid of gas regarding radial migration (Section 3): stars experience strong radial migration over the whole disc, while gas remains (on average) near its initial radius in the disc; however, in the inner galaxy, the bar transfers large amounts of gas to the central regions, affecting considerably the evolution of the developing bar/bulge. Here, we focus on radial migration of stars in the disc, leaving the evolution of the bulge for a future study. By 'radial migration' we mean here all types of radial displacement of stars, moving them away from their place of birth.

We studied the impact of radial migration on various aspects of the chemical evolution of the disc (Section 4), although our study was hampered by the use of the IRA and of a single metal (oxygen). Radial migration increases the stellar metallicity dispersion in all zones and all ages, but other factors contribute to that dispersion as well, namely the metallicity variations in the gas, due to incomplete mixing. Because of the rapid evolution in all the model zones, metallicity distributions differ little from one zone to another (their peak being close to the stellar yield), and radial migration does not change that result. On the other hand, radial migration flattens the metallicity profiles, bringing metal-poor stars from the outer to the inner (metal-rich) zones and metal-rich stars from the inner to the outer (metal-poor) zones. Because of that mixing, abundance profiles of old stellar populations of a given age appear flatter from what they were at the period of stellar birth; as a consequence, their observation cannot be used to infer the true evolution of the abundance profile. The extent of that effect, however, depends a lot on the metallicity profile of the disc: if it is relatively flat at the stars' birth, the effect will be negligible, but if it is quite steep, radial migration may not completely erase that signature. The same holds for azimuthal variations in the metallicities of gas and stars. We argue that such variations are not a safe diagnostics for radial migration, since they may have other origins (local infall of metal-poor gas or a metal-poor merger). Finally, we obtain a U-shaped colour profile, with old and red stars migrated from the inner to the outer disc (as already found in Roškar et al. 2008a).

Because of the limitations on chemical evolution imposed by the IRA adopted in the *N*-body+SPH simulation, we also studied the effects of radial migration on chemical evolution by adopting a different strategy. We have shown (Section 5) that those effects can be studied to a good accuracy by post-processing the results of a full *N*-body+SPH calculation with a simple chemical evolution model having detailed chemistry and a parametrized description of radial migration. A somewhat different coupling between an *N*-body+SPH code and a semi-analytical code of chemical evolution was recently performed by Minchev, Chiappini & Martig (2013), for the case of the Milky Way disk. We found that radial migration impacts on chemical evolution both indirectly (by affecting the age–metallicity relations and metallicity distributions of stars moved across the disc) and directly, by moving around the long-lived nucleosynthesis sources [SNIa or asymptotic giant branch (AGB) stars of $1.5\,\mathrm{M_\odot}$] and thus altering the abundance profiles of the gas; here (Section 5), we have shown how the radial profiles of O, Fe and D are affected in the case of our simulation, but other elements (like e.g. s-process elements produced in AGB stars) may be concerned as well. Our post-processing results show clearly that the full impact of radial migration on chemical evolution cannot be evaluated with numerical codes using IRA.

It should be stressed, however, that the impact of radial migration on chemical evolution depends on the system under study. Three factors have been identified up to now: strength of inhomogeneities in the gravitational potential, e.g. bar or spiral arms (stronger perturbations favouring larger effects); duration of the radial migration (the longer the bar acts, the larger the effects); and steepness

of abundance profiles at the time most of the stars are formed (steeper profiles favouring larger effects). Those factors may cancel each other and mask the effects of radial migration on chemical evolution: for instance, a strong bar driving metal-poor gas inwards will flatten the metallicity profile; the stars created from that gas will display quasi-similar abundances all over the disc, even in the case of strong radial migration.

This corresponds to the simulation studied here, although the reason for the flat early metallicity profile is the evolution as a closed box with a rapid early star formation. In the case of a galaxy evolving more slowly inside-out, steeper metallicity profiles are expected; however in that case, there is less time left to an average star for radial migration, so its impact on chemical evolution will not necessarily be more important. Notice that continuous infall of low metallicity gas, as expected in a galaxy like the Milky Way, should also attenuate the impact of radial migration on gas chemistry, by diluting radial abundance variations.

ACKNOWLEDGEMENTS

EA acknowledges financial support by the CNES and by the European Commission through the DAGAL Network (PITN-GA-2011-289313). We are grateful to the referee for his/her thorough and constructive report.

REFERENCES

Asplund M., Grevesse N., Sauval A. J., Scott P., 2009, ARA&A, 47, 481
Athanassoula E., 1992, MNRAS, 259, 345
Athanassoula E., 2012, MNRAS, 426, L46
Athanassoula E., Machado R. E. G., Rodionov S. A., 2013, MNRAS, 429, 1949
Bakos J., Trujillo I., Azzollini R., Beckman J. E., Pohlen M., 2011, Mem. Soc. Astron. Ital. Suppl., 18, 113
Bekki K., Tsujimoto T., 2011, ApJ, 738, 4
Binney J., Tremaine S., 2008, Galactic Dynamics, 2nd edn. Princeton Univ. Press, Princeton, NJ
Boissier S., Prantzos N., 1999, MNRAS, 307, 857
Bournaud F., Elmegreen B. G., Martig M., 2009, ApJ, 707, L1
Bovy J., Rix H.-W., Hogg D. W., 2012, ApJ, 751, 131
Brook C. B. et al., 2012, MNRAS, 426, 690
Brunetti M., Chiappini C., Pfenniger D., 2011, A&A, 534, A75
Buta R., 1995, ApJS, 98, 739
Cheng J. Y. et al., 2012, ApJ, 752, 51
Chiappini C., Matteucci F., Romano D., 2001, ApJ, 554, 1044
Comparetta J., Quillen A. C., 2012, preprint (arXiv:1207.5753)
Di Matteo P., Haywood M., Combes F., Semelin B., Snaith O. N., 2013, A&A, 553, A102
Edvardsson B., Andersen J., Gustafsson B., Lambert D. L., Nissen P. E., Tomkin J., 1993, A&A, 275, 101
Forbes J., Krumholz M., Burkert A., 2012, ApJ, 754, 48
Grand R. J. J., Kawata D., Cropper M., 2012a, MNRAS, 421, 1529
Grand R. J. J., Kawata D., Cropper M., 2012b, MNRAS, 426, 167
Greggio L., 2005, A&A, 441, 1055
Haywood M., 2012, in Reyl C., Robin A., Schultheis M., eds, EPJ Web Conf., Vol. 19, Assembling the Puzzle of the Milky Way. EDP Sciences, Les Ulis, id. 05001
Holmberg J., Nordström B., Andersen J., 2009, A&A, 501, 941
Hou J. L., Prantzos N., Boissier S., 2000, A&A, 362, 921
Lépine J. R. D., Acharova I. A., Mishurov Y. N., 2003, ApJ, 589, 210
Li Y., Bresolin F., Kennicutt R. C., Jr, 2013, ApJ, 766, 17
Loebman S. R., Roškar R., Debattista V. P., Ivezić Ž., Quinn T. R., Wadsley J., 2011, ApJ, 737, 8
Luck R. E., Lambert D. L., 2011, AJ, 142, 136
Maciel W. J., Costa R. D. D., 2009, in Andersen J., Nordström B., Bland-Hawthorn J., eds, Proc. IAU Symp. 254, Abundance Gradients in the Galactic Disk: Space and Time Variations. Cambridge Univ. Press, Cambridge, p. 38P
Matteucci F., Francois P., 1989, MNRAS, 239, 885
Minchev I., Famaey B., 2010, ApJ, 722, 112
Minchev I., Chiappini C., Martig M., 2013, preprint (arXiv:1208.1506)
Minchev I., Famaey B., Quillen A. C., Dehnen W., Martig M., Siebert A., 2012, A&A, 548, A127
Nieva M.-F., Przybilla N., 2012, A&A, 539, A143
Pilkington K. et al., 2012, MNRAS, 425, 969
Prantzos N., 2009, in Andersen J., Nordström B., Bland-Hawthorn J., eds, Proc. IAU Symp. 254, On the Chemical Evolution of the Milky Way. Cambridge Univ. Press, Cambridge, p. 381
Prantzos N., Aubert O., 1995, A&A, 302, 69
Roberts W. W., Jr, Huntley J. M., van Albada G. D., 1979, ApJ, 233, 67
Roškar R., Debattista V. P., Stinson G. S., Quinn T. R., Kaufmann T., Wadsley J., 2008a, ApJ, 675, L65
Roškar R., Debattista V. P., Quinn T. R., Stinson G. S., Wadsley J., 2008b, ApJ, 684, L79
Samland M., Gerhard O. E., 2003, A&A, 399, 961
Sánchez-Blázquez P., Courty S., Gibson B. K., Brook C. B., 2009, MNRAS, 398, 591
Schaller G., Schaerer D., Meynet G., Maeder A., 1992, A&AS, 96, 269
Schönrich R., Binney J., 2009, MNRAS, 396, 203
Sellwood J., Binney J., 2002, MNRAS, 336, 785 (SB02)
Shevchenko I. I., 2011, ApJ, 733, 39
Springel V., Hernquist L., 2003, MNRAS, 339, 289
Stanghellini L., Haywood M., 2010, ApJ, 714, 1096
Steinmetz M., 2012, Astron. Nachr., 333, 523
Wielen R., Fuchs B., Dettbarn C., 1996, A&A, 314, 438
Woosley S. E., Weaver T. A., 1995, ApJS, 101, 181

This paper has been typeset from a TEX/LATEX file prepared by the author.

3.2 Un modèle de la Voie Lactée avec migration radiale

De par la position que nous occupons dans la Voie Lactée (VL), cette galaxie offre des observations détaillées d'un grand nombre de propriétés galactiques, qui nous sont inaccessibles lorsque nous observons les autres galaxies. Des informations sur la composition chimique et la cinématique sont maintenant disponibles pour quelques milliers d'étoiles d'âges divers, à la fois dans le voisinage solaire, le long du disque Galactique, et en fonction de l'éloignement au plan de la Galaxie. Nous avons également un grand nombre de données concernant le contenu en gaz de la VL (ces composantes atomique et moléculaire, et sa composition chimique) en fonction du rayon galactocentrique. Par ailleurs, le satellite Gaia (lancé le 19 décembre 2013) offrira d'ici environ 5 ans, une encore plus grande quantité de données sur les étoiles, couvrant un rayon d'environ 8 kpc autour du Soleil. Ces données permettront d'étudier l'évolution des propriétés de la VL avec une précision largement améliorée.

Cette abondance de données, combinée avec les indices suggérant que la VL à évolué sans perturbation majeure durant environ les 8 derniers milliards d'années (e.g. Hammer et al., 2007, et références dans cet article), font de notre galaxie un laboratoire idéal pour tester les théories de l'évolution des galaxies. Cependant, les modèles actuels (N-corps+SPH dans le cadre ΛCDM) ont des difficultés à produire des disques de type tardif, e.g. Silk & Mamon (2012) et références dans cet article. Malgré un effort théorique intense et des propositions diverses de solution – basées sur un seuil de formation stellaire (Guedes et al., 2011) ou sur le feedback des étoiles (Übler et al., 2014) – aucun paradigme généralement accepté n'a émergé pour le moment.

Les propriétés chimiques de la Voie Lactée (relation âge-métallicité locale, distribution en métallicité locale, ratio d'abondance vs métallicité, profils d'abondance le long du disque) ont été largement étudiées longtemps avant l'arrivée des simulations numériques à grandes échelles. Ces études étaient réalisées à l'aide de modèles semi-analytiques simples, soit pour le voisinage solaire, soit pour le disque complet (avec des modèles en "anneaux indépendants") et ont révélé certains aspects clés de l'évolution chimique de la VL : le besoin d'une source supplémentaire de Fe, les SNIa, pour reproduire la diminution observée de O/Fe en fonction de la métallicité ; le besoin d'une accrétion de gaz dès les premiers temps de la Galaxie et pendant de longues périodes, pour reproduire la partie précoce de la distribution en métallicité des naines G, ainsi que la grande abondance du Deutérium aujourd'hui ; le besoin d'une variation, en fonction du rayon, de l'efficacité de la formation stellaire, afin de reproduire les gradients observés dans les profils radiaux d'abondance (e.g. Pagel, 2009; Matteucci, 2012). Ces résultats sont robustes qualitativement, mais pas quantitativement, à cause des larges incertitudes de mesures dans les données observationnelles (e.g. dispersion dans la relation âge-métallicité, forme de la distribution en métallicité), et aussi à cause des courants radiaux de gaz, dont le rôle encore mal compris. Bien qu'ils soient bien justifiés par la physique (e.g. Lacey & Fall, 1985), il n'a jamais été montré que les courants radiaux jouent un rôle important dans l'évolution chimique de la VL, à cause de l'impossibilité d'observer ou bien de déduire de la théorie les profils de vitesse de ces courants dans la Galaxie.

En interagissant avec la barre le gaz peut se déplacer radialement, et il en est de même pour les étoiles. Les effets de la migration radiale sur les profils d'abondance ont été étudiés, dans une certaine mesure, à l'aide de simulations N-corps+SPH par Friedli & Benz (1993) et Friedli, Benz & Kennicutt (1994). Dans les années 90, les observations ont révélé que la Voie Lactée a bien une barre centrale (Blitz & Spergel, 1991), mais sont origine, sa taille, et son âge ne sont toujours pas bien connus aujourd'hui. Par conséquent, son impact sur l'évolution chimique de la VL est difficile à évaluer quantitativement.

3.2.1 Ingrédients du modèle

Dans ce travail, nous présentons donc un modèle d'évolution de la Voie Lactée, incluant les mouvements radiaux du gaz et des étoiles. Dans notre modèle, la Voie Lactée est construite graduellement par accrétion de gaz primordial dans le potentiel gravitationnel d'un halo de matière noire "typique", de masse finale $10^{12} M_{\odot}$. L'évolution de ce halo est extraite de simulations cosmologiques ΛCDM produites par Li et al. (2007).

Les éléments caractéristiques de notre modèle sont :

- Pour le taux de formation stellaire (TFS) nous utilisons une prescription dépendante de la densité surfacique locale du gaz moléculaire. Cette prescription est issue de l'analyse de plusieurs jeux de données observationnelles concernant à la fois la formation stellaire aux grandes échelles (de l'ordre du kpc) et aux petites échelles (<1 kpc) (Krumholz, 2014). Nous calculons la densité de H_2 à l'aide des prescriptions semi-empiriques de Blitz & Rosolowsky (2006). Cette prescription est utilisée pour la première fois dans un modèle d'évolution de la Voie Lactée, les autres modèles utilisant majoritairement la loi de Schmidt-Kennicutt $\Psi \propto \Sigma_G^k$ où le taux de formation stellaire dépend de la densité surfacique du gaz total (HI+H2) avec $k = 1.5$. D'autres modèles ont exploré différentes possibilités (e.g. Boissier & Prantzos, 1999; Chiappini, Matteucci & Romano, 2001), que nous comparons aux observations de traceurs du TFS dans la Fig. 3.5 (panneaux du milieu et du bas). Nous constatons que le TFS dépendant de la densité surfacique du gaz moléculaire (courbes bleues) est celui qui coïncide le mieux avec les observations entre 3 et 13 kpc, avec la prescription adoptée par Chiappini, Matteucci & Romano (2001) (courbes vertes).
- Nous introduisons une prescription pour les courants radiaux de gaz, pour lesquels nous considérons le cas d'une barre similaire à celle de la Voie Lactée opérant pendant les derniers 4 Gyr, qui déplace le gaz vers vers l'intérieur et vers l'extérieur de la corotation avec la barre.
- Pour la migration radiale, nous considérons séparément les mouvements épicycliques des étoiles (le blurring) et les variations du rayon de l'orbite guide (churning). Notre traitement de la migration radiale est un mélange de différentes techniques utilisées dans divers articles. Comme dans Sellwood & Binney (2002) et Schönrich & Binney (2009) – mais contrairement à Minchev, Chiappini & Martig (2013, 2014) ou Kubryk,

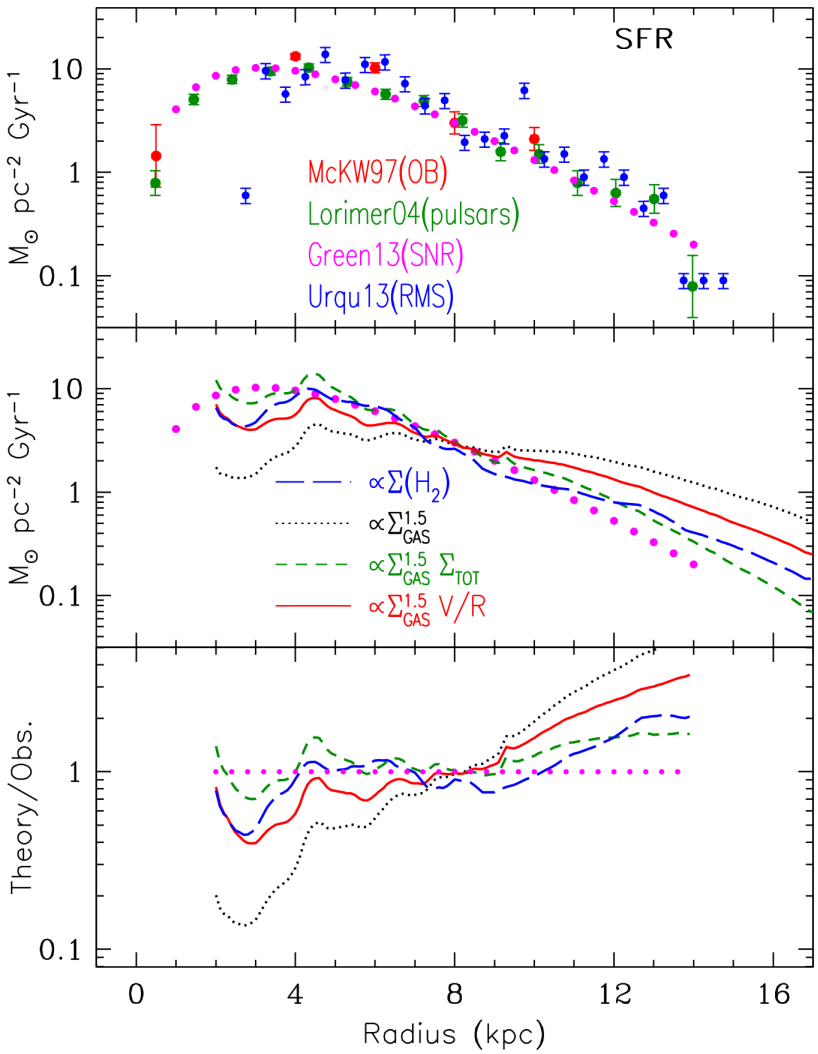

FIGURE 3.5 – **En haut** : profils de densité surfacique de divers traceurs du taux de formation stellaire (TFS) ; la courbe en points – sans barre d'erreur – est la forme analytique de Green (2014) issue de l'observation des rémanents de super novae, que nous considérons représentative du profil du TFS dans la VL. **Au milieu** : TFS théoriques ou empiriques comparés au profil des traceurs du TFS dans la VL (la courbe en point dans le panneau du haut). La l'expression des TFS est indiquée dans le panneau. Tous les profils sont normalisés à la même valeur à R =8 kpc. **En bas** : rapport entre les TFS théoriques ou empiriques et le profil représentatif.

Prantzos & Athanassoula (2013) – nous traitons séparément les mouvements épicycliques (blurring) et les variations du rayon de l'orbite guide (churning) des étoiles. Pour le blurring, nous adoptons un formalisme analytique basé sur l'approximation épicyclique. Et pour le churning, nous nous inspirons des simulations N-corps+SPH – comme dans Minchev, Chiappini & Martig (2013) et Kubryk, Prantzos & Athanassoula (2013) – et nous adoptons une description paramétrée, utilisant des coefficients de diffusion dépendants du temps et du rayon. De cette manière, nous sommes capables d'étudier quantitativement l'impact des mouvements épicycliques seuls sur la dispersion dans la relation âge-métallicité locale, et bien sûr, les effets combinés du churning et du blurring.

- Pour l'évolution chimique, nous avons utilisé les "rendements" stellaires récents de Nomoto, Kobayashi & Tominaga (2013), bien adaptés à l'étude de l'évolution de la Voie Lactée. Nous rappelons que le rendement stellaire est le taux de masse éjectée de différents éléments/isotopes (par les vents stellaires ou les super novae) par une étoile, par rapport à sa masse initiale ; et que les rendements dépendent de deux paramètres principaux : la métallicité initiale du gaz formant les étoiles, et la masse initiale des étoiles. Ces rendements sont utilisés dans les modèles pour calculer l'enrichissement chimique du milieu interstellaire, c'est-à-dire la quantité éjectée pour divers éléments chimiques (ici nous utilisons les 82 isotopes stables des données de Nomoto, Kobayashi & Tominaga (2013)) à la fin de la vie des étoiles. La grille que nous utilisons est composée de 6 métallicités initiales, allant de 0 à 3 fois la métallicité solaire $Z_\odot$, dont 4 métallicités initiales entre $1/20 Z_\odot$ et $2 Z_\odot$ ce qui permet de modéliser avec une meilleure précision [2] à la fois les zones internes (où le gaz atteint des métallicités élevées) et les zones externes (où le gaz reste peu métallique) de la Voie Lactée. De plus, elle contient à la fois des étoiles étoiles de masse intermédiaire et des étoiles massives, calculer pour les mêmes valeurs de métallicité, ce qui est un avantage considérable si on veut étudier aussi les produits des étoiles de masses intermédiaires, comme le C ou le N.
- Nous utilisons le formalisme de "Single Particle Population", qui est le seul compatible avec la migration radiale, car il permet de considérer les déplacements radiaux des sources de nucléosynthèse, et en particulier des SNIa (Kubryk, Prantzos & Athanassoula, 2013).

Nous comparons nos résultats à un grand nombre de données observationnelles, concernant l'évolution globale de la Voie Lactée, les profiles radiaux actuels de différentes quantités, et le voisinage solaire. Nous utilisons des données récentes pour les profiles radiaux du gaz atomique et du gaz moléculaire, ainsi que pour le Taux de Formation Stellaire (TFS). Pour l'évolution de la masse et du TFS de galaxies similaires à la Voie Lactée, nous utilisons les résultats de van Dokkum et al. (2013). Pour l'évolution du voisinage solaire, nous utilisons les données de Adibekyan et al. (2011) et Bensby, Feltzing & Oey (2014), incluant des relations âge-métallicité, des distributions de métallicité, et différents ratios d'abondance chimique pour

2. Les autres grilles de métallicité ont généralement deux métallicités initiales utilisables pour les étoiles du disque de la Voie Lactée (environ $1/20 Z_\odot$ et $2 Z_\odot$). Dans les modèles d'évolution Galactique, il faut ensuite interpoler, voire extrapoler, entre les valeurs données par les grilles.

les disques mince et épais. Enfin, pour les les échelles de longueur et les densités surfacique locales des disques minces et épais, nous utilisons les données issues de l'analyse de Bovy et al. (2012).

3.2.2 Résultats globaux

Notre modèle reproduit correctement les valeurs des principales observables "globales" du disque et du bulbe (ici R<2 kpc) de la Voie Lactée (Fig. 3.6), c'est-à-dire : les masses d'étoiles, de gaz atomique et moléculaire, les taux d'accrétion, le TFS, CCSN et SNIa. Nous obtenons des masses de HI et H_2 dans le bulbe, plus élevée que dans les observations, et un taux de CCSN dans la partie basse des valeurs compatibles avec les observations, à cause de la pente choisie pour l'IMF des étoiles massives. Nous avons un très bon accord entre l'évolution des masses stellaires du bulbe et du disque et les observations correspondantes de l'évolution "empilée" de galaxies similaires à la Voie Lactée (van Dokkum et al., 2013) : à la lumière de ces données, la Voie Lactée apparaît comme une galaxie disque assez moyenne.

Les profils actuels d'étoiles, de gaz (HI et H_2), de TFS, et de vitesses de rotations sont sont bien reproduites par le modèle (Fig. 3.7). Comme attendu, (e.g. Friedli & Benz (1993)) les courants radiaux produits par la barre aplatissent le profil du gaz entre 3 et 6 kpc et, en conséquence, les profils correspondant de TFS et O/H. Le profil de Fe/H est moins affecté, à cause de l'action des SNIa : le gaz poussé vers l'intérieur par la corotation dilue la métallicité en O et Fe dans les régions internes, mais les SNIa poussées vers l'intérieur compensent la dilution du Fe en relachant leur propre Fe. En considérant les incertitudes actuelles dans tous ces profils, nous pouvons dire que les valeurs que nous avons choisies pour la vitesse des courants de gaz, sont proches des valeurs les plus hautes possibles. Si la barre galactique a agit pendant les quelques derniers milliards d'années, elle doit avoir induit des vitesses radiales inférieures à ~0.5 km/s en moyenne azimutale (bien sûr, les vitesses radiales du gaz, le long de la barre, devraient avoir des valeurs plus élevées). Les profils d'abondance d'autres éléments chimiques et leur évolution font l'objet de l'article suivant.

3.2.3 Résultats locaux

Nous trouvons qu'avec le schéma de migration radiale adopté (où blurring et churning sont séparés), les régions significativement affectées sont entre 4 et 12 kpc, et nous trouvons l'impact le plus grand entre 5 et 9 kpc kpc. Les étoiles de ces régions sont formées en moyenne 1 ou 2 kpc plus à l'intérieur de leur position actuelle, et sont plus vieilles de 1 ou 2 Gyr en moyenne, par rapport aux étoiles formées *in-situ* (Fig. 10 de l'article en Sec. 3.2.5). Ceci implique notamment, que le Soleil s'est probablement formé ~1.2 kpc plus à l'intérieur que sa position actuelle ($R_\odot$ = 8 kpc). La métallicité moyenne dans cette région il y a 4.5 Gyr était [Fe/H]~0, alors que la métallicité du gaz au voisinage solaire actuel était plus basse de ~0.15 dex (Fig. 11 de l'article en Sec. 3.2.5). Cela explique quantitativement pourquoi la métallicité actuelle du gaz local – qui a augmenté depuis de 0.12 dex – est à peut près la même que celle

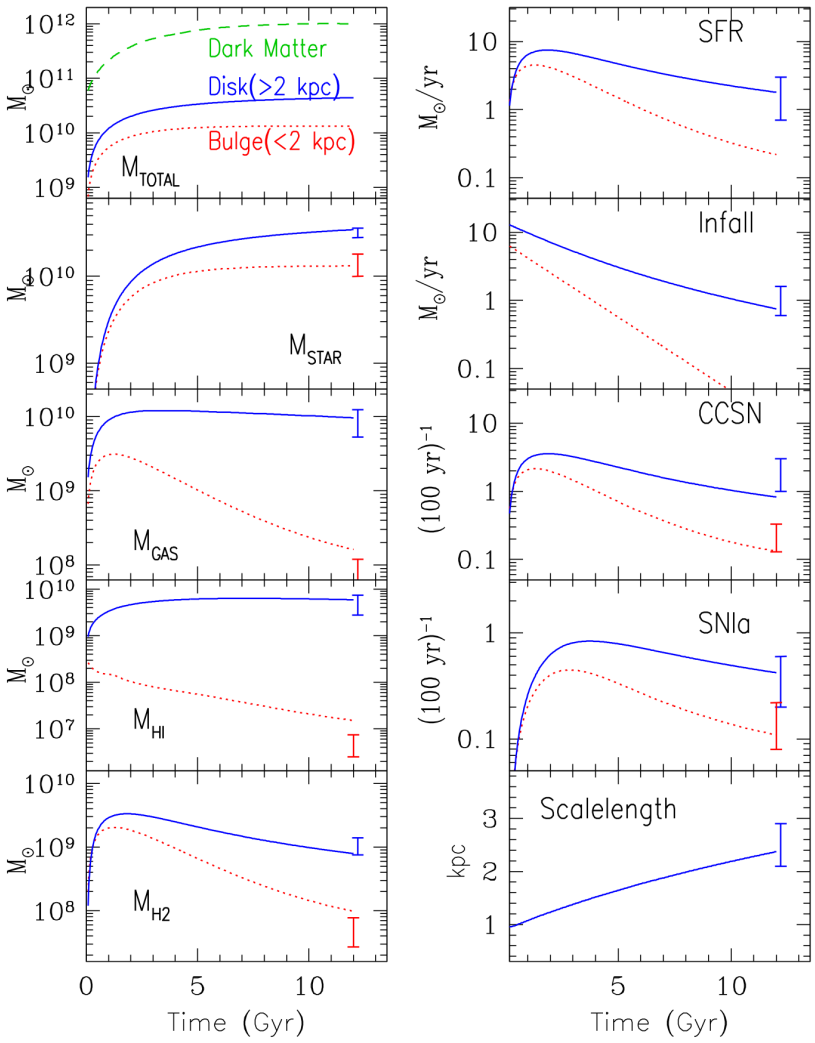

FIGURE 3.6 – Résultats de notre modèle d'évolution de la VL, comparés aux observations. Dans tous les panneaux : la *courbe bleue* indique l'évolution du disque (r >2 kpc), et la *courbe rouge* celle du bulbe (r <2 kpc). Les barres verticales à 12 Gyr indiquent les contraintes observationnelles (voir table 1 dans l'article en Sec. 3.2.5)

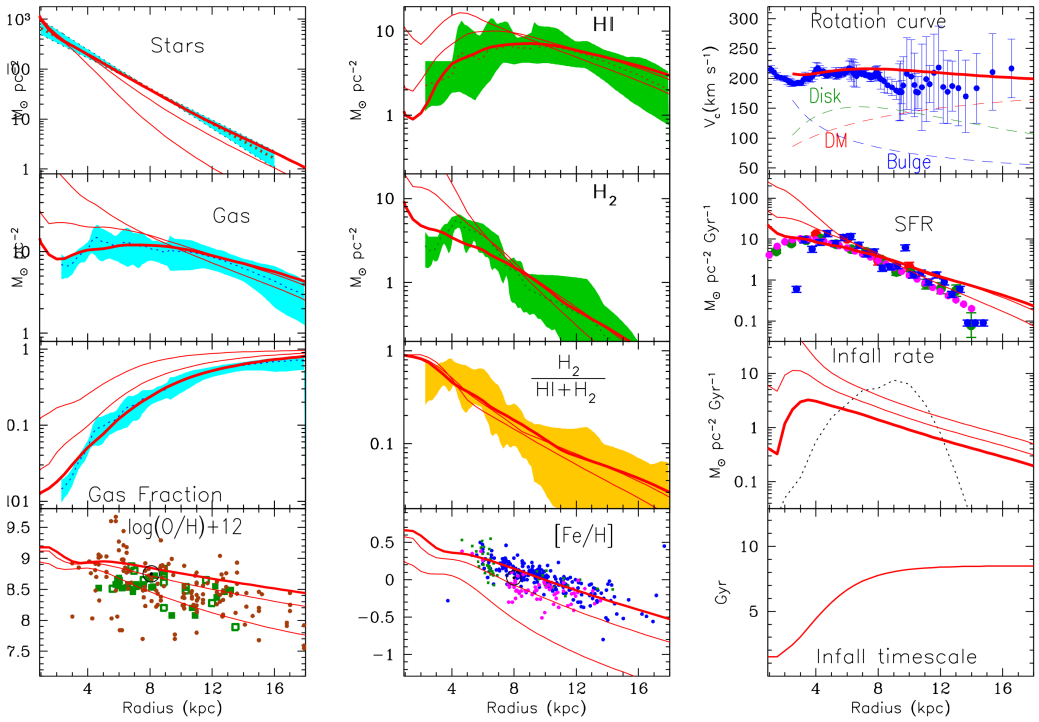

FIGURE 3.7 – Résultats globaux de notre modèle pour les profils principaux de la VL, et comparaison aux observations. Les résultats du modèle sont indiqués à 5, 8 Gyr (*courbes rouges en traits pleins fins*) et à 12 Gyr (*courbes rouges en trait épais*). Les panneaux montrent les résultats pour différentes quantité nommées dans chaque panneau, et les données observationnelles pour le disque actuel sont indiquées par les régions colorées ou les points.

du Soleil aujourd'hui.

Conformément à ce qui a déjà été montré dans des études précédentes, nous trouvons que la migration radiale amène au voisinage solaire principalement des étoiles vieilles et peu métalliques, ayant pour effet d'aplatir la relation âge-métallicité. Elle augmente également la dispersion en métallicité de tous les âges stellaires, la rendant plus large avec l'âge, comme cela avait été trouvé dans Sellwood & Binney (2002).

Nous soulignons que les observables locales de notre modèle concernent ce qui est communément appelé le "cylindre solaire", désignant toutes les étoiles trouvées à la fin de la simulation dans un cylindre de rayon 0.25 kpc autour du Soleil (quel que soit leur leur éloignement au plan galactique). Nous n'appliquons pas de biais observationnel à nos résultats. Pour cette raison, un résultat concordant aux observations n'implique pas nécessairement que le modèle est correct, mais seulement qu'il possède potentiellement des propriétés intéressantes. Le seul critère de sélection que nous sommes amené à utiliser est celui de l'âge des étoiles, afin de différencier le disque mince du disque épais (nous reviendrons sur ces résultats plus loin).

Résultat intéressant : Les observations "empilées" de galaxies de masse stellaire 5×10^{10} $M_{\odot}$ (i.e. de masse stellaire similaire à celle de de la VL) van Dokkum et al. (2013), permettent de construire l'évolution "moyenne" des galaxies observées de cette masse. Il est intéressant de noter que notre modèle d'évolution de la VL donne des résultats proches de cette évolution (Fig. 3.9), ce qui tendrait à montrer que la Voie Lactée est assez représentative des galaxies ayant une masse stellaire de 5×10^{10} $M_{\odot}$.

Résultat important : nous montrons quantitativement que – dans le cadre de ce modèle et avec l'avertissement du paragraphe précédent – les mouvements épicycliques ne peuvent pas produire les dispersion de métallicité observées (Fig. 3.8). En revanche, le schéma de migration que nous avons adopté reproduit correctement la dispersion dans la relation âge-métallicité issue des observations. Nous montrons que cette observable est l'un des traceurs les plus prometteurs pour l'étude de l'amplitude de la migration radiale dans la Voie Lactée, et qu'il devrait être examiner minutieusement dans les futures études observationnelles et théoriques. Ce résultat est important, car le fait qu'un mécanisme de migration radiale plus important que les épicycles soit nécessaire pour expliquer les observations de la composition chimique du voisinage solaire, est encore sujet à débat (e.g. Haywood (2012), Nieva & Przybilla (2012)).

Par ailleurs, le ratio d'abondance [O/Fe] ne montre que très peu de variations dans sa dispersion en fonction de l'âge stellaire, ce qui en fait un bien meilleur indicateur de l'âge des étoiles que la quantité [Fe/H] ; ce résultats reste valide pour les autres ratios impliquant des éléments α (quantités [α/Fe]), ce qui avait déjà été montré par Bovy et al. (2012).

Nous analysons l'origine des populations stellaires trouvées dans le voisinage solaire, en fonction de leur métallicité (Fig. 13 de l'article en Sec. 3.2.5). Nous trouvons que, pour toutes les métallicités, les étoiles sont ~1 Gyr plus vieilles en moyenne, que les étoiles formées localement ayant la même métallicité ; elles ont également une dispersion en âge de ~1-3

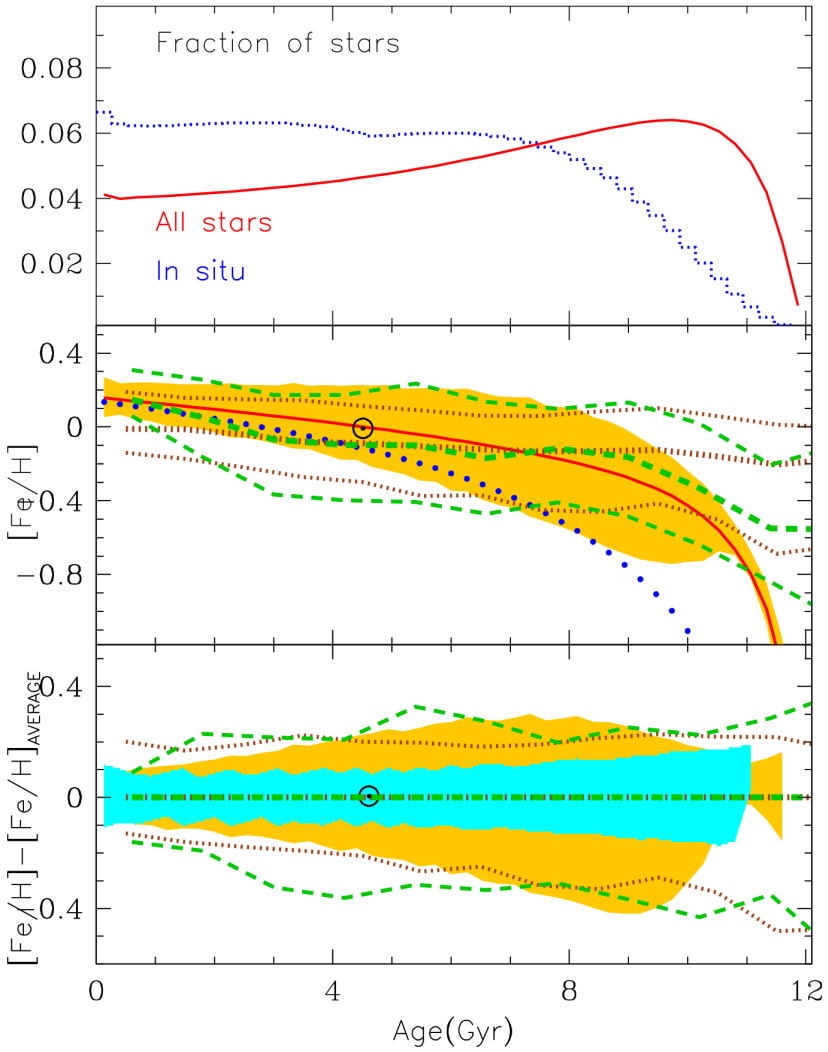

FIGURE 3.8 – Résultats de notre modèle sur l'évolution chimique du voisinage solaire, en fonction de l'âge des étoiles. **En haut** : parmi toutes les étoiles situées au voisinage solaire à la fin de la simulation, la *courbe bleue* indique la fraction d'étoiles nées *in-situ* pour chaque âge, la *courbe rouge* indique la fraction d'étoiles (quel que soit leur rayon d'origine) de chaque âge, présente au voisinage solaire. **Au milieu** : la relation âge-métallicité des étoiles. Pour notre modèle, la métallicité moyenne est indiquée par la (*courbe rouge pleine*) et la limite à $\pm 1\sigma$ par la (*zone colorée jaune*). *Les coubes vertes et marrons* indiquent la moyenne et la limite à $\pm 1\sigma$ pour deux jeux de données observationnelles (voir article en Sec. 3.2.5). **En bas** : dispersion dans les relations âge-métallicité présentées dans le panneau du milieu, avec les mêmes couleurs. La *zone bleue* indique la dispersion dans la relation âge-métallicité des étoiles dans le cas où seuls les épicycles déplacent les étoiles.

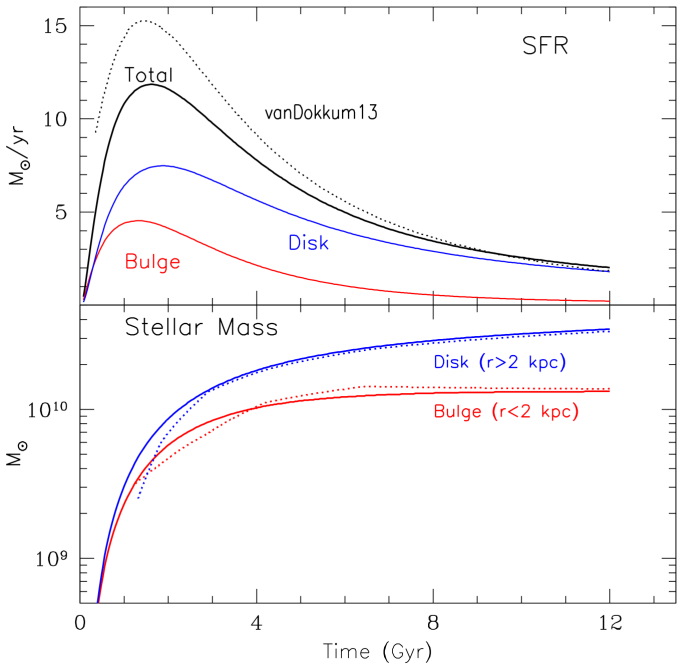

FIGURE 3.9 – Comparaison des résultats de notre modèle avec les observations "empilées" de galaxies de masse stellaire $\sim 5 \times 10^{10}$ $M_\odot$ (courbes *en points*) de van Dokkum et al. (2013). **En haut** : évolution du TFS total de notre modèle (*courbe noire pleine*), et contributions du bulbe et du du disque. **En bas** : évolution de la masse stellaire du bulbe (r <2 kpc) et du disque (r >2 kpc) dans notre modèle (courbes *pleines* rouges et bleues respectivement).

Gyr autour de l'âge moyen. Clairement, la migration radiale affecte considérablement la relation âge-métallicité, permettant à des étoiles jeunes de faible métallicité, de cohabiter avec des étoiles vieilles très métalliques. Dans notre modèle, les étoiles les moins métalliques du voisinage solaire ont ~11 Gyr et viennent, en moyenne, des régions à 5-6 kpc du centre Galactique ; et les étoiles de métallicité solaire ont ~4.5 Gyr et viennent de r ~7 kpc. Les étoiles locales les plus métalliques ([Fe/H]~0.3-0.4 $Z_{\odot}$) ont 3-4 Gyr, et viennent des régions internes de la Galaxie (~2-3 kpc). Nous trouvons que les étoiles d'âges et rayons de naissances différents contribuent, dans une certaine mesure, dans tous les bins de métallicité (Fig. 14 de l'article en Sec. 3.2.5).

3.2.4 Disque mince et disque épais

Gilmore & Reid (1983), ont identifié le disque épais comme une composante distincte de la Voie Lactée, sur la base de comptages d'étoiles vers le pôle Sud Galactique. Depuis lors, et malgré des études observationnelles et théoriques poussées, l'identité du disque épais reste difficile à saisir. Beaucoup de ses propriétés (si ce n'est toutes) diffèrent clairement de celles du disque mince, en particulier son âge, sa métallicité, ses ratios d'abondances, sa cinématique, sa distribution spatiale. Toutefois, il n'y a apparemment pas de frontière clairement définie séparant le disque mince du disque épais, et la communauté peine toujours à établir un tableau clair des relations (si elles existent) entre le disque épais et les autres composantes de la Galaxie (le bulbe, le halo, le disque mince). Ainsi, un grand nombre de scénarios pour la formation du disque épais ont été proposés, impliquant soit des influences extérieurs soit une évolution séculaire par migration radiale, e.g. Sales et al. (2009) ;Minchev, Chiappini & Martig (2013) ;Rix & Bovy (2013) et les références dans ces articles.

En particulier, la migration radiale a été suggérée comme un mécanisme possible de formation du disque épais par Schönrich & Binney (2009), qui ont développé un modèle semi-analytique et en ont étudié les résultats concernant les propriétés chimique et cinématiques. Ils ont notamment montré que leur modèle peut reproduire plusieurs propriétés clés du disque épais, juste par évolution séculaire : la morphologie (i.e. le profil vertical présentant une combinaisons de deux exponentielles au voisinage solaire), les gradients d'abondances verticaux et le comportement bi-modal dans le plan [O/Fe] vs [Fe/H], avec le disque épais ayant un ratio O/Fe plus élevé que le disque mince pour les mêmes valeurs de métallicité. Certains de ces résultats ont également été trouvés dans les simulations N-corps, e.g. Loebman et al. (2011). Mais d'autres travaux (Minchev et al., 2012), indiquent que la migration radiale aurait peu d'effets sur l'épaisseur des disques, et donc que l'évolution séculaire du disque n'est pas suffisante pour expliquer la formation du disque épais, alimentant le débat sur sa formation.

Dans notre modèle, nous n'avons pas de données sur la cinématique des étoiles, ni sur leur positions verticales. Pour séparer les étoiles de ces deux disques, nous utilisons alors un critère simple, déjà suggéré dans la littérature : l'âge des étoiles (une autre raison pour ce choix étant l'absence de direction verticale dans notre modèle, nous empêchant d'utiliser les critères

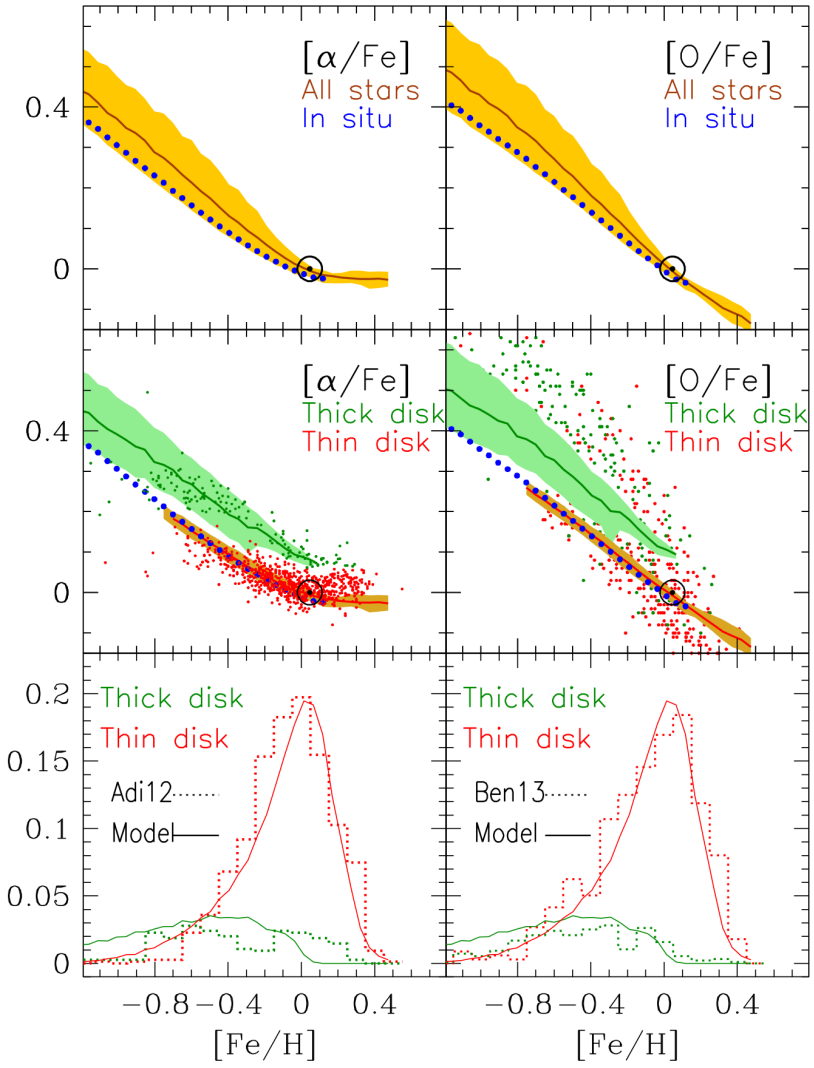

FIGURE 3.10 – Résultats de notre modèle concernant les disques minces et épais, et comparaison aux observations. **En haut** : [α/Fe] (à gauche) et [O/Fe] (à droite) en fonction de la métallicité [Fe/H], pour toutes les étoiles présentes aujourd'hui au voisinage solaire dans notre modèle (*courbe marron pleine*) et pour les étoiles formées *in-situ* (*courbes en points bleus*). **Au milieu** : [α/Fe] (à gauche) et [O/Fe] (à droite) vs. métallicité, pour les étoiles du disque épais (>9 Gyr, *courbes vertes*) et pour les étoiles du disque mince (<9 Gyr, *courbes rouges*). Les données observationnelles sont indiquées par les points avec les couleurs correspondantes. Dans les panneaux du haut et du milieu, les zones colorées indiquent les limites à $\pm 1\sigma$ de notre modèle. **En bas** : les distributions en métallicité du disque mince (*courbes rouges*) et disque épais (*courbes vertes*) de notre modèle. *Les histogrammes* indiquent les données observationnelles avec les couleurs correspondantes. À noté que le critère de sélection utilisé dans données observationnelles utilisées pour le panneau en bas à droite favorisent les étoiles du disque épais. Pour cette raison, nous avons baissé d'un facteur 3 arbitraire les valeurs observationnelles concernant le disque épais afin d'avoir une concordance avec notre modèle.

reposants sur la cinématique ou des quantités spatiales dans cette direction). Nous supposons que les étoiles plus vieilles que 9 Gyr, appartiennent au disque épais, et que les plus jeunes appartiennent au disque mince.

Nous évaluons quantitativement la structure radiale des disques mince et épais dans notre modèle. Nous trouvons que, du fait de formation graduelle du disque de l'intérieur vers l'extérieur, le disque épais a une échelle de longueur considérablement plus courte que le disque mince (Fig. 3.11), malgré le fait que les étoiles le constituant ont été bien plus affectées par la migration radiale que celles du disque mince. Les densités surfaciques locales des deux disques concordent très bien avec les récentes évaluations observationnelles, ce qui est vrai également pour l'échelle de longueur du disque épais. En revanche, pour le disque mince, nous obtenons une échelle de longueur ~1 kpc plus courte que celle estimée avec les observations. Au total, le disque épais représente environ 1/3 du disque stellaire complet (mince + épais), et représente 1/4 de la densité surfacique d'étoiles au voisinage solaire.

Résultat important 1 : Nous avons montré que le simple critère d'âge adopté ici, permet de reproduire assez bien le comportement observé de [α/Fe] vs. [Fe/H] pour les étoiles identifiées comme appartenant aux disques mince et épais selon différents critères (chimiques ou cinématiques) ; aussi, nous reproduisons les distributions de métallicité, avec une très bonne concordance avec les observations pour le disque mince, et de façon satisfaisante pour le disque épais (Fig. 3.10) ; et les profils surfaciques des deux disques. Ces résultats vont dans le sens de l'hypothèse selon laquelle le disque épais est simplement la partie du disque de la Voie Lactée qui s'est formée dans les premiers milliards d'années, et que le disque épais local est constitué en grande partie d'étoile venant des régions internes de la Galaxie par migration radiale. Toutefois, nous n'avons pas la dimension verticale (selon l'épaisseur du disque), ni la cinématique des étoiles dans notre modèle, nous ne pouvons donc pas comparer le critère d'âge avec les critères cinématiques ou de positions (selon l'éloignement au plan Galactique).

Résultat important 2 : nous étudions en détail l'évolution de nombreuses abondances d'éléments chimiques dans les disques minces et épais locaux, et nous comparons nos résultats à un grand nombre de données observationnelles issues des surveys récents. Nous montrons que de telles études nécessitent une grille fine et homogène de rendements d'étoiles (comme celle fournie dans Nomoto, Kobayashi & Tominaga (2013), que nous utilisons ici). Ce résultat est important car les études de l'évolution chimique de la VL dépandent beaucoup des rendements stellaires, Nous trouvons que pour certains éléments observés, i.e. le comportement de [α/Fe] vs [Fe/H], les observations peuvent être reproduites correctement à la fois pour le disque mince et le disque épais, mais les résultats sont bien moins satisfaisants pour d'autres éléments. Les données actuelles et à venir fourniront des contraintes fortes sur la nucléosynthèse stellaire, et sur l'évolution globale du disque de la Voie Lactée, en particulier en les combinant avec les données cinématiques et spatiales.

3.2.5 Article : Le voisinage solaire, le disque mince, le disque épais

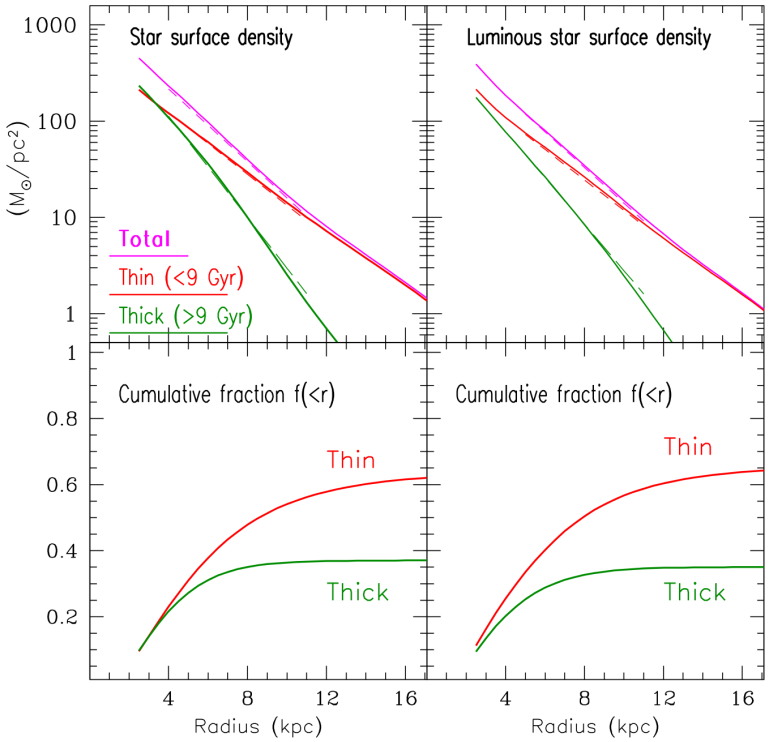

FIGURE 3.11 – Résultats de notre modèle concernant les disques minces et épais. **Colonne gauche** : étoiles et rémanents stellaires (issus de la mort des étoiles). **Colonne droite** : étoiles lumineuses uniquement. **En haut** : profils stellaires à la fin de la simulation : *magenta* : total ; *vert* : disque épais ; *rouge* : disque mince. Chaque courbe est ajustée entre 5 et 11 kpc par une exponentielle (*courbes en tirets*), les échelles de longueur et densités surfaciques à 8 kpc sont reportées dans la table 3 de l'article en Sec. 3.2.5. **En bas** : fractions cumulées de masse des disques minces et épais par rapport à la masse totale du disque (M_{disque}) : $M_{mince}(< r)/M_{disque}$ (*courbe rouge*), $M_{épais}(< r)/M_{disque}$ (*courbe verte*) en fonction du rayon.

Astronomy & Astrophysics manuscript no. Paper3_May1
June 18, 2014

Evolution of the Milky Way with radial motions of stars and gas

I. The solar neighborhood and the thin and thick disks

M. Kubryk[1], N. Prantzos[1] and E. Athanassoula[2]

[1] Institut d'Astrophysique de Paris, UMR7095 CNRS, Univ. P. & M. Curie, 98bis Bd. Arago, 75104 Paris, France
e-mail: kubryk@iap.fr,prantzos@iap.fr
[2] Aix Marseille Université, CNRS, LAM (Laboratoire d'Astrophysique de Marseille) UMR 7326, 13388, Marseille, France
e-mail: lia@lam.fr

Received ; accepted

ABSTRACT

Context. We study the role of radial migration of stars on the chemical evolution of the Milky Way disk.
Aims. In particular, we are interested in the impact of that process on the local properties of the disk (age-metallicity relation and its dispersion, metallicity distribution, evolution of abundance ratios) and on the morphological properties of the resulting thick and thin disks.
Methods. We use a model with several new or up-dated ingredients: atomic and molecular gas phases, star formation depending on molecular gas, yields from the recent homogeneous grid provided by Nomoto et al. (2013), observationally inferred SNIa rates. We describe radial migration with parametrised time- and radius-dependent diffusion coefficients, based on the analysis of a N-body+SPH simulation. We also consider parametrised radial gas flows, induced by the action of the Galactic bar.
Results. Our model reproduces well the present day values of most of the main global observables of the MW disk and bulge, and also the observed "stacked" evolution of MW-type galaxies (van Dokkum et al. 2013). The azimuthally averaged radial velocity of gas inflow is constrained to less than a few tenths of km/s. Radial migration is constrained by the observed dispersion in the age-metallicity relation. *Assuming* that the thick disk is the oldest (>9 Gyr) part of the disk, we find that the adopted radial migration scheme can reproduce quantitatively the main local properties of the thin and thick disk: metallicity-distributions, "two-branch" behaviour in the O/Fe vs Fe/H relation, local surface densities of stars. The thick disk extends up to ~11 kpc and has a scale length of 1.8 kpc, considerably shorter than the thin disk, because of the inside-out formation scheme. We also show how, in this framework, current and forthcoming spectroscopic observations can constrain the nucleosynthesis yields of massive stars for the metallicity range of 0.1 $Z_\odot$ to 2-3 $Z_\odot$.

Key words.

1. Introduction

The Milky Way (MW) offers the possibility of detailed observations of a large number of galactic properties, which are unaccessible in the case of other galaxies. Information on chemical composition and kinematics is now available for a few thousand stars of various ages, both in the solar vicinity, across the MW disk and away from the Galactic plane. A large amount of information also exists for the gaseous content of the Galaxy (its molecular and atomic components and its chemical composition) as a function of galactocentric radius.

This wealth of information, as well as the evidence for evolution without major perturbations in the past 8 Gyr or so (e.g. Hammer et al. (2007) and references therein), makes the MW an ideal test bed for theories of galaxy evolution. However, current models encounter difficulties in producing late-type disks, e.g. Silk & Mamon (2012) and references therein. Despite an intense theoretical effort and several claims for a solution to the problem - involving star formation threshold (Guedes et al. 2011) or stellar feedback (Übler et al. 2014) - no commonly accepted paradigm has emerged up to now.

The chemical properties of the MW (local age-metallicity relation, local metallicity distribution, abundance ratios vs metallicity, abundance profiles across the disk) have been extensively studied long before the era of large scale numerical simulations. Such studies were performed with simple numerical models, either for the solar neighborhood or for the whole disk (with "independent ring" models) and revealed some key aspects of the chemical evolution of the Galaxy: the need for a supplementary source of Fe (beyond massive stars), namely SNIa, to reproduce the observed decline of O/Fe with metallicity; the need of a long-term early infall, to reproduce the early part of the G-dwarf metallicity distribution and the high present-day abundance of deuterium; the need for a radial variation in the efficiency of star formation (and/or the corresponding infall timescale) in order to obtain the observed gradients in the radial abundance profiles (e.g. Pagel 2009; Matteucci 2012). The aforementioned results are robust qualitatively but not quantitatively, because of large uncertainties in the observational data (e.g. dispersion in the age-metallicity relation, shape of the metallicity distribution), and also because of the poorly understood role of radial gaseous flows. Although they are well justified on physical grounds - e.g. Lacey & Fall (1985) - radial flows were never shown conclusively to play an important role in the chemical evolution of the Milky Way, because of the impossibility to observe or to infer from theory the corresponding radial velocity profiles in the Galaxy.

The action of the bar can mix radially not only gas but also stars, and the effects of stellar radial motions on the abundance profiles have been studied to some extent with N-body+SPH codes by Friedli & Benz (1993) and Friedli et al. (1994). Observations in the 90ies revealed that the MW does have a bar (Blitz & Spergel 1991), but its origin, size and age are not well known yet; as a result, its impact on the evolution of the MW is difficult to evaluate quantitatively.

Independently of the role of the bar, Sellwood & Binney (2002) showed that, in the presence of recurring transient spirals, stars in a galactic disk could undergo important radial displacements: stars found at corotation with a spiral arm may be scattered to different galactocentric radii (inwards or outwards), a process which preserves overall angular momentum distribution and does not contribute to the radial heating of the stellar disk. Using a simple model, they showed how this process can increase the dispersion in the local metallicity vs age relation, well above the amount due to the epicyclic motion. This development paved the way for a large number of theoretical studies on radial migration, both with N-body codes (e.g. Roškar et al. 2008; Sánchez-Blázquez et al. 2009; Martínez-Serrano et al. 2009; Sales et al. 2009; Roskar 2010; Minchev & Famaey 2010; Minchev et al. 2011; Brunetti et al. 2011; Minchev et al. 2012b; Grand et al. 2012; Baba et al. 2013; Bird et al. 2013; Di Matteo et al. 2013; Kubryk et al. 2013; Grand et al. 2014) and with semi-analytical models (Lépine et al. 2003; Prantzos 2009; Schönrich & Binney 2009a; Minchev et al. 2013; Wang & Zhao 2013; Minchev et al. 2014). Because of the difficulty to produce realistic MW-like disks, the former class of models focused mostly on generic properties of radial migration (origins of it and impact on some observables), while the latter focused exclusively on the properties of the MW.

Roškar et al. (2008) investigated the implications of radial migration for the chemical evolution of galactic disks with N-body+SPH simulations. The main effects they found and analysed are: the resulting dispersion in the age-metallicity relation, the broadening of the local metallicity distribution, the flattening of observed past abundance profiles and the flattening of the observed past star formation history.

Schönrich & Binney (2009a) introduced a parametrised prescription of radial migration (distinguishing epicyclic motions from migration due to transient spirals) in a semi-analytical chemical evolution code. They found excellent agreement between the results of their model and observations of the solar neighborhood. They suggested that radial mixing could also explain the formation of the Galaxy's thick disk, by bringing to the solar neighborhood a kinematically "hot" stellar population from the inner disk. That possibility was subsequently investigated with N-body models, but controversial results are obtained up to now: while Loebman et al. (2011) find that secular processes (i.e. radial migration) are sufficient to explain the kinematic properties of the local thick disk, Minchev et al. (2012a) find this mechanism insufficient and suggest that an external agent (e.g. early mergers) is required for that. The issue is still under debate, e.g. Sales et al. (2009); Wilson et al. (2011); Navarro et al. (2011); Bekki & Tsujimoto (2011); Brook et al. (2012); Forbes et al. (2012); Steinmetz (2012); Liu & van de Ven (2012); Bird et al. (2013); Kordopatis et al. (2013); Haywood et al. (2013); Roškar et al. (2013). On the other hand, using mono-abundance populations (i.e. defined in the plane of [O/Fe] vs. [Fe/H]), Bovy et al. (2012b) conclude that the thick disk is not really a distinct component of the Milky Way, **as suggested in Schönrich & Binney (2009b)**; see also Rix & Bovy (2013) for a review.

Minchev & Famaey (2010) suggested a different mechanism for radial migration than transient recurring spirals, namely resonance overlap of the bar and spiral structure (Sygnet et al. 1988); this strongly nonlinear coupling leads to a more efficient redistribution of angular momentum in the disk and produces a stellar velocity dispersion increasing with time, in broad agreement with local observations. This bar-spiral coupling was studied in detail by Shevchenko (2011) and Brunetti et al. (2011). The latter study found that the extent of radial migration depends also on the kinematic state of the disk, being reduced in the case of kinematically hot disks; they also showed that radial migration can be assimilated to a diffusion process, albeit with time- and position-dependent diffusion coefficients. That idea was confirmed by the analysis of N-body+SPH simulations of a disk galaxy by Kubryk et al. (2013): they extracted such coefficients from the simulation of an early-type barred disk and, applying them in a semi-analytical model of that same disk, they showed that all the main features of the N-body+SPH simulation can be reproduced to a good accuracy. They also showed that radial migration moves around not only "passive" tracers of chemical evolution (i.e. long-lived stars, keeping on the surfaces the chemical composition of the gas at the time and place of their birth), but also "active" agents of chemical evolution, i.e. long-lived nucleosynthesis sources (mainly SNIa producing Fe and $\sim$1.5 $M_{\odot}$ stars producing s-process elements).

In this work we present a model for the evolution of the MW disk, which includes radial motions of gas and stars. The MW is built gradually by infall of primordial gas in the potential well of an evolving "typical" dark matter halo of final mass 10^{12} $M_{\odot}$. The star formation rate depends on the local surface density of molecular gas, after recent observational findings (Bigiel et al. (2008); Leroy et al. (2008); Krumholz (2014) and references therein). Gas radial flows are considered for the case of a MW-like bar operating for the last 6 Gyr. For the chemical evolution, we adopt recent sets of yields from Nomoto et al. (2013), providing a homogeneous and fine grid of data, well adapted to the case of the MW disk; we also adopt a phenomenological SNIa rate, based on the observed time-delay function of extragalactic SNIa (Appendix C). We adopt the formalism of Single Particle Population, which is the only one applicable to the case of radial migration, since it allows to consider the radial displacements of nucleosynthesis sources and in particular of SNIa (Kubryk et al. 2013).

Our treatment of radial migration of stars is a mixture of the techniques adopted in some pevious works in the field. As in Sellwood & Binney (2002) and Schönrich & Binney (2009a) - but unlike Minchev et al. (2013, 2014) or Kubryk et al. (2013) - we consider separately the epicyclic motion of stars (blurring) from the true variation of their guiding radius (churning). For the former, we adopt an analytic formalism based on the epicyclic approximation. For the latter, we are inspired by N-body+SPH simulations - as in Minchev et al. (2013) and Kubryk et al. (2013) - and we adopt a parametrised description, using time- and radius- dependent diffusion coefficients. In this way, we are able to study quantitatively the impact of epicyclic motion alone to the dispersion of the local age-metallicity relation and, of course, the collective impact of the two processes (blurring+churning).

The ingredients of our model are presented in Sec. 2 and some of them are described in more detail in Appendices B and C. Some of the observational constraints are presented in Sec. 2.5, while the adopted gas and SFR profiles are discussed in detail in Appendices A and B. The global evolution of the Galaxy (i.e. various quantities as a function of time and radius) is pre-

sented in Sec. 3 and the results are compared to observations; in particular, in Sec. 3.2 we discuss quantitatively the diffusion coefficients adopted in our model and the amount of the radial migration they produce along the disk. The results concerning the solar vicinity (age-metallicity relation and its dispersion, metallicity distribution, abundance ratios) are presented in Sec. 4.1 and 4.2. We then analyse the properties of the thick disk, which is *assumed* here to be just the old part of the disk (age >9 Gyr); we show that this assumption leads to results in fair agreement with most of the observed chemical and morphological properties of the thick disk (Sec. 4.3). A summary of the results is presented in Sec. 5.

2. The model

2.1. Building the Galaxy: Dark matter, baryonic infall and star formation

In our model, we construct the Galaxy "backwards", i.e. we are guided in the selection of the model parameters by the present day properties of the Milky Way (e.g. radial profiles of baryonic matter and rotational velocity, which depends also on the distribution of the dark matter halo). Unfortunately, none of the relevant observational data (rotation curve, surface density profiles of gas and stars, masses of the bulge and the disk) are accurately known yet. And even if this were the case, determination of the structural parameters of the various components of the Galaxy would still suffer from degeneracy problems; see e.g. the excellent summary of mass models of the Milky Way in Sec. 4 of Courteau et al. (2013).

For the purpose of this work, we describe the Milky Way as a superposition of three components: a DM halo, a bulge and a disk. The parameters adopted for the description of the evolution of each component are given in the next subsections. We notice, however, that the actual distribution of the baryonic material within the inner 2 kpc is much more complex than assumed here, because it can contain a number of components such as a boxy/peanut bulge, a disky bulge, a classical bulge as well as the inner extension of the Galactic disk. These have very different shapes, kinematics and formation histories. The boxy/peanut bulge is composed of disk material, but is vertically extended sticking clearly out of the Galactic disk, the classical bulge was formed well before the disk and can be described as spherical, while the disky bulge can be roughly described as younger and thinner than the Galactic disk (Athanassoula 2005). Our model, which is essentially 1D, cannot describe all this complexity; we will thus not extend our study to the region inwards of two kpc, which will be designated as " the bulge" here (we will use the term "disk" for the region outside 2 kpc).

2.1.1. Evolution of dark matter profile

The present day virial mass of the DM halo of the MW is typically estimated to M_{DH}=10^{12} $M_\odot$, although variations by a factor larger than two around that value are found in the literature, e.g. Rashkov et al. (2013) and references therein. Its density profile can be generically described by:

$$\rho(r) = \frac{\rho_0(r_0)}{(r/r_0)^\gamma\,[1+(r/r_0)^\alpha]^{(\beta-\gamma)/\alpha}}, \quad (1)$$

where ρ_0 and r_0 are, respectively, the characteristic mass/energy density and radius of the halo and α, β, γ are parameters with values inferred from simulations or from observations. Here we adopt a Navarro-Frenk-White profile with α=1, β=3, γ=1 and core radius r_0=25 kpc.

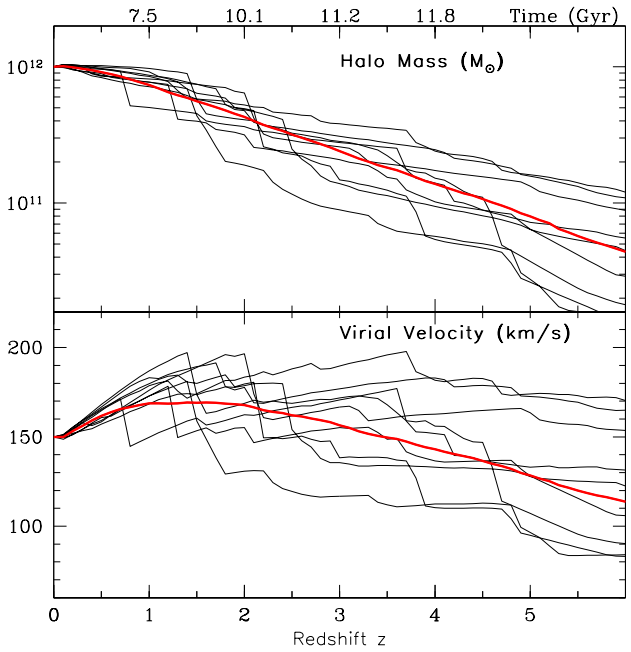

Fig. 1. Evolution of the mass (top) and the virial velocity (bottom) of several DM haloes with final mass 10^{12} $M_\odot$- out of the 200 extracted for this study - from the simulation of Li et al. (2007) (*thin curves*). In both panels, the *thick (red)* curves correspond to the average history of all the 200 DM haloes, which we assume here to represent the history of the Milky Way's DM halo.

For the evolution of the DM halo we use the simulations of Li et al. (2007), who calculated the growth of DM haloes in a ΛCDM model. We extracted about 200 DM haloes with final mass of 10^{12} $M_\odot$ from that simulation and we took an average over all masses at each redshift. We adopt this smoothed evolution (thick curve in Fig. 1) as a reasonable approximation for the evolution of the DM halo of the MW, at least for the past 8 Gyr, where no major merger is thought to have occurred. We do not account for any concentration effect due to the interaction of baryons with the DM halo, i.e. we assume that the DM halo has at all redshifts z the profile of Eq. 1, with the central density $\rho_0(z)$ varying with time as to have the mass $m_{DM}(z)$ of Fig. 1 enclosed within the virial radius.

2.1.2. Infall of baryonic matter

We assume that the MW is built gradually from gas infalling in the potential well of the DM halo. In fact, infall has been considered long before the current paradigm of galaxy formation was established, both on theoretical and observational grounds. Indeed, infall offers an elegant solution to the so-called "G-dwarf problem", namely the dearth of long-lived stars of low metallicity in the solar neighbourhood, with respect to the predictions of the simple "closed-box" model of chemical evolution (Pagel 2009); it is also required to keep the present-day abundance of deuterium in the local ISM to its nearly primordial value (Steigman et al. 2007); and finally, high velocity clouds of HI are observed on trajectories crossing the MW disk (e.g. Wakker et al. (1999) and references therein).

The infall rate, as a function of space and time, plays a crucial role in determining the properties of the MW disk (gas and abundance profiles), along with other ingredients, such as the star formation rate. At present, it cannot be determined from first principles (but see e.g. Naab & Ostriker (2006) for such an attempt, based on simplifying assumptions about the evolution of the disk within the DM halo). Marasco et al. (2012) have recently suggested a profile for the present- day infall rate density on the MW disk, based on a model of the Galactic fountain, used to simulate the HI emission of the Galaxy. Their profile peaks at a galactocentric distance of ∼9 kpc (slightly outside the solar neighbourhood) and corresponds to a global infall rate of ∼2 $M_\odot$/yr, compatible with the amount required to sustain the MW star formation without depleting its gaseous content. In view of the uncertainties in the parameters of the model, we do not consider their proposed infall profile as a tight constraint at present (see Sec. 3); it may become such if confirmed by future studies, especially if some hints on the past infall profile become also available.

In this work we *assume* (as in most studies of that kind) a radial profile for the infall rate as a function of time. Once the time variation of infall in each zone r is assumed (in most cases an exponential decay law, with a characteristic time scale $\tau(r)$), the gas infall rate per unit area of the disk $F_g r,(t)$ ($M_\odot$/pc^2/yr) is constrained by the requirement that its integral over time equals the total baryonic (i.e. stars+gas) surface density $\Sigma_{Tot,Obs}(r,T)$ at present time T:

$$\int_0^T F_g(r,t)dt \;=\; \Sigma_{Tot,Obs}(r,T) \qquad (2)$$

In the case of independent-ring disk models, Eq. 2 is used to fix uniquely and accurately $F_g(r,t)$. When radial migration is taken into account, the final baryonic profile depends not only on the integral of $F_g(r,t)$ over time, but also on the extent of migration. In those conditions, it becomes difficult to reproduce accurately $\Sigma_{Tot,Obs}(r,T)$ in the end of the simulation. Here we adopt - after some iterations - for $\int_0^T F_g(r,t)dt$ a profile which depends on our migration coefficients: the combination of the adopted infall and star formation prescriptions and the adopted radial migration scheme produces a quasi-exponential stellar profile in the end of the simulation.

Concerning the infall time-scales, we adopt for the bulge (hereafter taken as the region within r=2 kpc) τ=2 Gyr everywhere and for the disk r >2 kpc) a smoothly increasing function, reaching τ(20kpc)=8 Gyr. The adopted profile of $\tau(r)$ can be seen in the bottom right panel of Fig. 5.This form of the infall rate insures (i) continuity at the bulge-disk transition and (ii) a characteristic time-scale of ∼7-8 Gyr for the solar neighbourhood, which has been shown to help reproducing the local G-dwarf metallicity distribution **(Chiappini et al. 1997; Prantzos & Silk 1998)** [1]. The radial dependence of $\tau(r)$ implies that the gaseous disk (and, thereof, the stellar disk) is formed inside-out. We note that one may also consider cases with the same infall timescale over the whole disk, but with a strong radial dependence of the star formation efficiency (see next section): in such cases, the gaseous disk is formed everywhere at the same pace, but the stellar disk is still formed inside-out.

The composition of the infall is equally important when it comes to discuss the evolution of abundances and abundance ratios in the MW disk. Observations are of little help at present: they generally find low metallicities for gas clouds *presently* falling to the MW disk (∼0.1 $Z_\odot$, e.g. Wakker et al. 1999), but they provide no information on the past metallicity of such clouds or on their abundance ratios. In an attempt to overcome that difficulty, Schönrich & Binney (2009a) assumed that the infalling gas has a metallicity of 0.1 $Z_\odot$, but its enhancement in α-elements mirrors the one obtained by their model in some arbitrarily chosen outer zone specifically the one at 12.125 kpc.

Here we adopt the simplest possible (but still arbitrary) assumption, namely that the infalling gas has always primordial composition, i.e. only for i=H,D,^{3}He,^{4}He and ^{7}Li is the term $F_{g,i}(r,t)$=$F_g(r,t)X_i(r,t)$ different from zero (where $X_i(r,t)$ is the mass fraction of isotope i). This assumption hardly affects the results for the chemical evolution of the disk, but it allows for the existence of disk stars with metallicities lower than [Fe/H]=-1 (see Bensby (2013) and references therein).

2.1.3. Star formation

The most widely used SFR prescription in semi-analytical models of galactic evolution is the so-called "Schmidt-Kennicut" law, based on observations of quiescent and active disk galaxies: the surface density of the star formation rate is $\Psi \propto \Sigma_G^k$, where the gas surface density Σ_G runs over three orders of magnitude and the data suggest k=1.5 (Kennicutt & Evans 2012). It turns out that this form of the SFR, with k=1.5 is too flat to fit the MW data: Misiriotis et al. (2006) find k=2 from their modelling of the IR emission of the MW.

In their model of the MW, Boissier & Prantzos (1999) adopted a law of the form $\Psi(R) \propto \Sigma_G^{1.5} V(R)/R$; the factor $V(R)/R$ is $\propto 1/R$ for a flat curve of the rotational velocity $V(R)$ and is attributed to spiral waves inducing star formation with that frequency (Wyse 1986; Wyse & Silk 1989). On the other hand, Chiappini et al. (2001) adopted $\Psi(R) \propto \Sigma_{TOT}\Sigma_G^{1.5}$, where Σ_{TOT} is the total disk surface density (dominated in the inner Galaxy by the rapidly increasing stellar profile), and they introduced a cut-off in the SFR efficiency, below 2 $M_\odot$/pc^2. Both SFR laws reproduce satisfactorily several key properties of the MW disk. Those properties are also reproduced satisfactorily to various degrees by models adopting different combinations of SFR, infall and/or radial inflow prescriptions, e.g. (Matteucci et al. 1989; Prantzos & Aubert 1995; Portinari & Chiosi 1999; Naab & Ostriker 2006; Schönrich & Binney 2009a)).

The aforementioned laws make use of the total gaseous profile of the disk. Based on detailed, sub-kpc scale, observations of a large sample of disk galaxies, Bigiel et al. (2008) have found that the SFR appears to follow the H_2 surface density, rather than the HI or the total gas surface density. In a companion paper, Leroy et al. (2008) argued that the observed radial decline in star formation efficiency is too steep to be reproduced only by increases in the free-fall time or orbital time and they found no clear indications of a cut-off in the SFR. Based on an updated set of observational data, Krumholz (2014) concludes in his recent review that "the correlation between star formation and H_2 is the fundamental one".

Following these studies, we checked whether such a correspondence between the adopted SFR and molecular gas profiles also holds in the MW disk. For that purpose, we used up-to-date profiles of the atomic and molecular gas in the MW (see Appendix A) and and we adopted recent data for the SFR profile in the MW disk, including luminous massive stars, pulsars and SN remnants (see Appendix B). The comparison, as discussed in Appendix B appears to favor that idea, as also noticed (albeit

[1] **Notice that the metallicity distribution constrains directly the infall time-scale in models without radial migration; the latter has been shown to broaden slightly the metallicity distribution, as found in Roškar et al. (2008) and in this work (Sec. 4.2**

with older data sets) by Blitz & Rosolowsky (2006). We find that the SFR follows the H_2 profile to better than 30% in the 3-13 kpc range.

In view of this observational support, both for the MW disk (this work) and for external galaxies (Bigiel et al. 2008; Leroy et al. 2008), we adopt here a star formation law depending on the H_2 surface density. In order to calculate it in the model of chemical evolution, we adopt the semi-empirical method of Blitz & Rosolowsky (2006) to calculate the ratio R_{mol}=H_2/HI in a galactic disk (see Appendix A). We notice that this method provides two more observational constraints to disk models, namely the present-day radial profiles of atomic and molecular gas, which are not considered usually (see, however, Ferrini et al. (1994); Mollá & Díaz (2005)). We also notice that a SFR proprtional to the surface density of molecular gas has been recently used in disk models by Kang et al. (2012); Lagos et al. (2011); Fu et al. (2013).

2.2. Chemical evolution

We calculate the chemical evolution in a fully self-consistent way, i.e. by accounting for all the sources and sinks of the mass of a given isotope in a radial zone located at galactocentric distance r. Sinks are due to gas removal, either by local star formation $\Psi(r,t)$, by flow of gas outside the zone r or by removal of stars formed in the past in zone r by stellar migration. Sources are stars produced locally at all previous times and dying at time t within zone r, gas moved inside zone r at time t through radial inflows or infall from the intergalactic medium and finally, stars that have been formed in other regions and are dying in zone r at time t due to radial migration. Obviously, only long lived stars have time enough to migrate away from their birth place before dying and releasing their gas. As already emphasized in Kubryk et al. (2013), to this class belong: interesting metal producers like SNIa (for Fe-peak nuclei) and stars of ∼1.3-2 $M_\odot$ (importants producers of s-nuclei); "sinks" of isotopes, (i.e. long-lived stars ejecting material poor in a given isotope) which deplete deuterium and dilute the other metal abundances.

While in the independent ring models for disk evolution one may work with surface densities of all extensive properties as functions of galactocentric distance r, any coupling of the rings (through gaseous radial inflows or migration of stars) makes it necessary to work with properties integrated over the whole ring of radius r. In the following we shall consider the equations of chemical evolution by integrating all extensive quantities over the surface area of the ring centered at r

$$A(r) \;=\; \pi\,[(r+dr/2)^2-(r-dr/2)^2] \qquad (3)$$

The mass of gas in the ring is, obviously, $m_g(r) = A(r)\Sigma_g(r)$, where $\Sigma_g(r)$ is the gas surface density, and similar expressions hold for all other extensive quantities. The evolution of the mass (in $M_\odot$) of a given isotope i with mass fraction X_i in the zone r is given by

$$\frac{d(m_g X_i)}{dt} \;=\; -\psi X_i \;+\varepsilon_i \;+\; f_i \;+\; s_i \qquad (4)$$

where:

- $\psi(r,t)$ is the star formation rate in the whole ring ;
- $\varepsilon_i(r,t)$ is the rate of isotopic mass release in r by stars produced in all previous epochs everywhere in the disk (including the zone r) and are found in r at time t;
- $f_i(r,t)$ is the *net* rate of isotope i entering zone r from outside the disk (i.e. any infalling minus outflowing material); and
- $s_i(r,t)$ is the *net* rate of isotope i brought in zone r (i.e. gas entering minus gas leaving that zone) because of radial flows from adjacent disk regions.

The first term of the right hand member $\psi(r,t)$=$A(r)\Psi(r,t)$ has already been discussed in Sec. 2.1.3: the star formation rate density $\Psi(r,t) = \alpha\Sigma_{H2}(r,t)$ is proportional to the surface density of the molecular gas (Appendix B).

Since we do not consider outflows from the disk in this work, the term $f_i(r,t)$=$A(r)F_{g,i}(r,t)$ represents simply the infalling material in the disk and it is always positive. As already discussed in Sec. 2.1.2, the rate of gas infall (summed over all isotopes i) is only loosely constrained observationally, both in time and space, and so is its composition. Here we adopt for our baseline model an infall of primordial composition, exponentially declining in time with a radially dependent characteristic timescale $\tau(r)$, displayed graphically in Fig. 5 (bottom right panel).

The term $\varepsilon_i(r,t)$ is calculated as a sum over all zones $N_{r'}$ (including zone r) and all times $t' \le t$ of the ejection rate of isotope i, $E_i(r',t-t')$ from a single stellar population SSP formed at time $t-t'$ in zone r' and found in zone r at time t with a probability P:

$$\varepsilon_i(r,t) \;=\; \int_0^R \int_0^t dt'\psi(r',t')E_i(r',t-t')P(r,r',t-t')dr' \qquad (5)$$

where $\psi(r',t')dt'$ is the stellar mass created in the annulus r' at time t' during the timestep dt'. $E_i(r',t-t')$ is the ejection rate of isotope i at time t from a SSP of unit mass formed at time t' with the metallicity $Z(r',t')$ of the gas of zone r' at that time; it depends on the adopted stellar initial mass function and the adopted stellar yields and it is extensively discussed in Appendix C, where we provide information about the SNIa rates and yields. We consider 82 isotopes of all elements from H to Ge, summing their abundances at each time-step in order to calculate the abundances of the corresponding 32 elements. The term $E_i(r',t-t')$ includes also the contribution from SNIa.

The term $P(r,r',t-t')$ represents the probability that a star born at time t' in zone r' is found in time t in zone r, carrying with it the chemical composition $X_i(r',t')$ but also releasing material corresponding to that composition and to the age $t-t'$. It is normalized to $\int_0^R P(r,r',t-t')dr'$=1 and it is discussed in Sec. 2.3.

The use of the SSP formalism leads to the creation of "star particles" of variable mass $dm_s(r,t) = \psi(r,t)dt$ endowed with the set of chemical abundances $X_i(r,t)$ corresponding to the place and time of their formation. One may use then the same tools for the analysis of the results as in the case of the N-body simulations, and obtain a self-consistent comparison of results between semi-analytical models and N-body simulations, as e.g. in Kubryk et al. (2013).

Although we use two phases of the ISM, the ejecta of the stars are uniformly and "instantaneously" mixed localy in the total amount of gas. The reason is that the time-step in our model (∼30 Myr) is larger than the timescales of the mixing of the ejecta (a few Myr, typically) or the timescales for the survival of molecular clouds. Thus, the ISM in each zone (HI and H_2) is characterized by a unique composition at each time step.

2.3. Stellar migration

The orbit of a test particle (star) in the potential of a galactic disk is commonly described, to first order approximation, as the superposition of a main circular motion (defining the *guiding*

radius), and harmonic oscillations called epicycles. Following Schönrich & Binney (2009a), we call *blurring* the radial oscillations around the guiding radius and *churning* the modifications of the guiding radius. Churning may occur through resonant interactions of the star with non-axisymmetric structures of the gravitational potential (spirals, bar), causing changes in the angular momentum of the stars. The process conserves the overall distribution of angular momentum and does not add random motion, i.e. it does not "heat" the disk radially. In contrast, blurring conserves the angular momentum of individual stars but it heats radially the disk (the epicyclic radius increases with time).

In N-body schemes, the overall effects of both blurring and churning are naturally obtained. Semi-analytical models based on N-body simulations use the knowledge obtained from the N-body run to describe the extent of radial migration, without distinguishing between the two effects, e.g. Minchev et al. (2013); Kubryk et al. (2013); Minchev et al. (2014). Here, we follow SB02 and Schönrich & Binney (2009a) and we parametrise separately blurring and churning.

2.3.1. Epicyclic motion (blurring)

Up to now, two different types of parametrization of radial mixing have been introduced in the literature. Sellwood & Binney (2002) adopted a global mixing scheme, in which one assumes that a star born at radius r' at time t' may be found at time t (i.e. after time $\tau = t - t'$) in radius r with a probability $P(r, r', \tau)$ given by a Gaussian function

$$P(r, r', \tau) \;=\; (2\pi\sigma_\tau^2)^{-1/2} \exp\left[-\frac{(r-r')^2}{2\sigma_\tau^2}\right] \tag{6}$$

where σ_τ is the 1-σ dispersion in the radial displacement of the particles of age τ at radius r. SB02 adopt, for illustration purposes an expression for σ_τ which includes two terms, accounting for churning and blurring, respectively. To describe blurring in the solar neighbourhood, they assume a time-independent amplitude σ_b=0.16 R_0, where R_0=8 kpc is the guiding radius of the Sun and the term 0.16 describes the amplitude of epicyclic motion for a radial velocity dispersion of 34 km/s. Schönrich & Binney (2009a) treated also separately blurring and churning. For the former, they used the distribution function of angular momentum of stars and they made plausible assumptions on the radial and temporal dependence of the stellar radial velocity dispersion.

In this work, we adopt a simple description for the epicyclic motion and calculate its effects independently of those of churning. Our model is based on the epicyclic approximation (Binney & Tremaine 2008), where the oscillations of stars around their guiding radius are described by the resulting dispersion in their radial position σ_r as

$$\left\langle \sigma_r^2 \right\rangle \;=\; \frac{\left\langle \sigma_\upsilon(r)^2 \right\rangle}{\kappa_r^2} \tag{7}$$

where the frequency κ_r of harmonic oscillations at radius r is given as a function of the rotational velocity $V_C(r)$ by

$$\kappa_r \;=\; \sqrt{2}\,\frac{V_C(r)}{r} \tag{8}$$

and for the radial velocity dispersion $\sigma_\upsilon(r)$ we adopt the presently (time t=T) observed one in the Milky Way (Lewis & Freeman 1989), parametrised as

$$\sigma_\upsilon(r, T) \;=\; 40\ \mathrm{e}^{-(\mathrm{r}-\mathrm{R}_\odot)/8\ \mathrm{kpc}}\ \mathrm{km/s} \tag{9}$$

For the time dependence of the radial velocity dispersion we adopt

$$\sigma_\upsilon(r, t) = \max\left\{12, \sigma_\upsilon(r, \mathrm{T})\left(\frac{\mathrm{t}}{\mathrm{T}}\right)^{0.33}\right\}\ \mathrm{km/s} \tag{10}$$

which is in agreement with e.g. the evaluation of Holmberg et al. (2007) for local stars. The time dependence of the rotational velocity $V_C(r, t)$ is obtained self-consistently from our model. The resulting probabilities of epicyclic displacement are presented in Fig. 8 (middle panel). **Notice that the probability distribution obtained by Eq. 6 is not symmetric w.r.t. the birth radius r' of the stars, because the dispersion $\sigma_\tau(r)$ depends on the *final radius* r through Eqs. 7, 8 and 9**.

2.3.2. Radial migration (churning)

Two different types of parametrization of churning have been introduced in the literature. In their probabilistic scheme, SB02 assumed that the amplitude of the radial mixing of stars of age τ found at radius r (Eq. 6) is the sum of the blurring and churning terms $\sigma_{\tau,r} = (\sigma_b^2 + \sigma_c^2)^{1/2}$ where they adopt for the churning term in the solar neighbourhood σ_c=0.4 $R_0\sqrt{\tau/t_0}$, where t_0=12 Gyr is the present age of the local disk. On the other hand, Schönrich & Binney (2009a) adopt a local scheme, in which only stars from up to second-nearest neighbouring zones can exchange places during a time-step, with a probability adjusted to reproduce some observables in the solar neighbourhood, such as the metallicity distribution.

The parametrization of SB02 appears to be supported by the analysis of numerical simulations by Brunetti et al. (2011), who found that the radial displacement of stars in their simulation (concerning only stars, but no gas) can be described by Gaussian functions simulating a diffusion process. They caution that modelling the stellar migration as a diffusion process is valid only for time intervals less than the diffusion time-scale, which they estimate from the simulation results to be of the same order as the rotation period. In other terms, radial migration can be described as a diffusion process with diffusion coefficients depending both on time and (original) position. Their conclusions were confirmed by the analysis of a gas+star simulation (N-body+SPH) for a bared disk galaxy by Kubryk et al. (2013) who evaluated the diffusion coefficients as a function of time and position and applied them to a semi-analytical model of that same galaxy, including detailed chemistry. In that way, they were able to reproduce successfully the results of the N-body simulation (see their Fig. 15). **This implies that the implementation of radial migration through the procedure described in this section, successfully captures the main features of a N-body simulation.**

In a similar vein, Minchev et al. (2013) combined the analysis of a N-body+SPH simulation with a semi-analytical model to study in detail the effects of radial migration on the Milky Way disk. Their scheme of radial migration differs from the one of Kubryk et al. (2013) in that they evaluate the amount of diffusion not with analytical functions derived from the N-body simulations, but through sampling of the original and final stellar positions as a function of time.

In this work, we adopt a probabilistic description of churning, à la SB02, which combines some features from the aforementioned studies, except that the coefficients describing our probabilities are extracted from the N-body+SPH simulation that we analysed in Kubryk et al. (2013). Notice that in Kubryk et al. (2013), the coefficients extracted form the N-body simulation are total (i.e. churning+blurring) coefficients. For the pur-

pose of this work, we extract from that simulation the coefficients for churning *only*, by following the variations of the angular momentum of stars which correspond to variations of their guiding radius. We fit the corresponding radial distributions with Gaussian functions of 1-σ width as a function of birth radius r_i and time t since stellar birth :

$$\sigma(t, r_i) = a(r_i)t^N + b(r_i) \quad (11)$$

and we find $N \sim 0.5$. However, the disk galaxy analysed in Kubryk et al. (2013) has a strong and long bar, reaching a length of ∼8 kpc in the end of the simulation at 10 Gyr. In contrast, the Milky Way has a small bar, not necessarily as old as 10 Gyr (see next section); its effect on churning will then be smaller than in the aforementioned simulation. Indeed, if we adopt the coefficients of Kubryk et al. (2013) we obtain a large dispersion in the local age-metallicity relation in the framework of our model. We chose then to reduce these coefficients of Kubryk et al. (2013) while keeping their temporal and radial dependence, by applying the transformation

$$\sigma(t, r_i)_{thiswork} = \sigma(t/5, r_i)_{KPA2013} \quad (12)$$

i.e. we assume that the evolution at, say, t=10 Gyr in our model is similar to the one around t=2 Gyr in the simulation of Kubryk et al. (2013); physically, this corresponds to the epoch where the bar in the simulation has similar size to the one of the current MW bar. *A posteriori*, we shall see (Sec. 4) that this transformation leads to acceptable results for the observed dispersion in the local age-metallicity relation. The churning coefficients of our model are presented, discussed and compared to those of Schönrich & Binney (2009a) in Sec. 3.2.

The two migration mechanisms are treated independently of one another in our model, i.e. we can consider the effects of blurring or churning alone. This allows us to evaluate the impact of each one of them on the radial mixing of the disk and on the resulting dispersion in e.g. the age-metallicity relation in the solar neighbourhood (see Sec. 4). Of course, in our baseline model, both of them are considered.

The mechanism of radial migration discussed in this section, is not applied to the gas in our model. In contrast to the dissipationless stellar fluid, gas is dissipative and is little affected by that mechanism; this can be seen e.g. by comparing Figs. 4 (stars) and 5 (gas) in Kubryk et al. (2013). The bar, however, drives gas inwards and we describe this radial inflow in the next section.

2.4. Radial gas flows

Pioneering work of Tinsley & Larson (1978) and Mayor & Vigroux (1981) noticed the potential importance of radial gaseous flows for the chemical evolution of galactic disks. Lacey & Fall (1985) presented a systematic investigation of the causes of such flows, namely: i) viscosity of the gaseous layer of the disk, ii) mismatch of angular momentum between the gas of the disk and the gas infalling on it and iii) gravitational interactions between the gas and a bar or a spiral density wave in the disk. They noticed that in all cases it is difficult to predict the magnitude and the profile of the corresponding inflow velocity and explored with parametrized calculations the impact of such effects on the chemical evolution of the Galaxy.

Further parametrized investigations with simple 1D models of disk evolution are made in e.g. Clarke (1989); Sommer-Larsen & Yoshii (1990); Goetz & Koeppen (1992); Chamcham & Tayler (1994); Edmunds & Greenhow (1995); Thon & Meusinger (1998); Portinari & Chiosi (2000) and more recently in Spitoni & Matteucci (2011); Bilitewski & Schönrich (2012); Mott et al. (2013); Cavichia et al. (2014). They have various motivations (mostly to fit the abundance profiles, but also gas and star profiles) and they are generally applied to the study of the MW disk. As expected, results are not conclusive, because they depend not only on the parametrization of the unknown inflow velocity patterns, but also on the other unknown (and parameterized) ingredients of the models, especially the adopted SFR and infall profiles as functions of time. In fact, most of the studies focus on one (and seldomly more) causes of the radial inflows, i.e. either viscosity (e.g. Spitoni & Matteucci (2011) or infall (e.g. Bilitewski & Schönrich (2012)) or the impact of a galactic bar (e.g. Cavichia et al. (2014)), assuming a corresponding inflow velocity profile.

Among the alleged causes of radial inflows, the impact of a galactic bar is well established, both from simulations and from observations. Numerical simulations (Athanassoula 1992; Friedli & Benz 1993; Shlosman & Noguchi 1993) showed that the presence of a non-axisymmetric potential from a bar can drive important amounts of gas inwards of corotation (CR) fuelling star formation in the galactic nucleus, while at the same time gas is pushed outwards outside corotation. In a disk galaxy, this radial flow mixes gas of metal-poor regions into metal-rich ones (and vice-versa) In the past, bars were believed to flatten the chemical abundance profile in the disk because of the large scale streaming motions they induce, e.g., Friedli et al. (1994); Zaritsky et al. (1994); Martin & Roy (1994); Dutil & Roy (1999). But recent studies with two-dimensional (2D) higher spectral and spatial resolution integral field units show that there are negligible differences of abundance gradients between barred and unbarred galaxies, e.g. Sánchez et al. (2012). We notice that in our recent study with a high resolution N-body+SPH simulation of an isolated barred disk (Kubryk et al. 2013), we find that the bar drives indeed large amounts of gas from corotation inwards, but no significant gas displacement occurs outside corotation (see Fig. 5 in Kubryk et al. (2013)). It seems now that bars may be changing the chemical abundance profile inside the corotation radius but they have only a small impact outside the bar itself.

One of the (many) difficulties of introducing the effect of a bar on the radial gas flows of a galactic disk in semi-analytical models, is the uncertainty on its strength and length evolution. The length of the MW bar is estimated to 2.5-3 kpc (Babusiaux & Gilmore 2005; Bobylev et al. 2014), although higher values have also been reported (Cabrera-Lavers et al. 2007).

For the purpose of this work, we adopt a radial inflow velocity profile induced by a bar of current size R_B=3. kpc, having a corotation radius at R_C=1.2 R_B, a typical relation between bar length and corotation radius (e.g. Athanassoula 1992). The flow outside corotation is outwards and we assume it extends up to the outer Lindblad resonance (OLR), located at radius $R_{OLR} \sim 1.7\ R_B$ (e.g. Athanassoula et al. 1982), which corresponds to ∼6.2 kpc today. The flow velocity profile $\upsilon_f(r)$ has azimuthally averaged absolute velocities of a few tenths of km/s, similar to the one of Portinari & Chiosi (2000). The adopted velocity profile is displayed in Fig. 6.

Our treatment of infall and radial flow is not self-consistent: as Mayor & Vigroux (1981) and Lacey & Fall (1985) have pointed out, the two are coupled through conservation of angular momentum. However, a quantitative treatment of the effect implies that the angular momentum of the infalling gas is known; this is not the case, since the rotational profile of the infalling gas is unknown. A parametrised exploration of that effect is performed in the recent work of Bilitewski & Schönrich (2012).

Table 1. Global observational constraints for the MW

	Disk (>2 kpc)	Bulge (<2 kpc)
Stellar mass (10^{10} $M_\odot$)	3.-4. (1)	1.-2. (1)
Gas mass[a] (10^9 $M_\odot$)	8.1±4.5 (2)	1.1±0.8 (3)
HI mass (10^9 $M_\odot$)	4.9±2.5 (2)	0.005 (3)
H_2 mass (10^9 $M_\odot$)	0.9±0.4 (2)	0.05 (3)
SFR ($M_\odot$/yr)	0.65-3 (4)	—
Infall rate ($M_\odot$/yr)	0.6-1.6 (5,6)	—
CCSN rate (per 100 yr)	2±1 (7)	0.23±0.1 (7)
SNIa rate (per 100 yr)	0.4±0.2 (7)	0.14±0.06 (7)

a: Total includes 0.28 of He by mass fraction.
References:(1) Flynn et al. (2006); (2) This work (Appendix A); (3) Ferrière et al. (2007); (4) Robitaille & Whitney (2010); Chomiuk & Povich (2011); (5) Marasco et al. (2012); (6) Lehner & Howk (2011); (7) Prantzos et al. (2011).

Here, we simply ignore that effect, implicitly assuming that the infalling gas has the same angular momentum as the disk gas at the accretion radius.

2.5. Observational constraints for the Milky Way

A successful model of the chemical evolution of the Milky Way, especially one involving a large number of parameters (as all semi-analytical models featuring radial motions of stars and gas), should satisfy a large number of observational constraints, both global (concerning the whole Galaxy) and local ones (concerning the solar neighbourhood). Unfortunately, the values of most of the observational constraints depend heavily on underlying model assumptions. Thus, the mass of the bulge is estimated as low as 9×10^9 $M_\odot$ (McMillan 2011) or as high as 2.4×10^{10} $M_\odot$ (Picaud & Robin 2004). Similar uncertainties affect the stellar disk, e.g. (Flynn et al. 2006; McMillan 2011), concerning its scalelength (from ∼2 to more than 3 kpc) and total mass (from ∼3 to more than 5×10^{10} $M_\odot$. For the purpose of this work we adopt the results of the analysis of Flynn et al. (2006) (their Fig. 15), showing that for a local stellar surface density of 39 $M_\odot$/pc^2 (35.5 $M_\odot$/pc^2 "counted", plus an assumed 10% enhancement from azimuthal average of spiral arms) and for scalelengths in the range 2.2-3.5 kpc, the mass of the disk lies in the range 3-4 10^{10} $M_\odot$and the one of the bulge in the range 1-2 10^{10} $M_\odot$. The total stellar mass (bulge+disk) is much better constrained, $\sim 5\times 10^{10}$ $M_\odot$.

In Table 1 we present the basic observational facts concerning the present-day amounts of gas and stars in the bulge and the disk of the Milky Way. We also present adopted values and references for the rates of star formation, infall (fairly uncertain), core collapse supernovae (CCSN) and thermonuclear supernovae (SNIa). Radial profiles for all those quantities (except the uncertain profile of the infall rate and the unknown ones of supernovae rates) constitute also important constraints for the models and they are discussed in Appendices A and B. We include the rotational velocity of the gas in the constraints, since radial migration changes the distribution of the baryonic component and thus affects the rotation curve. Radial abundance profiles of stars and gas constitute equally important constraints, but they depend also on adopted nucleosynthesis yields. Here we consider only the O and Fe profiles and we leave a detailed discussion of all other elements for an accompanying paper.

The observational constraints for the solar neighbourhood include the "classical" ones: local amounts of gas and stars (Table 2), age-metallicity relation, metallicity distribution, abundance ratios vs metallicity. The introduction of stellar radial migration makes it possible to use some new constraints: Schönrich & Binney (2009a) suggested that this ingredient may help explain quantitatively the observed "two-branch" behaviour of the [O/Fe] vs [Fe/H] relation, namely the local thick vs. thin disk dichotomy. We confirm this here, using large data sets from recent surveys. We also use the observed (albeit yet uncertain) dispersion in the local age-metallicity relation as a supplementary constraint of our model. We shall refer to all those constraints in Sec. 4. **We draw, however, the attention to the fact that comparison of model results to observations is not a straightforward enterprise, because of various selection biases affecting the latter (magnitude limited, kinematic etc.). In our case, all local observables of this model concern the so-called "solar cylinder", that is all stars found in the end of the simulation in a cylinder of radius 0.25 kpc (half the size of our radial bin), perpendicular to the Galactic plane and centered on the solar position, at Galactocentric distance R_0=8 kpc. In those conditions, a successful comparison to observations does not imply that the model is necessarily correct, only that it possesses potentially interesting features. The wealth of current and forthcoming data (with e.g. RAVE, LAMOST, GAIA etc.) will make necessary the adoption by the models of the same selection criteria as the observational surveys, in order to draw meaningful and quantitative conclusions.**

Finally, we also compare our results to the "average histories" of mass building of Milky Way type galaxies (total stellar mass of $5\ 10^{10}$ $M_\odot$) from the recent analysis of HST+SDSS data from van Dokkum et al. (2013).

Table 2. Local observational constraints (surface densities of gas and stars - in $M_\odot$/pc^2 - at R_0=8 kpc)

Stellar mass[a]	38±2	*(1)*
Gas mass[b]	10.3±3.	*(2)*
HI mass	6.1±2.	*(2)*
H_2 mass	1.3±0.7	*(2)*

a: Total stars, includes stellar remnants
b: Total gas, includes 0.28 of He by mass fraction.
References:(1) Flynn et al. (2006); Bovy & Rix (2013); (2) This work (Appendix A).

3. Global evolution

The results of our model for all the main outputs (total mass, mass of stars and gas, either atomic or molecular, rates of star formation, infall, CCSN and SNIa, as well as the scalelength of the stellar disk) as a function of time are displayed in Fig. 2, both for the bulge (here taken to be the region within r=2 kpc) and the disk (r >2 kpc). They are compared to the observational data reported in Table 1, plotted at time t=12 Gyr.

The results reproduce fairly well the aforementioned present day observational constraints, with the exception of the gas amounts in the bulge, which our model overpredicts. We notice, however, that a significant fraction of the bulge gas is in the form of ionized gas (∼3 10^7 $M_\odot$, Ferrière et al. 2007, increasing the total gas amount of the bulge by ∼30%; if this is taken into account, the discrepancy with our model (which does not account for ionized gas) is reduced considerably. A smaller discrepancy appears in the present day rate of CCSN: both in the bulge and the disk, our model predicts values on the low side of the observations, despite the fact that the corresponding star formation rates are well reproduced. This discrepancy is due to the adopted

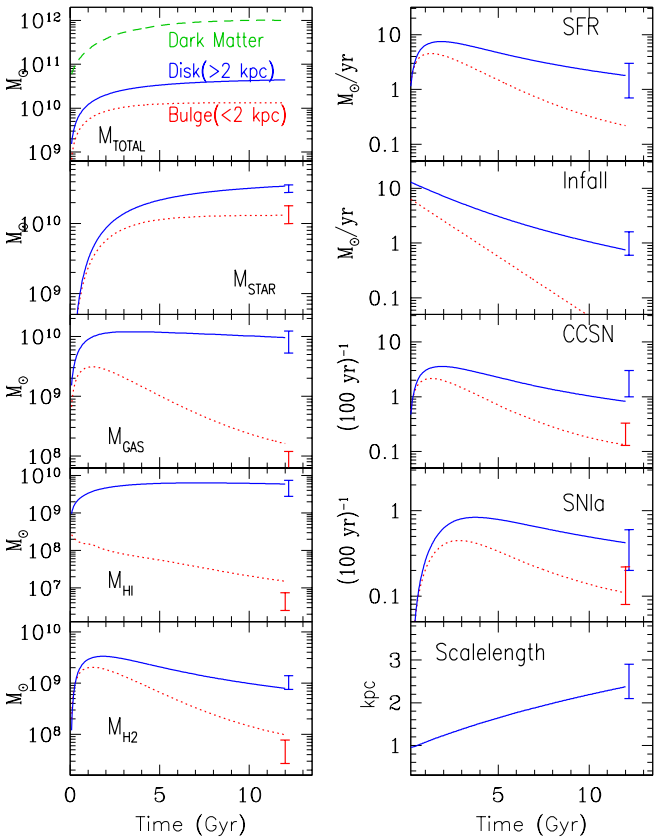

Fig. 2. Evolution of various quantities in the baseline scenario. In all panels, *solid blue* curves correspond to the evolution of the disk (r >2 kpc) and *dotted red* ones to that of the bulge (r <2 kpc), respectively. Vertical bars at 12 Gyr represent observational constraints (see text and Table 1).

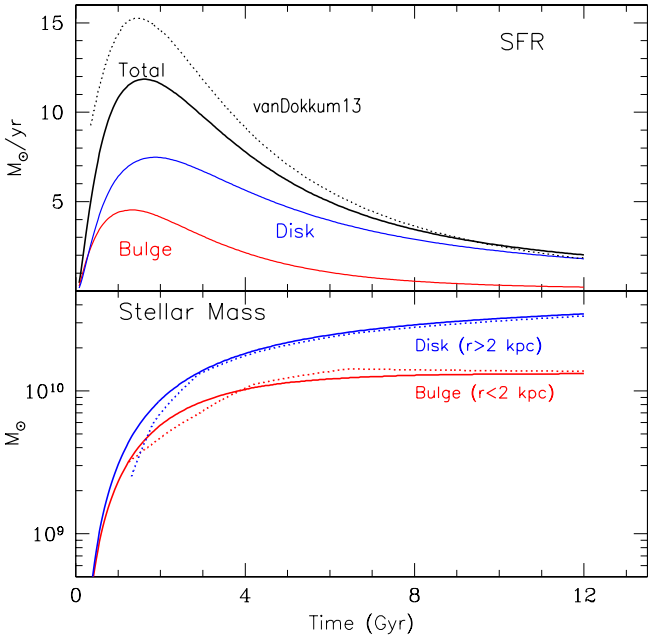

Fig. 3. Comparison of the model results to the observed "stacked" evolution of disk galaxies of stellar mass 5 10^{10} $M_\odot$ (*dotted* curves) from van Dokkum et al. (2013). *Top:* Evolution of the total SFR (black solid curve), decomposed into bulge and disk contributions. *Bottom:* Evolution of the stellar mass of the bulge (r <2 kpc) and of the disk (r >2 kpc) of the model (*solid* red and blue curves, respectively).

stellar IMF, which has a steep slope of x=-2.7 (the Scalo slope) above 0.5 $M_\odot$(see Appendix C for details).

Regarding the evolution of the gas, we notice that its mass in the disk remains quasi-constant after the first ~2 Gyr, while it decreases by almost a factor of 30 in the bulge. It is interesting to notice that the adopted prescriptions for the evaluation of the molecular fraction and the corresponding SFR (Sec. 3.1 and Appendix B) lead to a different evolution between the atomic and molecular contents of the bulge and the disk: the bulge is dominated today by H_2, while the disk is dominated by HI, as observed. Also, the total disk SFR, ~2 $M_\odot$/yr, corresponds fairly well to the observed one; this was not obvious *a priori*, because we assume that the SFR depends on the molecular gas which is concentrated in the inner Galaxy (see discussion below).

Finally, the scalelength of the stellar disk increases steadily from ~1.5 kpc at 2 Gyr to 2.3 kpc at 12 Gyr. The latter value is in reasonable agreement with values in the literature: 2.1±0.3 kpc from the TMGS survey (Porcel et al. 1998), 2.25 kpc from COBE/DIRBE data analysis (Drimmel & Spergel 2001), 2.15±0.14 kpc from the dynamical analysis of SEGUE G-dwarfs (Bovy & Rix 2013). In Sec. 4.3 we shall discuss further the issues of thin and thick disk scalelengths.

The question of whether the Milky Way is a typical spiral galaxy or not is an open one, since it appears underluminous for its rotational velocity of 220 km/s (Flynn et al. 2006; Hammer et al. 2007). One may also ask whether the Milky Way evolved as an average disk galaxy of the same present-day mass of 5 10^{10} $M_\odot$. In a recent study van Dokkum et al. (2013) provide relevant data by studying progenitors galaxies of that mass out to redshift z=2.5, using data from the 3D-HST and CANDELS Treasury surveys. They find that ~90% of the stellar mass of those galaxies was built since z=2.5, with most of the star formation occurring before z=1. Furthermore, the mass in the central 2 kpc of those galaxies increased by a factor of ~3 between z=2.5 and z=1, implying that bulges likely formed in lockstep with disks during that period. However, after z=1 the growth in the central regions gradually stopped but the disk continued to be built up.

In Fig. 3 we compare our results to those of van Dokkum et al. (2013) (their Fig. 4, where we converted redshifts in look-back time assuming a ΛCDM cosmology with parameters from the recent PLANCK analysis). It can be seen that our result for the total SFR (upper panel) lie slightly below the SFR of van Dokkum et al. (2013) (by ~20% at the peak of SFR, the difference gradually decreasing with time. At late times, there is a fairly good agreement between our model and the data. Concerning the stellar masses (lower panel), our results, both for the bulge (assumed to be the region of radius r <2 kpc, as in van Dokkum et al. (2013)) and the disk (r >2 kpc) are in fairly good agreement with the observed "stacked" evolution of MW-type galaxies. In the case of the bulge, the agreement for the early part of the evolution stems for our adoption of a rather long infall timescale for the bulge (τ=2 Gyr). At late times we always find a small increase in the mass of the bulge, due to migration from the inner disk (see Sec. 4). Overall, we conclude that our results are compatible with the idea that the MW evolved as a typical disk galaxy of present day stellar mass ~5× 10^{10} $M_\odot$.

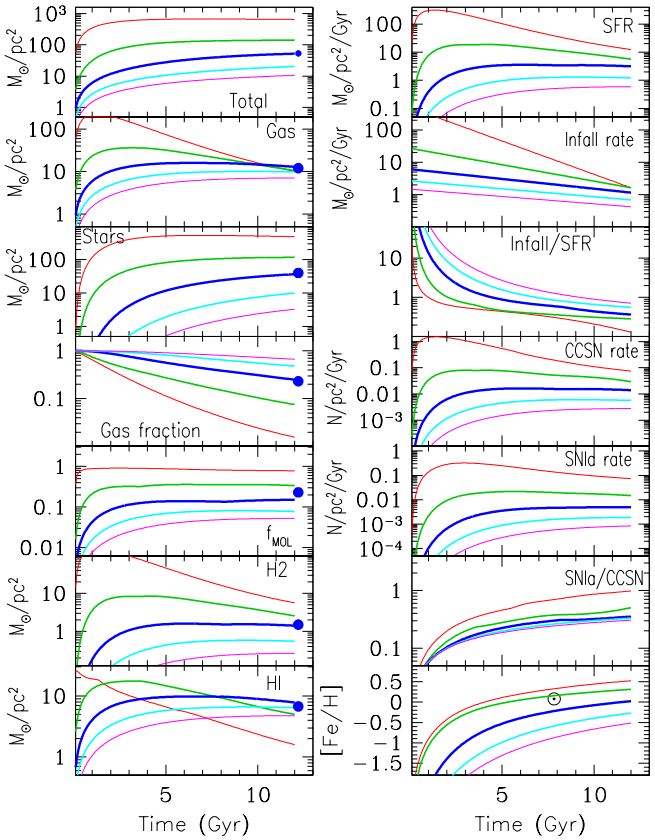

Fig. 4. Evolution of various quantities in the baseline scenario as a function of time, for five different radial zones, at 2(red), 5 (green), 8 (thick blue), 11 (cyan) and 14 (magenta) kpc. Observational data for local surface densities of gas and stars are indicated with filled circles at T=12 Gyr.

In Fig. 4 we present the evolution of several key observables for selected radial zones (2, 5, 8, 11, 14 kpc) of our model. The main common feature is the more rapid evolution of the inner disk, reflected in the earlier rise of the stellar surface density of the inner zones and in the more rapid decrease of the corresponding gas fractions. In the cases of the stellar and gaseous surface densities, the local observations at r=8 kpc (Table 2) are nicely reproduced.

A noticeable feature is the quasi-constancy of the molecular fraction f_{MOL} for most of the evolution; it is due to the fact that from the two factors assumed to affect it (Eq. B.3 to B.6 in Appendix B), the temporal profile of stellar density flattens at late times, while its early rise in the inner regions is compensated by the corresponding decrease of the gaseous profile.

The net gas depletion time scale (i.e. taking into account both the SFR and the infall rates) is shorter in the inner Galaxy than in the outer one: the ratio of the infall rate to the SFR becomes smaller than unity within ~1 Gyr at r=2 kpc but only after 10 Gyr at r=14 kpc. This gives a measure of the radially varying star formation efficiency of the model, due to the adopted SFR dependence on the molecular gas.

Finally, the evolution of [Fe/H] in the local gas (bottom right panel of Fig. 4) never saturates, even in the inner zones: there is always a steady albeit small increase of metallicity, even at late times. This result is in agreement with the work of Minchev et al. (2013), but it contrasts with the results of Schönrich & Binney (2009a), who find little evolution in metallicity for all the zones of their model after the first couple of Gyr. On the other hand, Minchev et al. (2013) do find a steady increase of [Fe/H] in all zones (as here), but at the same pace everywhere. In other terms, the metallicity gradient stays always the same in Schönrich & Binney (2009a) and approximately the same in Minchev et al. (2013), while it is reduced (in absolute value) in our case. This simple result, due to the different assumptions about the infall rate vs SFR of the different models, has important implications for the impact of the radial migration on the chemical properties of the disk.

3.1. Gaseous profiles and the SFR

Fig. 5 presents a synthetic view of the main results of our model, compared to observations. Except for the right top (velocity curve) and bottom (infall timescale) panels, all other panels display three profiles, at 4, 8 and 12 Gyr; the latter (thick curve) is to be compared with observational data.

As discussed in Sec. 2.1.2, the infall timescale of the disk as a function of radius (right bottom panel) is tailored to smoothly match the bulge timescale of $\tau(r<2$ kpc)~1.5 Gyr to the timescale of the outer disk while going through the value of $\tau(r=8$ kpc)~7-8 Gyr for the solar neighbourhood. The latter has been shown to provide a good fit to the local metallicity distribution in simple (independent-ring) models of the MW chemical evolution (e.g. Chiappini et al. (1997); Boissier & Prantzos (1999)) and we show that this is also the case here (Sec. 4), although the adopted SNIa rate and the effects of radial migration play also some role. The resulting profiles of infall rate appear in the right above-bottom panel. Because of the shorter infall timescales in the inner disk, the final infall profile peaks around 3 kpc.

In a recent work, Marasco et al. (2012) use a model of the Galactic fountain to simulate the neutral-hydrogen emission of the Milky Way. Their model was developed to account for external galaxies with sensitive HI data. For appropriate parameter values, their model reproduces well the observed HI emission of the MW. They find a global current value of ~2 $M_\odot$/yr for the MW and they derive the infall profile displayed in the right above-bottom panel (dashed curve), which peaks at ~9 kpc. In our model we obtain a similar value for the total present day infall rate (~1 $M_\odot$/yr, see Fig. 3), but our infall profile peaks at ~3 kpc. Bilitewski & Schönrich (2012) tested the Marasco et al. (2012) profile in their chemical evolution model with radial flows induced by the mismatch of angular momentum between the infalling gas and the disk (i.e. with flow velocities distinctively different from our adopted radial inflow pattern). Their best fit models (reproducing the Fe abundance profile) have an exponentially decreasing radial profile for the infalling gas, not a peaked one; when they introduce the Marasco et al. (2012) profile, they find a local minimum, at 9 kpc in the final [Fe/H] profile, which is totally uncorrelated to observations. We do not attempt such a test here and we simply notice that the existence of a peak in the present day infall profile appears naturally in our model, albeit not in the claimed position. Further studies and understanding of the properties of the gas accreted onto the MW, including its velocity profile, will provide much more severe constraints to evolution models of the Galaxy.

The radial profiles of gas (total, HI and H_2) are in rather good agreement with observations, for the largest part of the disk. In the inner disk, the presence of the bar plays an important role, inducing radial flows of both gas (see below) and stars. The mi-

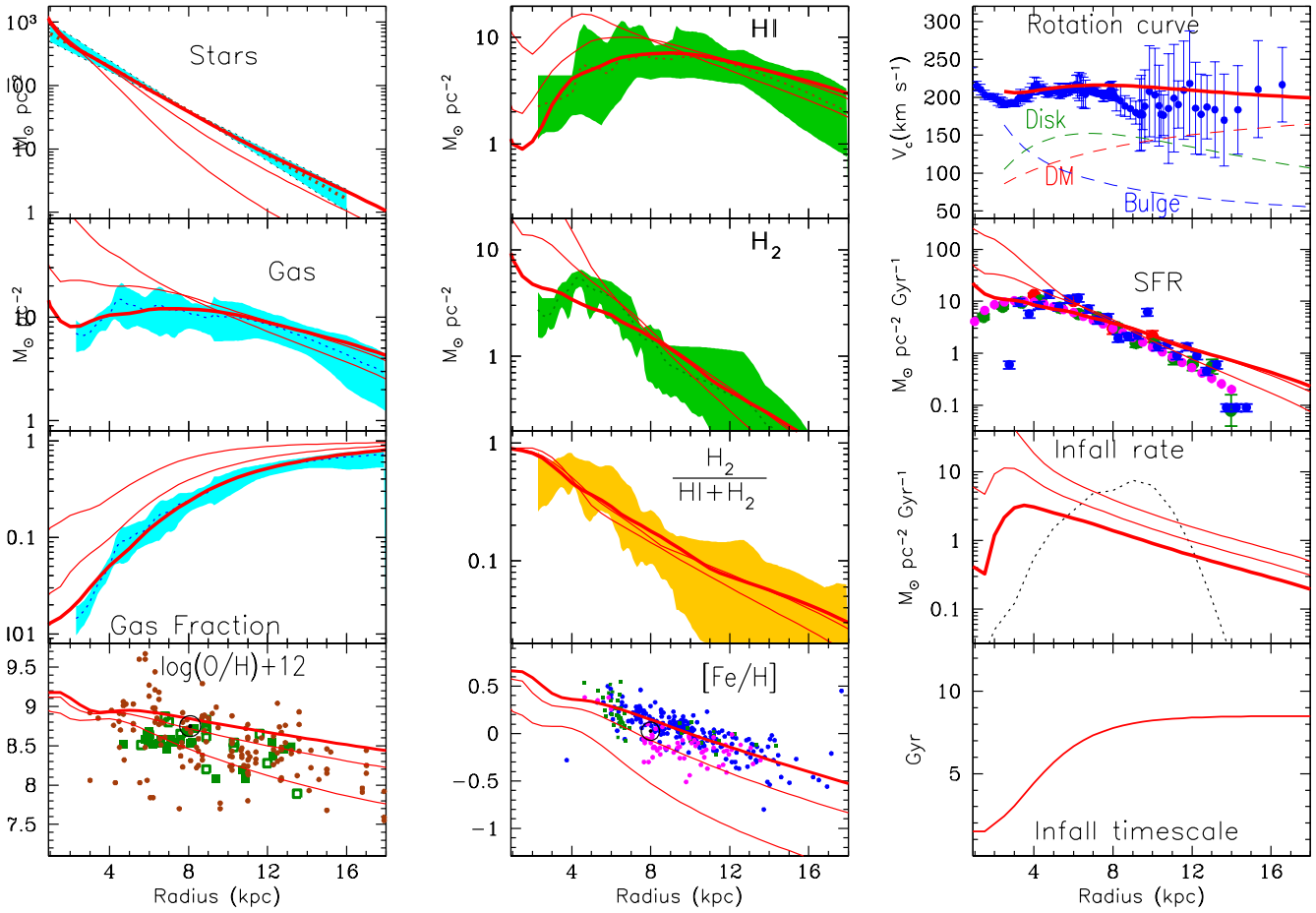

Fig. 5. Model profiles (*red solid* curves) at 4, 8 Gyr (*thin* curves) and at 12 Gyr (*thick* curves) of various quantities and comparison of the latter with observational data concerning the present-day disk of the Milky Way. For all gaseous profiles (gas, HI, H_2, gas fraction and molecular fraction), observational constraints are those discussed in Appendix A and presented in Fig. A.2. For stars, the shaded area is bounded by two exponential curves with scalelengths R_d=2.1 and 2.7 kpc, respectively, which fix the range of plausible values for the stellar disk; they are normalised to a surface density of Σ_*(R=8 kpc)=38±2 $M_\odot/pc^2$ in the solar neighbourhood. Data for the MW rotation curve are from Sofue (2012); the *dashed* curves represent the contributions of the bulge, disk and dark matter (blue, green and red), respectively (see text for the bulge contribution). Data for the star formation rate (SFR) profile are discussed in Appendix B and displayed in Fig. B.1. The observed present day profile of infall rate (*dotted* curve) is based on estimates of Marasco et al. (2012) (see text). The *bottom right* panel displays the adopted timescales for exponential infall. Data for Oxygen are from HI regions (Simpson et al. 1995; Afflerbach et al. 1997) and OB stars (Smartt & Rolleston 1997; Daflon & Cunha 2004) and for iron from Cepheids (Luck & Lambert 2011; Lemasle et al. 2013; Genovali et al. 2013).

grating long lived stars, had they remained in place, they could return their H-rich ejecta in the local ISM at late times. The overall result of those motions is a total gas profile going through a broad maximum at ~7 kpc, still compatible with the observations (Fig. 5, panel in left column and second row from the top). This is also true for the HI profile (middle top panel in Fig. 5).

The "dearth" of stars in the inner disk (with respect to an exponential profile) is due to radial migration. It has a clear impact on the molecular profile and, consequently, on the SFR in that region. Indeed, the molecular fraction f_2 is proportional to the product $\Sigma_{Gas}\Sigma_*^{0.5}$ (Eq. B.5) and, because of the reduced Σ_{Gas} in the region 3-5 kpc, it lays on the low side of the observational bounds (middle above-bottom panel in Fig. 5). Multiplied with the corresponding gas surface density (left below-top panel in Fig. 5), it leads to a lower than observed H_2 surface density in the "molecular ring" (middle below-top panel in Fig. 5). As a result, the corresponding SFR in that region is also lower by ~20% than the adopted observed profile (right below-top panel in Fig. 5). For the same reason, i.e. the dependence of the SFR on the product $\Sigma_{Gas}\Sigma_*^{0.5}$, the SFR in the outer disk decreases more slowly than its "observed" profile: in that region the profile of H_2 and, thereoff the SFR, is dominated by the slowly decreasing gas profile, contrary to the inner disk, where it is dominated by the rapidly increasing star profile.

The model rotation curve at t=12 Gyr compares fairly well to the data of Sofue (2013) (right top panel in Fig. 5). It peaks at ~212 km/s in the solar neighbourhood, where the contribution of the disk exceeds slightly the one of dark matter. This is slightly lower than the canonical IAU value of 220 km/s and clearly lower than some values recently proposed in the literature (see Bhattacharjee et al. (2013) and references therein). The rotation curve is used in all time-steps to evaluate the epicyclic

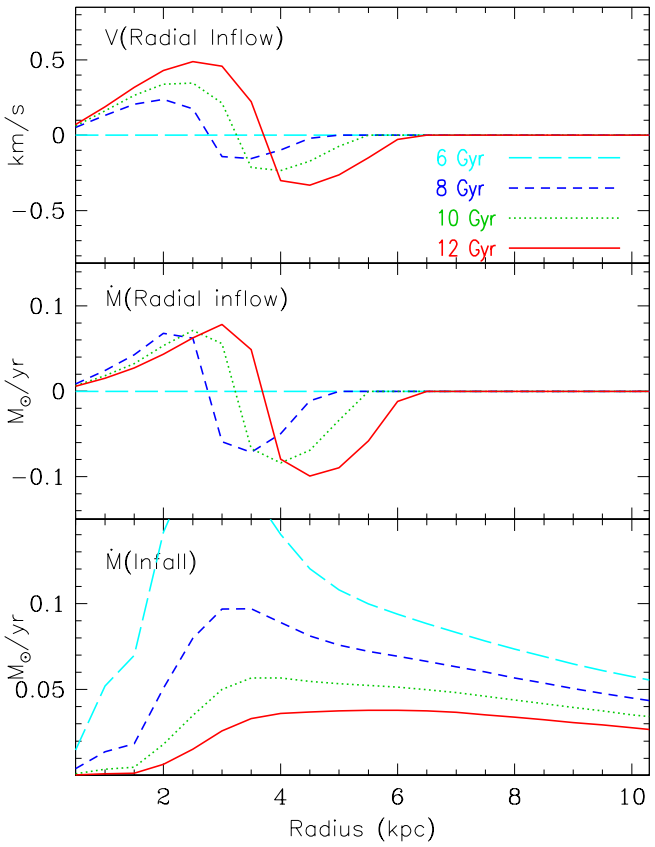

Fig. 6. *Top:* Adopted velocity profile for radial inflow. Positive velocities indicate flow inwards (towards the Galactic center) and negative ones an outward flow. The flow velocity is everywhere zero before the assumed appearance of the bar at t=6.5 Gyr. Profiles are given at t= 6, 8, 10 and and 12 Gyr (cyan long-dashed, blue short-dashed, green dotted and red solid, respectively). As corotation moves outward (see text), the flow pattern moves also. *Middle:* Corresponding mass flow profiles through radial zones r *Bottom:* Corresponding mass infall profiles (rate of mass infalling over the ring of radius r and width Δr=0.5 kpc, at t=6, 8, 10 and and 12 Gyr.

motion and the extent of blurring in the disk (see Sec. 2.3.1). We notice that the contribution of the material within 2 kpc to the total rotation curve is not straightforward to calculate. Given that the boxy/peanut bulge (which is the main contributor in mass within 2 kpc) is vertically extended, we model the bulge rotation curve for radii beyond 2 kpc using the spherical approximation, which should not be worse than a number of other approximations made here. We will refrain from modelling the rotation curve within 2 kpc.

The gaseous profiles are affected by the radial inflow induced by the bar, which is modelled here as shown in Fig. 6. It is assumed that the bar appears after t=6 Gyr and that it grows in size, its radius increasing from 2 kpc at 6 Gyr to 3 kpc at 12 Gyr and its corotation radius from 2.4 kpc initially to 3.6 kpc in the end. Simulations show indeed that in disks with large gas fractions, the appearance of a bar can be delayed for several Gyr (Athanassoula et al. 2013), compard to cases with no gas. It then grows with time, while slowing down, pushing the corotation resonance outwards, as in our model. The velocity profile has positive values (towards the Galactic center) inside corotation and negative ones (towards the anti-center) outside corotation and up to the OLR. Maximum absolute values of the (azimuthally averaged) radial flow velocity are 0.5 km/s. Higher values for the adopted duration of the bar would lead to substantial depletion of the gaseous layer in the inner disk, impossible to replenish by infall. Indeed, the middle and bottom panels of Fig. 6 display the net radial flow rate through the ring of radius r (middle) and the rate of infall onto that same ring (bottom). Around corotation, the former (calculated as $f_r = 2\pi\, r\, \upsilon_r\, \Sigma_g(r)$) is higher than the latter. Although our model is nothing more than a toy model (since none of the adopted parameters can be observationally determined at present), we notice that the range of the velocity values are similar to the ones adopted in Portinari & Chiosi (2000) for the case of a simulated bar (their figure 13), i.e. υ_r <0.5 km/s.

The present day profiles of gas and SFR reflect short-term features of the Milky Way and they do not constitute strong constraints; indeed, on a timescale of 10^7 yr, comparable to the time-step of our model, they may change considerably. Constraints obtained through time integrated profiles (with negligible late variations within short timescales) are more severe in that respect. The profiles of stars and metallicity belong to this class. As already discussed (see Sec. 2.4 and references therein) one of the main effects of the radial flow induced by a bar is to flatten the abundance gradients in the region around the corotation (the other one being to fuel star formation in the central regions). This is clearly seen in the final oxygen profile (left bottom panel of Fig. 5), which displays a flattening in the region 3-5 kpc. The iron profile (middle bottom panel of Fig. 5) is less affected, because the sources of Fe (mainly SNIa) are less affected by those of O (CCSN) in that region. The latter are distributed as the gas, which has a flat profile in that region, whereas the former - belonging to an older population - have a steeper distribution. The evolution of the metallicity profiles is similar to the one obtained in many other studies (e.g. Boissier & Prantzos (1999); Hou et al. (2000)) and reflects the inside-out formation of the disk, with the profiles flattening with time. Those profiles will be widely used in Sec. 4 to study the main observables in the solar neighbourhood. A detailed study of the evolution of the abundance profiles of all the elements of our model, both in the gas and in the stellar populations, is left for a future work (Kubryk et al. in preparation).

Fig. 7 displays the star formation profiles of our models as a function of the local gas surface density for three different epochs: at t=4, 8 and 12 Gyr, respectively. Comparison is made to the data compiled by Krumholz et al. (2012) for a large number of star-forming galaxies. It can be seen that our values lie in the low range of the observed SFR values for a given gas surface density. In particular, the rate at 12 Gyr presents the steep rise at Σ_{Gas} ~10 $M_\odot$/pc^2 that is "observed" in the MW disk; however, it is slightly smaller than "observed" in the inner disk and slightly larger than "observed" in the outer disk. These discrepancies are also displayed in the SFR profile presented in Figs. 5 (right below-top panel) and B.2. The key point here is the absence of a correlation between the SFR and the local gas surface density in both the data and the model. It implies that some other factor is at play, namely molecular gas, as discussed in Appendix B and in the recent review by Krumholz (2014).

3.2. Stellar profiles

The model stellar profiles result from the combined history of star formation and radial migration. The former is discussed in the previous section. Here we analyse the impact of stellar radial migration.

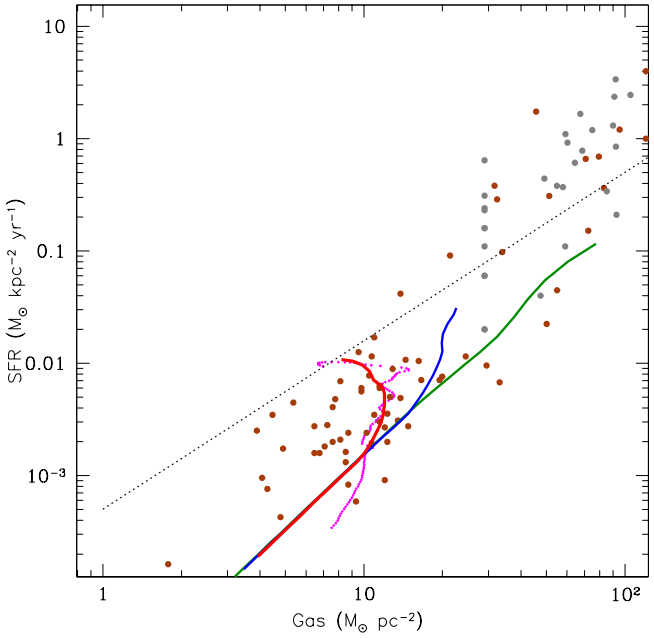

Fig. 7. SFR vs. gas surface density. Model results are displayed for three different epochs, after times 4 Gyr (green curve), 8 Gyr (blue) and 12 Gyr (red). The latter is compared to the observationally inferred SFR profile of the Milky Way (dotted magenta curve), obtained as discussed in Appendix B. The data points concern extragalactic measurements, compiled by Krumholz et al. (2012) (see also Fig. B.2). The dotted line is $\propto \Sigma_{Gas}^{1.5}$.)

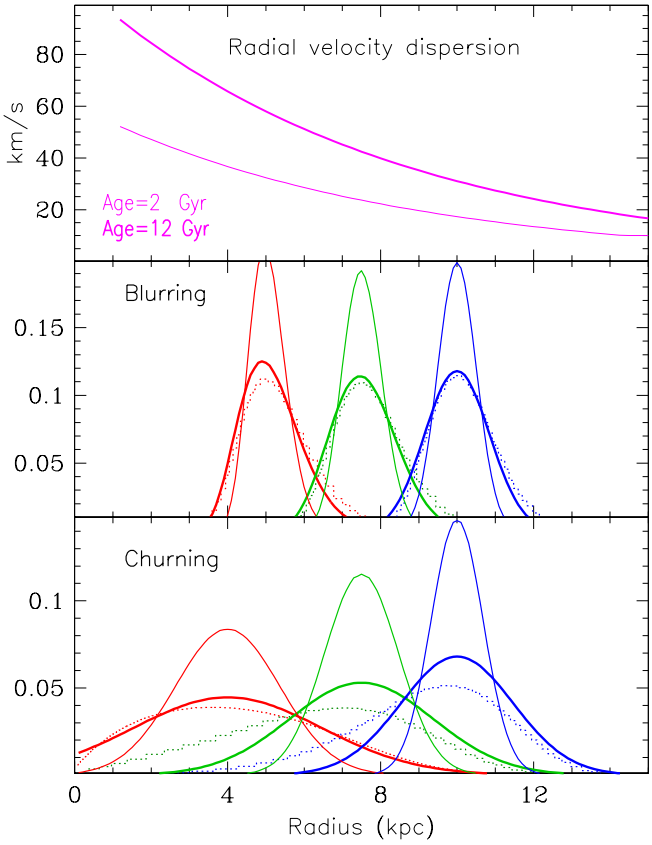

Fig. 8. *Top:* Model radial velocity dispersion at 2 Gyr (thin curve) and 12 Gyr (thick curve). *Middle:* Probabilities of blurring. *Bottom:* Probabilities of churning. In all panels our results (solid curves) are displayed for for stars of home radius r=5, 7.6 and 10 kpc, and for 2 Gyr (thin) and 12 Gyr (thick curves). The latter should be compared to the corresponding quantities reported in Schönrich & Binney (2009a) (*dotted histograms*).

The adopted radial velocity dispersion profile $\sigma_{v,r}$ appears in Fig. 8 (top panel) for two epochs, at t=2 Gyr and 12 Gyr[2]. The corresponding local values (at r=8 kpc) are 21 km/s and 40 km/s, respectively. We calculate then the probabilities of radial displacement due to epicyclic motion and we show the results for the same two epochs and three different radial zones in the middle panel. The thick solid curves correspond to an age of 12 Gyr, i.e. to $\sigma_{v,r}$=40 km/s for the stars in the solar neighborhood and may be compared to the corresponding curve obtained by Schönrich & Binney (2009a) (dotted curve in middle panel). Our formulation of the epicyclic motion produces similar distributions to those of Schönrich & Binney (2009a) in the solar neighborhood and beyond, and somewhat narrower distributions in the innermost disk, but the overall agreement is quite good.

The corresponding probability functions for churning appear in the lower panel of Fig. 8. They are evaluated as discussed in Sec. 2.3.2 and are broader than those of blurring. In the inner disk, they are not very different for the ones adopted in Schönrich & Binney (2009a), but they are clearly narrower than the latter in the outer disk: in the simulation of Kubryk et al. (2013), less radial migration occurs in the outer regions.

In the top panel of Fig. 9 we present the total probabilities (blurring + churning) of a stellar population born in a given radius (here: 4, 8 and 12 kpc, respectively) to be found in some other disk radius r after times 4, 8 and 12 Gyr. We recall that the radial bin in our simulation has a size Δr=0.5 kpc. As discussed in Sec. 2.3 (see also Fig. 8) for the blurring and churning probabilities separately, the probability of finding a star from the inner disk to the outer one is larger than the inverse, because of the larger variations in the gravitational potential perturbations in the inner disk than in the outer disk.

The middle panel of that figure displays the fractions of stars born in those same radii, that are found at radius r in the end of the simulation; those fractions are the time integrated probabilities of the upper panel, weighted by the corresponding SFR(r, t) history. This explains why the distribution of the outer region is more peaked and less wide than the inner one in the middle panel than in the top one: stars are formed in the inner disk earlier than in the outer one, on average, because of the inside-out formation scheme adopted here. As a result, inner disk stars have on average more time to migrate than those formed in the outer disk. Even if the probability distributions in the top panel were identical at all birth radii (assuming for instance the same potential inhomogeneities over all the disk), those in the middle panel would still be wider in the inner disk, simply because of the inside-out star formation. Quantitatively, one sees that 1-2 % of the stars born in the region of radius 4±0.25 kpc are found in the end of the simulation in radius r=8±0.25 kpc. On the other hand, only 13% of the stars born in radius r=8±0.25 kpc are found in that radial bin in the end. However, if the two adjacent

[2] We calculate the profile of radial velocity dispersion and the corresponding epicyclic amplitudes at each time step; here we show the results for only two ages.

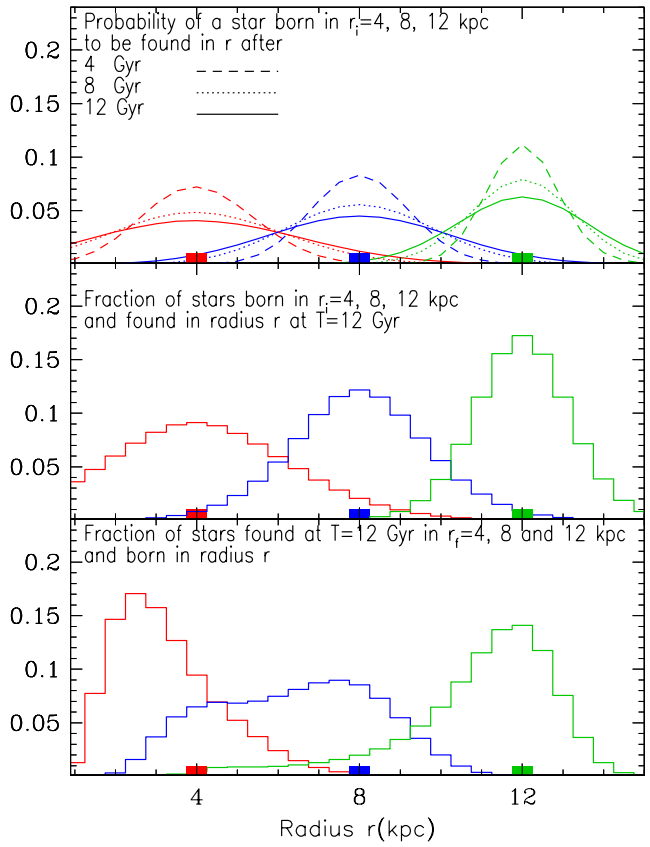

Fig. 9. *Top*: Probabilities of stellar migration (blurring + churning) adopted in this work (see text); they are shown for three birth radii (4, 8 and 12 kpc) and for three snapshots (after 4, 8 and 12 Gyr). *Middle*: Fractions of stars which are born in radii 4, 8 and 12 kpc and are found in galactocentric radius r in the end of the simulation, at T=12 Gyr. *Bottom*: Fractions of stars found in the end of the simulation in radii 4, 8 and 12 kpc according to their birth radius *r*. In all panels, radial bins are Δr=0.5 kpc wide, as indicated by the bin width of the histograms and the size of the coloured boxes.

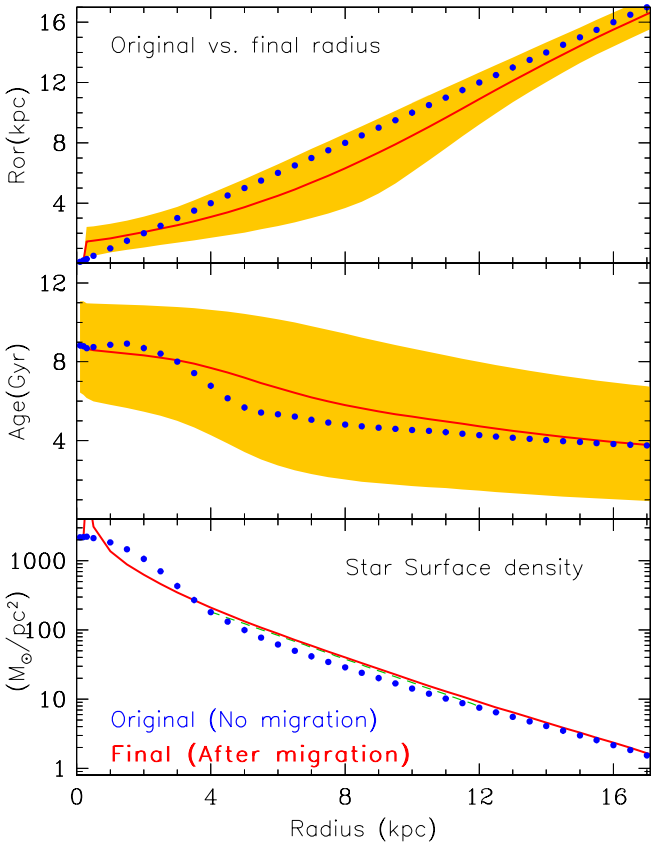

Fig. 10. Average radius of origin of stars (*top*), average stellar age (*middle*) and star surface density profile (*bottom*), as a function of galactocentric radius. In all panels, the *continuous* (red) curve corresponds to the results of the model with radial migration (churning+blurring), while the *dotted* (blue) curve shows the results with no radial migration. In the *top* and *middle* panels, the *shaded aerea* contains the $\pm 1\sigma$ values - containing ±34% of the stars - around the average. In the bottom panel, a best fit exponential with scalelength r_d=2of the exponentially decreasing outwards.25 kpc in the 3 to 13 kpc region and with $\Sigma(r$=8 kpc)= 38 $M_\odot/pc^2$ is also displayed (green dashed line).

bins on either side of that radius are also considered (to account for epicyclic motions of amplitude ±1. kpc), one sees that the fraction of stars born in that region and still found there in the end, is ∼52%, i.e. more than half of the stars formed in that "extended solar neighbourhood" - defined as r=8±1 kpc - remain in place.

The bottom panel in Fig. 9 displays the fractions of stars found in the end of the simulation in final galactocentric radii r_f=4, 8 and 12 kpc, respectively, and born in other positions r in the disk. These fractions integrate not only the probability distributions (upper panel) and the SFR histories (as in the middle panel), but also the fact that there is more mass in the inner disk than in the outer one, because the surface density profile decreases exponentially outwards. For that reason, the resulting fractions are asymmetric in each radius, with larger fractions originating from the inner disk than from the outer one. Thus, from all the stars presently found in the bin at r=8±0.25 kpc, only ∼10% are formed in that bin; if the "extended solar neighbourhood" is considered, as before, the corresponding fraction rises to 38%. Only 7% of the remaining stars originate outside the extended solar neighbourhood (at radii r >9. kpc), while 55% of the stars of that region are formed in r <7 kpc and have migrated here; ∼12 % of its stars have migrated from r <4 kpc. In contrast, a negligible amount of stars presently found in r=13 kpc originates from r=8 kpc.

The impact of radial migration (blurring+churning) on some radial properties of the disk appears in Fig. 10. The top panel displays the initial (r_i) vs. final (r_f) star radius. The blue dotted line is the diagonal ($r_i = r_f$) while the solid curve indicates the average value $\overline{r_i}$ and the shaded area the $\pm 1\sigma$ values around that average. It can be seen that stars presently found in the region 5< r_f <10 kpc, originate from regions located on average ∼1.-2. kpc inwards. On the other hand, stars presently found in the bulge (here taken to be the region r <2 kpc) have a significant fraction of them originating from the inner disk, from up to 3 kpc. Finally, stars beyond r=13 kpc are very little affected by radial migration on average (at least with the adopted scheme for churning). We note that Minchev et al. (2013) find a bimodal distribution function for the average birth radius of stars presently in the solar neighbourhood (their Fig. 3, right): the maximum is located in the region ∼5.6 kpc and a secondary maximum is found

at ~7 kpc, compared to a single maximum at ~6.2 kpc in our model. It is difficult to compare the two models, since they are based on different N-body simulations and different descriptions of the radial migration. We suspect that it is the stronger bar and larger OLR radius in their case that produces a more extended mixing of stars from the inner regions to the solar neighborhood, while we have "calibrated" our bar to the one of the MW size.

The aforementioned results explain also the average age of stars in each galactocentric radius (middle panel in Fig. 10): the average age of stars formed in the bulge (r <2 kpc) is ~9 Gyr, in the solar neighbourhood ~5 Gyr and beyond 12 kpc it is 4 Gyr. Stars presently found in the region 5< r_f <11 kpc are, on average, 1-2 Gyr older than those formed *in situ*, because their population has been altered by the radial migration of stars from the inner disk. Again, beyond r=13 kpc, the average stellar age is not affected. It should be noticed that a uniform age dispersion of ~ ±3 Gyr is found at all radii.

It is clear that radial migration, as implemented in our model, affects the stellar disk mostly in the 4 to 12 kpc region. This can be also seen in the final surface density profile (bottom panel in Fig. 10), which presents a slight but significant deviation from a pure exponential in that region. As a result, the stellar profile cannot be reproduced with a single exponential, but rather with two exponentials. This feature also appears in the study of Schönrich & Binney (2009a), obviously for the same reasons, since the adopted coefficients for radial migration are not too different in the two studies, as discussed above. It is not clear, however, that this is a generic feature of such models, since it may also depend, to some extent, on the boundary conditions, i.e. the normalisation of the infall rate profile.

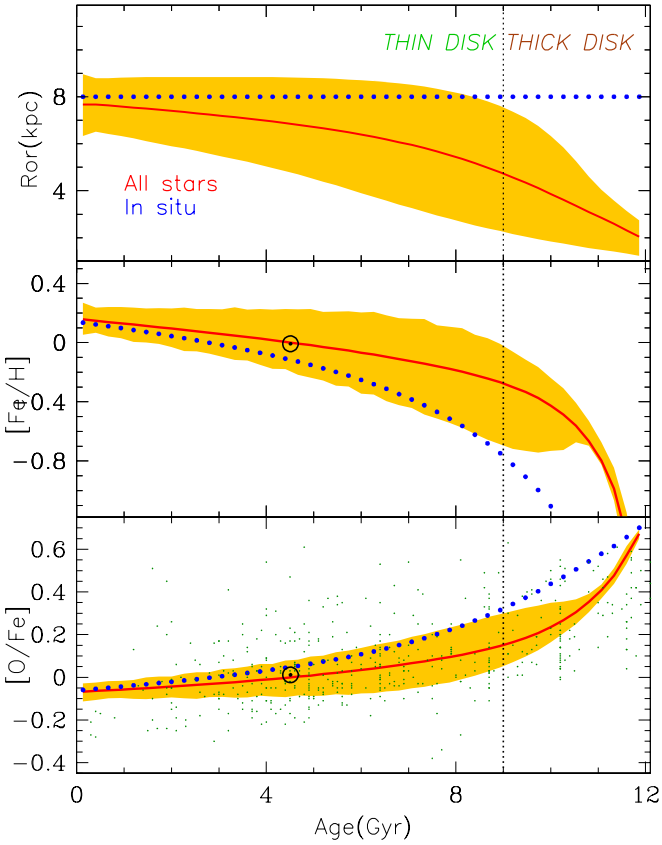

Fig. 11. Solar neighbourhood: Average birth radius (*top*), average [Fe/H] (*middle*) and average [O/Fe] of stars (*bottom*) as function of their age. In all panels, the *dotted* (blue) curves display the results for stars formed *in situ* and the *solid* (red) curves the results for all stars found at T=12 Gyr in radius r=8±0.25 kpc. The *shaded aereas* in all panels enclose ±1σ values around the corresponding averages. Data points are from the survey of Bensby et al. (2014). The dotted vertical line at 9 Gyr separates the thin from thick disk stars, according to the assumption made here (see Sec. 4.1. The symbol ⊙ denotes the position of the Sun in the corresponding panel, as well as in Figs. 12, 13 and 14.

4. Local evolution

The results discussed in the previous section for the whole disk help understanding in detail the results obtained for the solar neighbourhood, defined here as the radial bin at r=8±0.25 kpc. Fig. 11 displays the average birth radius of stars found in this zone in the end of the simulation, as a function of their age. In the absence of any radial migration, the birth radius would be the horizontal line at r=8 kpc. As expected - in view of the discussion in sec. 3.2 - the average birth radius when radial migration is considered, is close to 8 kpc for the youngest stars, but it decreases steadily for older stars. The reason for that decrease is twofold: first, the older stars have more time to migrate from other regions and, in particular, from the inner disk; second, the SFR at r=8 kpc is low in the first few Gyr, while it is quite high in the inner disk during that same period (see top right panel in Fig. 4). Thus, the old stars migrating here from the inner disk overwhelm by number the few old stars formed locally. A local "average star" of age=4.5 Gyr originates from r ~7 kpc, whereas stars older than 8 Gyr were born inwards of 5.5 kpc, on average. Equally interesting is the spread in birth radii which increases as a function of age (the associated 1-σ dispersion in the birth radius is indicated by the shaded area). Thus, ~2/3 of the local stars of solar age have birth radii ranging between 5.5 and 8.5 kpc, while 2/3 of those with an age of 8 Gyr were born between 2.5 and 8 kpc. Their birth place impacts on their chemical composition and affects significantly the properties of the solar neighborhood. We notice that the same behaviour of birth radius vs. age, not only qualitatively but also quantitatively, is obtained in the N-body simulation of e.g. Loebman et al. (2011); Brook et al. (2012), which are not tuned to reproduce a Milky Way disk: the oldest stars of their simulation presently in the "solar cylinder" (between 7 and 9 kpc from the center), have home radii as small as 2 kpc.

4.1. The local age-metallicity relation and its dispersion

The impact of radial migration on the chemical evolution of the local disk appears in the middle and bottom panels of Fig. 11. The local average age-metallicity relation (middle panel, red solid curve) is flatter than the one for the locally born stars (blue dotted curve); the latter represents the metallicity evolution of the local ISM. The difference is nul for the youngest stars and increases with stellar age: it is ~0.1 dex for a stellar age of 4.5 Gyr and 0.4 dex for 8 Gyr old stars. The reason is that stars from the inner disk dominate the local old stellar population, and the inner regions have undergone a more rapid chemical evolution (see bottom right panel in Fig. 4). The flattening depends on both the adopted radial migration scheme (the churning coefficients) and the whole history of the disk (the inside-out formation and the resulting abundance profiles). We notice here that Minchev et al. (2013) obtain a less pronounced flattening in the solar neighbor-

hood (with respect to the local gas evolution, their Fig. 4); this is probably due to the fact that the metallicity evolution differs little from one radial zone to another in their model, whereas we obtain substantial differences (Fig. 4), as a result of the inside-out formation.

Our model curve of [Fe/H] increases slowly but steadily with time, by 0.1 dex in the last 4.5 Gyr and by a larger amount (~0.4 dex in the previous 5 Gyr period, between 4.5 and 9 Gyr). As discussed in the previous paragraphs, the increase is even more pronounced for the stars formed in situ (i.e. the local gas evolution, displayed as a dotted curve in the middle panel of Fig. 11), which amounts to 0.2 dex for the last 4.5 Gyr.

The behaviour of metallicity vs age plays an extremely important role in studies of galactic chemical evolution. It probes the degree of gas processing through star formation and metal release (a strong late star formation favouring a fast late increase of metallicity), the role played by infall (a strong late infall dilutes the metal content of the gas and stops the increase in metallicity), etc. Most of the successful models of local chemical evolution predict a continuous rise of the metallicity with time, as this one; see e.g. Boissier & Prantzos (1999); Goswami & Prantzos (2000); Chiappini et al. (1997); Naab & Ostriker (2006); Schönrich & Binney (2009a) for independent-ring models, but also in models with radial migration, e.g. Minchev et al. (2013, 2014). The near solar value for the metallicity of the gas obtained at 12 Gyr is in agreement - within observational errors - with observations of nearby young stars (Nieva & Przybilla 2012). Since the gas is locally well mixed today - and presumably at earlier times as well - the fact that the metallicity of the Sun 4.5 Gyr ago is larger than the corresponding gas value in our model, implies that the Sun was not born locally, but migrated from inner galactic regions as suggested in Wielen et al. (1996). We notice that in our model, the average stellar metallicity 4.5 Gyr ago is practically solar (red solid curve in middle panel of Fig. 11) and higher than the corresponding gaseous metallicity by 0.15 dex: a "typical" local star of age 4.5 Gyr has a solar metallicity. Combined with the upper panel of the same figure, it implies that the chemical composition of the Sun is indeed representative of the 4.5 Gyr old local stellar population, which has an *average* home radius of ~7 kpc (at least in the framework of this particular model). Although it is rather early to draw definitive conclusions, it appears that the hypothesis that the Sun was formed inwards (by 1-2 kpc) of its present galactic position, is the most convenient in order to explain several observational facts (see Nieva & Przybilla (2012) for an updated discussion and references).

The bottom panel of Fig. 11 displays the O/Fe vs age relation. It starts at values around [O/Fe]~0.5 for the oldest stars - where only CCSN enrich the ISM - and then decreases smoothly to [O/Fe]~0 for the youngest stars, because of the steady Fe input from SNIa. The average stellar value of [O/Fe] at a given age (red solid curve) is lower than the one corresponding to the evolution of the local ISM (blue dotted curve), because it is dominated by stars from the inner regions where evolution occurred at a more rapid pace: as can be seen in the right above-bottom panel of Fig. 4, the ratio of SNIa/CCSN increases more rapidly in the inner disk than in the solar neighbourhood, implying that the O/Fe ratio decreases more rapidly in those inner zones; this is also reflected in the composition of the stars that have migrated in r=8 kpc from those regions.

The decrease of [O/Fe] with time is more rapid for the older stars and considerably slower for those younger than 9 Gyr; the latter corresponds to a quasi-equilibrium between CCSN and SNIa rates at late times (Fig. 4). This distinctive behaviour in the decrease of [O/Fe] for old and young stars is also apparent in the work of Haywood et al. (2013) who reanalysed a sample of local stars with high quality abundance determinations (their Fig. 6 and 7). However, they interpret their data as two clearly differing regimes with different slopes of [α/Fe] vs age, while we find just a gradual decline of the [α/Fe] ratio, albeit with a strong reduction of the corresponding slope with time.

An interesting feature in Fig. 11 is the dispersion introduced by radial migration in the [Fe/H] and [O/Fe] vs. age relations. The 1-σ dispersion is quite important in the former case and it will be further analysed below. However, we notice that the dispersion in the [O/Fe] relation is quite small (~0.1 dex) at every age; the reason is the quasi-similar evolution of the SNIa/CCSN ratio in all radial zones of our model (right above-bottom panel of Fig. 4), except those of the bulge. This fact justifies the use of [O/Fe] as a proxy for age.

Anticipating on the contents of the next section concerning the issue of the thick disk, we notice that stars both older and younger than ~9 Gyr cover a wide range of overlapping [Fe/H] values (respectively, from less than -1 to ~0 and from -0.7 to 0.3) and also overlapping ranges of [O/Fe] values (from 0.6 to ~0.1 and from 0.3 to <0, respectively). As already done in Binney & Sanders (2013) and Haywood et al. (2013), we shall classify those stars as belonging to the thick and thin disks, respectively; we shall explore the consequences of that assumption in the next section.

In the top panel of Fig.12, the blue dashed curve displays the fraction of stars born at 8 kpc as a function of stellar age, while the red solid curve displays the corresponding fraction of all stars present at r=8 kpc (i.e. born anywhere but found in 8±0.25 kpc in the end of the simulation). The fraction of stars born in-situ is a decreasing fraction of stellar age, because of the SFR rate history (see Fig. 4, top right panel). On the other hand, the fraction of all stars currently in the solar neighborhood increases between 0 and 8 Gyr because large numbers of old stars have migrated to the solar neighbourhood, shifting the average age to higher values (see Fig. 10). In particular, almost all stars older than 10 Gyr have been formed inwards of r=5 kpc, on average. We notice that a similar result concerning the formation of stars presently found in the solar neighbourhood vs. those formed in situ was found in Roškar et al. (2008), i.e. their Fig. 3 (bottom left panel).

This result has some important implications: It implies that radial migration makes it impossible to try to infer the past local star formation rate through star counts as function of stellar age (e.g. Rocha-Pinto et al. (2000)): most of the old stars presently found here were formed elsewhere, whereas the opposite holds for the younger stars. For that same reason, it becomes impossible to use the method of the luminosity function of white dwarfs in order to infer the star formation history of the solar neighbourhood, e.g. Isern et al. (2013) and references therein.

In the middle panel of Fig. 12 we compare the model [Fe/H] vs age relation to data of two recent major surveys. We display observational data from a re-analysis of the Geneva-Copenhagen survey (Casagrande et al. 2011) and from the survey of Bensby et al. (2014). In both cases, we determine average values and ±1-σ widths around those averages in the [Fe/H] vs age relation, by using age bins of 1 Gyr; we apply the same statistics to our model stars. Both sets of observational data display a quasi-constant [Fe/H]~0 for ages up to 9 Gyr (in fact, a fairly small decrease of 0.1 dex for Casagrande et al. (2011) or 0.2 dex for Bensby et al. (2014)). In contrast, our model presents a sizeable metallicity evolution, as discussed above.

In order to make a better comparison of the metallicity dispersion vs age between observations and the model, we show in the bottom panel of Fig. 12 the 1-σ dispersion around the aver-

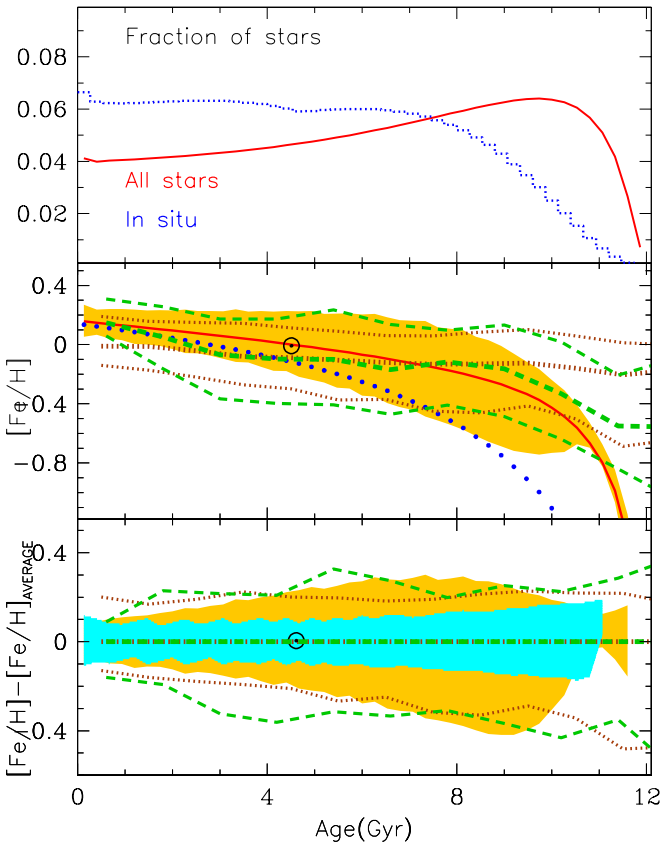

Fig. 12. Solar neighbourhood: *Top*: Fraction of all stars ever born *in situ* in the solar neighbourhood (blue *dotted*) and fraction of all stars found in the solar neighbourhood at T=12 Gyr (red *solid*) as a function of stellar age. Average [Fe/H] of stars (*middle*) and 1-σ dispersion around the average (*bottom*) as function of stellar age, compared to observations. The *solid* (red) curve in the middle panel displays the results for all stars found at T=12 Gyr in radius r=8±0.25 kpc. In both panels, the *shaded (yellow) areas* represent the ±1σ limits of the model; the brown (*dotted*) and green (*dashed*) curves represent the corresponding averages and ±1σ limits of the observations of Casagrande et al. (2011) and Bensby et al. (2014), respectively. The narrower *blue shaded aerea* in the *bottom* panel shows the results of a calculation with blurring only.

age value. We display our results for blurring only (blue shaded aerea) and for blurring plus churning (yellow shaded area), and we compare with the corresponding dispersions of the data in Bensby et al. (2014) (green dashed curves) and Casagrande et al. (2011) (brown dotted curves). We notice some differences between the two data sets, the one of Bensby et al. (2014) having a slightly larger dispersion than the one of Casagrande et al. (2011); **this may be due to kinematic biases and to magnitude selection effects**.

The epicyclic motion, as calculated in our model, produces a uniform dispersion of ±0.1 dex for most stellar ages; only the older ones - age >9 Gyr - have a slightly larger dispersion, up to ±0.2 dex. The epicyclic motion is not sufficient to explain the observed dispersion in the age-metallicity relation. When churning is also considered, dispersion increases steadily, up to ±0.3-0.4 dex. For thick disk stars (assumed here to be older than 9 Gyr), the model dispersion starts decreasing. The reason is that these old local stars are formed almost exclusively in the innermost disk regions, where the very rapid evolution produced a quasi-identical age-metallicity relation; as a result, these stars show smaller dispersion in their metallicities. Our analysis of the data of Casagrande et al. (2011) and Bensby et al. (2014) shows no such decrease for old stars. We notice however, that a reanalysis of the data of the GCS survey and of Adibekyan et al. (2011) by Haywood et al. (2013), leads to a decreasing dispersion in [Fe/H] for the older stars, in line with our model (at least qualitatively).

In summary, the dispersion in the age-metallicity relation stems from the extent of churning (which is related to the inhomogeneities of the gravitational potential) *and* the SFR history of the disk. Comparison of theoretical dispersions to observed ones constrains the combination of those processes, not the just churning (or churning+blurring). Comparison to other data, e.g. past and present metallicity gradients, will be necessary to disentangle the various effects.

4.2. The local metallicity distribution

In the absence of stellar migration, the number of stars as a function of their age constitutes the best and most direct tracer of the past star formation history of a given region. Because of the lack of reliable stellar age estimates, metallicity is often used as proxy for age. Assuming that no stars enter or leave the system, the metallicity distribution (MD) probes not only the past star formation, but also the influence of any gaseous flows: outflows shift its peak to lower metallicity values (they reduce the "effective yield"), while inflows make it narrower than in the absence of gaseous flows (i.e. the so called "closed box" model). The situation becomes more complicated when Fe is used as a tracer of metallicity - which is usually the case - because more than half of galactic Fe is produced by SNIa, the rate of which is not related to the star formation rate in a simple way. And it becomes even more complex in the case of stellar radial migration, because the MD probes then not the local star formation history, but the history of a large fraction of the galactic disk. In those conditions, it is difficult to make robust inferences from the observed MD about some particular model ingredient (either the SF history, the SNIa rate, the infall rate, any radial inflows or the extent of radial migration), since all of them play some role in shaping the MD. Despite the degeneracy of the problem, the MD is an important constraint of the overall model of galactic evolution.

In Fig. 13 we present our results for the local MD. The lower panel displays the MD of stars formed *in situ* (dotted histogram) which peaks at 0.08 dex and terminates abruptly at 0.1 dex. It also displays the MD obtained with only the epicyclic motion considered (dashed histogram), which peaks at the same metallicity and is slightly broader, extending up to 0.15 dex. Finally, the total MD - including blurring and churning - is shown (red curve): it is considerably broader than the previous two distributions and extends up to [Fe/H]=0.4. It was already pointd out by Chiappini (2009) that the local evolution cannot produce stars as metal-rich as [Fe/H]=0.4. Here we show that the conclusion holds even if epicyclic motion is considered. Only radial migration can account for such stars in the solar neighbourhood.

The upper panel of Fig. 13 shows the average age of the local stars, for those formed *in situ* (blue dotted curve) and for all stars (red solid curve). The latter are always older than the former, by 1 Gyr for the less metallic ones and by 2.5 Gyr for those of [Fe/H]=0. For higher metallicities, there are no stars formed *in situ* and the average age of those present in the solar neighborhood - coming from inner regions - is around 3-4 Gyr. The corresponding 1-σ dispersion in ages is ∼1 Gyr for the less

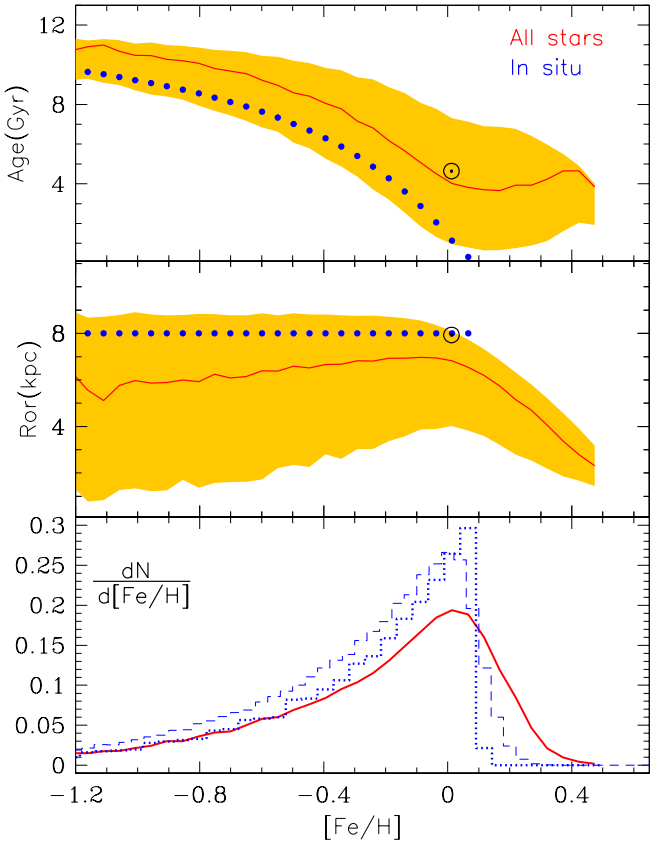

Fig. 13. Solar neighborhood: Average age of stars (*top*), average birth radius (*middle*) and number distribution of stars (metallicity distribution, *bottom*) as function of their metallicity. In all panels, the *dotted* (blue) curves display the results for stars formed *in situ* and the *solid* (red) curves the results for the average values of all stars found at T=12 Gyr in radius r=8±0.250 kpc. The *shaded aereas* in the *top* and *middle* panels enclose $\pm 1\sigma$ values around the corresponding averages. The *dashed* histogram in the lower panel is calculated with the effect of epicycles only.

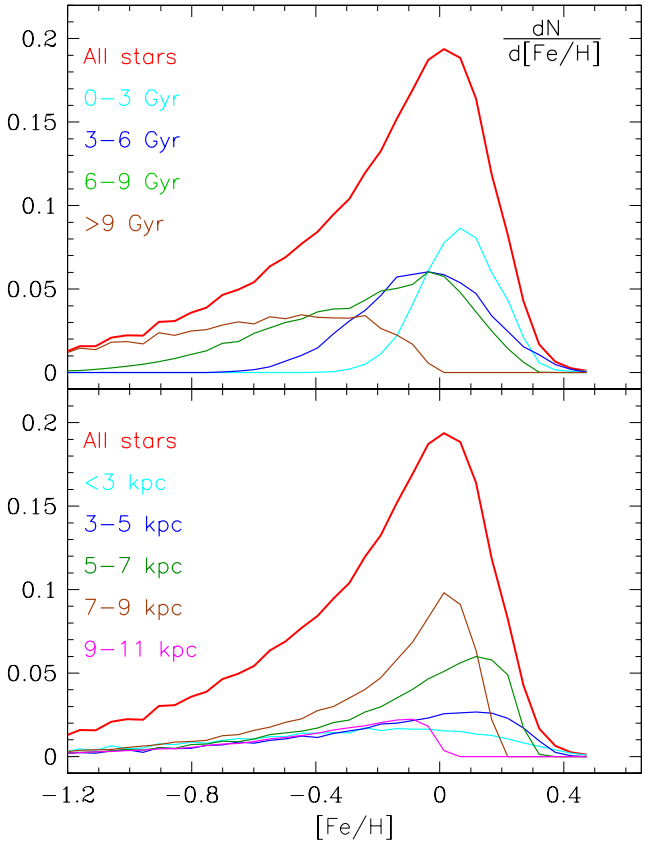

Fig. 14. Solar neighborhood: *Top:* Metallicity distribution in the region of radius r=8±0.25 kpc, with the age ranges of the corresponding stellar populations. *Bottom:* Metallicity distribution in the region of radius r=8±0.25 kpc, with the radial ranges of the birth radii of the corresponding stellar populations.

metallic stars (which are quite old anyway) and it increases to more than 2 Gyr for the metal-rich stars.

The middle panel of Fig. 13 shows the average birth radius of the local stars. The old and less metallic ones originate from r ∼6 kpc, whereas those with solar metallicity originate from r ∼7 kpc; the average birth radius of all local stars is at r ∼6.5 kpc, as stated in Sec. 2.3. Star more metallic than the Sun have birth radii increasingly closer to the galactic center, with those of [Fe/H]=0.4 coming from the region around 2 kpc.

The results of the last two paragraphs are presented in greater detail in Fig. 14. The upper panel displays the MDs of four age ranges, namely 0-3 Gyr, 3-6 Gyr, 6-9 Gyr and >9 Gyr. The more the stars are young, the more their MD is narrow (because metallicity increases less rapidly at late times) and more it peaks to higher [Fe/H] values. The lower panel displays the MDs of five radial ranges, namely <3 kpc, 3-5 kpc, 5-7 kpc, 7-9 kpc(="extended solar neighborhood"), 9-11 kpc; there are practically no stars entering the solar neighborhood from beyond 11 kpc in our model. Most stars originate from the 7-9 kpc range and their MD peaks at [Fe/H]=0. The smaller the average birth radius of stars (down to 3 kpc), the more they contribute to the most metallic stars at [Fe/H]=0.4. Stars from the 9-11 kpc range do not contribute to metallicities higher than solar.

Our results present similarities, but also some differences with those of Minchev et al. (2013). In both cases, the majority of stars originate from the 7-9 and 5-7 kpc ranges, while the most metallic stars come inwards of 5 kpc. However, the peaks of the MDs in the 3-5 and 5-7 kpc ranges are at lower metallicities than the one of the 7-9 kpc range (their Fig. 3, middle panel). In our case, the peaks of the MDs in the 3-5 and 5-7 kpc ranges are found at higher metallicities than the one of the 7-9 kpc range. Also, the importance of the 3-5 kpc range is larger in their case than in our model, probably implying a stronger influence from the bar.

4.3. Thin vs. thick disk: age, composition, structure

Gilmore & Reid (1983) identified the thick disk as a distinct component of the MW, on the basis of star counts towards the South Galactic pole. Since then, and despite an intense observational and theoretical investigation, the identity of the thick disk remains elusive. It clearly differs from the thin disk in many, if not all of its main properties, namely age, metallicity, abundance ratios, kinematics, spatial distribution; still, there are no well defined boundaries distinguishing the thin and thick disks and no clear picture yet of the relationship - if any - of the thick

disk to the other galactic components (bulge, halo, thin disk). Thus, a large number of formation scenarios of the thick disk have been proposed up to now, involving either external influences or secular evolution through radial mixing, e.g. Sales et al. (2009); Minchev et al. (2013); Rix & Bovy (2013) and references therein.

In particular, radial migration has been suggested as a potential thick disk formation mechanism by Schönrich & Binney (2009a), who developed a semi-analytical model (similar in some respects to the present one) and investigated extensively the resulting chemical and kinematic properties. In particular, they showed that for some values in the parameter space, their model can reproduce several key properties of the thick disk just by secular processes: morphology (i.e. the two-slope vertical star density profile in the solar neighbourhood), the vertical abundance gradient and the puzzling "**two-branch**" behaviour of O/Fe vs Fe/H, with the thick disk displaying larger O/Fe values than the thin disk for the same range of metallicities. Some of those results were also found in N-body simulations, e.g. Loebman et al. (2011), but others, especially the claimed dynamical behaviour of thick disk stars, were not confimed and are still under debate (see e.g. Minchev et al. (2013)) and references therein).

In this work we do not consider any properties of the disk vertical to the plane (either chemical or kinematic) and we focus on its radial properties, in particular concerning the solar neighbourhood. In view of the uncertainties as to the best defining feature of the thick disk, we adopt the simplest possible criterion, namely age. Following Binney & Sanders (2013) and Haywood et al. (2013), we assume that the thick disk is simply the early period of the MW disk formation, lasting from -12 to -9 Gyr, whereas the thin disk corresponds to the subsequent 9 Gyr of evolution. There is no physical ingredient in our model that marks the transition between the two eras: star formation, infall and radial migration all over the disk are continuous functions of time and space. Still, the consequences of that simple assumption are quite important, as can be seen in Fig. 15, where various data are plotted as a function of [Fe/H] and compared to relevant observations.

In the upper panels of Fig. 15 we display the evolution of [α/Fe] (left)[3] and [O/Fe] (right) vs [Fe/H] for all the stars currently present in the radial bin r=8±0.25 kpc (solid curve) and for those born in situ (dotted curve). As expected, the curve of the [α/Fe] evolution of the in situ stars lies lower than the one of all the stars present in the solar cylinder; the latter is affected by old stars migrated from inner regions, which have higher [α/Fe]for the same value of [Fe/H]. The same holds for [O/Fe].

In the middle panels of Fig. 15 we display separately the evolutions of the "old" stars (>9 Gyr, aka thick disk) and of the "young" stars (<9 Gyr, aka thin disk). As expected from the results already presented in Fig. 11, thick disk stars cover a wide range of metallicities extending to approximately solar, while thin disk stars appear around [Fe/H]~-0.8 and extend up to [Fe/H]~0.4. The former have higher [α/Fe] values than the latter and never reach [α/Fe]<0.1, in rough agreement with observations. In fact, the [α/Fe] evolution of the total stellar population (solid curve in upper panel) coincides with the one of the thick disk at low metallicities and converges progressively

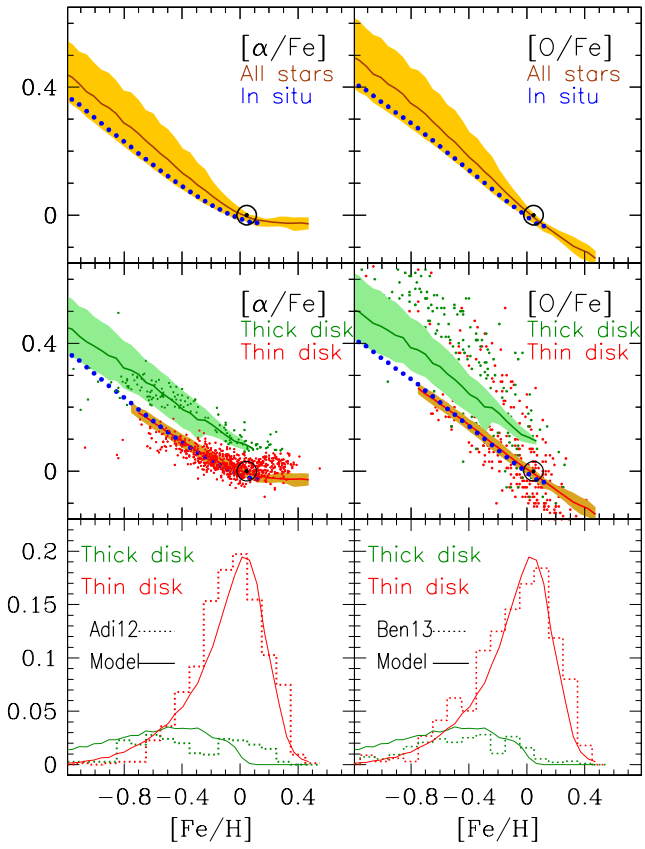

Fig. 15. Solar neighborhood: *Top:* [α/Fe] (*left*) and [O/Fe] (*right*) vs. metallicity, for all stars present today (*solid* brown curve) and for all stars born in situ (*dotted* blue curve). *Middle:* [α]/Fe (*left*) and [O/Fe] (*right*) vs. metallicity, for stars of the thick disk (>9 Gyr, *green* curve) and for stars of the thin disk (<9 Gyr, *red* curve). They are compared to corresponding data from Adibekyan et al. (2011) (left) and from Bensby et al. (2014) (right). In *top* and *middle* panels the *shaded aereas* enclose the ±1σ values around the corresponding model averages. In the *bottom* panel, the thin (red) and thick (green) disk metallicity distributions (solid curves) are compared to the corresponding observed ones (red and green *dotted histograms*). Data in the left bottom panels from Adibekyan et al. (2011, 2013) and in the right bottom panels from Bensby et al. (2014); in the latter case, the numbers for the thick disk are arbitrarily reduced by a factor of 3 to match roughly the model results, since the adopted selection criteria in that work favor the presence of thick disk stars in the sample (see text).

to the one of the thin disk at higher metallicities. Our average trends of [α/Fe] vs [Fe/H] are in good agreement with the data of Adibekyan et al. (2013)[4], both for the thick and the thin disk and we consider this to be a successful test of the idea that the thick disk can be identified with the component of the disk older than 9 Gyr. We notice that the model 1-σ dispersion of [α/Fe] of the thick disk is larger than the corresponding one of the thin disk.

In the case of the thin disk, the evolution of [α/Fe] corresponds practically to the one of the *in situ* formed stars (the dotted curve, same as in the upper panel), an important feature

[3] We assume that [α/Fe]=([Mg/Fe]+[Si/Fe])/2, although Adibekyan et al. (2011) assume that [α/Fe]=([Mg/Fe]+[Si/Fe]+[Ti/Fe])/3; however, the adopted massive star yields of Nomoto et al. (2013) - but also other yields, e.g. Woosley & Weaver (1995) - fail to reproduce the observed behaviour of Ti as an α element in the halo of the MW. For that reason, we adopt two α elements with well behaved yields.

[4] We classify stars in the sample of Adibekyan et al. (2011) into thin and thick disk by applying the criterion (dividing line in the [O/Fe] vs [Fe/H] plane) suggested in Adibekyan et al. (2013).

already identified in the work of Schönrich & Binney (2009a). However, this does not imply that thin disk stars are mostly formed in situ: a large fraction of thin disk stars are formed in other galactic regions and migrated in the solar neighbourhood, during the last 9 Gyr. But in the beginning of that period, the value of [α/Fe] *all over the inner disk* was already reduced to ~0.2 - because of the previous activity of SNIa - and it evolved very slowly afterwards (see Fig. 11, bottom panel).

Our results for [O/Fe] vs [Fe/H] are displayed in the right top and middle panels of Fig. 15 and they are compared with the data of Bensby et al. (2014) [5]. The behaviour is qualitatively, but not quantitatively, similar to the one of [α/Fe]. Although oxygen is an α element, its evolution is slightly different from the one of [α/Fe] here, because we included Si in the definition of [α/Fe]: a non-negligible amount of Si is produced by SNIa, while this is not the case for oxygen. As a result, [O/Fe] varies more than [α/Fe] extending both to higher and lower values. However, despite the resulting large variation of [O/Fe], our results do not match satisfactorily the data of Bensby et al. (2014) which extend from [O/Fe]>0.6 to values lower than -0.2. The decline of [O/Fe] in the data is much steeper than in our model. It is difficult to say whether this discrepancy is due to the model (inadequate yields or SNia rates) or to the data (uncertainties in the oxygen abundances).

In the bottom panel of Fig. 15 we present the resulting metallicity distributions for the thin and thick disk, and we compare them to the data of Adibekyan et al. (2013) (left) and Bensby et al. (2014) (right). The metallicity distribution of the thick disk is already presented in Fig. 14 (top panel): it is the curve corresponding to stars old than 9 Gyr. It is quite broad, it extends up to [Fe/H]~0 and it peaks at [Fe/H]~-0.6 to -0.5. the thin disk MD of the model is much narrower, it extends up to [Fe/H]~0.45 and it peaks at [Fe/H]~0.

The thin disk MD is in excellent agreement with the data of both Adibekyan et al. (2013) and Bensby et al. (2014). As for the thick disk MD, it extends only up to [Fe/H]=0 and thus it does not reach the metallicity range of *high-alpha metal-rich stars* (*hamr*) in the sample of Adibekyan et al. (2013), which appears to be bi-modal in that respect; this bi-modality, which has yet to be confirmed, cannot be explained in the framework of our model. The sample of Bensby et al. (2014) is biased in favor of thick disk stars (it contains 234 stars in a total of 629), so we reduced the proportion of its thick disk a factor of 3, to bring it in agreement with our results in Fig. 15.

The results of Fig. 15 confirm the suggestion of Schönrich & Binney (2009a) that radial migration can explain the two branches observed in the [O/Fe] vs [Fe/H] relation. They also provide further support to the idea that the local thick disk was formed by that process, since they reproduce successfully the local distributions of both the thick and the thin disk. However, the absence of any features in our model (either morphological or kinematic) concerning the direction vertical to the Galactic plane, does not allow us to explore further this issue.

We now turn to the radial distribution of the thick and thin disks in our scenario. In Fig. 16 we show (upper panel) the radial surface density profiles of stars older and younger than 9 Gyr, respectively, after radial migration. The region that "suffered" mostly from radial migration, being depleted by its stars, is the region between 2 and 4 kpc, i.e. the bar corotation region. Stars from that region have migrated both to the bulge and outwards,

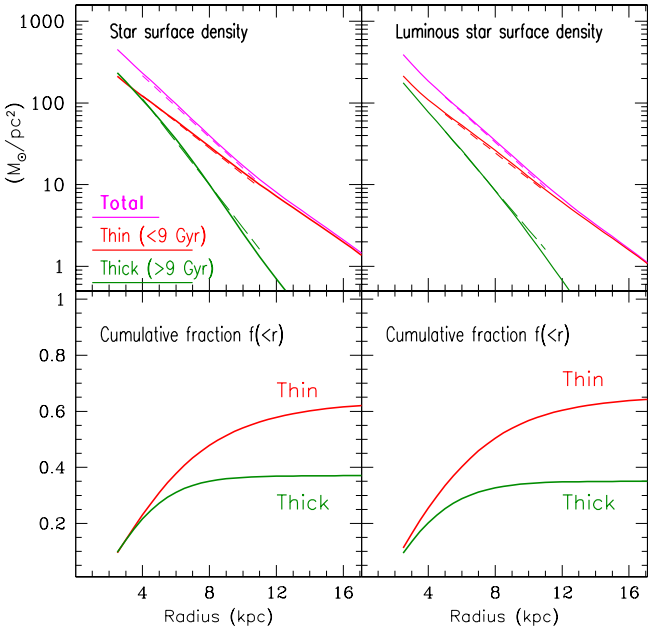

Fig. 16. Thins vs. thick disk: *Left:* Stars plus stellar remnants; *Right:* Luminous stars only. *Top:* Present day stellar profiles: *magenta*: Total; *green*: (thick disk); *red*: thin disk. In all curves, there is an attached best-fit exponential (dashed line of same colour) in the 5-11 kpc range, with scalelengths and column densities at R_0=8 kpc as reported in Table 3. *Bottom:* Cumulative fraction of the thin and thick disk masses with respect to the correspondning total disk mass M_{disk}: $M_{thin}(< r)/M_{disk}$ (red curve) and $M_{thick}(< r)/M_{disk}$ (green curve) as a function of radius r.

mostly in the region between 5 and 8 kpc (see upper panel in Fig. 10). The spatial distribution of the old stellar population (>9 Gyr, i.e. the thick disk according to our assumption) has been altered by that process considerably more than the one of the young stellar population: it presents a more pronounced "bump" than the thin disk in the region 5-8 kpc.

The surface densities of stars+remnants of the model in the solar neighbourhood are 10 $M_\odot/pc^2$, 28 $M_\odot/pc^2$and 38 $M_\odot/pc^2$, respectively for the thick disk, the thin disk, and the total (thin+thick). In comparison, the recent work of Bovy & Rix (2013) who analyzed the dynamics of 16 269 G-type dwarfs from SEGUE (sampling the radial range 5 kpc < r < 12 kpc) leads to a dynamically determined surface density of stars+remnants Σ_*=38±4 $M_\odot/pc^2$at r=8 kpc. In our case, stellar remnants contribute for 5 $M_\odot/pc^2$, and stars still shining for 33 $M_\odot/pc^2$(our IMF extending from 0.1 $M_\odot$ to 100 $M_\odot$, we have no brown dwarfs included). We notice that in their analysis of the local surface density contributed by mono-abundance populations, Bovy et al. (2012a) find a total surface density contributed by stars of Σ_*=30±1 $M_\odot/pc^2$, which depends slightly on the adopted IMF: for a Kroupa (2001) IMF, they obtain Σ_*=32 $M_\odot/pc^2$, in excellent agreement with our results. The respective contributions to the surface densities of the thin and thick disks appear in Table 3. Locally, the thick disk (defined as including all stars older than 9 Gyr) contains about 1/3 of the column density of the thin disk. The total baryonic surface density in the solar neighbourhood, including 13.2 $M_\odot/pc^2$ for the total gas, is 51.2 $M_\odot/pc^2$. This is in agreement with the local baryonic contribution of Σ_{gas} + Σ_*=55±5 $M_\odot/pc^2$ estimated in Zhang et al. (2013) or Σ_{gas} + Σ_*=51±4 $M_\odot/pc^2$ estimated in Bovy & Rix (2013).

[5] We use the criterion suggested by Bensby et al. (2014) for the classification into thin and thick disk, namely probabilities higher than 2 for the former and smaller than 0.5 for the latter.

Table 3. Properties of the Galactic disks (r>2 kpc).

	Thin	Thick	Total	
Σ(8kpc): Stars	24.5	8.5	33	$M_\odot/pc^2$
Σ(8kpc): Stars+Remnants	28	10	38	$M_\odot/pc^2$
Σ(8kpc): Remnants	3.5	1.5	5	$M_\odot/pc^2$
Scalelength: Stars	2.7	1.8	2.35	kpc
Scalelength: Stars+Remnants	2.7	1.65	2.25	kpc
Mass: Stars+Remnants	2.2	1.2	3.4	10^{10} $M_\odot$

The surface density profiles of the thick and the thin disks in our model, as well as the total stellar one, cannot be fitted with single exponentials over the whole radial range of 3 kpc to 16 kpc. The reason is the depletion of the inner disk due to radial migration (but also due to gas flows away from bar corotation at late times). We obtain, however, rather satisfactory fits with a single exponential for a limited radial region, here taken to be between 5 and 11 kpc. The best fit results for the thin and the thick disks and their sum, both for the case of luminous stars and for stars plus stellar remnants, appear in Table 3 and in Fig. 16 (as dashed lines).

The scalelength of the total (stars plus stellar remnants) disk of our model (2.25 kpc) is in excellent agreement with the recent dynamical estimate of Bovy & Rix (2013) for the Milky Way: 2.15±0.14 kpc. We notice that their analysis of the combination of constraints from rotation-curve shape and surface-density measurements leads to a local value for the rotational velocity of V_c = 218 ± 10 km/s, which is not very different from the value of 212 km/s of our model (see Fig. 5). The total stellar mass of our disk is lower than the value of 4.6 10^{10} $M_\odot$ obtained by Bovy & Rix (2013), because they obviously include the region inside 2 kpc in their calculation of the disk mass, while we do not include it. For those reasons, our estimate of the total stellar disk mass of 3.4 10^{10} $M_\odot$(end point of our calculations in Fig. 2) corresponds to the total stellar mass outside r=2 kpc. If we add the final stellar mass 1.3 10^{10} $M_\odot$ that we find inside 2 kpc, we obtain a total stellar mass of 4.7 10^{10} $M_\odot$, again in agreement with the estimates of Bovy & Rix (2013).

We find systematically a thick disk more centrally condensed than the thin disk, i.e. with a scalelength shorter by ∼1 kpc. The reason is the inside-out star formation of the Galaxy: the old stellar population is more centrally condensed than the young one and radial migration does not change that feature (although it certainly attenuates it).

The scalelength of the stellar thick disk in our model is on the lower side of the values derived recently from observations. Bensby et al. (2011), analysing high quality spectra of red giants from the inner and the outer disk, showed that for Galactocentric distances beyond 10 kpc, only chemical patterns associated with the local thin disk are found, even for stars far above the Galactic plane. They evaluated the scalelength of the thick disk to 2.0 kpc, *assuming* that the one of the thin disk is 3.8 kpc.

Cheng et al. (2012) studied the α/Fe of 5620 stars from the SEGUE survey in the region of galactocentric distance 6 < R/kpc < 16 and distance from the plane 0.15 < $|Z|/kpc$ < 1.5. They found that the high-α (thick-disk) population has a short scale length: $1.8^{+2.1}_{-0.5}$ kpc), while the the low-α population (associated with the thin disk) has a scalelength of 3.4 kpc. A similar analysis of Bovy et al. (2012b) finds somewhat larger values (2.01±0.05 kpc for the thick and 3.6±0.2 kpc for the thin disk) but with considerably smaller uncertainties. Our value for the scalelength of the stellar only thick disk (1.8 kpc) is in good agreement with the aforementioned studies ; however, the scalelength of our thin disk is substantially smaller than those obtained in these studies.

As already discussed extensively in the literature (e.g. Rix & Bovy (2013) and references therein) the radial extension of the thin and thick disks can be used to constrain various scenarios for thick disk formation. In particular, the lack of high-α stars at r >10 kpc and large distances from the plane, constrains the strength of migration due to transient spiral structure: it cannot be very efficient beyond that distance. In our case, the thick disk has a short scalelength and the efficiency of radial migration is indeed small beyond r=11-12 kpc, as seen in e.g. the profiles in the top and middle panels of Fig. 10). However, the thin disk appears also to be shorter than in the observations.

The lower panels of Fig. 16 display the corresponding cumulative fractions of the thin and thick disks as a function of distance r. As already stated in Sec. 3 and Fig. 4, we define here the disk as the region of radius r >2 kpc, the region inside belonging to the bulge. The resulting fractions differ very little in the two cases (stars+ remnants and stars only): the thick disk contributes almost as much as the thin disk in the inner Galaxy (where a large fraction of the stars was formed in the first 3 Gyr) and its contribution gradually lags behind the one of the thin disk with radius. On the total, the thick disk weights about half the mass of the thin disk, i.e. their stellar masses are 1.2 10^{10} $M_\odot$ and 2.2 10^{10} $M_\odot$, respectively.

The derived mass ratio of the thick and thin disks of the MW M_{thick}/M_{thin} ∼1/2 is substantially higher than expected from observations of external disk galaxies by Yoachim & Dalcanton (2006): they find that $M_{thick,*}/M_{thin,*}$ is a decreasing function of the rotational velocity of disks, ranging from 1-2 at V_C ∼70 km/s to 0.2 at V_C ∼200 km/s; the ratio we find is almost 3 times larger than the latter value. On the other hand, based on *Spitzer* observations of a sample of ∼30 galaxies, Comerón et al. (2011) find that thick and thin disks have, typically, similar masses. Our value of 0.5 lies between those two results.

4.4. Abundances in local thin and thick disks

Up to now, we used only two elements, namely O and Fe, to study the chemical evolution of the MW disks. These are key elements in galactic chemical evolution studies, because they are abundant and easy to measure. However, the evaluation of oxygen abundances in stars is not straightforward (see e.g. the monography by Stasinska 2012 and references therein), while the evolution of Fe is affected by uncertainties on its massive star yields and on the rate of SNIa.

A wealth of data from recent and forthcoming surveys will allow one to explore the diagnostic potential of many more elements - produced mainly in massive stars - complementing thus the information obtained from O and Fe. Such observations will also help to constrain the stellar yields, which suffer still from large uncertainties in some cases (see Romano et al. (2010) for a recent study of the impact of stellar yields on the chemical evolution of the MW). As we emphasize in Appendix C, the yields of Nomoto et al. (2013) that we adopted here are particularly adapted to the study of the galactic disk, because they cover a uniform grid of 6 initial metallicities (Z=0, 0.001, 0.002, 0.004, 0.008, 0.02 and 0.05, i.e. from 0 to about 3 times solar); they provide a uniform and fine metallicity grid[6] covering the metal-

[6] Uniform in the sense that yields from both low mass and massive stars are provided for the same metallicities. Fine in the sense of having several data points within a small metallicity range (in a logarithmic scale).

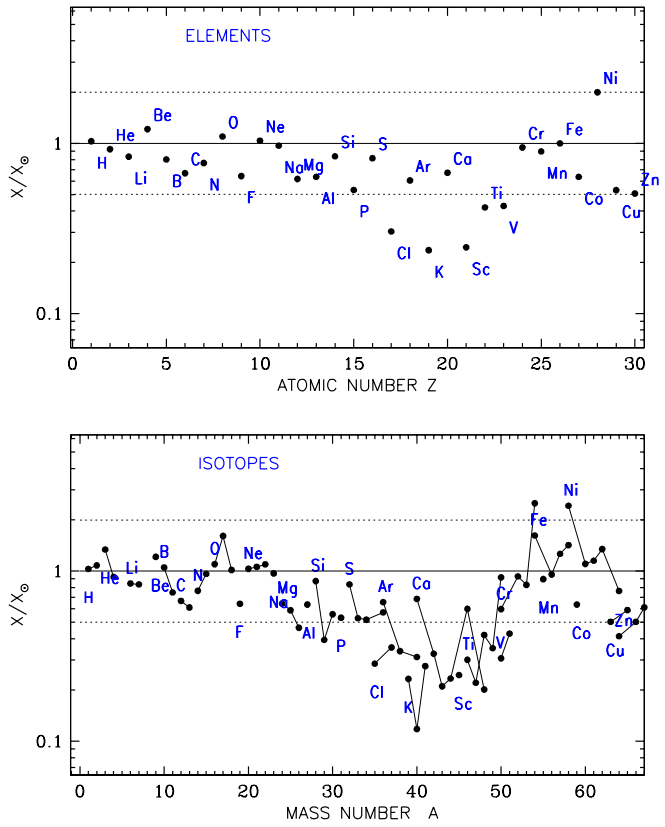

Fig. 17. Average composition of 4.5 Gyr old stars in the solar neighbourhood, elemental (*top*) and isotopic (*bottom*) compared to the observed solar composition. Most elements and isotopes are co-produced within a factor of two of their solar value. The corresponding values for the local ISM 4.5 Gyr ago are ~0.1-0.15 dex lower for all elements but H and He. No normalisation of the results is made here.

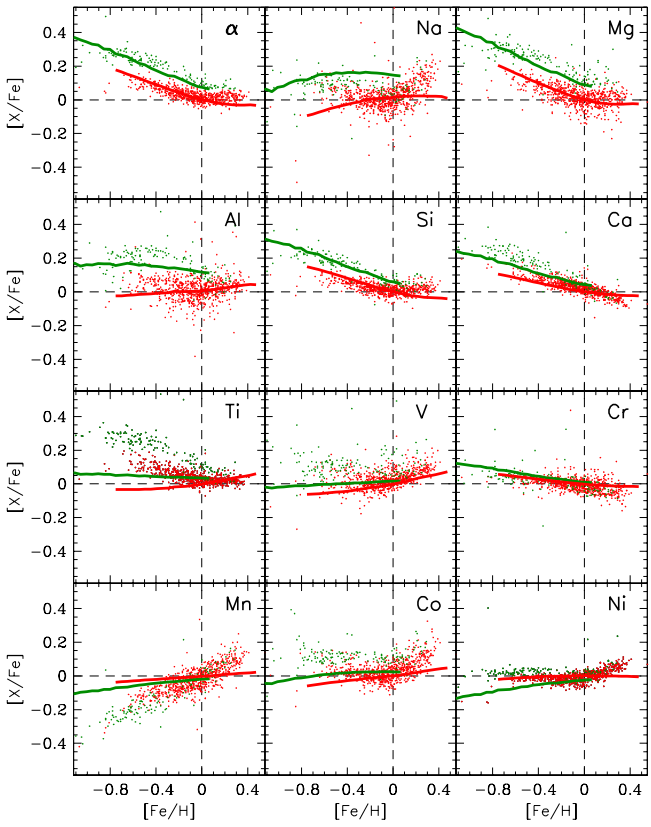

Fig. 18. [X/Fe] vs [Fe/H] for various intermediate mass elements in the solar neighbourhood: comparison of the average stellar abundances of the model to data of Adibekyan et al. (2013). The data are split into thick disk (green) and thin disk (red) according to the prescription of Adibekyan et al. (2013), in the middle panel of their Fig. 2). The model results are normalised such as the average abundance over all stars çof age=4.5 Gyr that are present today in the solar neighbourhood is solar (see text).

licities encountered all over the Milky Way during the major period of its life. They enable a detailed study of both the inner and the outer MW regions.

The yields presented in Nomoto et al. (2013) have also some flaws, as other sets of yields used in GCE studies, e.g. Woosley & Weaver (1995). Figure 17 presents our results for the average composition of local stars of 4.5 Gyr. As discussed in previous sections, the O and Fe abundances are very close to solar, making possible the analysis of Sec. 4. For other elements, however, the situation is less satisfactory: this is the case for all elements between (and including) P and Ti and most of their isotopes, which are severely underproduced. Obviously, if the yields were taken at face value, the observed evolution of those elemental ratios vs. Fe/H would not be reproduced.

We assume here that the isotopic yields of Nomoto et al. (2013) differ from the "real life" yields by various factors (of the order of a few), but their metallicity dependence is correct. We correct for those factors by normalising the average composition of local stars 4.5 Gyr old to be exactly solar and we apply the derived correction factor for each isotope to its evolution at all places. In that way, *we force all isotopic abundances and ratios to be exactly solar for an average local star of age 4.5 Gyr, because we assume that the Sun is such an average star*. We proceed then with the analysis of thin vs thick disk as in the previous section for O vs Fe.

We display our results in Fig. 18, and we compare them with data from the survey of Adibekyan et al. (2013) for the local thin and thick disks. It can be seen that the observations of the α elements are nicely reproduced in the framework of our model: the model accounts quantitatively for the evolution of Mg, Si, Ca and Cr in both the thin and thick disks. A qualitative agreement is also obtained for the cases of Na and Al, while Co and Ni reproduce well the data for the thin disk only. In contrast, the model fails to reproduce Ti (which behaves observationally as an α element), V, Mn and Co. The failure of the adopted yields to reproduce these observations does not necessarily imply that there is something wrong with the yields, at least not in all cases. After all, the solar abundances of a large number of elements still suffer from systematic uncertainties and are subject to revision (see e;g. Scott et al. 2014 for the Fe group elements). Cross-checks with respect to other observational data (concerning e.g. the halo stars) should be made and the role of the IMF investigated before concluding. We notice here that there is certainly a problem with the Nomoto et al. (2013) yields for the cases of Ti and V, as can be seen from Fig. 10 in that work, where comparison is

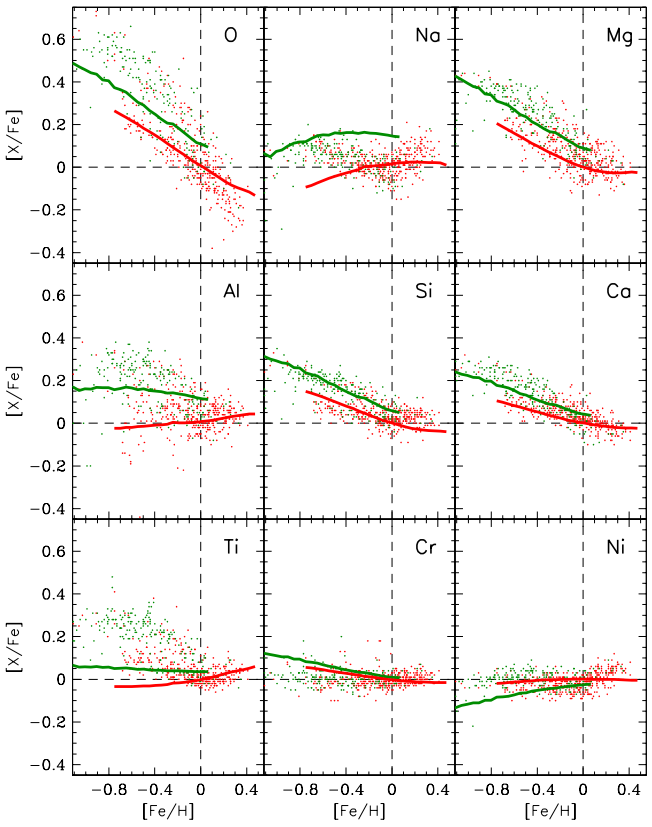

Fig. 19. [X/Fe] vs [Fe/H] for various intermediate mass elements in the solar neighbourhood: comparison of model to data of Bensby et al. (2014) The data are split into thick disk (green, P >2) and thin disk (red, P <0.5) according to the probabilities P given in Bensby et al. (2014). The model results are normalized such as the average abundance over all stars of age=4.5 Gyr that are present today in the solar neighbourhood, is solar.

made of a simple GCE evolution model with halo and local disk data: it is obvious that, even after normalisation to solar values, the observed evolution of Ti and V can not be reproduced.

In a similar vein, we compare our results to the data of the Bensby et al. (2014) survey in Fig. 19. The agreement of the model to observations of α-elements Mg, Si and Ca is excellent, as in Fig. 18; in contrast, the evolution of oxygen is poorly reproduced, as discussed in Sec. 4.3. The agreement with Al and Na is qualitatively, but not quantitatively, good and the failure in the case of Ti as bad as before.

We notice that the separation into thin and thick disks is made on the basis of different criteria in Adibekyan et al. (2013) and Bensby et al. (2014): chemical vs kinematic, respectively. Despite that, there is rather good agreement between the two data sets, making a comparison of model to the data meaningful. Here we attempted such a comparison for the first time, showing the important potential of such detailed observations to constrain both stellar yields and evolutionary models for the MW disk.

5. Summary

In this work we present a model for the evolution of the MW disk, involving radial motions of gas and stars. The MW is built gradually by infall of primordial gas in the potential well of a "typical" dark matter halo of final mass 10^{12} $M_{\odot}$, the evolution of which is extracted from numerical simulations (Sec. 2.1). Star formation depends on the local surface density of molecular gas, which is calculated by semi-empirical prescriptions of Blitz & Rosolowsky (2006) (Sec. 2.1.3 and Appendix B). For the radial flows of gas, we consider only the case of a MW-like bar operating for the last 4 Gyr and driving gas inwards and outwards of corotation (sec. 2.4). We consider separately the epicyclic motion of stars (blurring) from the true variation of their guiding radius (churning). For the former, we adopt an analytic formalism based on the epicyclic approximation; for the latter, we adopt a parametrised description, using time- and radius- dependent diffusion coefficients, extracted from a N-body+SPH simulation and adapted to the case of the MW disk (Sec. 2.3). For the chemical evolution, we adopt recent sets of yields from Nomoto et al. (2013), providing a homogeneous and fine grid of data, well adapted to the case of the MW disk (Appendix C). We adopt the formalism of Single Particle Population, which is the only one applicable to the case of radial migration, since it allows to consider the radial displacements of nucleosynthesis sources and in particular of SNIa (Kubryk et al. 2013).

We compare our results to an extended set of observational data, concerning the global evolution of the MW, the present-day radial profiles of various quantities and the solar cylinder. We adopt recent data sets for the radial profiles of the atomic and molecular gas (Appendix A) and the SFR (Appendix B). For the mass and SFR evolution of MW-like disk galaxies we consider the results of van Dokkum et al. (2013). For the local evolution, we adopt data from the surveys of Adibekyan et al. (2011) and Bensby et al. (2014), including age-metallicity relations, metallicity distributions and various abundance ratios for the thin and thick disks. Finally, for the scalelengths and local surface densities of the thin and thick disk, we considered data from the analysis of Bovy et al. (2012b).

Our model reproduces well the present day values of all the main "global" observables of the MW disk and bulge (here taken to correspond to regions outside and inside r=2 kpc, respectively), namely: stellar, atomic and molecular gas masses, rates of infall, SFR, CCSN and SNIa (Fig. 2). We obtain a higher mass of HI and H_2 in the bulge than observed and a CCSN rate on the low side of the observations, due to tour use of a steep IMF in the massive star range (slope X=1.7). We obtain a very good agreement between the model evolution of the bulge and disk stellar mass and the corresponding observations of the "stacked evolution" of MW-type disks of van Dokkum et al. (2013) (Fig. 3): in the light of these data, the MW appears as a fairly average disk galaxy. We notice, however, a deficiency, of the order of 20% in the early SFR of the model with respect to the observations.

The present day profiles of stars, gas (HI and H_2), SFR and rotational velocity are also well reproduced by the model (Fig. 5). As expected (e.g. Friedli & Benz 1993) radial gas flows induced by the bar flatten the gaseous profile in the region 3-6 kpc and, consequently, the corresponding profiles of SFR and O/H. The Fe/H profile is less affected, because of the action of SNIa: gas driven inwards by corotation dilutes the metallicity of both O and Fe in the inner regions, but SNIa driven inwards compensate for the Fe dilution by releasing their own Fe. An inspection of Fig. 5 shows clearly that the radial profiles in the inner disk can constrain significantly the extent of gaseous and stellar motions induced by a bar in the 3-6 kpc region. Taking at face value the present-day uncertainties in all those profiles we can say that the velocity values that we adopted for the radial flow of gas (Fig. 6) are close to the upper limit of what should be expected. If the

Galactic bar has operated for the past few Gyr, it must have induced *azimuthally averaged* radial velocities of the gas of less than ∼0.5 km/s (of course, radial gas velocities *along the bar* would have higher values). The abundance profiles of other elements and their evolution will be considered in a forthcoming paper (Kubryk et al. 2014).

The main focus of this study is the impact of stellar radial migration on the properties of the Galactic disk. We find that, with the adopted scheme for radial migration (blurring+churning), the regions mostly affected are those in the range 4-12 kpc and in particular the zone between 5 and 9 kpc. Stars in those regions are formed on average ∼1-2 kpc inwards of their current position and are, on average, ∼1-2 Gyr older than locally formed stars (Fig. 10). This implies, in particular, that the Sun was probably formed ∼1.2 kpc inwards of its present position of R_0=8 kpc from the Galactic center. The average metallicity in that region 4.5 Gyr ago was [Fe/H]∼0, while the local gas metallicity at that time was ∼0.15 dex lower (Fig. 11). This explains quantitatively why the present day local gas metallicity - which has increased since then by 0.12 dex - is ∼solar today.

As already shown in previous studies, we find that radial migration brings mostly old and metal-poor stars in the solar neighborhood, thus flattening the age-metallicity relation. It also increases considerably the dispersion in metallicity at every age, making it larger with age, as found in Sellwood & Binney (2002); however, dispersion decreases for the oldest stars in our model, because they originate from the inner regions which underwent a rapid and fairly similar evolution.

We emphasize that the local observables of our model concern the so-called "solar cylinder", that is all stars found in the end of the simulation in a cylinder of radius 0.25 kpc (half the size of our radial bin), perpendicular to the Galactic plane and centered on the solar position, at Galactocentric distance R_0=8 kpc. We do not apply any selection biases on those results in order to compare with specific observations. For that reason, a successful comparison to observations does not imply that the model is necessarily correct, only that it possesses potentially interesting features.

We show quantitatively that - at least in the framework of this model and with the caveat of the previous paragraph - epicyclic motions cannot produce the observed metallicity dispersion; in contrast, our adopted radial migration scheme reproduces well available observations of dispersion in the age-metallicity relation (Fig. 12). We argue that this observable provides one of the most powerful probes of the extent of radial migration in the MW and it should be scrutinized in future observational and theoretical studies. On the other hand, the local [O/Fe] abundance ratio is found to have very little dispersion with age, making it a much better proxy for age than [Fe/H]; this is also true for other [α/Fe] ratios.

We analyse the origin of the stellar populations presently found in the solar neighborhood as a function of their metallicity (Fig. 13). We find that, at all metallicities, stars are ∼1 Gyr older, on average, than locally formed stars of the same metallicity; they also display an age dispersion of ∼1-3 Gyr around the average age. Cleary, radial migration affects dramatically the relation between age and metallicity, allowing for young stars of low metallicity to co-exist with old stars of high metallicity. In our model, the less metallic local stars are ∼11 Gyr old and originate, on average, from the region at r ∼5-6 kpc, while stars of solar metallicity are ∼4.5 Gyr old and originate from r ∼7 kpc. The most metallic local stars ([Fe/H]∼0.3-0.4 $Z_\odot$) are 3-4 Gyr old and originate from the inner Galaxy, at r ∼2-3 kpc. We find that stars of different ages and different birth radii contribute to some extent to all metallicity bins (Fig. 14).

To handle the issue of the thin vs thick disk we adopt a simple criterion already suggested in the literature, namely age (another reason for that choice being the absence of the z-direction in our model, making it impossible to use kinematic or spatial quantities in that direction). *We assume that stars older than 9 Gyr belong to the thick disk and younger ones to the thin disk.* That simple criterion allows us to reproduce fairly well the observed [α/Fe] vs. Fe/H behaviour of stars *classified as belonging to the thin and thick disks on the basis of different criteria* (chemical or kinematic); at the same time, we reproduce the corresponding metallicity distributions, very well for the thin disk and satisfactorily for the thick disk (Fig. 15). Both results provide strong support to the idea that the thick disk is simply the early part of the MW disk (corresponding to the first few Gyr of its formation) and that the local thick disk results largely from the radial migration of stars from the inner disk.

We evaluate quantitatively the radial structure of the thin and thick disks in our model. We find that, because of the inside-out formation adopted, the thick disk has a considerably shorter scalelength than the thin disk (Fig. 16), despite the fact that it has undergone a much more important radial migration than the latter. The local surface densities of both disks are in excellent agreement with recent evaluations and this is also true for the scalelength of the thick disk; however, we obtain a thin disk with a scalelength shorter by ∼1 kpc than the one observationally determined. Overall, the thick disk accounts for 1/3 of the total stellar disk and for 1/4 of the local stellar disk surface density.

Finally, we investigate in detail the evolution of several elemental abundances in the local thin and thick disk and we compare our results to the large data sets obtained from recent surveys. We argue that such a study requires fine and homogeneous grids of stellar yields (such as the one provided by Nomoto et al. (2013), adopted here). We find that several observed features, i.e. the behaviour of [α/Fe] vs Fe/H, can be reproduced fairly well for both the thick and thin disks, but the situation is much less satisfactory for other elements. Current and forthcoming data in this field will provide powerful constraints on stellar nucleosynthesis and the overall evolution of the MW disk, especially when combined with kinematic and spatial information.

Acknoweledgments: We are grateful to T. Bensby for providing data before their publication and advice on their use. EA acknowledges financial support to the DAGAL network from the People Programme (Marie Curie Actions) of the European Union's Seventh Framework Programme FP7/2007-2013/ under REA grant agreement number PITN-GA-2011-289313 and from the CNES (Centre National d'Etudes Spatiales - France). We also acknowledge partial support from the PNCG (Programme National Cosmologie et Galaxies - France).

Appendix A: Gas in the MW disk

In Fig. A.1 we present the data adopted for the gas profiles of the MW. Atomic hydrogen (HI) is displayed in the upper panel and molecular hydrogen (H_2) is displayed in the middle panel. In both cases, data are from Dame (1993),Olling & Merrifield (2001) and Nakanishi & Sofue (2003). The data have been rescaled to a distance of R_0=8 kpc of the Sun from the Galactic center. Notice that Olling & Merrifield (2001) adopted the results of Wouterloot et al. (1990) outside the solar circle and those of Bronfman et al. (1988) inside it. The bottom panel shows the total gas surface density Σ_G=1.4(HI+H_2), the factor 1.4 accounting

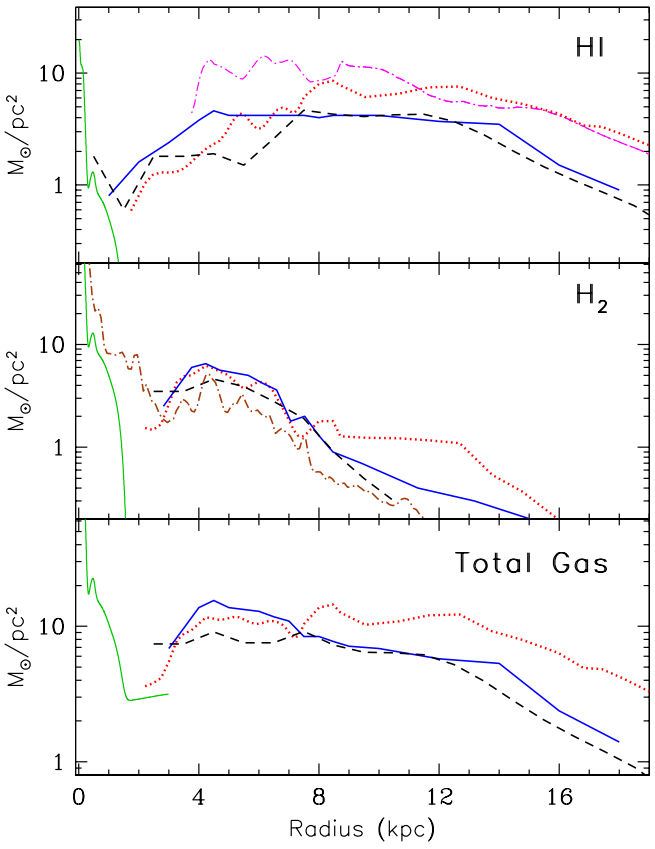

Fig. A.1. Surface density profiles of atomic hydrogen HI(top), molecular hydrogen H_2(middle) and total gas Σ_G=1.4 (HI+H_2) (bottom). Disk data (beyond 2 kpc) are from: Dame (1993), solid; Olling & Merrifield (2001), dotted ; and Nakanishi & Sofue (2003, 2006), dashed. The dot-dashed curve in the HI panel corresponds to data from Kalberla & Dedes (2008) and in the H_2 panel to data from Pohl et al. (2008). Bulge data (inner 2 kpc) in all panels are from Ferrière (2001).

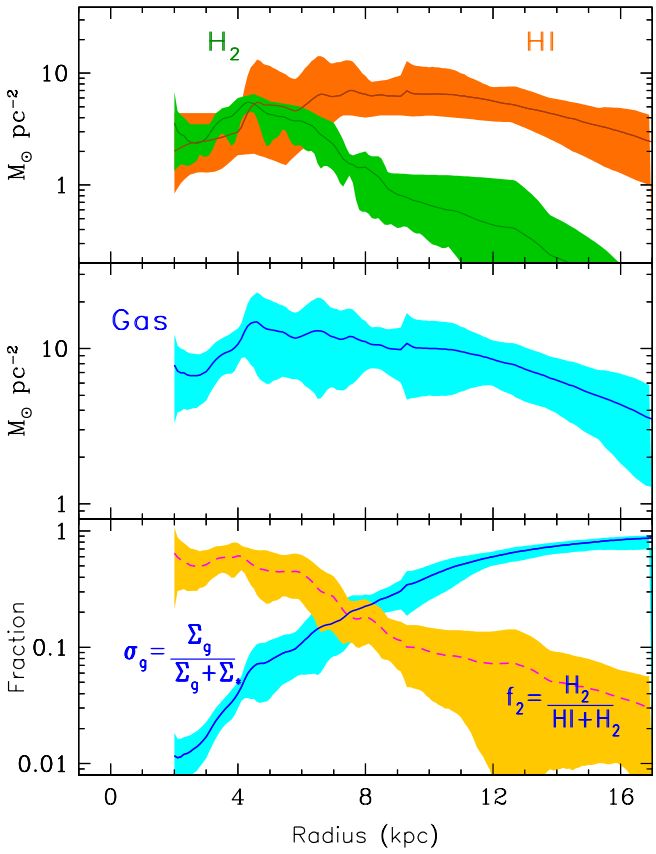

Fig. A.2. Average profiles of the previous figure. *Top*: atomic and molecular hydrogen; *middle*: total gas ; *bottom*: fractions of gas (solid) and molecular gas (dashed). For the latter panel, an exponential stellar density profile with a scale-length of 2.3 kpc normalised to Σ_*(R=8 kpc)=38 $M_\odot/pc^2$is adopted, while the molecular fraction is evaluated with the formalism of Sec. B.

for the presence of ~28% of He. In all panels, the data for the inner Galaxy (R<2 kpc) are from Ferrière et al. (2007) and they are provided for completeness, since the evolution of the bulge is not studied here.

Despite systematic differences in the data, the gas profiles in the three panels of Fig. A.1 share some common features:

- The HI profile is essentially flat in the 4-12 kpc region.

- The H_2 profile displays the well known "molecular ring" in the 4-5 kpc region and declines rapidly outwards.

- The total gas profile is approximately constant (or slowly declining outwards) in the 4-12 kpc region; it is more rapidly declining inside the molecular ring, as well as outside 13 kpc, where it has a scalelength of 3.75 kpc (Kalberla & Dedes 2008).

In order to minimize systematic uncertainties in the following, we shall adopt as the "reference gaseous profiles" for the MW disk the averages of the aforementioned observed profiles as a function of galactocentric radius. They appear in Fig. A.2, top panel for HI and H_2 and middle panel for the total gas. We adopt as a typical uncertainty in each radius, either 50% of the average value (typical statistical uncertainty in e.g. Nakanishi & Sofue (2006) or half the difference between the minimal and maximal value in each radial bin (whichever is larger). The resulting values for the total galactic content of HI, H_2 and gas

Table A.1. Gas in the MW disk (2-19 kpc) in 10^9 $M_\odot$.

	HI	H_2	Total[1]
Dame (1993)	3.25	1.12	6.10
Olling & Merrifield (2001)	5.85	1.21	9.90
Nakanishi & Sofue (2003, 2006)	2.75	0.71	4.86
Kalberla & Dedes (2008)	7.7		
Pohl et al. (2008)		0.55	
Adopted average	4.90±2.2	0.9±0.35	8.2±3.5

1: Total includes 0.28 of He by mass fraction.

appear in Table A.1. The derived masses appear lower than the ones obtained with the mass model of the ISM in the Milky Way of Misiriotis et al. (2006), who find total masses of M_{H_2}=1.3 x 10^9 $M_\odot$ and M_{HI}=8.2 x 10^9, respectively, but they match the FIR emission of the whole Galaxy, whereas we quote here results for the 2-19 kpc range; there are considerable amounts of HI in the outer disk, as discussed in e.g. Kalberla & Dedes (2008).

We find then that the Galactic disk has a total gaseous content of ~8.2±3.5 10^9 $M_\odot$in the 2-19 kpc range. Assuming an exponential stellar profile with a scalelength R_d=2.3 kpc for the MW disk, normalised to a local (R_0=8 kpc) surface density $\Sigma_{*,0}$=38 $M_\odot/pc^2$ (Flynn et al. 2006), we find a total stellar mass of 3.2 10^{10} $M_\odot$ and we obtain the radial profile of the gas fraction $\sigma_G(R)=\frac{\Sigma_G}{\Sigma_G+\Sigma_*}$. It is displayed in the bottom panel of Fig. A.2

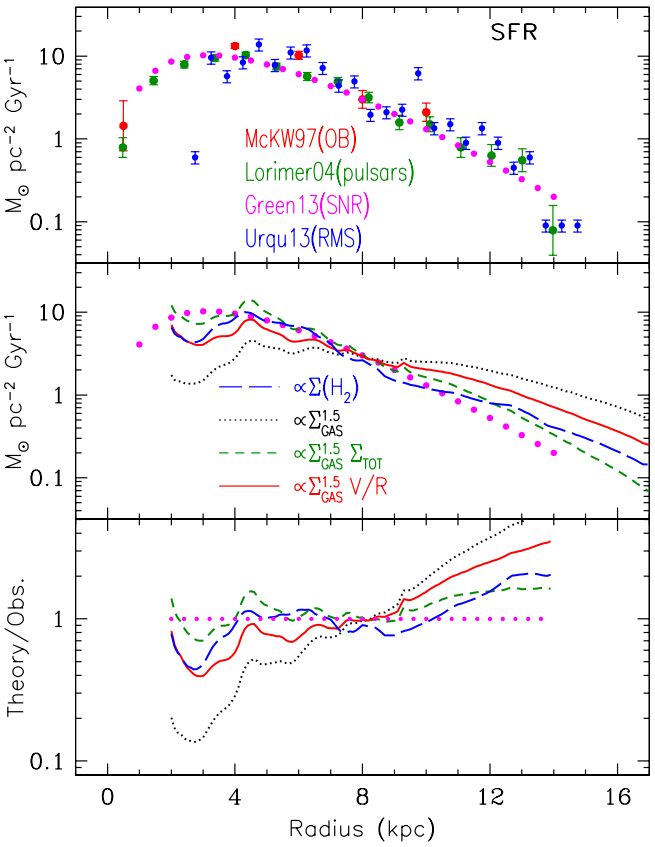

Fig. B.1. *Top*: Observed surface density profiles of various SFR tracers (see text); the dotted curve - with no error bars- is the analytical form suggested by Green (2013) and it is here adopted as representative of the MW SFR profile. *Middle*: Theoretical or empirical SF rates compared to the adopted profile of SFR tracers (the dotted curve from the upper panel); all profiles are normalised to the same value in R_0=8 kpc. *Bottom*: ratio of the theoretical or empirical profiles to the adopted observed one.

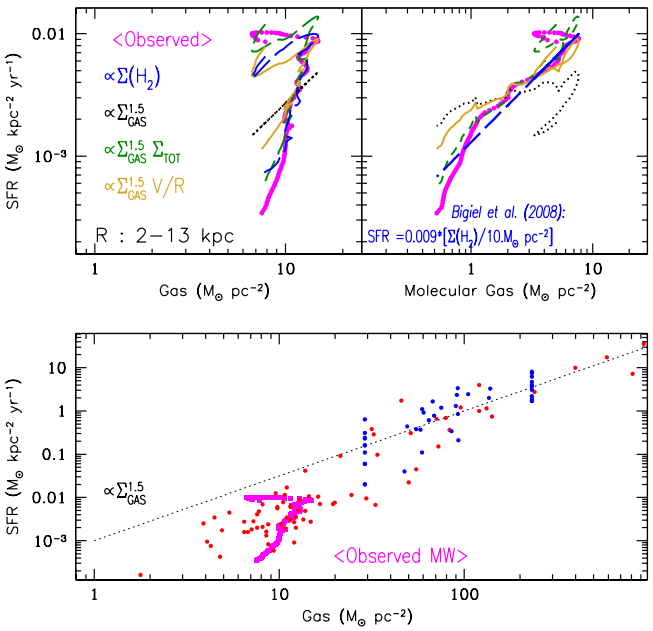

Fig. B.2. it Top: SFR surface density vs total gas surface density (*left*) and vs. H_2 (*right*) for the MW disk, in the region between 2 and 13 kpc. In both panels, curves represent the same quantities as in Fig. B.1; the long dashed curve (SFR$\propto \Sigma(H_2)$) corresponds quantitatively to the fit of Bigiel et al. (2008) to extragalactic data and fits quite well the adopted "observed" SFR profile in the MW disk. *Bottom*: The "observed" SFR vs. gas relation in the MW is compared to a compilation of extragalactic data from Krumholz et al. (2012).

and it is a monotonically increasing function of radius. Integrating as before the gaseous and stellar profiles over the disk region between 2 and 19 kpc we find an average gas fraction of σ_G=0.20±0.05 for the disk. If the bulge (of stellar mass ∼1.5 10^{10} $M_\odot$ iand negligible gas) is also included, the gas fraction of the MW is found to be ∼14%.

In that same panel we display the molecular fraction $f_2(R)=\frac{\Sigma_{H2}}{\Sigma_{HI}+\Sigma_{H2}}$, which shows a plateau of f_2 ∼0.65 in the region of the molecular ring (3-6 kpc) and decreases strongly outwards, down to a few % (albeit with large uncertainties).

Appendix B: Star formation in the MW disk

Star formation in the MW is discussed in the recent review of Kennicutt & Evans (2012). They discuss only "traditional" tracers of star formation, also used in extragalactic studies, like FIR emission. In their Fig. 7, they display a radial distribution of the SFR, claimed to be based on data from Misiriotis et al. (2006), who made a full 3D model of the Galactic FIR and NIR emission observed with COBE. Misiriotis et al. (2006) found that their modelling of the IR emission corresponds to a SFR$\propto \Sigma_G^2$ and they compared their findings to a compilation of old star formation tracers for the MW provided in Boissier & Prantzos (1999), who considered HII regions, but also pulsars and supernova remnants. Here we consider such tracers related to massive, short-lived, stars and their residues: pulsars, supernova remnants (SNR), and OB associations. Those objects have ages up to a few My for SNR and up to a few tens of My for OB associations and isolated radio-pulsars, so they can probe recent star formation.

Galactic radial distributions of luminous massive stars, pulsars, SNR and OB associations appear in Fig. B.1.The distribution of luminous massive stars is from Urquhart et al. (2013); the one displayed on Fig. B.1 is the average between the southern and northern hemispheres and is considered to be complete for luminisities above 2 10^4 $L_\odot$. The pulsar distribution (Lorimer 2004; Lorimer et al. 2006) contains more than 1000 pulsars. All distributions have a broad pic in the region of the molecular ring and their radial variation agrees well with the much sparser data of Williams & McKee (1997) on OB associations. Lorimer et al. (2006) proposed an analytical fit to the pulsar distribution, which is in perfect agreement with the one proposed for the distribution of Galactic SNR in the recent compilation of Green (2013), who used 56 bright SNR (to avoid selection effects). The latter distribution (thick dotted curve, corresponding to model C of that work) is also displayed in the upper panel of Fig. B.1 and is given by

$$\Psi(R) = A \left(\frac{R}{R_0}\right)^B \exp\left[-C(\frac{R-R_0}{R_0})\right] \quad \text{(B.1)}$$

where R_0=8 kpc and parameters B=2. and C=5.1 (Lorimer et al. (2006) give B=1.9 and C=5.).

There is reasonably good agreement between all the SFR tracers of Fig. B.1, with the exception of the one for luminous massive stars of the RMS survey (Urquhart et al. 2013), which differs considerably from the others inside 4 kpc (were selection biases are expected to be more important, even for such luminous stars) and displays an unexpected enhancement in the region around 9 kpc. Baring those differences, we shall adopt Eq. B.1 as the expression for the radial dependence of the SFR in the MW disk, after normalising it (by putting A=3.5 $M_\odot$/kpc^2/y) to the total SFR rate of the Milky Way Ψ_{MW}=2 $M_\odot$/y (Chomiuk & Povich 2011):

$$2\pi \int \Psi(R) R dR \; = \; \Psi_{MW} \tag{B.2}$$

In the middle panel of Fig. B.1 we compare the "observed" SFR profile with various theoretical or empirical profiles in the literature, which make use of the corresponding profiles of total or molecular gas discussed in this section. All of them are normalised to the adopted observed value of the SFR in the solar neighborhood.

The most widely used SFR prescription is the so-called "Schmidt-Kennicut" law, based on observations of quiescent and active disk galaxies: $\Psi \propto \Sigma_G^k$, where the gas surface density Σ_G runs over three orders of magnitude and the data suggest k=1.5. It turns out that this form of the SFR, with k=1.5 is too flat to fit the MW data: Misiriotis et al. (2006) find k=2 from their modelling of the IR emission of the MW. Also, it is well known that a steeper function is required in galactic chemical evolution models in order to explain the observed abundance gradients in the MW disk.

Boissier & Prantzos (1999) adopted a law of the form $\Psi(R) \propto \Sigma_G^{1.5} V(R)/R$; the factor $V(R)/R$ is $\propto 1/R$ for a flat curve of the rotational velocity $V(R)$ and is attributed to spiral waves inducing star formation with that frequency (Wyse 1986; Wyse & Silk 1989). On the other hand, models by Chiappini (2001) adopt $\Psi(R) \propto \Sigma_{TOT}\Sigma_G^{1.5}$, where Σ_{TOT} is the total disk surface density (dominated in the inner Galaxy by the rapidly increasing stellar profile), and they introduced a cut-off in the SFR efficiency, below 2 $M_\odot$/pc^2. Both SFR laws appear also in the middle and lower panels of Fig. B.1: they fit relatively well the "observed" SFR profile and it turns out that the corresponding models reproduce satisfactorily several key properties of the MW disk.

The aforementioned laws make use of the total gaseous profile of the disk. Based on a detailed, sub-kpc scale, observations of a large sample of disk galaxies, Bigiel et al. (2008) have found that the SFR appears to follow the H_2 surface density, rather than the HI or the total gas surface density. In a companion paper, Leroy et al. (2008) argued that the observed radial decline in star formation efficiency is too steep to be reproduced only by increases in the free-fall time or orbital time and they found no clear indications of a cut-off in the SFR.

Following these studies, we check whether such a correspondence between the adopted SFR and molecular gas profiles also holds in the MW disk. The comparison, presented in the middle and lower panels of Fig. B.1, is favorable to that idea: the SFR follows the H_2 profile to better than 30% in the 3-13 kpc range.

Fig. B.2 displays the data in a different way, namely SFR surface density vs gas (total or molecular) surface densities. In the top left panel, it appears that the "observed" SFR varies too steeply with the total gas density and it cannot be fit with a simple Schmidt-Kennicutt" law $\Psi \propto \Sigma_G^{1.5}$; a strong radial dependence of the SF efficiency, such as the aforementioned ones, is required to improve the situation. In the top right panel it is seen that the "observed" SFR increases almost linearly with H_2, and that the SFR proposed by Bigiel et al. (2008), Ψ=0.009 Σ_{H2}/(10 $M_\odot$/pc^2), reproduces quite well the data [Notice that the measurement of Bigiel et al. (2008) concern H_2 surface densities above 3 $M_\odot$/pc^2, i.e. they correspond to the upper half of the figure; it appears that, at least in the case of the MW, that dependence is prolonged to even smaller surface densities]. In the bottom panel of Fig. B.2 the "observed" SFR vs. gas relation in the MW disk is compared to data of a sample of disk galaxies from Krumholz et al. (2012). It is clearly seen that the MW disk SFR corrsponds to a small range of gas surface densities and thus the extragalactic data of SFR vs. gas cannot be used as guide to the MW SFR; in contrast, data on MW SFR vs. H_2 cover a larger dynamical range of H_2 and offer convincing evidence for a linear relationship between the two quantities.

In view of this observational support, both for the MW disk (this work) and for external galaxies (Bigiel et al. 2008; Leroy et al. 2008), we adopt here a star formation law depending on the H_2 surface density. In order to calculate it in the model of chemical evolution we adopt the suggestion (based on empirical grounds) of Blitz & Rosolowsky (2006), that the ratio R_{mol}=H_2/HI in a galactic disk dependson the mid-plane hydrostatic pressure P_{ext} and is given by

$$R_{mol} \; = \; \left(\frac{P_{ext}}{P_0}\right) \tag{B.3}$$

where P_0 is a reference pressure, or, numerically

$$R_{mol} \; = \; \left[\frac{P_{ext}/k}{(4.3 \pm 0.6x10^4}\right]^{0.92\pm0.10} \tag{B.4}$$

where k is Boltzmann's constant.

The mid-plane pressure is evaluated as

$$\frac{P_{ext}}{k} \; = \; 272 \, \mathrm{cm^{-3}K} \left(\frac{\Sigma_G}{10 \; M_\odot/\mathrm{pc}^2}\right)\left(\frac{\Sigma_*}{10 \; M_\odot/\mathrm{pc}^2}\right)^{0.5}\left(\frac{\upsilon_G}{\mathrm{km/s}}\right)\left(\frac{h_*}{\mathrm{pc}}\right) \tag{B.5}$$

i.e. it depends on the total gas surface density Σ_G,the star surface density Σ_*, the gas velocity dispersion υ_G and the stellar scale-height h_*.

By adopting typical values of υ_G=10 km/s and h_*=300 pc and the gas and star profiles of Fig. B.3, we find a rather good agreement between the observed and theoretically calculated molecular fractions in the MW disk

$$f_2 \; = \; \frac{R_{mol}}{R_{mol}+1} \tag{B.6}$$

as seen in the top panel of Fig. B.3. The resulting radial profiles $H_2(R) = f_2(R)\,\Sigma_G(R)$ and $HI(R) = [1 - f_2(R)]\Sigma_G(R)$ also compare favourably to the observed ones (middle panel). Finally, the corresponding

$$\Psi(R) \; = 0.009 \; f_2(R) \left(\frac{\Sigma_G(R)}{10 \; M_\odot/\mathrm{pc}^2}\right) \; M_\odot/\mathrm{kpc}^2/\mathrm{yr} \tag{B.7}$$

reproduces fairly well the "observed" SFR profile of the MW disk in the 4-12 kpc region, and somewhat less succesfully outside that region (bottom panel).This agreement was already noticed in Blitz & Rosolowsky (2006), albeit with older data concerning the gas and SFR profiles of the MW.

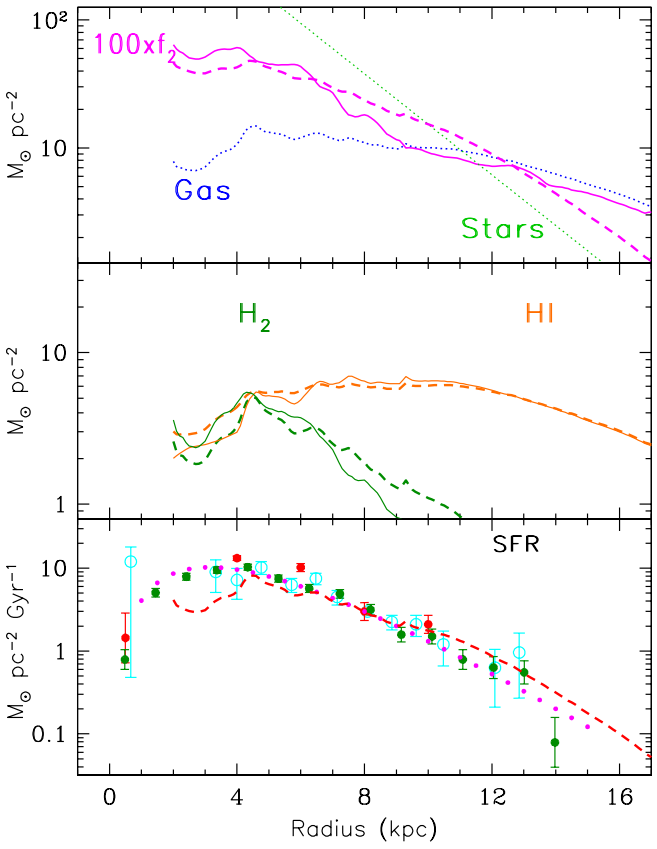

Fig. B.3. *Top:* Observed molecular fraction $f_2=\frac{H_2}{HI+H_2}$ (*solid* curve) and theoretical one (*dashed*), obtained with the prescription of Eq. B.6 from the displayed gaseous and stellar profiles (*dotted*). *Middle*: Observed (*solid* curves) vs. theoretical (*dashed* curves) profiles of HI and H_2; the latter are obtained from the observed gas profile and the theoretically evaluated molecular fraction f_2 (both in the top panel), as $\Sigma(H_2)=f_2 x\ \Sigma_G/1.4$ and $\Sigma(HI)=(1-f_2)x\ \Sigma_G/1.4$. *Bottom*: Observed SFR profiles in the MW disk, vs a theoretical SFR (*dashed*) curve), obtained from the theoretical profile of the molecular gas in the middle panel.

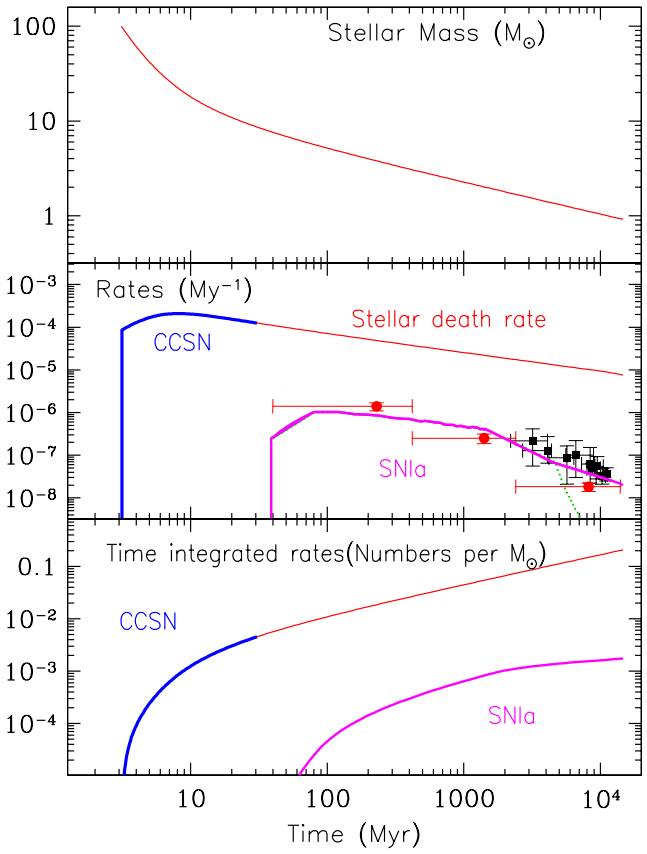

Fig. C.1. *Top*: Stellar mass vs. lifetime. *Middle:* Stellar death rate after an initial "burst" forming 1 $M_\odot$ of stars: $dN/dt = dN/dM\ x dM/dt$, where dN/dM is the stellar IMF and dM/dt the derivative of the curve in the top panel. The thick portion of the curve (up to ~35 My, corresponding to a star of 8 $M_\odot$) is the rate of CCSN. The bottom right part of the middle panel displays the corresponding SNIa rate (the time delay distribution or TDD) adopted in this work (thick curve); it is a mixture of the Greggio (2005) formulation for the SD scenario up to 4.5 Gyr and an extrapolation $\propto t^{-1}$ after that time, in order to fit the data points from Maoz et al. (2012) (filled circles) and from Maoz et al. (2010) (squares). *Bottom*: Time-integrated numbers of CCSN (thick portion of upper curve), single stars of mass M<8 $M_\odot$(thin portion of upper curve) and SNIa (lower curve), as a function of time, for an initial "burst" of 1 $M_\odot$.

Appendix C: Chemical evolution

In studies of galactic chemical evolution, the changes of the chemical composition of the system are described by a system of integrodifferential equations. The *mass of element/isotope i* in the gas is $m_i = m_G X_i$, (where m_G is the mass of the gas and X_i is the mass fraction of i) and its evolution is given by:

$$\frac{d(m_G\ X_i)}{dt} = -\Psi X_i + E_i\ (+\text{infall or outflow) terms} \qquad (C.1)$$

i.e. star formation at a rate Ψ removes element i from the ISM at a rate ΨX_i, while at the same time stars inject in the ISM that element at a rate $E_i(t)$. The *rate of ejection of element i by stars* is given by:

$$E_i(t) = \int_{M_t}^{M_U} Y_i(M)\ \Psi(t-\tau_M)\ \Phi(M)\ dM \qquad (C.2)$$

where the star of mass M, created at the time $t-\tau_M$, dies at time t (if its lifetime τ_M is lower than t) and releases a mass $Y_i(M)$ in the form of element/isotope i (*stellar yield* of i from mass M). $\Phi(M) = dN/dM$ is the Initial Mass Function, assumed to be independent of time t. M_t is the mass of the smallest star that has lifetime $\tau_M = t$ and M_U is the most massive star of the IMF;

Because of the presence of the term $\Psi(t-\tau_M)$, Eq.C.1 and C.2 have to be solved numerically (except if specific assumptions, like the Instantaneous Recycling Apprroximation - IRA - are made). The integral C.2 is evaluated over the stellar masses, properly weighted by the term $\Psi(t-\tau_M)$ corresponding in each mass M. It is explicitly assumed in that case that *all the stellar masses created in a given place, release their ejecta in that same place.*

This assumption does not hold anymore if stars are allowed to travel away from their birth places before dying. In that case, the mass $E_i(t)$ released in a given place of spatial coordinate R and at time t is the sum of the ejecta of stars born in various places R' and times $t-t'$, with different star formation rates

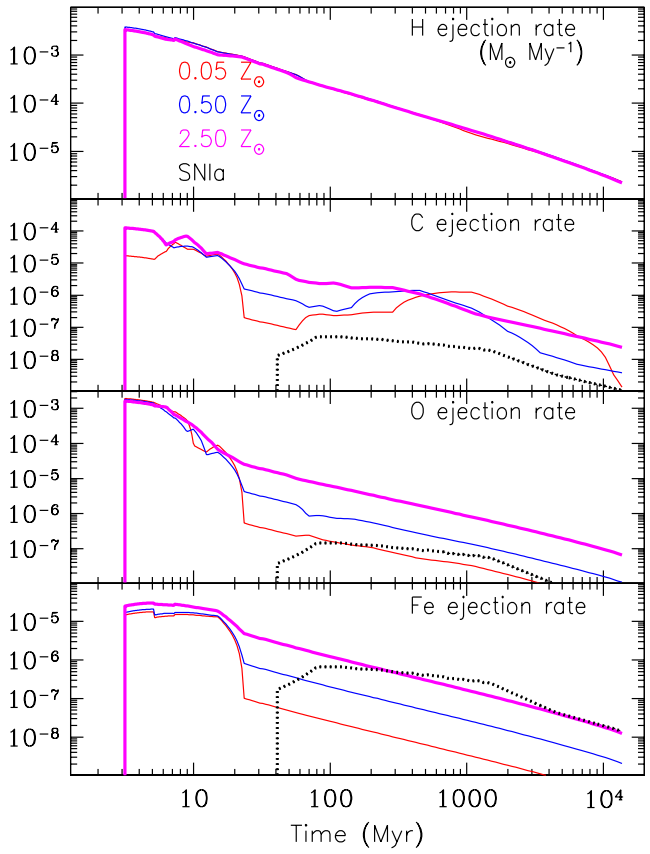

Fig. C.2. Ejection rates of hydrogen, carbon, oxygen and Fe from a stellar population of 1 $M_\odot$as a function of time. Yields are from Nomoto et al. (2013).The curves represent different metallicities, as indicated in the top panel . The dotted curves show the contribution of SNIa (resulting from a SSP of 1 $M_\odot$) to the production of those elements.

$\Psi(t', R')$ for all stellar masses M with lifetimes $\tau_M < t-t'$ Instead of Eq. C.2, the *isochrone* formalism, concerning instantaneous "bursts" of star formation or Single Stellar Populations (SSP), has to be used then. Eq.C.2 is re-written as

$$E_i(t) = \int_{\tau_{M_U}}^{t} \Psi(t')dt' \left(\frac{Y_i(M)dN}{dt'}\right)_{t-t'} \quad (C.3)$$

where $dN = \Phi(M)dM$ is the number of stars between M and $M+dM$ and $\Psi(t-t')dt'$ is the mass of stars (in $M_\odot$) created in time interval dt' at time t'. The term $(dN/dt')_{t-t'}$ represents the stellar death rate (by number) at time t of a unit mass of stars born in an instantaneous burst at time $t-t'$. The term $Y_i(M)dN/dt$ represents the corresponding rate of release of element i in $M_\odot$/yr.

Expression C.3 is equivalent to expression C.2 and it is used in N-body+SPH simulations (see Lia et al. (2002) or Wiersma et al. (2009)), since it allows one to account for the ejecta released in a given place by "star-particles" produced with different star formation rates in other places (see main text). It incorporates naturally the metallicity dependence of the stellar yields and of the stellar lifetimes, both found in the term $Y_i(M, Z)(dN/dt)(Z)$.

As in Boissier & Prantzos (1999), we use here the stellar lifetimes $\tau(M, Z)$ of Schaller et al. (1992) for stars in the mass range 0.1-120 $M_\odot$and for two metallicities $Z_\odot$and 0.05 $Z_\odot$(covering the metallicity of the MW disk during its whole evolution except, perhaps, its earliest phases).

We adopt the stellar IMF of Kroupa (2002) in the mass range 0.1-100 $M_\odot$, but with a slope x=-2.7 in the range 1-100 $M_\odot$(the "Scalo slope"), since the "Salpeter slope" of -2.35 overproduces metals in the evolution of the Solar neighborhood. Moreover, the "Scalo" slope is similar to the one of the Integrated Galactic IMF (IGIMF) suggested in e.g. Kroupe recent, which is appropriate for galactic evolution studies .

We adopt the yields provided by Nomoto et al. (2013)[7] They concern both low and intermediate mass stars in the mass range 0.9 to 3.5 $M_\odot$(calculations from Karakas (2010)) and for massive stars in the range 11-40 $M_\odot$. They are particularly adapted to the study of the galactic disk, because they cover a uniform grid of 6 initial metallicities (Z=0, 0.001, 0.002, 0.004, 0.008, 0.02 and 0.05, i.e. from 0 to about 3 times solar), allowing for a detailed study of both the inner and the outer MW regions. This constitutes a clear advantage over other sets of widely used yields (e.g. Woosley & Weaver (1995)). The massive star models of Nomoto et al. (2013) have mass loss but no rotation; yields of hypernovae (very energetic explosions) are also provided but we do not use them here. We include all 82 stable isotopic species from H to Ge. We calculate their evolution and we sum up at each time step to obtain the corresponding evolution of their elemental abundances. We notice that the use of the yields in chemical evolution calculations requires some interpolation in the mass range of the super-AGB stars (6 or 8 to 11 $M_\odot$).

We force the sum of the ejected masses of all isotopes of a star to be equal to the original stellar mass minus the one of the compact residu (white dwarf, neutron star or black hole). This is important in order to ensure mass conservation in the system during the evolution. We interpolate logarithmically the yields in metallicity and in the mass range between 3.5 and 11 $M_\odot$, and we include a detailed treatment for the production of the light nuclides Li,Be and B by cosmic rays (Prantzos 2012).

For the rate of SNIa we adopt a semi-empirical approach: the observational data of recent surveys are well described by a power-law in time, of the form $\propto t^{-1}$, e.g. Maoz & Mannucci (2012) and references therein. At earliest times, the DTD is unknown/uncertain, but a cut-off must certainly exist before the formation of the first white dwarfs (~35-40 Myr after the birth of the SSP). We adopt then the formulation of Greggio (2005) for the single-degenerate (SD) scenario of SNIa. That formulation reproduces, in fact, quite well the observations up to ~4-5 Gyr (see Fig.C.1, middle panel). For longer timescales, where the SD scenario fails, we simply adopt the t^{-1} power law. The corresponding SNIa rate at time t from all previous SSP is obtained as

$$R_{SNIa}(t) = \int_0^t \Psi(t')DTD(t-t')dt' \quad (C.4)$$

As in GP2000 we adopt the SNIa yields of Iwamoto et al. (1999) for Z=0 and Z=$Z_\odot$, interpolating logarithmically in metallicity between those values.

In Fig. C.1 we show the results for a SSP concerning the stellar death rates, including the CCSN rate, the SNIa rate (middle panel) and the corresponding time-integrated rates. With the

[7] Particular care is required from users of those yields. The ones for low mass stars are *net yields* for all metallicities *except* Z=0. The ones of massive stars are *total yields* coming out through the final explosion. One has to include then the composition of the envelope (calculated as the mass of the star minus the mass of the remnant minus the sum of the explosion ejecta), assumed to have the initial composition.

adopted IMF, there are about 4.5 10^{-3} CCSN and 1.2 10^{-3} SNIa for every $M_{\odot}$ of stars formed.

In Fig. C.2 we present the ejection rates for H, C, O and Fe as a function of time, for single stars (3 initial metallicities) and for SNIa. SNIa produce more than half of solar Fe and they have minor contributions to the production of "light" metals like C or O (but substantial ones to the production of Si or Ca).

We made extensive tests of the implemented SSP formalism (Eq. C.3) against the "classical" one (Eq. C.1) and we found excellent agreement in all cases.

References

Adibekyan, V. Z., Figueira, P., Santos, N. C., et al. 2013, A&A, 554, A44
Adibekyan, V. Z., Santos, N. C., Sousa, S. G., & Israelian, G. 2011, A&A, 535, L11
Afflerbach, A., Churchwell, E., & Werner, M. W. 1997, ApJ, 478, 190
Athanassoula, E. 1992, MNRAS, 259, 345
Athanassoula, E. 2005, MNRAS, 358, 1477
Athanassoula, E., Bosma, A., Creze, M., & Schwarz, M. P. 1982, A&A, 107, 101
Athanassoula, E., Machado, R. E. G., & Rodionov, S. A. 2013, MNRAS, 429, 1949
Baba, J., Saitoh, T. R., & Wada, K. 2013, ApJ, 763, 46
Babusiaux, C. & Gilmore, G. 2005, MNRAS, 358, 1309
Bekki, K. & Tsujimoto, T. 2011, ApJ, 738, 4
Bensby, T. 2013, ArXiv e-prints
Bensby, T., Alves-Brito, A., Oey, M. S., Yong, D., & Meléndez, J. 2011, ApJ, 735, L46
Bensby, T., Feltzing, S., & Oey, M. S. 2014, A&A, 562, A71
Bhattacharjee, P., Chaudhury, S., & Kundu, S. 2013, ArXiv e-prints
Bigiel, F., Leroy, A., Walter, F., et al. 2008, AJ, 136, 2846
Bilitewski, T. & Schönrich, R. 2012, MNRAS, 426, 2266
Binney, J. & Sanders, J. L. 2013, ArXiv e-prints
Binney, J. & Tremaine, S. 2008, Galactic Dynamics: Second Edition (Princeton University Press)
Bird, J. C., Kazantzidis, S., Weinberg, D. H., et al. 2013, ApJ, 773, 43
Blitz, L. & Rosolowsky, E. 2006, ApJ, 650, 933
Blitz, L. & Spergel, D. N. 1991, ApJ, 379, 631
Bobylev, V. V., Mosenkov, A. V., Bajkova, A. T., & Gontcharov, G. A. 2014, ArXiv e-prints
Boissier, S. & Prantzos, N. 1999, MNRAS, 307, 857
Bovy, J. & Rix, H.-W. 2013, ApJ, 779, 115
Bovy, J., Rix, H.-W., & Hogg, D. W. 2012a, ApJ, 751, 131
Bovy, J., Rix, H.-W., Liu, C., et al. 2012b, ApJ, 753, 148
Bronfman, L., Cohen, R. S., Alvarez, H., May, J., & Thaddeus, P. 1988, ApJ, 324, 248
Brook, C. B., Stinson, G. S., Gibson, B. K., et al. 2012, MNRAS, 426, 690
Brunetti, M., Chiappini, C., & Pfenniger, D. 2011, A&A, 534, A75
Cabrera-Lavers, A., Hammersley, P. L., González-Fernández, C., et al. 2007, A&A, 465, 825
Casagrande, L., Schönrich, R., Asplund, M., et al. 2011, A&A, 530, A138
Cavichia, O., Mollá, M., Costa, R. D. D., & Maciel, W. J. 2014, MNRAS, 437, 3688
Chamcham, K. & Tayler, R. J. 1994, MNRAS, 266, 282
Cheng, J. Y., Rockosi, C. M., Morrison, H. L., et al. 2012, ApJ, 752, 51
Chiappini, C. 2009, in IAU Symposium, Vol. 254, IAU Symposium, ed. J. Andersen, Nordströara, B. m, & J. Bland-Hawthorn, 191–196
Chiappini, C., Matteucci, F., & Gratton, R. 1997, ApJ, 477, 765
Chiappini, C., Matteucci, F., & Romano, D. 2001, ApJ, 554, 1044
Chomiuk, L. & Povich, M. S. 2011, AJ, 142, 197
Clarke, C. J. 1989, MNRAS, 238, 283
Comerón, S., Elmegreen, B. G., Knapen, J. H., et al. 2011, ApJ, 741, 28
Courteau, S., Cappellari, M., de Jong, R. S., et al. 2013, ArXiv e-prints
Daflon, S. & Cunha, K. 2004, ApJ, 617, 1115
Dame, T. M. 1993, in American Institute of Physics Conference Series, Vol. 278, Back to the Galaxy, ed. S. S. Holt & F. Verter, 267–278
Di Matteo, P., Haywood, M., Combes, F., Semelin, B., & Snaith, O. N. 2013, A&A, 553, A102
Drimmel, R. & Spergel, D. N. 2001, ApJ, 556, 181
Dutil, Y. & Roy, J.-R. 1999, ApJ, 516, 62
Edmunds, M. G. & Greenhow, R. M. 1995, MNRAS, 272, 241
Ferrière, K., Gillard, W., & Jean, P. 2007, A&A, 467, 611
Ferrini, F., Molla, M., Pardi, M. C., & Diaz, A. I. 1994, ApJ, 427, 745
Flynn, C., Holmberg, J., Portinari, L., Fuchs, B., & Jahreiß, H. 2006, MNRAS, 372, 1149
Forbes, J., Krumholz, M., & Burkert, A. 2012, ApJ, 754, 48
Friedli, D. & Benz, W. 1993, A&A, 268, 65
Friedli, D., Benz, W., & Kennicutt, R. 1994, ApJ, 430, L105
Fu, J., Kauffmann, G., Huang, M.-l., et al. 2013, MNRAS, 434, 1531
Genovali, K., Lemasle, B., Bono, G., et al. 2013, A&A, 554, A132
Gilmore, G. & Reid, N. 1983, MNRAS, 202, 1025
Goetz, M. & Koeppen, J. 1992, A&A, 262, 455
Goswami, A. & Prantzos, N. 2000, A&A, 359, 191
Grand, R. J. J., Kawata, D., & Cropper, M. 2012, MNRAS, 421, 1529
Grand, R. J. J., Kawata, D., & Cropper, M. 2014, MNRAS, 439, 623
Green, D. A. 2013, ArXiv e-prints
Greggio, L. 2005, A&A, 441, 1055
Guedes, J., Callegari, S., Madau, P., & Mayer, L. 2011, ApJ, 742, 76
Hammer, F., Puech, M., Chemin, L., Flores, H., & Lehnert, M. D. 2007, ApJ, 662, 322
Haywood, M., Di Matteo, P., Lehnert, M. D., Katz, D., & Gómez, A. 2013, A&A, 560, A109
Holmberg, J., Nordström, B., & Andersen, J. 2007, A&A, 475, 519
Hou, J. L., Prantzos, N., & Boissier, S. 2000, A&A, 362, 921
Isern, J., Artigas, A., & García-Berro, E. 2013, in European Physical Journal Web of Conferences, Vol. 43, European Physical Journal Web of Conferences, 5002
Iwamoto, K., Brachwitz, F., Nomoto, K., et al. 1999, ApJS, 125, 439
Kalberla, P. M. W. & Dedes, L. 2008, A&A, 487, 951
Kang, X., Chang, R., Yin, J., et al. 2012, MNRAS, 426, 1455
Karakas, A. I. 2010, MNRAS, 403, 1413
Kennicutt, R. C. & Evans, N. J. 2012, ARA&A, 50, 531
Kordopatis, G., Gilmore, G., Wyse, R. F. G., et al. 2013, MNRAS, 436, 3231
Kroupa, P. 2001, MNRAS, 322, 231
Kroupa, P. 2002, Science, 295, 82
Krumholz, M. R. 2014, ArXiv e-prints
Krumholz, M. R., Dekel, A., & McKee, C. F. 2012, ApJ, 745, 69
Kubryk, M., Prantzos, N., & Athanassoula, E. 2013, MNRAS, 436, 1479
Lacey, C. G. & Fall, S. M. 1985, ApJ, 290, 154
Lagos, C. D. P., Baugh, C. M., Lacey, C. G., et al. 2011, MNRAS, 418, 1649
Lehner, N. & Howk, J. C. 2011, Science, 334, 955
Lemasle, B., François, P., Genovali, K., et al. 2013, A&A, 558, A31
Lépine, J. R. D., Acharova, I. A., & Mishurov, Y. N. 2003, ApJ, 589, 210
Leroy, A. K., Walter, F., Brinks, E., et al. 2008, AJ, 136, 2782
Lewis, J. R. & Freeman, K. C. 1989, AJ, 97, 139
Li, Y., Mo, H. J., van den Bosch, F. C., & Lin, W. P. 2007, MNRAS, 379, 689
Lia, C., Portinari, L., & Carraro, G. 2002, MNRAS, 330, 821
Liu, C. & van de Ven, G. 2012, MNRAS, 425, 2144
Loebman, S. R., Roškar, R., Debattista, V. P., et al. 2011, ApJ, 737, 8
Lorimer, D. R. 2004, in IAU Symposium, Vol. 218, Young Neutron Stars and Their Environments, ed. F. Camilo & B. M. Gaensler, 105
Lorimer, D. R., Faulkner, A. J., Lyne, A. G., et al. 2006, MNRAS, 372, 777
Luck, R. E. & Lambert, D. L. 2011, AJ, 142, 136
Maoz, D. & Mannucci, F. 2012, PASA, 29, 447
Maoz, D., Mannucci, F., & Brandt, T. D. 2012, MNRAS, 426, 3282
Maoz, D., Sharon, K., & Gal-Yam, A. 2010, ApJ, 722, 1879
Marasco, A., Fraternali, F., & Binney, J. J. 2012, MNRAS, 419, 1107
Martin, P. & Roy, J.-R. 1994, ApJ, 424, 599
Martínez-Serrano, F. J., Serna, A., Doménech-Moral, M., & Domínguez-Tenreiro, R. 2009, ApJ, 705, L133
Matteucci, F. 2012, Chemical Evolution of Galaxies
Matteucci, F., Franco, J., Francois, P., & Treyer, M.-A. 1989, Rev. Mexicana Astron. Astrofis., 18, 145
Mayor, M. & Vigroux, L. 1981, A&A, 98, 1
McMillan, P. J. 2011, MNRAS, 414, 2446
Minchev, I., Chiappini, C., & Martig, M. 2013, A&A, 558, A9
Minchev, I., Chiappini, C., & Martig, M. 2014, ArXiv e-prints
Minchev, I. & Famaey, B. 2010, The Astrophysical Journal, 722, 112
Minchev, I., Famaey, B., Combes, F., et al. 2011, A&A, 527, A147
Minchev, I., Famaey, B., Quillen, A. C., et al. 2012a, A&A, 548, A127
Minchev, I., Famaey, B., Quillen, A. C., et al. 2012b, A&A, 548, A126
Misiriotis, A., Xilouris, E. M., Papamastorakis, J., Boumis, P., & Goudis, C. D. 2006, A&A, 459, 113
Mollá, M. & Díaz, A. I. 2005, MNRAS, 358, 521
Mott, A., Spitoni, E., & Matteucci, F. 2013, MNRAS, 435, 2918
Naab, T. & Ostriker, J. P. 2006, MNRAS, 366, 899
Nakanishi, H. & Sofue, Y. 2003, PASJ, 55, 191
Nakanishi, H. & Sofue, Y. 2006, PASJ, 58, 847
Navarro, J. F., Abadi, M. G., Venn, K. A., Freeman, K. C., & Anguiano, B. 2011, MNRAS, 412, 1203
Nieva, M.-F. & Przybilla, N. 2012, A&A, 539, A143
Nomoto, K., Kobayashi, C., & Tominaga, N. 2013, ARA&A, 51, 457
Olling, R. P. & Merrifield, M. R. 2001, MNRAS, 326, 164
Pagel, B. E. J. 2009, Nucleosynthesis and Chemical Evolution of Galaxies
Picaud, S. & Robin, A. C. 2004, A&A, 428, 891
Pohl, M., Englmaier, P., & Bissantz, N. 2008, ApJ, 677, 283
Porcel, C., Garzon, F., Jimenez-Vicente, J., & Battaner, E. 1998, A&A, 330, 136
Portinari, L. & Chiosi, C. 1999, A&A, 350, 827
Portinari, L. & Chiosi, C. 2000, A&A, 355, 929

Prantzos, N. 2009, in IAU Symposium, Vol. 254, IAU Symposium, ed. J. Andersen, B. Nordström, & J. Bland-Hawthorn, 381–392
Prantzos, N. 2012, A&A, 542, A67
Prantzos, N. & Aubert, O. 1995, A&A, 302, 69
Prantzos, N., Boehm, C., Bykov, A. M., et al. 2011, Reviews of Modern Physics, 83, 1001
Prantzos, N. & Silk, J. 1998, ApJ, 507, 229
Rashkov, V., Pillepich, A., Deason, A. J., et al. 2013, ApJ, 773, L32
Rix, H.-W. & Bovy, J. 2013, A&A Rev., 21, 61
Robitaille, T. P. & Whitney, B. A. 2010, ApJ, 710, L11
Rocha-Pinto, H. J., Scalo, J., Maciel, W. J., & Flynn, C. 2000, A&A, 358, 869
Romano, D., Karakas, A. I., Tosi, M., & Matteucci, F. 2010, A&A, 522, A32
Roskar, R. 2010, PhD thesis, University of Washington
Roškar, R., Debattista, V. P., & Loebman, S. R. 2013, MNRAS, 433, 976
Roškar, R., Debattista, V. P., Quinn, T. R., Stinson, G. S., & Wadsley, J. 2008, ApJ, 684, L79
Sales, L. V., Helmi, A., Abadi, M. G., et al. 2009, MNRAS, 400, L61
Sánchez, S. F., Rosales-Ortega, F. F., Marino, R. A., et al. 2012, A&A, 546, A2
Sánchez-Blázquez, P., Courty, S., Gibson, B. K., & Brook, C. B. 2009, MNRAS, 398, 591
Schaller, G., Schaerer, D., Meynet, G., & Maeder, A. 1992, A&AS, 96, 269
Schönrich, R. & Binney, J. 2009a, MNRAS, 396, 203
Schönrich, R. & Binney, J. 2009b, MNRAS, 399, 1145
Scott, P., Asplund, M., Grevesse, N., Bergemann, M., & Sauval, A. J. 2014, ArXiv e-prints
Sellwood, J. & Binney, J. 2002, MNRAS, 336, 785
Shevchenko, I. I. 2011, ApJ, 733, 39
Shlosman, I. & Noguchi, M. 1993, ApJ, 414, 474
Silk, J. & Mamon, G. A. 2012, Research in Astronomy and Astrophysics, 12, 917
Simpson, J. P., Colgan, S. W. J., Rubin, R. H., Erickson, E. F., & Haas, M. R. 1995, ApJ, 444, 721
Smartt, S. J. & Rolleston, W. R. J. 1997, ApJ, 481, L47
Sofue, Y. 2012, PASJ, 64, 75
Sofue, Y. 2013, ArXiv e-prints
Sommer-Larsen, J. & Yoshii, Y. 1990, MNRAS, 243, 468
Spitoni, E. & Matteucci, F. 2011, A&A, 531, A72
Steigman, G., Romano, D., & Tosi, M. 2007, MNRAS, 378, 576
Steinmetz, M. 2012, Astronomische Nachrichten, 333, 523
Sygnet, J. F., Tagger, M., Athanassoula, E., & Pellat, R. 1988, MNRAS, 232, 733
Thon, R. & Meusinger, H. 1998, A&A, 338, 413
Tinsley, B. M. & Larson, R. B. 1978, ApJ, 221, 554
Übler, H., Naab, T., Oser, L., et al. 2014, ArXiv e-prints
Urquhart, J. S., Figura, C. C., T. J., T., et al. 2013, ArXiv e-prints
van Dokkum, P. G., Leja, J., Nelson, E. J., et al. 2013, ApJ, 771, L35
Wakker, B. P., Howk, J. C., Savage, B. D., et al. 1999, Nature, 402, 388
Wang, Y. & Zhao, G. 2013, ApJ, 769, 4
Wielen, R., Fuchs, B., & Dettbarn, C. 1996, A&A, 314, 438
Wiersma, R. P. C., Schaye, J., Theuns, T., Dalla Vecchia, C., & Tornatore, L. 2009, MNRAS, 399, 574
Williams, J. P. & McKee, C. F. 1997, ApJ, 476, 166
Wilson, M. L., Helmi, A., Morrison, H. L., et al. 2011, MNRAS, 413, 2235
Woosley, S. E. & Weaver, T. A. 1995, ApJS, 101, 181
Wouterloot, J. G. A., Brand, J., Burton, W. B., & Kwee, K. K. 1990, A&A, 230, 21
Wyse, R. F. G. 1986, ApJ, 311, L41
Wyse, R. F. G. & Silk, J. 1989, ApJ, 339, 700
Yoachim, P. & Dalcanton, J. J. 2006, AJ, 131, 226
Zaritsky, D., Kennicutt, Jr., R. C., & Huchra, J. P. 1994, ApJ, 420, 87
Zhang, L., Rix, H.-W., van de Ven, G., et al. 2013, ApJ, 772, 108

3.2.6 Profils des abondances chimiques

Les profils d'abondance des éléments chimiques constituent une propriétés clés des disques galactiques. Ils dépendent de l'histoire du disque et de divers effets physiques qui l'ont affecté : la formation stellaire, accrétion et l'éjection de gaz, les courants radiaux de gaz, la migration radiale, et les effets de marées ou les fusions avec d'autres galaxies. En particulier, l'étude de la pente de ces profils permettait (avant que la migration radiale ne soit prise en compte) de reconstruire directement l'histoire de la Voie Lactée, mettant en évidence la formation progressive du disque de l'intérieur vers l'extérieur : les zones internes évoluant plus rapidement que les zones externes, la métallicité augmente plus rapidement vers le centre créant une forte pente dans les profils d'abondance chimique ; cette pente s'atténue ensuite lorsque l'évolution chimique des zones externes rattrape celle des zones internes. Cette évolution devait se retrouver dans l'observation des profils d'abondances en fonction de l'âge des étoiles : une pente forte pour les étoiles âgées, et qui se réduit pour les étoiles de plus en plus jeunes.

Mais avec la migration radiale des étoiles, il a été montré par Roškar et al. (2008a) que plus les étoiles sont âgées, plus leur profil est plat, ce qui vient du fait que les vieilles étoiles ont plus de temps pour se déplacer dans le disque. Ainsi la pente des profils est fortement influencée par la migration, ce qui brouille l'interprétation de ces observables. Dans ce cadre, comprendre précisément comment la migration radiale affecte ces profils, permet d'extraire de ces marqueurs de nouvelles informations concernant l'histoire du disque.

Dans notre modèle, les profils d'abondances dans les étoiles ne peuvent pas être caractérisés par une pente unique (Fig. 5 de l'article en Sec. 3.2.7) parce qu'ils s'aplatissent vers l'extérieur du disque, en conséquence du TFS adopté ; et vers l'intérieur du disque, en conséquence des courants de gaz induits par la barre, qui ramène du gaz des régions plus externes (moins métalliques) vers les régions internes (plus métalliques) ce qui a pour effet d'en diluer la composition chimique. Nous trouvons que les profils d'abondances s'aplatissent aussi avec le temps, à cause de la formation progressive du disque de l'intérieur vers l'extérieur : dans les premiers temps, les zones internes forment beaucoup d'étoiles et s'enrichissent rapidement en métaux, alors que la formation stellaire est très faible dans les régions plus à l'extérieur, ce qui produit un fort gradient dans les profils de métallicité dans les premiers temps du modèle ; par la suite la métallicité des régions externes rattrape en partie celle des régions internes lorsque la formation stellaire démarre dans ces zones, ce qui diminue le gradient de métallicité du disque. Mais la confirmation observationnelle de l'aplatissement des profils avec le temps, devient impossible à cause de la migration radiale. En effet, d'après ce qui vient d'être dit, le gradient métallicité devrait être de plus en plus fort quand on observe des étoiles de plus en plus âgées. Toutefois, plus les étoiles sont âgées, plus elles ont le temps de migrer dans le disque et de se mélanger, ce qui aplati (voir inverse) les profils de métallicité de ces étoiles (Fig. 6 de l'article en Sec. 3.2.7). Cet effet de la migration avait été décrit par Roškar et al. (2008a), nous le confirmons dans notre modèle. Nous comparons également nos résultats avec Minchev, Chiappini & Martig (2014) (panneau du milieu Fig. 7 de l'article en Sec. 3.2.7) qui trouvent des profils assez similaires aux notre.

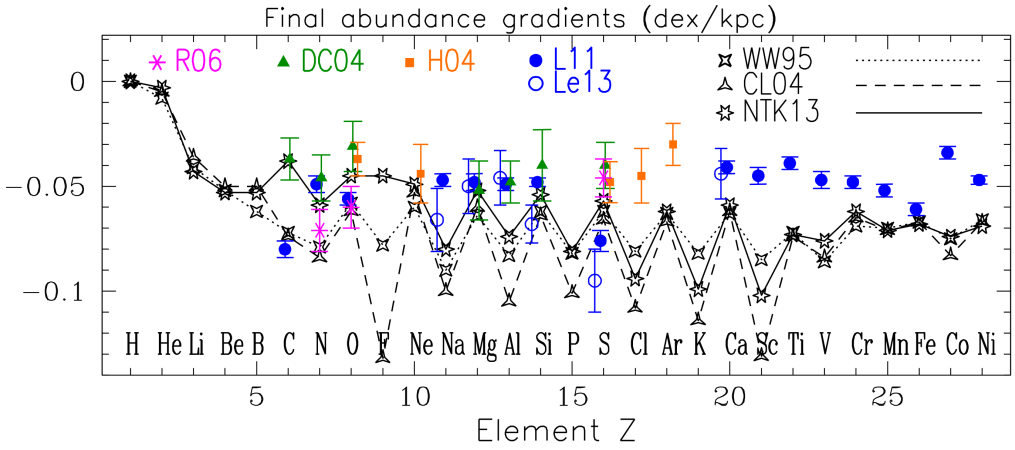

FIGURE 3.12 – Gradients d'abondances actuels de H à Ni : modèle avec différentes grilles de rendements vs. observations. Les symboles de couleurs indiquent différents jeux d'observations, et les symboles non colorés indiquent les résultat obtenu avec notre modèle, en changeant juste la grille de rendements utilisée.

Résultat important : Nous présentons les résultats du modèle pour tous les éléments entre C et Ni. Du point de vue théorique, nous insistons sur les différences systématiques dans les profils d'abondances finaux causées par différentes grilles de rendements stellaires. Nous trouvons que, globalement, les gradients d'abondances obtenus avec ces grilles coïncident bien avec les observations (en supposant qu'ils puissent être décrit par une pente unique), mais nous trouvons également des écarts systématiques (voir Fig. 3.12, les pentes obtenues sont systématiquement 0.01-0.02 dex/kpc plus grandes (en valeur absolue) que celles issues des observations). Nous discutons le fait que, si cette différence est confirmée, elle pourrait être corrigée en modifiant certains ingrédients de notre modèle : en imposant une accrétion de gaz plus rapide vers les régions externes du disque, ou en imposant pour le gaz accrété une métallicité plus élevée que la métallicité primordiale (métallicité du gaz après la Big Bang). Nous trouvons également un effet intéressant suivant les numéros atomiques pair-impaires des éléments, avec des pentes plus élevées pour les éléments impairs. Cet effet (qui dépend par ailleurs de la métallicité initiale des étoiles), discuté dans le contexte des ratio d'abondances dans les étoiles du halo, est trouvé ici pour la pour la première fois et il est générique, i.e. il concerne toutes les grilles de rendements stellaires. Cependant, il n'apparaît pas dans les données observationnelles. Si ces données sont confirmées, alors certains aspects de la nucléosynthèse dans les étoiles devront être revus.

L'évolution de nos profils d'abondance dans le gaz concordent bien avec les observations extragalactiques à au redshift compilées par Jones et al. (2013) (panneau bas Fig. 7 de l'article en Sec. 3.2.7). Cependant, ces observations sont encore affectées par des incertitudes trop importantes pour que des conclusions fermes soient dérivées de leur comparaison avec le modèle.

3.2.7 Article : Les profils d'abondances chimiques

Astronomy & Astrophysics manuscript no. Paper4_v2
July 14, 2014

Evolution of the Milky Way with radial motions of stars and gas

II. The evolution of abundance profiles from H to Ni

M. Kubryk[1], N. Prantzos[1] and E. Athanassoula[2]

[1] Institut d'Astrophysique de Paris, UMR7095 CNRS, Univ. P. & M. Curie, 98bis Bd. Arago, 75104 Paris, France
e-mail: kubryk@iap.fr,prantzos@iap.fr
[2] Aix Marseille Université, CNRS, LAM (Laboratoire d'Astrophysique de Marseille) UMR 7326, 13388, Marseille, France
e-mail: lia@lam.fr

Received ; accepted

ABSTRACT

Context. We study the role of radial motions of stars and gas on the evolution of abundance profiles in the Milky Way disk.
Aims. We investigate, in a parametrized way, the impact of radial flows of gas and radial migration of stars induced mainly by the Galactic bar and its iteraction with the spiral arms.
Methods. We use a model with several new or up-dated ingredients (atomic and molecular gas phases, star formation depending on molecular gas, recent sets of metallicity-dependent stellar yields from H to Ni, observationally inferred SNIa rates), which reproduces well most global and local observables of the Milky Way.
Results. We obtain abundance profiles flattening both in the inner disk (because of radial flows) and in the outer disk (because of the adopted star formation law). The gas abundance profiles flatten with time, but the corresponding stellar profiles appear to be steeper for younger stars, because of radial migration. We find a correlation between the stellar abundance profiles and O/Fe, which is a proxy for stellar age. Our final abundance profiles are in overall agreement with observations, but slightly steeper (by 0.01-0.02 dex kpc^{-1}) for elements above S. We find an interesting "odd-even effect" in the behaviour of the abundance profiles (steeper slopes for odd elements) for all sets of stellar yields; however, this behaviour does not appear in observations, suggesting that the effect is, perhaps, overestimated in current stellar nucleosynthesis calculations.

Key words.

1. Introduction

The abundance profiles of chemical elements constitute one of the key properties of galactic disks. They depend on the past history of the disk and the various physical effects that affected it: star formation, infall and outflows, radial flows of gas, radial motions of stars and tidal interactions or mergers with other galaxies. Most semi-analytical studies of abundance profiles were performed in the framework of the so-called "independent-ring" model, where the galactic disk is simulated as an ensemble of independently evolving annuli (e.g. Guesten & Mezger (1982); Matteucci et al. (1989); Ferrini et al. (1994); Prantzos & Aubert (1995); Chiappini et al. (1997); Boissier & Prantzos (1999); Hou et al. (2000); Prantzos & Boissier (2000)) and concerned the MW disk, for which a large number of other constraints, both local and global are available. Those studies focused mainly on the interplay between the local star formation and infall rates, or the impact of variable stellar IMF. They also revealed the key issue of the evolution of the abundance profile, some studies supporting a flattening of it with time (e.g. Ferrini et al. (1994); Prantzos & Aubert (1995); Hou et al. (2000) while others concluded the opposite (e.g. Tosi (1988); Chiappini et al. (1997)).

Pioneering work of Tinsley & Larson (1978) and Mayor & Vigroux (1981) noticed the potential importance of radial gaseous flows for the chemical evolution of galactic disks. Lacey & Fall (1985) presented a systematic investigation of the causes of such flows, and explored with parametrized calculations the impact of such effects on the chemical evolution of the Galaxy. Further parametrized investigations with simple 1D models of disk evolution are made in e.g. Tosi (1988); Clarke (1989); Sommer-Larsen & Yoshii (1990); Goetz & Koeppen (1992); Chamcham & Tayler (1994); Edmunds & Greenhow (1995); Portinari & Chiosi (2000) and more recently in Spitoni & Matteucci (2011); Bilitewski & Schönrich (2012); Mott et al. (2013); Cavichia et al. (2014). They have various motivations (mostly to fit the abundance profiles, but also gas and star profiles) and they are generally applied to the study of the MW disk. As expected, results are not conclusive, because they depend not only on the parametrization of the unknown inflow velocity patterns, but also on the other unknown (and parameterized) ingredients of the models, especially the adopted SFR and infall profiles as functions of time. Among the alleged causes of radial inflows, the impact of a galactic bar is well established, both from simulations and from observations. Numerical simulations (Athanassoula 1992; Friedli & Benz 1993; Shlosman & Noguchi 1993) showed that the presence of a non-axisymmetric potential from a bar can drive important amounts of gas inwards of corotation (CR) fuelling star formation in the galactic nucleus, while at the same time gas is pushed outwards outside corotation. In a disk galaxy, this radial flow mixes gas of metal-poor regions into metal-rich ones (and vice-versa) and may flatten the abundance profile (e.g. Friedli et al. (1994); Zaritsky et al. (1994); Martin & Roy (1994); Dutil & Roy (1999)), although Sánchez et al. (2012) find little difference in that respect between barred and non-barred disks. The study of Kubryk et al. (2013) suggests

that bars may be changing the chemical abundance profile inside the corotation radius but they have only a small impact outside it, while Martel et al. (2013) find a rather complex situation of continuous exchange of gas and metals between the bar and the central region of the disk.

The investigation of radial motions of stars - due to inhomogeneities of the galactic gravitational potential - on the chemical evolution of disks, has a more recent history. The role of the bar has been studied to some extent with N-body+SPH codes by Friedli & Benz (1993) and Friedli et al. (1994). Observations in the 90ies revealed that the MW does have a bar (Blitz & Spergel 1991), but its size and age are not well known yet. Sellwood & Binney (2002) showed that, in the presence of recurring transient spirals, stars in a galactic disk could undergo important radial displacements: stars found at corotation with a spiral arm may be scattered to different galactocentric radii (inwards or outwards), a process which preserves overall angular momentum distribution and does not contribute to the radial heating of the stellar disk. Using a simple model, they showed how this process can increase the dispersion in the local metallicity vs age relation, well above the amount due to the epicyclic motion. Minchev & Famaey (2010) suggested that resonance overlap of the bar and spiral structure (Sygnet et al. 1988) produces a more efficient redistribution of angular momentum in the disk. This bar-spiral coupling was studied in detail with N-body simulations by Brunetti et al. (2011) who found that radial migration can be assimilated to a diffusion process, albeit with time- and position-dependent diffusion coefficients. That idea was confirmed by the analysis of N-body+SPH simulations of a disk galaxy by Kubryk et al. (2013) who showed that radial migration moves around not only "passive" tracers of chemical evolution (i.e. long-lived stars, keeping on the surfaces the chemical composition of the gas at the time and place of their birth), but also "active" agents of chemical evolution, i.e. long-lived nucleosynthesis sources (mainly SNIa producing Fe and ∼1.5 $M_{\odot}$ stars producing s-process elements).

The implications of radial migration for the chemical evolution of MW-type disks were studied with N-body codes by Roškar et al. (2008) , who found that the stellar abundance profiles flatten with stellar age, even if the gaseous abundance profiles were steeper in the past. Schönrich & Binney (2009) introduced a parametrised prescription of radial migration (distinguishing epicyclic motions from migration due to transient spirals) in a semi-analytical chemical evolution code. They suggested that radial mixing could explain not only local observables (e.g. the dispersion in the age-metallicity relation) but also the formation of the Galaxy's thick disk, by bringing to the solar neighborhood a kinematically "hot" stellar population from the inner disk. That possibility was subsequently investigated with N-body models, but controversial results are obtained up to now: while Loebman et al. (2011) find that secular processes (i.e. radial migration) are sufficient to explain the kinematic properties of the local thick disk, Minchev et al. (2012) find this mechanism insufficient and suggest that an external agent (e.g. early mergers) is required for that.

Following the pioneering work of Schönrich & Binney (2009), the properties of the MW disk were studied in detail with semi-analytical models accounting for radial migration by Minchev et al. (2013) and Kubryk et al. (2014). The three models differ in several ways: Schönrich & Binney (2009) use a toy-model of star transfer between adjacent radial zones (with coefficients tuned to reproduce properties of the local disk), whereas the other two are inspired by the results of N-body simulations (but they adopt different implementation techniques of those results). Radial gaseous flows are included in Schönrich & Binney (2009) and Kubryk et al. (2014), but not in Minchev et al. (2013); however, in the former case, they concern mainly the outer disk, where in Kubryk et al. (2014) the inner disk, since they simulate the action of a bar. The dimension vertical to the galactic plane is considered in Schönrich & Binney (2009) and Minchev et al. (2013), but not in Kubryk et al. (2014). Finally, the star formation and radial infall laws are different in the three works. All models consider explicitly Fe production by SNIa (albeit with different prescriptions for the SNIa rate) and the finite lifetimes of stars.

Despite those differences, all three models find good agreement with the main observables of the MW, both locally (dispersion in age-metallicity relation, metallicity distribution, the characteristic "two-branch" behaviour between thick and thin disk in the O/Fe vs Fe/H plane) and globally (stellar and abundance profiles). This agreement suggests that, despite their sophistication, such models still involve too many parameters and suffer from degeneracy problems. We note here the difference in the final abundance gradient of Fe/H between Schönrich & Binney (2009) and Minchev et al. (2014), who find slopes of the corresponding exponential profiles of -0.1 dex $kpc^{-1}$and -0.06 dex kpc^{-1}, respectively. Recent observations of statistically significant samples of Cepheids are consistent with the latter value, as we shall discuss in Sec. 3.

In this work, we study the evolution of abundance profiles of all elements from H to Ni in the MW, using the model presented in Kubryk et al. (2014, hereafter KPA2014). The plan of the paper is as follows: The main ingredients of the model are briefly presented in Sec. 2, where we also discuss some of the results concerning the impact of radial migration on the disk properties. We illustrate that impact by comparing a model with radial migration to one without it. In Sec. 3 we discuss in some detail the profiles of the most important metals, namely O (Sec. 3.1) and Fe (Sec. 3.2) and we compare them to a large number of recent observations from various metallicity tracers. The impact of radial migration on the evolution of the abundance profiles is discussed in Sec. 3.3, where we compare our results to those of a similar study (Minchev et al. 2014) and to a compilation of extragalactic observations by Jones et al. (2013). In Sec. 3.4 we adress the issue of the O/Fe ratio; in view of the small dispersion displayed by that ratio as a function of time, it can be used as a robust proxy for stellar age in studies of the evolution of the abundance profiles in the disk. In Sec. 3.5 we present our results for all elements from H to Ni and we compare them to several sets of observational data. We find good overall agreement with observations, but a systematically larger (in absolute value) slope of the abundance profiles for the Fe-peak elements compared to observations. We also reveal - and we draw attention to - interesting differences between the results obtained with different sets of stellar yields, as well as a manifestation of the "odd-even" effect of nucleosynthesis, which does not appear, however, in the observational data. A summary of the results is presented in Sec. 4.

2. The model

The model presented in KPA14 for the evolution of the MW disk, involves radial motions of both gas and stars. The MW disk is built gradually by infall of primordial gas in the potential well of a "typical" dark matter halo of final mass 10^{12} $M_{\odot}$, the evolution of which is extracted from numerical simulations. The infall timescale is a monotonically increasing function of galactocentric radius, ranging from 1 Gyr at 1 kpc to 7 Gyr at

7 kpc and slightly increasing further outwards (see Fig. 1). Star formation depends on the local surface density of molecular gas, which is calculated by the semi-empirical prescriptions of Blitz & Rosolowsky (2006): the SFR depends on a combination of the stellar surface density profile (steeply decreasing with radius) and the gas surface density profile (essentially flat today). This allows us to use the final profiles of atomic and molecular gas as supplementary constraints to the model (see Fig. 6 in KPA14). The adopted prescription produces a steep profile of H_2 (as observed in the Galaxy) and, thereoff, a steep SFR profile in the inner disk during most of the Galactic evolution; this impacts directly on the corresponding abundance profiles, as we discuss below. For the radial flows of gas, we consider only the case of a MW-like bar operating for the last 6 Gyr and driving gas inwards and outwards of corotation. The radial velocity profile of the ges flow induced by the bar is similar to the one adopted in Portinari & Chiosi (2000) (their Case B for the bar), but not exactly the same: Portinari & Chiosi (2000) consider additional radial flows inwards, acting all over the disk, while we limit ourselves to the case of the bar alone. The adopted radial velocity profile is given in Fig. 1.

We considered separately the epicyclic motion of stars (blurring) from the true variation of their guiding radius (churning), as in Schönrich & Binney (2009). For the former, we developed an analytic formalism based on the epicyclic approximation; for the latter, we adopted a parametrised description, using time- and radius- dependent diffusion coefficients, extracted from the N-body+SPH simulation of KPA13, which concerns a disk galaxy with a strong bar; as discussed in KPA2014, we adapted those transfer coefficients taking into account the smaller size of the MW bar. For the chemical evolution, we adopted recent sets of metallicity-dependent yields from Nomoto et al. (2013), providing a homogeneous and fine grid of data, well adapted to the case of the MW disk. For comparison purposes, we also used older yields from Woosley & Weaver (1995) and Chieffi & Limongi (2004). We adopted the stellar IMF of Kroupa (2002) with a slope of X=1.7 (the Scalo slope) for the high masses. For the rate of SNIa, we adopted the empirical law of $R_{SNIa} \propto t^{-1.1}$, after the observed delayed time distribution of those objects in external galaxies (see e.g. Maoz et al. (2012) and references therein). In contrast with usual practice in studies of galactic chemical evolution, we adopted the formalism of Single Particle Population (SSP), which is the only one applicable to the case of radial migration, since it allows one to consider the radial displacements of nucleosynthesis sources and in particular of SNIa (see KPA13 for a discussion of that effect). Finally, we adopted a large and diverse set of recent observational data to constrain our model.

Our model reproduces well the present day values of most of the main global observables of the MW bulge (assumed to correspond to radii r <2 kpc) and disk (r >2 kpc): present-day masses of stars, atomic and molecular gas, star formation rates as well as core collapse supernova (CCSN) and SNIa rates (see Fig. 2 in KPA14). The corresponding radial profiles of all those quantities (azimuthally averaged) are also reproduced in a satisfactory way (Fig. 6 in KPA14). The azimuthally averaged radial velocity of gas inflow in the bar region is constrained to be less than a few tenths of km/s in the framework of that model. The local properties of the MW disk, i.e. metallicity distribution and age-metallicity relation, are also well reproduced. In particular, following Sellwood & Binney (2002), we showed how radial migration can be constrained by the observed dispersion in the age-metallicity relation. . We emphasize, however, that the observational samples that we used - from Bensby et al. (2014) for the age-metallicity relation and from Adibekyan et al. (2011)

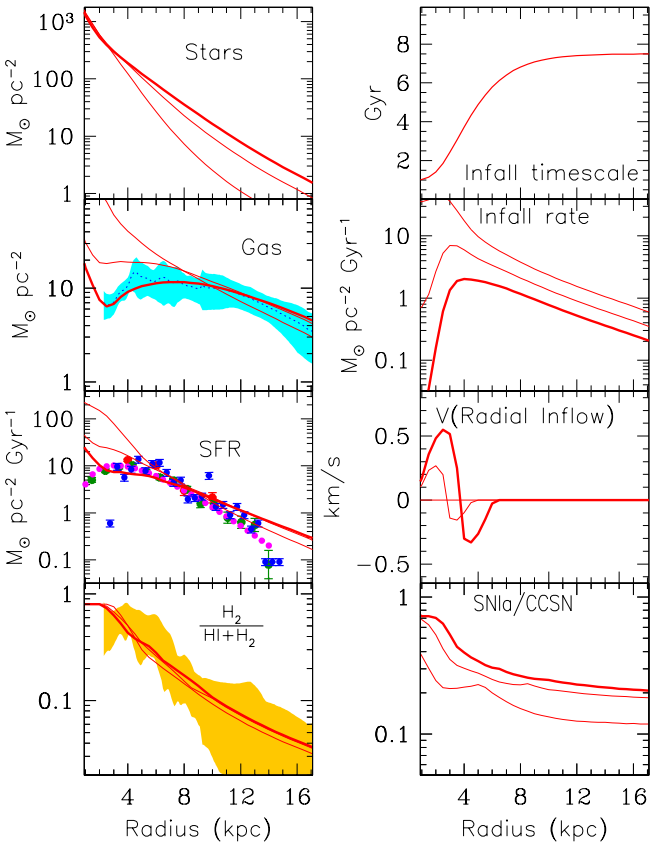

Fig. 1. *Left* (from top to bottom): Model profiles of stars, gas, SFR and molecular gas fraction f_{Mol} at 4, 8 (*thin* curves) and 12 Gyr (*thick* curve). The curve at 12 Gyr is compared to observational data for the present-day profiles of the correspoding quantities (*shaded aereas* for the stars, gas and f_{Mol} and points with error bars for the SFR); data sources are provided in KPA14. *Right* (from top to bottom): Infall timescales, infall rates, velocity profiles of radial inflow (positive values towards the Galactic center), ratio of SNIa/CCSN ; in all panels but the top one, the three curves correspond to 4, 8 and 12 Gyr (thickest curve).

and Bensby et al. (2014) for the metallicity distribution - have various selection biases (kinematic, limited by magnitude or volume), which have not been applied to our results: the model predictions for the solar neighborhood concern the "solar cylinder", of diameter 0.5 kpc (the size of our radial bin), centered on the Sun.

Assuming that the thick disk is the oldest (>9 Gyr) part of the disk, we found that the adopted radial migration scheme can reproduce quantitatively the main local properties of the thin and thick disk: metallicity-distributions, the characteristic "two-branch" behaviour of the local O/Fe vs Fe/H relation, local surface densities of stars (10 $M_\odot$/pc^2 and 28 $M_\odot$/pc^2 for the thick and thin disk, respectively). The thick disk extends up to ~11 kpc and has a scale length of 1.8 kpc; this is consistent with recent evaluations (e.g. Bovy & Rix 2013 and references therein) and it is considerably shorter than the one of the thin disk, consistent with the inside-out formation scheme.

Some of the main results of the model relevant for this work appear in Fig. 1. The inside-out formation of the disk is evidenced by the evolution of both the infall rate profile and the stellar profile. The gaseous profile, mostly flat today, with a local

surface density of ~12 $M_{\odot}/pc^2$, is well reproduced. The profile of the molecular fraction $f_{Mol} = \frac{H_2}{(HI+H_2)}$ is well reproduced also, after the prescriptions of Blitz & Rosolowsky (2006). As already mentioned, this profile plays an important role in our model, because it determines the molecular profile and, thereoff, the profile of the star formation rate $\Psi(r) = f_{Mol}(r)\Sigma_{Gas}(r)$.

The profile of the SNIa/CCSN ratio (bottom right panel) becomes steeper as one moves from the outer to the inner Galaxy, because the SNIa rate - being a mixture of old and young population objects - follows a combination of the stellar and gas profiles. The steep stellar profile increases substantially the SNIa/CCSN ratio in the inner disk; the outer disk, populated mostly by gas and young stars, has essentially SNIa belonging to the young stellar population, as the CCSN: as a result, the SNIa/CCSN ratio in the outer disk is practically constant. Notice that similar results for the SNIa/CCSN ratio are obtained in the independent-ring model for the MW disk by Boissier & Prantzos (2009), both with the numerical prescription of Greggio (2005) and with an analytical prescription for the SNIa rate (their Fig. 11). In the present study, a fraction of SNIa - those belonging to the old stellar population - is affected by radial migration, mostly in the region 3-12 kpc (see next paragraph). All these features affect directly the resulting O and Fe profiles, as well as those of all other elements (see discussion in next section).

Some aspects of the stellar radial migration of the model appear in Fig. 2. The top panel displays the fraction of stars born in radius r (in a radial bin of width $\Delta r = \pm 0.25$ kpc) and found in the end in all other radii. It can be seen that the action of the bar brings a large fraction of the stars of the inner disk in the outer regions: some stars born in r=3 kpc are found int he solar neighborhood in the end of the simulation. As we show in KPA14, these are the most metallic stars presently found in the solar neighborhood, with metallicities [Fe/H]~0.4 and they are 3-5 Gyr old. In contrast, a negligible fraction of the stars born in r >12 kpc reaches the solar vicinity.

The middle left panel of Fig. 2 displays the original vs final guiding radii of stars. Stars found in the radial range 3-14 kpc have been formed, on average, inwards of their present position; the effect is most pronounced for stars in the region 6-9 kpc, where the average outwards displacement reaches Δr ~1.5 kpc, and it is reduced to negligible values inside 4 kpc and outside 14 kpc. Also, the dispersion around those average values is large in the 6-9 kpc range and decreases outside it. Clearly, however, radial migration affects to some extent regions at all galactocentric distances. We stress that the extent of radial migration depends strongly on the adopted (time- and radius-dependent) diffusion coefficients and on the morphology of the disk galaxy: a larger amount of radial migration is expected in the case of barred disks, through the coupling of the bar to the spiral arms (Minchev & Famaey 2010).

Finally, the bottom panel of Fig. 2 displays the average age of the stellar populations as function of Galactocentric radius, both for all the stars and for the stars formed *in situ*. In the latter case, the average age varies little with radius outside r=6 kpc, because the adopted profile of the infall timescale (Fig. 1) varies little in that region. However, radial migration brings older (on average) stars from the inner disk in intermediate radii: as a result, a clear age gradient is developed throughout the disk (solid curve in Fig. 2 bottom).

As emphasized in KPA14, the impact of radial migration on the properties of the disk is not intuitively straightforward, because migrating stars may return their gas (metal-rich, if originating from the inner disk or metal-poor if originating from the outer disk) in places far away from their home radius; this gas may affect the local metallicity and also fuel star formation (depending on the local star formation efficiency). The situation becomes even more complex in the case of a bar: the bar drives inwards gas - also fuelling star formation in the inner disk - which is more metal poor, in general, than the local gas and thus the metallicity in the inner disk decreases; the overall result depends, however, also on the ratio of the local infall rate to the SFR and on the previous history of the disk (which determines the metallicity at a given time). Oxygen is affected differently than Fe, because the main source of the latter, namely SNIa, is affected by radial migration, while the source of O (massive stars) is not.

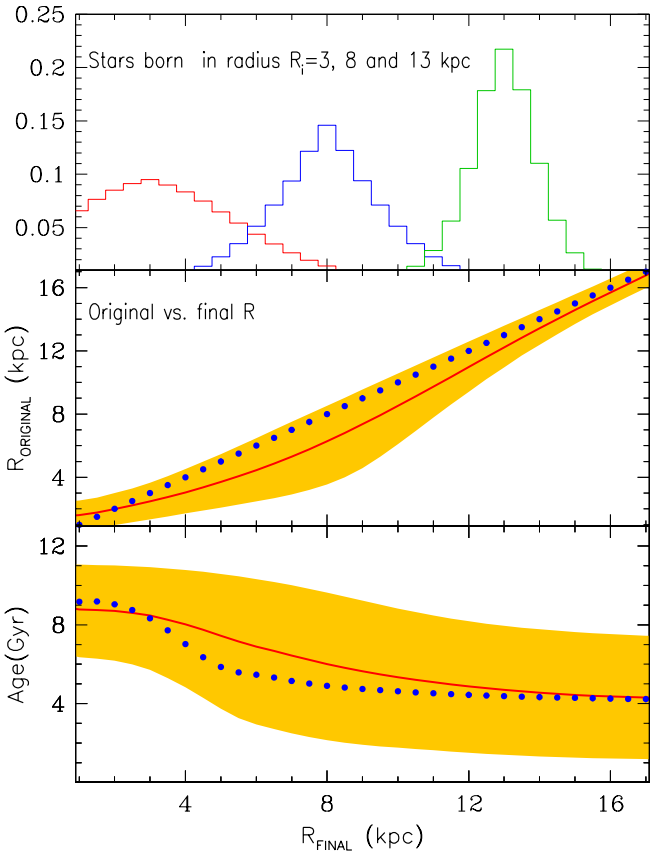

Fig. 2. *Top:* Fractions of stars born in radii r_{Origin}=3, 8 and 13 kpc and found in radius r_{Final} at t=12 Gyr. *Middle:* Original vs final guiding radii of stars (*solid curve*); the shaded aerea includes ±1 σ values (i.e. from 16% to 84% of the stars) and the dotted diagonal line indicates the stellar guiding radii in the absence of radial migration. *Bottom:* Average age of stars vs Galactocentric radius (*solid curve*); the shaded aerea includes ±1 σ values and the *dotted* curve indicates the average age of stars formed *in-situ*.

We attempt an illustration of this complex behaviour in Fig. 3, where we plot the ratio of several quantities of the model (with radial migration and radial inflow) to those same quantities obtained by an identical model (same boundary conditions, same SFR and infall rates) without radial migration or radial inflow. One can easily see that the quantities affected mostly by radial migration are the long-lived stars and SNIa: their radial profiles are affected over most of the disk. The radial profiles of SNIa are affected to smaller extent than those of stars, because a substantial fraction of SNIa results from a young population, unaffected

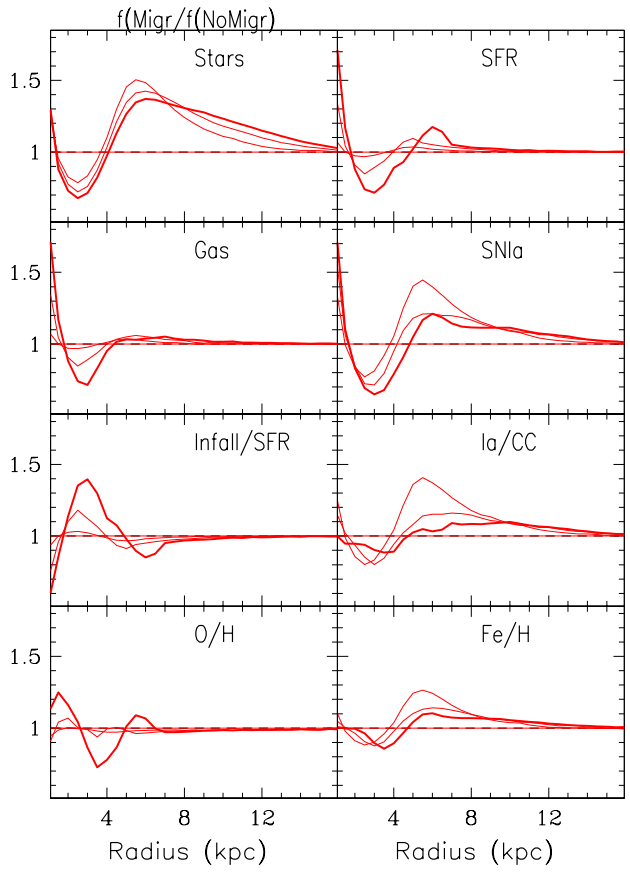

Fig. 3. *Top:* Comparison of various properties of our model, expressed as the ratio of a given quantity in the case of radial migration to the same quantity when stars do not migrate. From top to bottom, *left*: star surface density, gas surface density, gas fraction, O/H profile; *right*: SFR surface density, SNIa rate, ratio of SNIa/CCSN, Fe/H profile. In all panels, *thick curves* represent results at 12 Gyr and thin curves at 8 and 4 Gyr, respectively (as in Fig. 1).

by radial migration (~40% of them explode within 1 Gyr after the formation of their progenitor system, see Fig. C1 in Appendix C of KPA2013); in contrast, most stars are low-mass and long-lived (~90% by number for a normal IMF) and their population is affected by radial migration.

Gas is affected mainly not by radial migration, but by the radial inflow induced by the bar. Its surface density is depleted in the 2-4 kpc region and slightly increased outside it; notice that the latter increase is also due, to a small extent, to the gas returned to the ISM by the migrating, dying stars. The evolution of the gas profile is reflected in the one of the SFR profile, which is also affected by the radially dependent fraction f_{H_2} of molecular gas: there is less SFR in the 2-4 kpc region than without radial migration and gas inflow. That region is also the one corresponding to the peak of the infall rate during the late evolution of the disk (see Fig. 1), and shows a higher infall/SFR ratio than the model with no radial migration. For those reasons (smaller SFR and higher dilution of the metallicity through the primordial infall), this region is found to have a lower O/H ratio than in the model with no radial migration. The decrease in the Fe/H ratio is smaller, because some Fe is contributed in those zones by SNIa migrating inwards. But the largest impact on the chemical evolution concerns the SNIa migrating outwards: they increase the Fe content of the region between 5 and 8 kpc by ~30% after 4 Gyr and by ~10% in the end of the simulation. As a result, the final Fe/H radial profile is somewhat steeper than in the model without radial migration.

Overall, the effects of radial migration on the profiles of stars, SNIa, SNIa/CCSN ratio and Fe/H appear to become less important at late times. This result appears counter-intuitive, at first sight, because more radial migration occurs at longer timescales (everything else kept equal). Our counter-intuitive result is due to the inside-out formation of the disk. At early times, there are few stars (and SNIa) in the outer Galaxyl: any radial transfer from the inner regions (where a large stellar population has been formed) to the outer ones, increases the surface density of the latter by a large amount. At late times, the stellar population is in place all over the disk: the impact of radial migration from the inner to the outer disk (where a lot of stars are formed *in situ*) is proportionally smaller then.

KPA13 performed a similar exploration of the effects of radial migration for the case of a N-body+SPH simulation concerning a barred disk galaxy, evolving without gaseous infall (as a closed box). They found that, in that case, the strong bar induced a much larger amount of radial migration all over the disk, affecting particularly its outmost regions. As discussed in KPA14, we adapted the description of the radial migration of that model to the one of the MW, by taking into account the size of the bar in the two cases. The smaller bar of the MW implies smaller extent of radial migration than in the barred disk of KPA13.

3. Abundance evolution

Our model includes the detailed evolution of 83 isotopes, from H to Zn. The abundances of the corresponding 32 elements are obtained at each time step by summing over the isotopic ones.

IN KPA14 we have found that the adopted parameters of the model (SFR efficiency, infall timescale, SNIa rate, IMF, etc.) allow us to reproduce quite well the solar abundance of O and Fe for the *average 4.5 Gyr old star* in the solar neighborhood[1] The average birth radius of those stars is found to be at a Galactocentric distance of ~6.5 kpc, i.e. ~1.5 kpc inwards of the present day position of the Sun. This implies that the Sun is an average star of 4.5 Gyr in the Solar neighborhood as far as its chemistry is concerned, but such stars are not born *in situ*, they have migrated here from the inner disk.

Regarding the other elements and isotopes, we find that the agreement with the solar abundances is quite good for most of them (to better than a factor of 2, see Fig. 17 in KPA14). In several cases, however, and in particular in the region of Sc to Mn, a clear underabundance is obtained with the adopted yields of Nomoto et al. (2013). The reason of that disagreement is obviously a deficiency of the yields. A similar deficiency is obtained when using those yields to study the evolution of the halo(see Fig. 10 in Nomoto et al. (2013)). To cure for that, we normalised the model results as to have the average abundances of the 4.5 Gyr old stars currently present in the solar neighborhood equal to their solar values, i.e. we corrected the stellar yields (integrated over the IMF) to various degrees (by 2% for O, up to a factor of 4 for V). In that way, we were able to compare the corresponding evolution of all the abundance ratios X/Fe vs Fe/H to observational data of two recent surveys (Adibekyan et al. 2011;

[1] We calculate the average metallicity $< [Z/H] >= \frac{\Sigma N_i [Z/H]_i}{\Sigma N_i}$ of stars of age A found in zone r, where N_i is the number of stars with metallicity $[Z/H]_i$ in that zone.

Table 1. References for adopted data on Cepheids, B-stars, HII-regions, planetary nebulae (PN) and Open clusters (OC).

Element	Cepheids	B-stars	H-II	PN	OC
C	1	4,5			
N	1	4,5	6	7	
O	1	4,5	6	7,8	
Ne				7	
Na	1				
Mg	1	4,5			
Al	1	4,5			
Si	1	4,5			
S		4,5	6	7	
Ar				7	
Ca	1				
Sc	1				
Ti	1				
V	1				
Mn	1				
Cr	1				
Fe	1,2,3				9,10,11
Co	1				
Ni	1				

1: Luck & Lambert (2011), 2: Lemasle et al. (2013), 3: Genovali et al. (2014), 4:Gummersbach et al. (1998), 5: Daflon & Cunha (2004), 6: Rudolph et al. (2006), 7: Henry et al. (2004), 8:Henry et al. (2010), 9: Magrini et al. (2009), 10: Yong et al. (2012), 11: Frinchaboy et al. (2013)

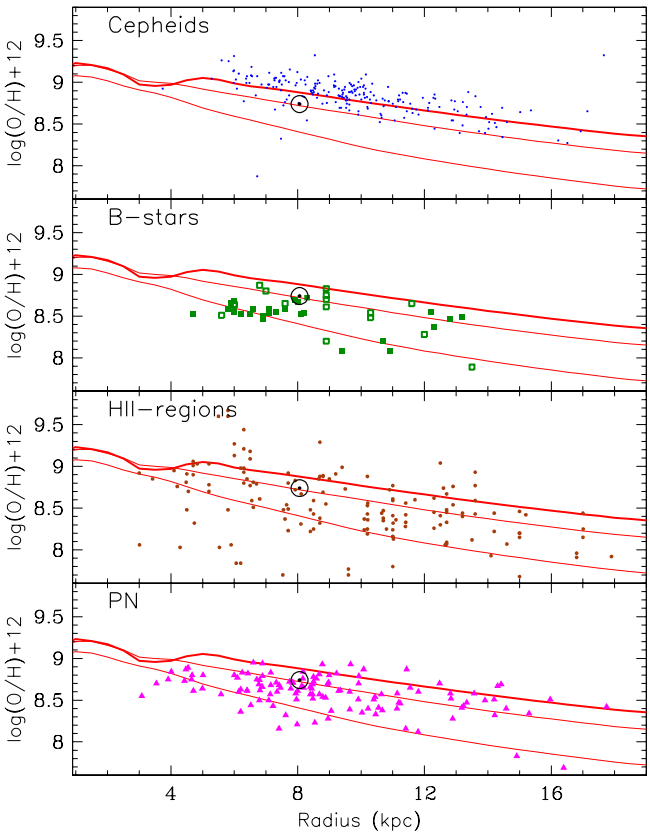

Fig. 4. Oxygen abundance profiles of Cepheids, B-stars, HII regions, and planetary nebulae (PN); data sources are in Table 1. The adopted solar value of log(O/H)+12=8.73 is from Asplund et al. (2009). Model curves (from bottom to top, in all panels) represent the gaseous abundance profile at time 4, 8 and 12 Gyr (*thick curve*), respectively.

Bensby et al. 2014) concerning the local thin and thick disks separately. We showed how such detailed comparisons in the future will provide valuable constraints to both stellar nucleosynthesis and chemical evolution models.

Here we extent the investigation of the abundance evolution to the whole disk for all the elements of our model; we leave the isotopic evolution for a future paper. We use abundance data from various sources and different classes of objects: Cepheids, B-stars, HII regions, planetary nebulae (PN) and open clusters. The first three concern young objects: Cepheids have masses >3 $M_{\odot}$ and, depending on their metallicity, they are younger than 300-400 Myr, while B-stars and HII regions are less than a few 10^7 Myr old; on the other hand, PN and open clusters correspond to objects with ages up to several Gyr. The sources of the adopted data are presented in Table 1.

3.1. Oxygen profiles

Oxygen is a major product of the nucleosynthesis of massive stars (M>10 $M_{\odot}$). Being short-lived (lifetime <20 Myr), such stars have no time to migrate away from their birth sites (less than a 100 pc, as suggested by the fact that all CCSN localised up to now in external galaxies are within spiral arms and/or regions of active star formation). As a result, the radial O profile is not affected by radial migration. It is strongly affected, however, by gas radial inflows, as found in numerous studies, with semi-analytical and N-body+SPH models, e.g. Mayor & Vigroux (1981); Lacey & Fall (1985); Friedli et al. (1994); Portinari & Chiosi (2000); Spitoni & Matteucci (2011); Bilitewski & Schönrich (2012); Cavichia et al. (2014), etc. The results presented here depend directly on the adopted treatment of radial inflow, which corresponds to the action of the galactic bar, as described in Sec. 2. Among the aforementioned studies, only Portinari & Chiosi (2000) and Cavichia et al. (2014) considered explicitly radial flows induced by the Galactic bar.

In Fig. 4 we display the evolution of the gaseous profile of oxygen in our model at three different times (4, 8 and 12 Gyr, respectively). The O profile results from the joint action of three different factors:

- the inside-out formation of the disk, affected by both the adopted infall profile (shorter time-scale in the inner disk, Fig. 1, top right) and the larger efficiency of star formation in the inner disk (because of the larger molecular fraction there, Fig. 1, bottom left).

- the radial inflow, which affects the gaseous profile and all the abundance profiles in the inner galaxy (r <6 kpc).

In the 2-4 kpc region, the combination of the action of the bar (which pushes gas partly towards the center and partly towards the outer disk) to the metal-poor infall leads to a local depression of O/H with respect to adjacent regions. This is due to the fact that the O rich gas pushed inwards and outwards from that region is replenished by the metal poor infall, the rate of which happens to be maximum in that region (Fig. 1). In adjacent regions the effect is smaller, because the late infall rate is less intense there.

The disk beyond radius r ~6 kpc is not affected by radial inflows. The resulting O/H profile is smoothly decreasing outwards, but it cannot be described by a single exponential over the whole radial range: its slope is steeper at small radii and flat-

ter at larger ones. If it is fitted with a single exponential, then the slope depends on the radial range considered. In this work, we shall consider as baseline values those in the range 5-14 kpc, where most of the observational data are available.

There are several shortcomings and uncertainties in the analysis of the observed O abundances of different types of objects across the Galactic disk, which are presented in the recent monograph of Stasińska et al. (2012). The various surveys lead to widely different results for the O/H abundance gradient $dlog(O/H)/dr$ (in dex kpc^{-1}), ranging from small values (-0.023±0.06 in the PN sample of Stanghellini & Haywood (2010) in the 2-17 kpc range) to high ones (-0.056±0.013 in the Cepheid sample of Luck & Lambert (2011) in the 5-16 kpc range).

In Fig. 4 we compare our results to the data of some recent, representative surveys, of the aforementioned tracers. We do not plot all the data on the same figure, since this would create confusion and increase artificially the scatter, because of systematic uncertainties between different analysis techniques (see Stasińska et al. (2012). It can be seen that our results are in overall agreement with the various observations. There are practically no data corresponding to the inner disk (r <4 kpc), where our model predicts lower values than in adjacent reasons, as discussed above. We notice, however, that in their study of PN in the direction of the Galactic bulge, Chiappini et al. (2009) identified a subsample of 44 objects which actually belong to the inner disk population (a few kpc from the Galactic center) and have an average value of log(O/H)+12=8.52±0.23, i.e. less than expected from the extrapolation of the Henry et al. (2010) data for PN in that region. It is not yet clear whether that difference is due to systematic uncertainties between the two studies - Chiappini (2009) collected line intensities from the literature, unlike Henry et al. (2010) - or to a genuine decline of the oxygen profile in the inner disk, in qualitative agreement with our results.

3.2. Iron profiles

While O is exclusively the product of massive stars, Fe has two sources: massive stars and thermonuclear supernovae. From the nucleosynthesis and chemical evolution points of view, Fe is then far more complicated to deal with than O. The reasons are

- The Fe yield of massive stars, exploding as CCSN, are difficult to calculate from first principles, since CCSN explosions are not well understood yet. Observations suggest that Fe yields depend on the energy of the explosion (e.g. Hamuy (2003)) but this parameter is not systematically taken into account in yield calculations.

- Most of solar Fe appears to come not from CCSN but from SNIa (on the basis of the observed decline of O/Fe in disk stars), but is is difficult to relate in a unique way the rate of SNIa to that of CCSN (see, however, Appendix C in KPA2014).

Radial migration introduces one more layer of complexity in the story of Fe. As shown in Kubryk et al. (2013), a fraction of SNIa - mainly those resulting from the oldest stellar populations - may be affected by radial migration as single stars are. The effect is quite important in the disk of the simulation of Kubryk et al. (2013), which displays a long and strong bar, its semi-major axis reaching in the last evolutionary stages between 6 and 8 kpc.

In this work, the effect of radial migration appears to be rather small for SNIa and Fe production (see right panels in Fig. 3). The reason is that star formation proceeds at a quasi-constant rate over most of the disk, creating a large number of SNIa *at late times*; in those conditions, the migration of some old SNIa progenitors from the inner disk, modifies little the situation (and, in any case not beyond a galactocentric radius of r ∼12 kpc). In

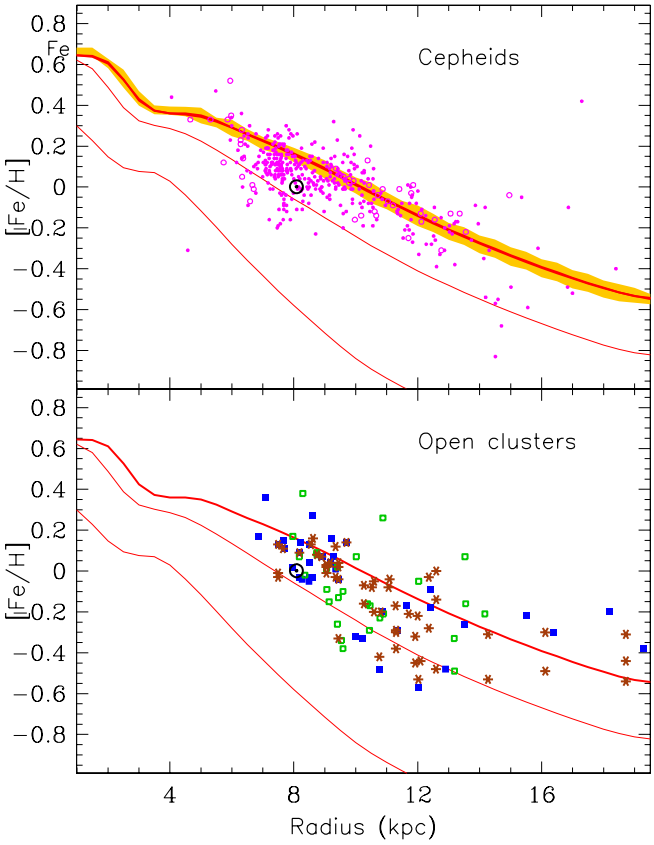

Fig. 5. Iron abundance profiles of Cepheids (top) and open clusters (bottom). Data sources are provided in Table 1. Symbols in the upper panel correspond to Ref. 3 and in the lower panel to Refs. 9 (blue filled squares), 10 (brown asterisks) and 11 (green open squares), respectively. Curves corespond to model results at time 4, 8 and 12 Gyr (thick curve), respectively). The thick red curve in the *top* panel corresponds to the average metallicity of a young stellar population of age 0.2±0.2 Gyr (Cepheids) and the shaded aerea represents the corresponding ±1-σ dispersion.

contrast, in the simulation of Kubryk et al. (2013), there is very little star formation in the whole disk after the first couple of Gyr, due to the lack of accreting gas; as a result, the radial migration of SNIa progenitors from the inner disk during the subsequent 8 Gyr of evolution (under the action of the strong bar), increases considerably the SNIa population and the concomitant Fe production in the outer disk.

Our results for the Fe/H profile are displayed in Fig. 5, at three different times: 4, 8 ad 12 Gyr, respectively. In the latter case, we display in the upper panel the average metallicity of stars aged between 0 and 0.4 Gyr, (i.e. covering the range of Cepheid ages), along with the corresponding range of ±1-σ values. Being young objects, Cepheids have no time to migrate away from their birth places and theirs radial profile after migration (displayed here) is practically the same as the one they have at their birth. The upper panel shows clearly that radial migration introduces very little dispersion in [Fe/H] for such young objects. If the observed dispersion in the sample of Genovali et al. (2014) is real and not due to measurement errorss, then its origin should be due to other factors (e.g. uncertainties in radial distance estimates, azimuthal variation of Fe/H, etc.)

A few other features of the Fe/H profile in Fig. 5 are worth noticing:

- The profile flattens off in the 3-5 kpc region, instead of presenting there a decrease, as the O profile does. The reason is that in this region, at late times there is a population of old progenitors of SNIa (formed early on) which produces some Fe and compensates for the deficiency of CCSN there; this is not the case for O, as we discussed in the previous section. This contribution of old SNIa turns out to be sufficient to smooth the Fe/H profile in that region.

- Outside that region, the Fe/H profile decreases rather steeply, more steeply in any case than the corresponding O profile. The reason is that the ratio of SNIa/CCSN is always higher in the inner disk than in the outer disk (see right bottom panel of Fig. 1), because the former has both an old and a young population of progenitors, while the latter has only a young population. As a result, Fe production is more important proportionally to the one of O in the inner disk, and the resulting Fe profile is steeper.

- In the outer disk, the Fe profile is less steeply decreasing, for the same reasons as the O profile (see previous section), namely the star formation efficiency of the adopted prescription for the SFR. Again, the profile cannot be described by a single exponential.

Comparison to observations is reasonably good, given the dispersion in the data. In the case of the open clusters, dispersion appears to be even larger than in the case of Cepheids; here, however, the (poorly determined) age of the clusters, which covers a range of several Gyr, certainly contributes to this effect. Although our Fe profile flattens in the outer disk, we never obtain a quasi-constant Fe/H abundance beyond $r \sim 15$ kpc, in contrast to the observational findings of Yong et al. (2012) and Heiter et al. (2014) for open clusters.

Compared to other models in the literature, our results are closer to those of Naab & Ostriker (2006), as far as the overall Fe profile is concerned, which is also steeper in the inner disk and progressively flattens outwards. Manifestly, this is due to the similar dependence of the SFR on radius in the two cases, steeper in the inner disk and flatter in the outer disk. In our case, this dependence results from the adopted SFR proportional to the molecular gas (Fig. 1, left panels), while in the case of Naab & Ostriker (2006) it results from the adopted law $SFR \propto \Sigma_{GAS}/\tau_{DYN}$, with the dynamical timescale $\tau_{DYN} \propto r$ for a flat rotation curve: the factor $1/\tau_{DYN}$ varies considerably in the inner disk and much less outside 10 kpc.

3.3. Evolution of abundance profiles

The abundance profiles of gas and stars depend on the interplay between star formation, infall, radial inflow and radial migration of stars. Observations of the final profiles alone can hardly shed light on this complex interplay. The history of the abundance profiles, if observed through some tracer of well determined age, could help in that respect: indeed, some semi-analytical models predict gradients steeper in the past (e.g. Hou et al. (2000)) while others predict that gradients are flatter for older objects (e.g. Chiappini et al. (2001)). As discussed in Pilkington et al. (2012), who surveyed 25 models (both semi-analytical and with N-body+SPH codes), models may also differ widely as to the rate of change of the gradients with time (see Gibson et al. (2013) for an update).

Observations of planetary nebulae of different age classes suggested that O gradients were steeper in the past (Maciel & Costa 2009). However, the systematic uncertainties affecting age and distance estimates of those objects make it difficult to use them as tracers of the past gradient evolution at present. Even worse, radial migration modifies considerably the radial profiles of stellar populations, as found in Roškar et al. (2008), by mixing metal-rich stars from the inner regions in the outer disk. In those conditions, it becomes difficult to use abundance profiles of old objects to infer directly the chemical evolution history of a galactic disk. Still, such observations, combined to other data (e.g. photometry profiles, stellar gradients as a function of distance from the galactic plane, etc.) and to appropriate models - taking properly into account the observational biases - may provide valuable information on the history of the Galaxy.

In Fig. 6 we display the evolution of the Fe profiles of our model for all the stars ever born (right bottom panel) and for stars of different age ranges. We show the average metallicity for stars formed *in situ* (dotted curves)[2] and for all stars found in radius r at the end of the simulation (solid curves); the latter population has been affected by radial migration. It can be seen that for the younger stars (up to 4 Gyr old) the differences between the corresponding profiles is small, for two reasons: i) radial migration does not have time to shuffle stars away from their birth places, and (most importantly) ii) at late times, the abundance profile is flatter than in earlier period, so that even an efficient radial migration cannot produce a large effect, because the abundance differences between different radii are small in any case. Still, radial migration increases steadily the dispersion in metallicity with age at all radii.

For stars older than the Sun, the effect of radial migration on the abundance profiles becomes more and more important, as it makes the profiles appear today flatter than they were at the time of the stellar birth, and flatter than the ones of younger stellar populations (despite the fact that the corresponding gaseous profile was steeper in the past). In particular, the oldest stars (presumably belonging to the thick disk) have a quasi-flat profile in the inner region, extending up to 6 kpc; beyond 9-10 kpc, however, the corresponding metallicity drops rapidly to values characteristic of halo stars.

The impact of radial migration on the past abundance profiles of a galactic disk was first identified by Roškar et al. (2008): in their Fig. 2 they show how the older stars of their simulation (>5 Gyr) have a quasi-flat metallicity profile throughout the disk. Although it is difficult to compare directly our results with other models of similar scope, because of the many different assumptions involved (see KPA2014 for a brief description of the differences between the models of Schönrich & Binney (2009), Minchev et al. (2013) and KPA2014), we attempt here such a comparison to the results of Minchev et al. (2014). In their Fig. 9 (top left), they provide results for the stellar abundances of practically all stars of their model (found in the end of the simulation within a distance of 3 kpc from the galactic plane), as function of galactocentric radius and stellar age. There are differences and similarities with our results, but it is not clear whether the latter are due to similarities in the models or to different boundary conditions. In particular, they also find that the older stars have a flatter abundance profile than the younger ones; however, this is probably due not to radial migration, but to the fact that in their case the abundance profile of gas is also flatter in early time than lately, a characteristic feature of the model of Chiappini et al. (2001). In their case, dispersion in metallicity is more

[2] This is not the same thing as the average gas metallicity during the corresponding time interval: the average stellar metallicity is weighted with the star formation rate during that period, whereas the average gas metallicity is not.

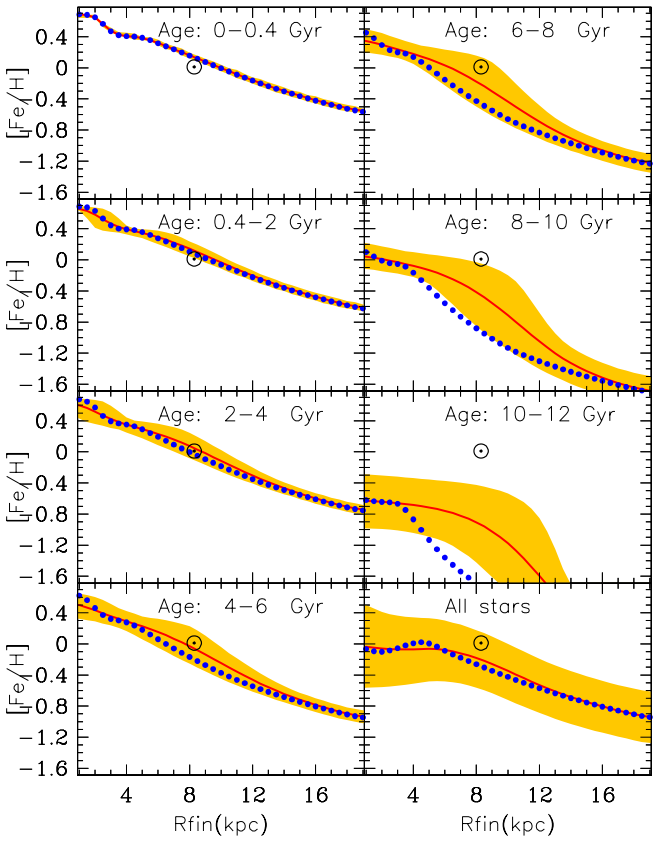

Fig. 6. *Top* Evolution of the Fe profile for stars of different ages, born *in situ* (*dotted* curves) and presently found at radius R_{fin} (*solid*); the *shaded* aerea indicates the $\pm 1\ \sigma$ range of values.

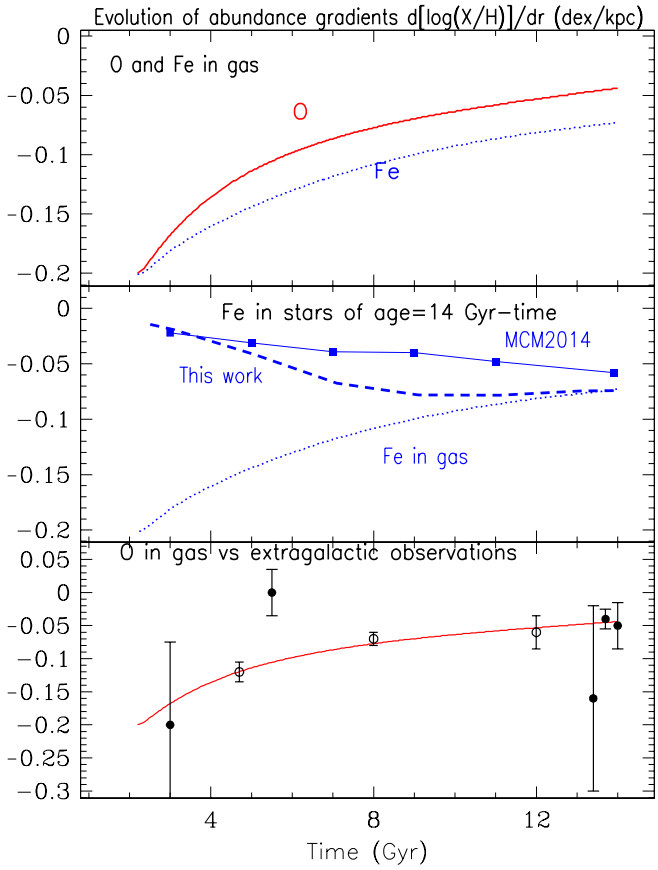

Fig. 7. *Top*: Evolution of the gaseous O and Fe abundance gradients. *Middle*: The evolution of the gaseous Fe gradient (*dotted, same as in top panel*) is compared to the evolution of the stellar Fe gradient, as it appears today after stellar migration (*thick dashed*). The squares, connected by solid segments represent the results of Minchev et al. (2014) (their Table 2) for all stars found within distance Z <3 kpc from the galactic plane. *Bottom*: The evolution of the O abundance gradient in the gas (same as in top panel) is compared to the extragalactic data compiled from Jones et al. (2013); notice that the three *open symbols* correspond to an evaluation of MW data, which is superseded by the recent one of Maciel & Costa (2013), who find no clear indications for an evolution of the abundance gradient. .

important for older stars than for young ones, as in our case and probably for the same reason, i.e. more time for radial migration being available to older objects and/or larger epicyclic motions; however, this dispersion appears to extend further outwards for the younger stellar population, whereas the opposite is obtained in our case. Finally, the older stars in their simulation display a quasi-flat abundance profile all over the disk, whereas our corresponding metallicity profiles plummet beyond 9-10 kpc. This difference is simply due to the fact that we start our simulation with gas of primordial composition, whereas they adopt an initial metallicity of 0.1 $Z_{\odot}$. Such differences may have negligible impact in some cases (i.e. for almost any observable concerning the solar neighborhood), but turn out to be crucial in others.

We show the evolution of the O and Fe abundance gradients in Fig. 7. In the top panel we display the evolution of the gradients in the gaseous phase. As already discussed, gaseous gradients decrease in absolute value with time, i.e. the abundance profiles become flatter with time (at least in the framework of this type of models). Hou et al. (2000) performed the first comparison between the evolution of the O and Fe abundance gradients and found that Fe gradients are steeper than those of O - by ∼0.1 dex - because of the role of SNIa: the ratio of SNIa/CCSN is larger in the inner disk than in the outer one (see Fig. 1). We confirm this result here, but we obtain a larger difference between the two gradients - ∼0.25 dex - because of the more efficient star formation in the inner disk and the role of radial migration: the latter increases by ∼10% the abundance of Fe, but not the one of O, in the region outside 6 kpc (see bottom panels in Fig. 3).

As discussed in the previous paragraphs, radial migration modifies the *presently observed* evolution of stellar profiles. This is illustrated in the middle panel of Fig. 7, where the evolution of the Fe gradient in the gas is compared to the Fe gradient of stellar population as a function of their age. The gradients are the same for the last ∼2 Gyr (see also Fig. 6) but beyond that age the two curves start deviating: the one corresponding to the stellar population becomes flatter with age. For the oldest stars, the gradient is close to zero, i.e. the abundance profile is practically flat. Our results are qualitatively similar to those of Minchev et al. (2014), also displayed in Fig. 7, although the evolution is milder in the their case.

It is difficult to compare directly the "age effect" of radial migration on the abundance profile to observations, because of the uncertainties in stellar age estimates. However, there is an indirect way, through the fact that older stars are, on average

located further away from the plane of the disk than younger ones, because of the increase in the vertical velocity dispersion with stellar age. Thus, analysing a sample of old, main sequence stars belonging to the thin and thick disks from the SEGUE survey, Cheng et al. (2012) find that the Fe gradient in the region 6< r(kpc)<16 increase from -0.065 dex kpc^{-1}at vertical distance from the plane Z=0.2 kpc to a positive value at Z >1 kpc; this is a clear signature of older stellar populations having flatter abundance profiles, as found in Roškar et al. (2008); Minchev et al. (2014) and in this work. However, our model lacks the vertical dimension to the galactic plane and thus we cannot compare directly to the data of Cheng et al. (2012): at every distance from the plane there is a mixture of stellar populations, the contributions of older stars increasing with the distance. Our results presented in Fig. 7 (middle panel) include all stars found today between galactocentric radii of 4 and 11 kpc. Qualitatively, they are in agreement with the observations, since they suggest a gradient close to nul for the oldest stars and close to -0.07 dex/kpc for the youngest ones. A detailed comparison to the observations would require a model including the z dimension (vertical to the plane), including the observational biases, i.e. slices at appropriate distances from the plane, as in Minchev et al. (2014). Alternatively, such a comparison would be possible if a volume limited sample with accurate stellar ages were available.

The bottom panel of Fig. 7 illustrates another way of comparing model results to observations of abundance gradient evolution. The results concern the evolution of the oxygen abundance gradient in the gas (as in top panel). The data are from observations of oxygen in high redshift lensed disk galaxies, from the recent compilation of Jones et al. (2013); they find that the metallicity gradients flatten with time, by a factor of 2.6±0.9, on average, between redshifts 2.2 and 0, although they acknowledge that the discrepancy with the MASSIV data - the highest data point in the bottom panel of Fig. 7 - warrants further investigation. Barring that puzzling discrepancy, we find a rather fair agreement of the high redshift data with our results. It should be stressed, however, that the comparison may not be meaningful after all, because its not clear whether those isolated high redshift systems are progenitors of MW-like disks.

3.4. O/Fe profile

The variation of the O/Fe ratio provides important information on the evolutionary status of a galaxian system: high O/Fe values (typically ~3 times solar) indicate a rather young system, enriched only by the ejecta of CCSN, while ~solar values indicate systems several Gyr old, enriched also by SNIa. The transition from high O/Fe (and, more generally, high α/Fe) to low O/Fe values constitutes one of the key tracers of the chemical evolution of the local Galaxy (the halo to disk transition) and of nearby dwarf galaxies as well.

In the case of the MW disk,the O/Fe ratio is expected to vary, from high values in the "young" outer disk, to lower ones in the older inner disk, in the framework of the inside-out formation scheme. In Fig. 8 (top panel), we plot the O/Fe radial profile for stellar populations of ages 11, 8, 4 and 0 Gyr (from top to bottom), for all the stars found in a given region in the end of the simulation (solid curves) and for stars formed in situ (dotted curves). The decrease (with time) of O/Fe occurs first in the inner galaxy and progressively moves outwards. The youngest objects have [O/Fe]~0.1 in the outer disk and ~-0.25 in the innermost regions, whereas for the oldest objects the ratio varies from 0.5 to 0.4. As in the case of the Fe/H profile, radial migration modifies the O/Fe profiles by bringing evolved stellar populations (of

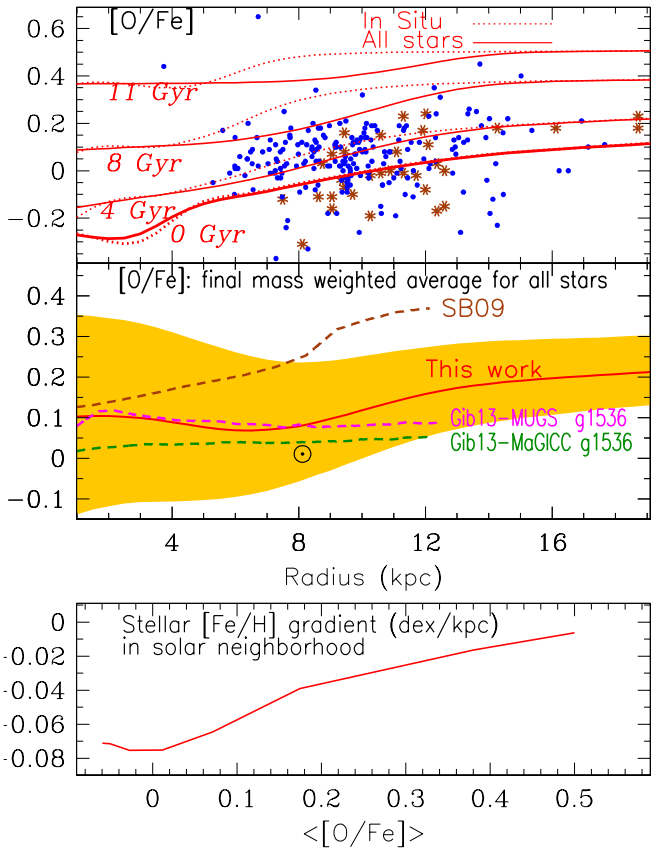

Fig. 8. *Top* Evolution of the O/Fe profile. Data are for Cepheids (*filed circles*, fromLuck & Lambert (2011)) and for open clusters (Yong et al. (2012), *asterisks* and Frinchaboy et al. (2013), *squares*). *Dotted* curves correspond to model stars of average ages 11, 8, 4 and 0.2 Gyr (from top to bottom) formed *in situ* and *solid* curves to stellar populations of the same age found today at radius r. *Middle:* Mass weighted stellar [O/Fe] profile vs radius. The *solid* red curve indicates our results and the *shaded aerea* the corrsponding ±1-σ range. The *dashed* curves are from Fig. 2 of Gibson et al. (2013) and indicate results of Schönrich & Binney (2009) and Gibson et al. (2013), the latter obtained with two different models (see text). *Bottom*: The stellar Fe/H gradient of stars found today in the region 5-11 kpc is plotted vs. the average [O/Fe] ratio of those stars (see text).

lower O/Fe) into outer regions; the effect is more important for the oldest stars and affects the region between 4 and 12 kpc.

Similar results, at least qualitatively, appear in Fig. 9 (bottom left panel) of Minchev et al. (2014), where the [Mg/Fe] profile is plotted for stars of different ages. Mg being an α element, a comparison to the O/Fe profile is meaningful [3]. They obtain a variation of [Mg/Fe] for their youngest stars ranging from ~-0.16 at r=6 kpc to ~0.1 at r=16 kpc, as well as a flat Mg/Fe profile for the oldest stars; both results are in fair agreement with ours.

Fig. 8 (top panel) displays observational data from Cepheids and open clusters of various ages. As with the corresponding Fe/H profile of Fig. 5, the dispersion in the O/Fe ratio at every galactocentric radius is quite large and cannot be explained with our models; radial migration can play only a marginal role in that respect, for so young objects. No clear trend with radius

[3] Notice, however, that halo stars appear to have, in general higher [O/Fe] than [Mg/Fe] ratios at a given metallicity.

appear in the case of Cepheids, while the data for open clusters are marginally consistent with such a trend, as discussed in Yong et al. (2012).

In the middle panel of Fig. 8, we plot the results for the mass weighted average of all stars at the end of our simulation. We obtain a rather flat profile in the inner disk. The average [O/Fe]~0.1 in that region corresponds to stars older than 8 Gyr, as inferred through a comparison to the upper panel, which have been mixed throughout the inner disk by radial migration. In the outer disk, less affected by radial migration, the average [O/Fe] ratio increases slowly but steadily, up to a value of 0.2. The overall 1-σ dispersion is much larger in the inner disk than in the outer one, as indicated by the shaded aerea. We compare our results to the corresponding ones reported in Fig. 2 of Gibson et al. (2013) and reproduced in the middle panel of our Fig. 8. The semi-analytical model of Schönrich & Binney (2009) displays a much steeper slope of [O/Fe] vs. radius, which may result from less radial mixing than in our case or from a much larger gradient of stars formed *in situ*. We think that both reasons contribute to the difference with our results, taking into account that Schönrich & Binney (2009) obtain quite large Fe gradients (dlog(Fe/H)/dr~-0.1 dex kpc^{-1}) and that they consider radial mixing induced only by the transient spiral mechanism of Sellwood & Binney (2002) and not by the more efficient bar-spiral interaction of our model. On the other hand, both models of Gibson et al. (2013) display a very flat profile of [O/Fe] over the whole disk, which is rather difficult to understand, in view of the enhanced SNIa/CCSN ratio in the inner disk expected from inside-out formation schemes (as discussed in Sec. 2), unless if a very efficient radial mixing occurs for the stars over the whole disk. It is clear, however, that for different reasons, not necessarily well analysed yet, different models make different predictions for the profiles of metallicity and of various abundance ratios and only observations will help clarifying the situation.

Finally, the bottom panel of Fig. 8 illustrates another use of the O/Fe ratio to probe the evolution of the Galactic disk. As found in KPA2014, the O/Fe ratio declines monotonically with time and displays very little dispersion from radial mixing at any age. It constitutes thus a natural "chronometer" as argued in Bovy et al. (2012) and it can be used in cases where stellar ages are not known or accurately measured. Toyouchi & Chiba (2014) have analysed 18500 disk stars from the SDSS and HARPS surveys and plotted the Fe/H gradients as a function of the [α/Fe] values of the corresponding stellar populations. They found that, starting with youngest stars (lowest [α/Fe] values), the gradient first decreases, i.e. it becomes more negative and then increases, reaching positive values. However, they found large systematic differences between the samples of the two surveys (concerning the absolute values of the gradients and the turning points in [α/Fe]). We display our results in the bottom panel of Fig. 8, showing a qualitative agreement with the findings of Toyouchi & Chiba (2014): starting with the youngest stars, the Fe/H gradient shows first a small decline, as slightly older stellar populations are probed (with a steeper Fe gradient because too young to be affected by radial migration); then, older populations are probed, more and more affected by radial migration and displaying flatter Fe/H profiles (as also indicated in the middle panel of our Fig. 7). The oldest stars have a nearly flat Fe/H profile, but we never find a positive gradient, as Toyouchi & Chiba (2014) do. We stress again that a meaningful comparison to observations should involve models properly accounting for observational biases.

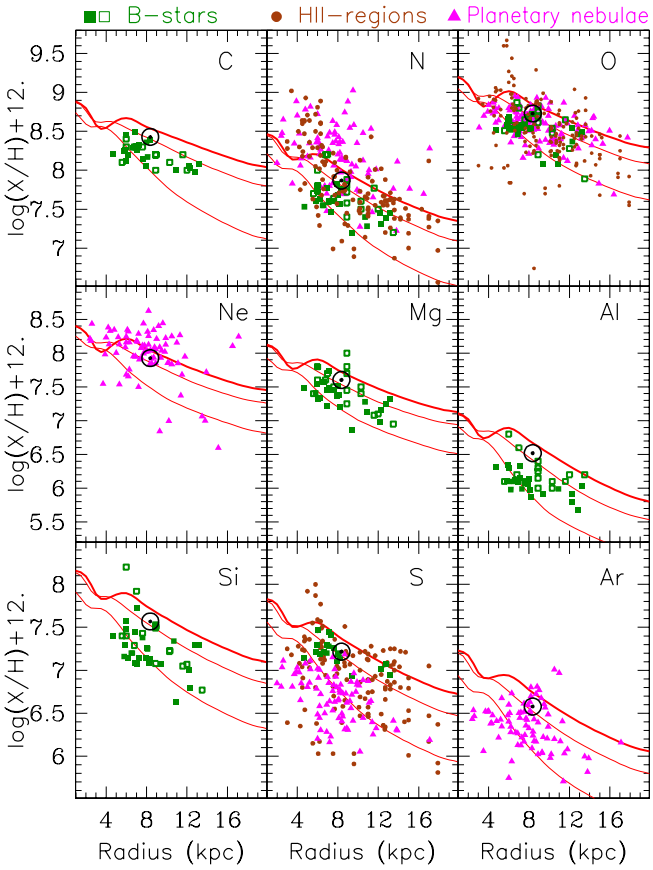

Fig. 9. Abundance profiles from C to Ar and comparison to data from PN (magenta *triangles*), B-stars (green *squares*) and HII-regions (brown *dots*); data sources are provided in Table 1. Model curves correspond to gaseous profiles at time 4, 8 and 12 Gyr (*thick*), respectively.

3.5. Other elements

Oxygen and iron are the most frequently observed elements in the solar neighborhood and the MW disk. Their abundances (as a function of time and/or space) constitute important constraints on the chemical evolution of the Galaxy. The other elements play a marginal role in that respect: their observations mainly serve to support conclusions obtained through the observations of O and Fe or to constrain stellar nucleosynthesis models.

In Fig. 9 we present our results for eight more elements, with abundance profiles derived from observations of B-stars, HII-regions and planetary nebulae. In most cases, available data are for the region 4-12 kpc, with the exceptions of N and S (and, of course, O) where observations of H-II regions and PN extend up to 17 kpc. The inclusion of PN, presumably covering a wide range of ages, increases considerably the dispersion at every radius.

Among the 9 elements of Fig. 9, those heavier than N are almost exclusively products of massive stars; Si and heavier elements receive a small, but non negligible contribution from SNIa, that we take into account through the adopted yields of SNIa from Iwamoto et al. (1999). All those elements are produced as "primaries", i.e. their stellar yields depend little on the initial metallicity of the stars. C and N have a complex nucleosynthetic origin, since they are produced both by massive and and intermediate mass stars. Their yields from massive stars are

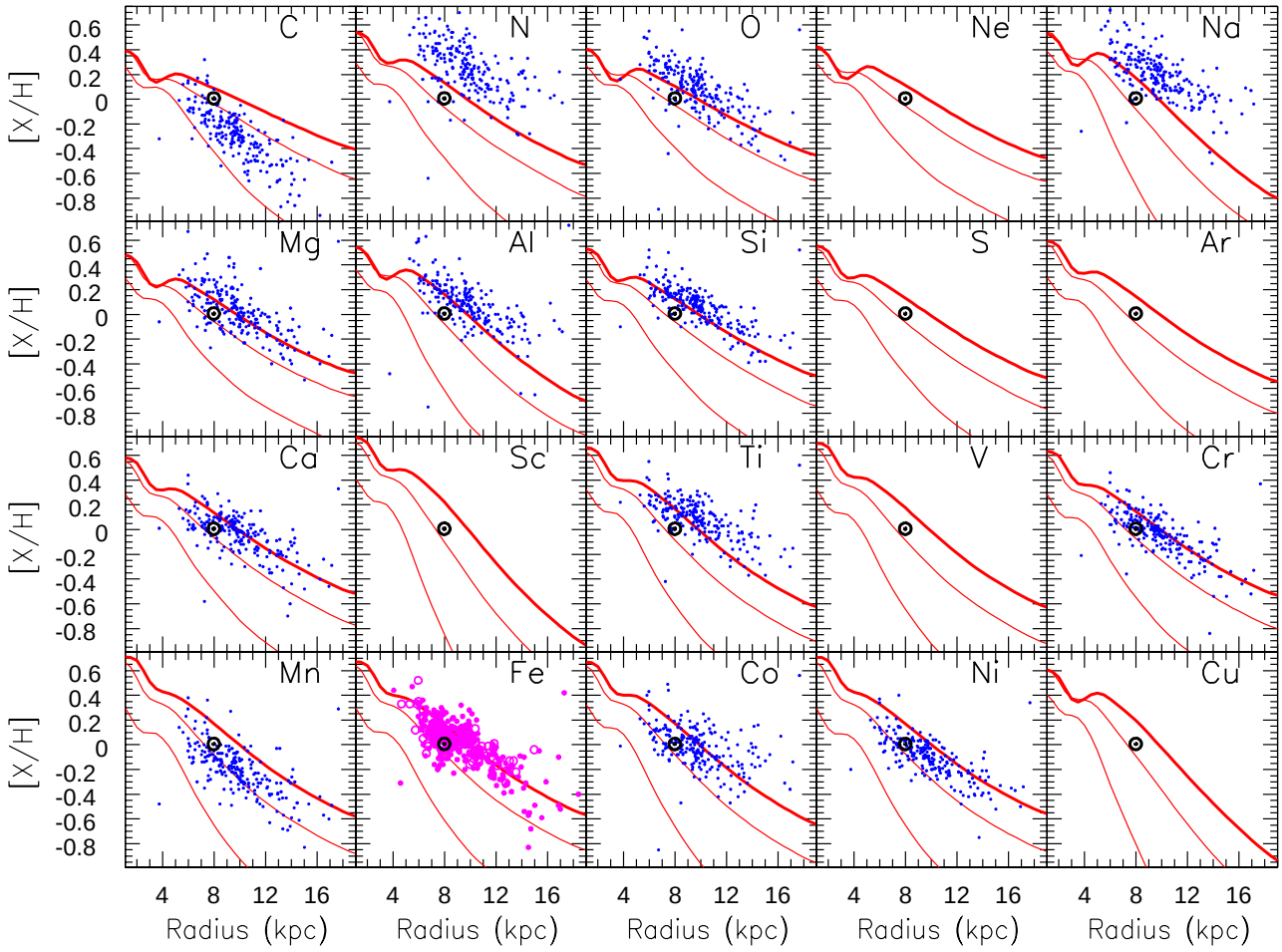

Fig. 10. Abundance profiles from C to Zn and comparison to Cepheid data (from Luck & Lambert (2011), except for Fe data, provided in Genovali et al. (2014)). Model curves correspond to the gaseous profiles after 4, 8 and 12 (*thick curve*) Gyr, respectively.

sensitive to yet poorly understood (and metallicity-dependent) stellar properties, as mass loss and rotation. In lower mass stars, C is produced in the shell He-burning of the AGB phase and ejected in the ISM through the 3d dredge-up, while N may be produced in the bottom of the convective envelope of the AGB star ("Hot-bottom burning") at the expense of C. N is, in principle, a "secondary" element (being synthesized from the initial C and O during the CNO cycle, its yield depends on the initial metallicity); yet, it may be produced essentially as primary in the "hot-bottom burning" of intermediate mass AGB stars and in fast rotating massive stars.

The yields from Nomoto et al. (2013) that we adopted in this work, include yields from low-mass stars from Karakas (2010), but the ones for massive star concern non-rotatings stars. Given the complexity of the nucleosynthesis of C and N, we consider that a dedicated study for the evolution of those two elements would be necessary and we do not attempt it here.

The results displayed in Fig. 9 present similar features to those already discussed for O, namely a flattening of the abundance profiles with time (due to the inside-out formation) and a slightly hollow profile in the bar region at late times (due to the combined action of the bar and of metal-poor infall). Available data, however, display either too large differences (e.g. between B-stars and PN for S) or too large dispersion (in the case of PN data) or they are too scarce (e.g. for C) to allow for any serious constrains, either on the model or on the yields. (Fig. 7, middle panel)

In Fig. 10 we compare our results for all elements between C and Ni to a homogeneous data set for Cepheids (Luck & Lambert 2011), large enough for a statistically meaningful comparison with models. Still, Cepheids are relatively massive (>3 $M_{\odot}$) and evolved stars, having gone through the first dredge-up. This implies that they are expected to exhibit large amounts of N at their surface, formed *in situ* at the expense of C, and perhaps of O; Na is also possibly affected by H-burning in those stars. In consequence, none of those four elements observed in Cepheids can be used as tracer of the chemical evolution of the Galaxy (but they may certainly be used as probes of the internal nucleosynthesis of Cepheids).

Concerning the other elements, one sees that observed abundances are systematically higher than solar in the solar neighborhood (except for Mn and Ni), in rough agreement with theoretical expectations. Our final abundance profiles are globally in agreement with the data, although the obtained slope is, in general, slightly larger than the observationally inferred one, as we discuss below. Finally, the Cepheid data do not extend into the bar region, as to allow us to probe the predictions of the model there.

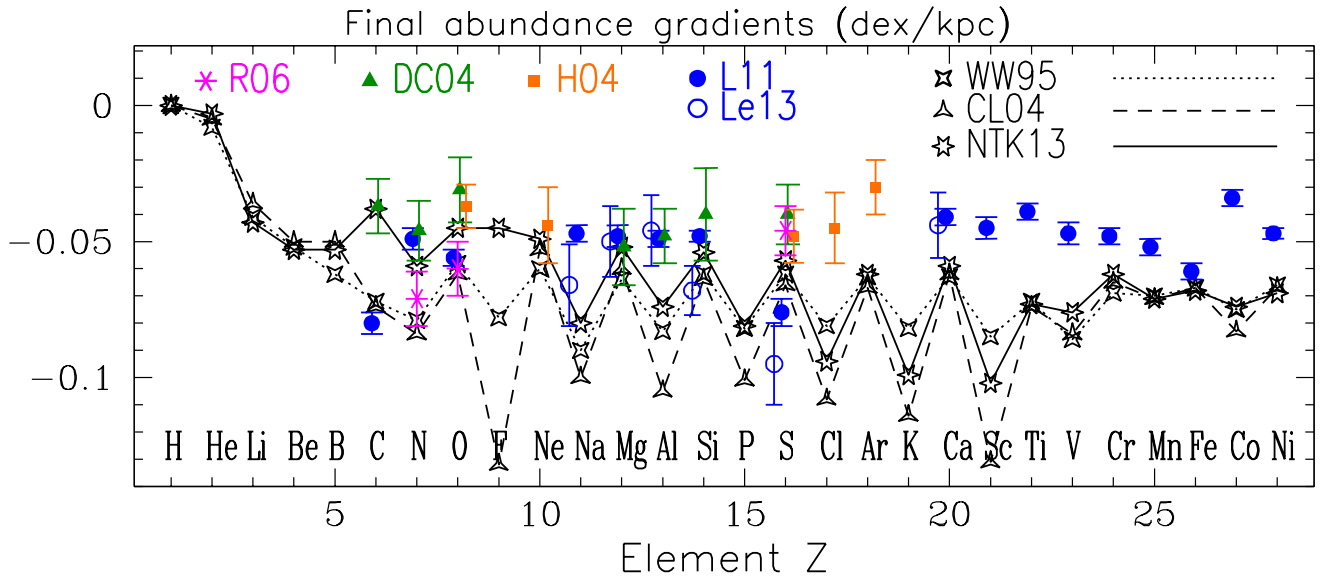

Fig. 11. Present day abundance gradients from H to Ni: models vs. observations. Observations are from H-II regions (Rudolph et al. 2006), B-stars (Daflon & Cunha 2004), Planetary nebulae (Henry et al. 2004) and Cepheids (Luck & Lambert 2011; Luck et al. 2011; Lemasle et al. 2013). Model results are obtained with the model described here and three different sets of yields, from Nomoto et al. (2013) Woosley & Weaver (1995) and Chieffi & Limongi (2004), as indicated by the open symbols and discussed in the text.

In Fig. 11, we present a quantitative comparison of the gradients of all elements between H and Ni to the data set of Cepheids from Luck & Lambert (2011), complemented with a few other data presented here for completeness. We notice, however, that the abundance profiles are not necessarily perfect exponentials to be fit by straight lines of a single slope in logarithmic space. In our case they are not, and the slope depends on the radial range considered: here we take the range 4-17 kpc, to compare directly with the slopes provided by Luck & Lambert (2011) for that same range. The other data sets correspond, however, to different radial ranges, making a direct comparison difficult.

In order to give an idea of the theoretical uncertainties, we provide results for 3 different runs of the same model using 3 different sets of yields. The first one is from Nomoto et al. (2013) (mass range for massive stars: 13-40 $M_{\odot}$) using the low-mass yields of Karakas (2010) (1-6 $M_{\odot}$), as discussed throughout this work. The second set adopts the massive star yields of Woosley & Weaver (1995) (12-40 $M_{\odot}$) and the ones of van den Hoek & Groenewegen (1997) (0.9-8 $M_{\odot}$) for intermediate mass stars. The third one adopts the massive star yields of Chieffi & Limongi (2004) (13-35 $M_{\odot}$) and those of van den Hoek & Groenewegen (1997) for intermediate mas stars. All those yields are metallicity-dependent, but they cover different ranges of masses and metallicities. The limited cover of the mass grid by all the data sets implies the need for interpolation between the low-mass and massive star ranges, and extrapolation between the most massive star of the calculated yields and the most massive star of the adopted IMF, here taken to be 100 $M_{\odot}$; these operations introduces numerical biases in the results. Regarding the metallicities, the yields of Nomoto et al. (2013) are provided for a finer grid and extend to supersolar metallicities, both features being essential for a consistent study of the evolution of the MW disk. The calculations of massive stars involve different ingredients, e.g. no mass loss in Woosley & Weaver (1995) and Chieffi & Limongi (2004) vs mass loss in Nomoto et al. (2013), different prescriptions for some key nuclear reaction rates or the various mixing mechanisms and the description of the final supernova explosion. Similar differences characterise the physics underlying the yields of intermediate mass stars, e.g. the treatment of hot-bottom burning. Those differences, as well as other important ingredients (not considered in those calculation, like e.g. rotation) make any attempt for a systematic comparison between sets of yields rather futile. We provide such a comparison only for illustrative purposes, being fully aware that the overall theoretical uncertainties should be larger than found here. We simply notice that, in all cases we keep the same IMF and the same prescription for the rate and yields of SNIa.

An inspection of Fig. 11 shows that the observed gradients of all elements between C and Ni lie in the narrow range of dlogX/dr ∼-0.04 to -0.06 dex kpc^{-1}, with the exception of C and (curiously) S. Taking into account the larger error bars, the data for other tracers are in good agreement with those of Cepheids.

Theoretical results present some features common to all sets of adopted yields.

i) quasi-identical slopes for the Fe-peak elements, dominated by SNIa;

ii) quasi-identical slopes for all α-elements beyond Ne;

iii) a distinctive difference in the slopes of even vs odd elements, the former been smaller in absolute value than the latter. To our knowledge, it is the first time that the "odd-even" effect of nucleosynthesis, known to affect the behaviour of the abundance ratios in low metallicity stars (e.g. Goswami & Prantzos (2000), is put in evidence in the case of the Galactic abundance gradients.

There are also some noticeable differences between the various sets of yields.

- The yields of Nomoto et al. (2013) produce flatter profiles for C,N and O than those of Woosley & Weaver (1995) or Chieffi

& Limongi (2004); we find that this is due mainly to te ipact of the yields of low-mass stars (from Karakas (2010) in the former case), which have a more pronounced "hot-bottom burning" than the yields of van den Hoek & Groenewegen (1997) adopted in the latter two cases.

- the "odd-even" effect appears to be more pronounced with the yields of Woosley & Weaver (1995) than with those of Nomoto et al. (2013), and even more so with the yields of Chieffi & Limongi (2004).

- F is a particular case, since Woosley & Weaver (1995) and Nomoto et al. (2013) include the effect of ν-induced nucleosynthesis during the final SN explosion, while Chieffi & Limongi (2004) do not.

Comparing model results to observations, one sees a significant offset of the former - by ∼0.2 dex downwards - for all elements beyond Cl *except Fe*. For lighter elements, there is satisfactory agreement (within error bars) for the even elements, but significant discrepancy for the odd ones.

Some conclusions may be drawn from the comparison between model and observations on the one hand, and between different sets of yields on the other. First, if the systematic discrepancy of ∼0.01-0.02 dex between model results and observations is confirmed, some key ingredients of the model should be revised: this could be the case, for instance, of the timescales of the infall rate, which should be lower in the outer disk than adopted here (as to favour a more rapid evolution and larger final abundances in that region); alternatively, a metal-enriched composition of the infalling gas could be adopted, instead of the primordial one adopted here. Second, it is interesting to see whether the abundance gradients present any systematic trends with the atomic number of the element, i.e. either steeper profiles for Fe-peak elements or the "odd-even" effect. If this turns out not to be the case, then the yields of nucleosynthesis should be revised and the role of the IMF scrutinized (because more massive stars produce larger ratios of α/Fe). In any case, the abundance profiles of a large number of elements should be accurately established, on a radial basis as large as possible. Then, the abundance profiles could be used to probe stellar nucleosynthesis, a role played already by abundance ratios in low metallicity halo stars.

4. Summary

In this work we study the abundance profiles of elements between H and Ni in the MW disk, using a semi-analytical model involving radial motions of gas and stars. We adopt parametrised descriptions of those radial motions, which are based on N-body simulations for the case of stars and on a simple analytical prescription for the gas radial velocity profile and are inspired by the presence of a bar in the Milky Way. Other key ingredients of the model is the assumption of a SFR dependent on the molecular gas and the use of a fine grid of recent stellar yields from Nomoto et al. (2013), which include up-dated yields of low-mass stars from Karakas (2010) and cover a large range of initial metallicities. The model reproduces successfully a large number of observations concerning the solar neighborhood and the disk of the MW, as discussed in KPA14; they include the local age-metallicity relation and metallicity distribution, the α/Fe vs Fe/H relation and the surface density profiles of the thin and thick disks, as well as the profiles of stars, SFR, HI and H_2, and the total amounts of gas, stars, SFR, CCSN and SNIa rates in the disk and the bulge of the MW.

In Sec. 2 we present the key model ingredients and we show how the radial motions affect the profiles of stars, gas, SFR, SNIa and Fe. We find that the effect concerns mainly the inner disk, because of the key role played by the Galactic bar in radial migration according to our assumptions; its effect on the disk is found to be negligible beyond 12 kpc, with the adopted prescriptions. The effect on the Fe profile in the inner disk is rather small (of the order of 10% and it is due to the role of SNIa from long-lived progenitors, which have time enough to migrate away from their birth place.

In Sec. 3 we present our results and we compare them to a large number of observational data from various metallicity tracers (H-II regions, B-stars, PN, Cepheids and open clusters). We notice that the data base is not homogeneous and does not cover uniformly the radial extent of the MW disk.

Our abundance profiles cannot be characterised by a unique slope, since they flatten progressively towards the outer disk (as a result of the adopted SFR prescription) and towards the inner disk (as a result of the radial flow induced by the bar). We find that the abundance profiles flatten with time, as a result of the inside-out formation of the disk. But the observational confirmation of this effect in the MW becomes impossible because of the effect of radial migration, which cancels and even inverts it. We confirm (Sec. 3.3) the main effect of radial migration on the abundance profiles found by Roškar et al. (2008), namely the flattening of the past abundance profiles of stars, which becomes more pronounced for the older stellar populations. We compare quantitatively our results (Fig. 7, middle panel) to those of Minchev et al. (2014), who find similar, albeit somewhat flatter, abundance profiles.

The evolution of our gaseous abundance profiles is in fair agreement with the extragalactic, high redshift, data compiled by Jones et al. (2013), which are too uncertain at present, however, to draw firm conclusions (Fig. 7, bottom panel). In Sec. 3.4 we present the evolution of our [O/Fe] profiles. The evolution of both [Fe/H] and [O/Fe] profiles, modified by radial migration, is encoded in the stellar populations currently present in the local disk and is revealed by preliminary observations of those quantities in stars at different distances from the plane of the disk. Our 1D model lacks the dimension vertical to the plane that would allow us to perform a meaningful comparison to such observations, but the results discussed in Sec. 3.4 are in qualitative agreement with the data (the profiles are expected to flatten with distance from the plane).

In Sec. 3.5 we present our results for all elements between C and Ni. From the theory point of view, we stress the systematic differences in the final abundance profiles due to the different sets of stellar yields (the physics of both low and high mass stars still suffering by several uncertainties). We find a rather good agreement with observationally derived slopes of abundance profiles (assuming they can be described by a single exponential) but also some systematic differences (see Fig. 11: in particular, we obtain slopes systematically 0.01-0.02 dex larger (in absolute value) than the observed ones. We argue that this difference, if definitively established, could be cured by some revision of basic ingredients of the model, namely the need for smaller infall timescales in the outer disk or a non-primordial composition for the infalling gas. We also find an interesting "odd-even" effect of larger slopes for odd elements. This metallicity-dependent effect, already discussed in the context of abundance ratios X/Fe in halo stars, is found here for the first time and it is generic, i.e. it concerns all sets of stellar yields. However, it does not appear in the observational data; if observations are confirmed, then some of the stellar nucleosynthesis results should be revised.

Acknowledgments: EA acknowledges financial support to the DAGAL network from the People Programme (Marie Curie Ac-

tions) of the European Union's Seventh Framework Programme FP7/2007-2013/ under REA grant agreement number PITN-GA-2011-289313 and from the CNES (Centre National d'Etudes Spatiales - France). We also acknowledge partial support from the PNCG (Programme National Cosmologie et Galaxies - France).

References

Adibekyan, V. Z., Santos, N. C., Sousa, S. G., & Israelian, G. 2011, A&A, 535, L11
Asplund, M., Grevesse, N., Sauval, A. J., & Scott, P. 2009, ARA&A, 47, 481
Athanassoula, E. 1992, MNRAS, 259, 345
Bensby, T., Feltzing, S., & Oey, M. S. 2014, A&A, 562, A71
Bilitewski, T. & Schönrich, R. 2012, MNRAS, 426, 2266
Blitz, L. & Rosolowsky, E. 2006, ApJ, 650, 933
Blitz, L. & Spergel, D. N. 1991, ApJ, 379, 631
Boissier, S. & Prantzos, N. 1999, MNRAS, 307, 857
Boissier, S. & Prantzos, N. 2009, A&A, 503, 137
Bovy, J. & Rix, H.-W. 2013, ApJ, 779, 115
Bovy, J., Rix, H.-W., Liu, C., et al. 2012, ApJ, 753, 148
Brunetti, M., Chiappini, C., & Pfenniger, D. 2011, A&A, 534, A75
Cavichia, O., Mollá, M., Costa, R. D. D., & Maciel, W. J. 2014, MNRAS, 437, 3688
Chamcham, K. & Tayler, R. J. 1994, MNRAS, 266, 282
Cheng, J. Y., Rockosi, C. M., Morrison, H. L., et al. 2012, ApJ, 746, 149
Chiappini, C. 2009, in IAU Symposium, Vol. 254, IAU Symposium, ed. J. Andersen, Nordströara, B. m, & J. Bland-Hawthorn, 191–196
Chiappini, C., Górny, S. K., Stasińska, G., & Barbuy, B. 2009, A&A, 494, 591
Chiappini, C., Matteucci, F., & Gratton, R. 1997, ApJ, 477, 765
Chiappini, C., Matteucci, F., & Romano, D. 2001, ApJ, 554, 1044
Chieffi, A. & Limongi, M. 2004, ApJ, 608, 405
Clarke, C. J. 1989, MNRAS, 238, 283
Daflon, S. & Cunha, K. 2004, ApJ, 617, 1115
Dutil, Y. & Roy, J.-R. 1999, ApJ, 516, 62
Edmunds, M. G. & Greenhow, R. M. 1995, MNRAS, 272, 241
Ferrini, F., Molla, M., Pardi, M. C., & Diaz, A. I. 1994, ApJ, 427, 745
Friedli, D. & Benz, W. 1993, A&A, 268, 65
Friedli, D., Benz, W., & Kennicutt, R. 1994, ApJ, 430, L105
Frinchaboy, P. M., Thompson, B., Jackson, K. M., et al. 2013, ApJ, 777, L1
Genovali, K., Lemasle, B., Bono, G., et al. 2014, A&A, 566, A37
Gibson, B. K., Pilkington, K., Brook, C. B., Stinson, G. S., & Bailin, J. 2013, A&A, 554, A47
Goetz, M. & Koeppen, J. 1992, A&A, 262, 455
Goswami, A. & Prantzos, N. 2000, A&A, 359, 191
Greggio, L. 2005, A&A, 441, 1055
Guesten, R. & Mezger, P. G. 1982, Vistas in Astronomy, 26, 159
Gummersbach, C. A., Kaufer, A., Schaefer, D. R., Szeifert, T., & Wolf, B. 1998, A&A, 338, 881
Hamuy, M. 2003, ArXiv Astrophysics e-prints
Heiter, U., Soubiran, C., Netopil, M., & Paunzen, E. 2014, A&A, 561, A93
Henry, R. B. C., Kwitter, K. B., & Balick, B. 2004, AJ, 127, 2284
Henry, R. B. C., Kwitter, K. B., Jaskot, A. E., et al. 2010, ApJ, 724, 748
Hou, J. L., Prantzos, N., & Boissier, S. 2000, A&A, 362, 921
Iwamoto, K., Brachwitz, F., Nomoto, K., et al. 1999, ApJS, 125, 439
Jones, T., Ellis, R. S., Richard, J., & Jullo, E. 2013, ApJ, 765, 48
Karakas, A. I. 2010, MNRAS, 403, 1413
Kroupa, P. 2002, Science, 295, 82
Kubryk, M., Prantzos, N., & Athanassoula, E. 2013, MNRAS, 436, 1479
Kubryk, M., Prantzos, N., & Athanassoula, L. 2014, ArXiv e-prints
Lacey, C. G. & Fall, S. M. 1985, ApJ, 290, 154
Lemasle, B., François, P., Genovali, K., et al. 2013, A&A, 558, A31
Loebman, S. R., Roškar, R., Debattista, V. P., et al. 2011, ApJ, 737, 8
Luck, R. E., Andrievsky, S. M., Kovtyukh, V. V., Gieren, W., & Graczyk, D. 2011, AJ, 142, 51
Luck, R. E. & Lambert, D. L. 2011, AJ, 142, 136
Maciel, W. J. & Costa, R. D. D. 2009, in IAU Symposium, Vol. 254, IAU Symposium, ed. J. Andersen, Nordströara, B. m, & J. Bland-Hawthorn, 38P
Maciel, W. J. & Costa, R. D. D. 2013, Rev. Mexicana Astron. Astrofis., 49, 333
Magrini, L., Sestito, P., Randich, S., & Galli, D. 2009, A&A, 494, 95
Maoz, D., Mannucci, F., & Brandt, T. D. 2012, MNRAS, 426, 3282
Martel, H., Kawata, D., & Ellison, S. L. 2013, MNRAS, 431, 2560
Martin, P. & Roy, J.-R. 1994, ApJ, 424, 599
Matteucci, F., Franco, J., Francois, P., & Treyer, M.-A. 1989, Rev. Mexicana Astron. Astrofis., 18, 145
Mayor, M. & Vigroux, L. 1981, A&A, 98, 1
Minchev, I., Chiappini, C., & Martig, M. 2013, A&A, 558, A9
Minchev, I., Chiappini, C., & Martig, M. 2014, ArXiv e-prints
Minchev, I. & Famaey, B. 2010, The Astrophysical Journal, 722, 112
Minchev, I., Famaey, B., Quillen, A. C., et al. 2012, A&A, 548, A127
Mott, A., Spitoni, E., & Matteucci, F. 2013, MNRAS, 435, 2918
Naab, T. & Ostriker, J. P. 2006, MNRAS, 366, 899
Nomoto, K., Kobayashi, C., & Tominaga, N. 2013, ARA&A, 51, 457
Pilkington, K., Few, C. G., Gibson, B. K., et al. 2012, A&A, 540, A56
Portinari, L. & Chiosi, C. 2000, A&A, 355, 929
Prantzos, N. & Aubert, O. 1995, A&A, 302, 69
Prantzos, N. & Boissier, S. 2000, MNRAS, 313, 338
Roškar, R., Debattista, V. P., Quinn, T. R., Stinson, G. S., & Wadsley, J. 2008, ApJ, 684, L79
Rudolph, A. L., Fich, M., Bell, G. R., et al. 2006, ApJS, 162, 346
Sánchez, S. F., Rosales-Ortega, F. F., Marino, R. A., et al. 2012, A&A, 546, A2
Schönrich, R. & Binney, J. 2009, MNRAS, 396, 203
Sellwood, J. & Binney, J. 2002, MNRAS, 336, 785
Shlosman, I. & Noguchi, M. 1993, ApJ, 414, 474
Sommer-Larsen, J. & Yoshii, Y. 1990, MNRAS, 243, 468
Spitoni, E. & Matteucci, F. 2011, A&A, 531, A72
Stanghellini, L. & Haywood, M. 2010, ApJ, 714, 1096
Stasińska, G., Prantzos, N., Meynet, G., et al., eds. 2012, EAS Publications Series, Vol. 54, Oxygen in the Universe
Sygnet, J. F., Tagger, M., Athanassoula, E., & Pellat, R. 1988, MNRAS, 232, 733
Tinsley, B. M. & Larson, R. B. 1978, ApJ, 221, 554
Tosi, M. 1988, A&A, 197, 33
Toyouchi, D. & Chiba, M. 2014, ApJ, 788, 89
van den Hoek, L. B. & Groenewegen, M. A. T. 1997, A&AS, 123, 305
Woosley, S. E. & Weaver, T. A. 1995, ApJS, 101, 181
Yong, D., Carney, B. W., & Friel, E. D. 2012, AJ, 144, 95
Zaritsky, D., Kennicutt, Jr., R. C., & Huchra, J. P. 1994, ApJ, 420, 87

4 Conclusions et perspectives

4.1 Synthèse des résultats obtenus

La migration radiale des étoiles dans les disques galactiques, est un sujet de recherche récent mais qui a pris de plus en plus d'importance au cours de ces dix dernières années, en particulier depuis le travail de Sellwood & Binney (2002), qui ont révélé que la migration pourrait jouer un rôle majeur dans l'évolution des galaxies. En effet, l'étude théorique de ce phénomène physique (à l'aide de simulations N-corps+SPH ou semi-analytiques) montre qu'il est susceptible de modifier le paradigme de l'évolution galactique, et de brouiller les marqueurs observationnels classiquement utilisés pour reconstruire l'histoire galactique. Il a été montré que la migration radiale affecte en particulier les observations locales ou globales de la composition chimique des étoiles du disque (profils d'abondances, relation âge-métallicité, distributions en métallicité), les observations cinématiques (la dispersion de vitesse des étoiles pourrait être modifiée lorsqu'elles migrent radialement), la composition chimique du milieu interstellaire (par la migration des progéniteurs de SNIa et des étoiles de masses intermédiaires), et même la morphologie du disque (disque épais, profils photométriques des disques). L'impact de la migration est donc potentiellement considérable, et nécessite des études théoriques minutieuses des différents effets qu'elle produit, afin de mettre en évidence les indices observationnels qui pourraient être utilisés pour quantifier son amplitude et pour pouvoir reconstruire l'histoire des disques.

Dans ce contexte, les observations de la Voie Lactée sont d'une grande importance, car il est possible de résoudre les étoiles individuellement, et d'estimer leurs âges, leurs distances, leurs vitesses, ainsi que leur composition chimique. La Voie Lactée sert donc de laboratoire pour tester les modèles d'évolution galactique, en comparant les résultats aux nombreuses observations disponibles.

Dans ce travail, nous avons étudié la migration radiale des étoiles dans les disques galactiques, et analysé ses effets sur l'évolution de la Voie Lactée. Ce travail s'inscrit dans la lignée de différentes études sur la migration, portant à la fois sur la dynamique de la migration et sur son impact sur l'évolution chimique galactique. Pour mener à bien cette étude, nous

avons utilisé deux types d'outils : d'une part une simulation N-corps+SPH afin d'étudier les mouvements des étoiles dans un modèle galactique réaliste, et d'autre part des simulations semi-analytiques d'évolution des disques, que nous avons utilisées pour construire un modèle détaillé de l'évolution de notre Galaxie.

L'étude de simulation N-corps+SPH nous a permis de mettre en évidence un nouveau mécanisme de migration radiale dans les galaxies ayant une barre centrale en évolution séculaire. Nous avons montré que ce mécanisme concerne peut d'étoiles, mais que dans certaines conditions, il peut entraîner les étoiles vers l'extérieur sur de très longues distances, et affecter ainsi les observations des régions externes des disques. Toutefois, ce nouveau mécanisme ne devrait avoir que très peu d'influence sur l'évolution de la Voie Lactée. Aussi, grace à l'analyse de cette simulation, nous avons pu dériver des coefficients de diffusion stellaire dépendant du rayon galactocentrique et du temps, permettant de construire un modèle de migration radiale paramétré par ces coefficients.

Nous avons introduit cette description parametrisée des déplacements radiaux des étoiles dans un code semi-analytique d'évolution chimique galactique, et ainsi simuler l'impact de la migration radiale sur l'évolution des disques. Nous avons montré que notre méthode de "post-processing" des simulations N-corps+SPH par des simulations semi-analytique permet d'étudier avec précision et avec plus de détails l'évolution chimique des galaxies simulées en N-corps+SPH, qui ont généralement une chimie assez rudimentaire. Nous pouvons ainsi étudier un plus grand nombre d'éléments/isotopes, les effets d'une variation de l'IMF ou du taux des SNIa, etc. ; cette étude détaillée est impossible en pratique avec un code N-body. Nous avons montré en particulier que l'Approximation du Recyclage Instantané utilisée dans les simulations N-corps ne permet pas une modélisation précise de l'évolution chimique, car elle ne permet pas aux sources de nucléosynthèse de longue durées de vie (e.g. SNIa ou étoiles de masse intermédiaire) de migrer dans le disque. Grâce à notre modèle semi-analytique augmenté de la migration radiale, nous avons réalisé la première étude de l'impact de la migration des sources de nucléosynthèse, et montré que le déplacement de ces sources peut avoir un impact significatif sur l'évolution du gaz interstellaire, en affectant la production du Fe par les SNIa ou des éléments s- par les étoiles de masse intermédiaire.

Sur la base de ces travaux, nous avons ensuite construit un modèle semi-analytique de l'évolution de la Voie Lactée, incluant les effets de la migration radiale (en ajustant les coefficients de diffusion mentionnés plus haut). Dans ce modèle, nous avons inclu de nouveaux ingrédients, qui le différencie des modèles proposés jusqu'alors : un taux de formation stellaire dépendant du gaz moléculaire, des rendements stellaires ("yields") récents, bien adaptés au cas de la Voie Lactée, une migration radiale séparée en deux composantes (un "blurring" analytique tiré de l'approximation épicyclique, et un "churning" modélisé avec des coefficients de diffusion inspirés par l'analyse d'une simulation N-corps). Notre modèle est validé par la comparaison des résultats à des nombreuses données observationnelles de la VL, concernant aussi bien les paramètres globaux (masse du gaz et des étoiles, taux de formation stellaire, taux des supernovae, etc.) et leurs profils radiaux que le voisinage solaire. En passant, nous trouvons que

l'évolution de la VL est tout à fait "typique", comparée à l'évolution "moyenne" des galaxies disques analogues, observées à redshift élevé.

Par la suite, nous analysons les effets de la migration radiale sur l'évolution de la Voie Lactée. Nous montrons que les mouvements épicycliques ne sont pas suffisants pour expliquer la dispersion observée dans la relation âge-métallicité du voisinage solaire, et que d'autres mécanismes sont nécessaires (du moins, dans le cadre de notre modèle). Nous montrons que les effets de la migration peuvent être observés dans cette relation et nous suggérons que les futures études observationnelles devraient porter une attention particulière à ce marqueur.

Nous retrouvons certains résultats déjà obtenus par d'autres équipes : la distribution en métallicité des étoiles du voisinage solaire ne peut pas être reproduite sans migration radiale (les étoiles les plus metalliques du voisinage solaire ne peuvent être formées locallement mais dans les zones internes), le voisinage solaire est constitué d'un mélange d'étoiles d'âges variés, chaque tranche d'âge ayant des distributions en métallicité aseez larges, et par conséquent il n'y a pas de relation unique entre âge et métallicité des étoiles locales (conformément aux observations).

Nous montrons qu'un critère simple sur l'âge des étoiles pour distinguer le disque mince du disque épais (le dernier correspondant à des étoiles plus âgées que 9 Gyr) permet de reproduire de façon satisfaisante la morphologie des deux disques (densité stellaire locale, échelle de longueur), ainsi que la double branche caractéristique observée dans le plan [α/Fe] vs [Fe/H] au voisinage solaire. Dans le cadre de ce modèle, la migration radiale joue un rôle important dans la formation du disque épais en dispersant dans une large partie du disque les étoiles vieilles et peu métalliques des régions centrales, qui sont formées en premier. Nos résultats vont donc dans le sens d'une formation du disque épais par des processus d'évolution séculaire du disque, selon l'idée avancée par Schönrich & Binney (2009). Toutefois, comme nous n'avons ni la dimension verticale, ni la cinématique stellaire dans notre modèle, nous ne pouvons pas analyser les autres propriétés caractéristiques du disque épais et établir une conclusion plus solide.

Enfin, nous analysons les profils radiaux d'abondances dans le disque de la VL avec notre modèle, et nous comparons avec un grand nombre d'observations concernant divers éléments chimiques. Nous retrouvons le fait que la migration radiale peut aplatir ces profils avec le temps (initialement démontré par Roškar et al. (2008a)), les effets les plus marqués étant obtenus pour les populations d'étoiles les plus vieilles, qui ont plus de temps pour se déplacer et donc pour se mélanger dans le disque. En raison de cet effet de la migration radiale, il s'avère impossible d'observer directement les profils passés d'abondances chimiques dans les populations stellaires ; seule une étude combinant modèles et observations (en fonction de la distance au plan galactique, les populations les plus vieilles étant situés plus loin que les populations plus jeunes, en moyenne) permettrait de déduite l'histoire passée de la Voie Lactée.

Avec notre modèle, nous avons pu étudier l'impact des grilles théoriques de rendements

stellaires : nous montrons que les gradients d'abondances chimiques observés sont assez bien reproduits quels que soient les modèles de rendements stellaires utilisés, mais nous notons un écart systématique de 0.01-0.02 dex/kpc entre les modèles et les observations pour les éléments plus lourds que le Ne. Cela pourrait impliquer la nécessité d'une modification des certains ingrédients de notre modèle de la Voie Lactée. Nous obtenons également un effet générique (valable pour toutes les grilles des rendements stellaires étudiés), lié à la parité du numéro atomique des éléments chimiques, qui n'est pas présent dans les observations. Ce dernier résultat est important car, s'il est confirmé, il impliquerait que certains aspects des modèles de rendements stellaires devraient être revus.

4.2 Perspectives

Les travaux réalisés lors de cette thèse ont plusieurs suites possibles.

En premier lieu, il serait intéressant de continuer à améliorer notre modèle semi-analytique en ajoutant notamment la dimension verticale du disque. Cette étape nécessiterait une étude préalable de l'impact de la migration radiale sur la dispersion des vitesses radiales et verticales à l'aide de simulations N-corps (en continuité de l'étude menée par Minchev et al. (2012)), afin d'élaborer un modèle quantitatif liant le déplacement radial aux dispersions de vitesses, qui puisse être inclus dans le code semi-analytique. Et également d'inclure la cinématique des étoiles, peut être en se basant sur l'approximation épicyclique, ce qui pourrait peut être résoudre également le problème du couplage entre migration et dispersions de vitesses (à condition de savoir quelle quantité se conserve lors de la migration (Minchev et al., 2012)). Cette amélioration du code, pourrait en particulier permettre une étude plus approfondie du lien (éventuel) entre le disque épais et la migration radiale,

Toujours dans la continuité de ces travaux sur l'évolution chimique, nous avons entrepris d'introduire dans le code de simulation N-corps+SPH (Gadget3) une description plus réaliste de l'évolution chimique (pas d'approximation de recyclage instantané, inclusion d'une douzaine d'isotopes, des SNIa avec un taux déduit des observations). Cette amélioration du code est importante car elle permettra d'étudier l'interaction entre migration radiale et évolution chimique de façon plus précise qu'avec les méthodes de "post-processing" par les simulations semi-analytiques. Cependant, ces dernières resteront indispensables pendant longtemps encore, pour une étude détaillée des différents paramètres (impact des grilles des rendements stellaires, de l'IMF, du taux des SNIa etc.)

Concernant l'impact de la migration sur l'évolution des galaxies, une future étude pourrait concerner les propriétés des disques extragalactiques. En effet, les phénomènes à l'origine des différents traits morphologiques peuvent résulter autant de processus internes (présence de sous-structures induisant de la migration radiale, interactions avec le halo de matière noire, taux de formation stellaire, écoulements du gaz) que de processus faisant intervenir l'environnement externe des galaxies (accrétion de gaz extragalactique, interaction gravitationnelle avec des galaxies satellites, fusion de galaxies). Une telle étude pourrait porter sur les

principaux traits morphologiques des disques : échelle de longueur des disques exponentiels, brisure des profils de densité surfaciques, profils de couleurs en "U", et disques épais. Les questions auxquelles il serait possible de répondre sont les suivantes : quelle est l'origine de ces traits caractéristiques ? Comment sont-ils liés à la présence de sous-structures dans les disques ? Quel est le rôle de la migration radiale des étoiles dans leur formation ? Et si possible, quel est le rôle joué par l'environnement extragalactique ? Il pourrait notamment être possible d'étudier l'impact du nouveau mécanisme de migration que nous avons mis en évidence, sur l'évolution des régions externes.

Enfin, concernant l'histoire de la Voie Lactée, nous avons vu que la migration radiale empêche l'interprétation directe des observations, et qu'il est nécessaire de construire des modèles combinant les différents processus à l'œuvre lors de son évolution, et de comparer les résultats aux données observationnelles afin de reconstruire l'histoire de la Galaxie. Dans ce cadre, il est a noté que seulement une petite partie de la Voie Lactée a été observée de façon systématique, par les relevés RAVE, SEGUE et APOGEE. Cette région s'étend jusqu'à des distances de 2-3 kpc autour du Soleil. Par conséquent, les futures données astrométriques de Gaia (couvrant des distances atteignant ~10 kpc autour du Soleil, avec des erreurs de ~10% seulement), complémentées par les données spectroscopiques de 4MOST, permettront de contraindre les modèles sur un plus grand volume de la Voie Lactée. De plus, ces données permettront des études précises en fonction de l'âge des étoiles, de leur position (et notamment leur éloignement au plan Galactique), de leur cinématiques, et de leur composition chimique. Les futurs grands relevés fourniront donc des contraintes plus fortes sur les modèles d'évolution, et ainsi, permettront de reconstruire plus finement l'histoire de notre Galaxie.

Table des figures

Table des figures

Bibliographie

Adelman-McCarthy J. K. et al., 2007, ApJS, 172, 634

Adibekyan V. Z., Santos N. C., Sousa S. G., Israelian G., 2011, A&A, 535, L11

Aguerri J. A. L., Méndez-Abreu J., Corsini E. M., 2009, A&A, 495, 491

Alimi J.-M. et al., 2012, ArXiv e-prints

Asplund M., Grevesse N., Sauval A. J., Scott P., 2009, ARA&A, 47, 481

Athanassoula E., 1992, MNRAS, 259, 345

Athanassoula E., 2002, ApJLett, 569, L83

Athanassoula E., 2003, MNRAS, 341, 1179

Athanassoula E., Bienayme O., Martinet L., Pfenniger D., 1983, A&A, 127, 349

Athanassoula E., Misiriotis A., 2002, MNRAS, 330, 35

Baba J., Saitoh T. R., Wada K., 2013, ApJ, 763, 46

Babusiaux C., Gilmore G., 2005, MNRAS, 358, 1309

Bakos J., Trujillo I., Azzollini R., Beckman J. E., Pohlen M., 2011, Memorie della Societa Astronomica Italiana Supplementi, 18, 113

Bekki K., Tsujimoto T., 2011, ApJ, 738, 4

Bensby T., Feltzing S., Oey M. S., 2014, A&A, 562, A71

Bertin G., Lin C. C., Lowe S. A., Thurstans R. P., 1989a, ApJ, 338, 78

Bertin G., Lin C. C., Lowe S. A., Thurstans R. P., 1989b, ApJ, 338, 104

Binney J., Tremaine S., 1987, Galactic dynamics

Bird J. C., Kazantzidis S., Weinberg D. H., 2012, MNRAS, 420, 913

Bird J. C., Kazantzidis S., Weinberg D. H., Guedes J., Callegari S., Mayer L., Madau P., 2013, ApJ, 773, 43

Blitz L., Rosolowsky E., 2006, ApJ, 650, 933

Blitz L., Spergel D. N., 1991, ApJ, 379, 631

Bobylev V. V., Mosenkov A. V., Bajkova A. T., Gontcharov G. A., 2014, Astronomy Letters, 40, 86

Boissier S., Prantzos N., 1999, MNRAS, 307, 857

Booth C. M., Schaye J., 2009, MNRAS, 398, 53

Bournaud F., Elmegreen B. G., Martig M., 2009, ApJLett, 707, L1

Bovy J., Rix H.-W., Liu C., Hogg D. W., Beers T. C., Lee Y. S., 2012, ApJ, 753, 148

Brook C. B. et al., 2012, MNRAS, 426, 690

Brunetti M., Chiappini C., Pfenniger D., 2011, A&A, 534, A75

Casagrande L., Schönrich R., Asplund M., Cassisi S., Ramírez I., Meléndez J., Bensby T., Feltzing S., 2011, A&A, 530, A138

Chiappini C., 2009, in IAU Symposium, Vol. 254, IAU Symposium, Andersen J., Nordströara, m B., Bland-Hawthorn J., eds., pp. 191–196

Chiappini C., Matteucci F., Romano D., 2001, ApJ, 554, 1044

Comparetta J., Quillen A., 2012, Arxiv preprint arXiv :1207.5753

Contopoulos G., Grosbol P., 1989, A&A Rev., 1, 261

Contopoulos G., Papayannopoulos T., 1980, A&A, 92, 33

Di Matteo P., Haywood M., Combes F., Semelin B., Snaith O. N., 2013, A&A, 553, A102

D'Onghia E., Vogelsberger M., Hernquist L., 2013, ApJ, 766, 34

Edvardsson B., Andersen J., Gustafsson B., Lambert D. L., Nissen P. E., Tomkin J., 1993, A&A, 275, 101

Forbes J., Krumholz M., Burkert A., 2012, ApJ, 754, 48

Friedli D., Benz W., 1993, A&A, 268, 65

Friedli D., Benz W., Kennicutt R., 1994, ApJLett, 430, L105

Fuchs B., 2001, A&A, 368, 107

Genel S. et al., 2008, ApJ, 688, 789

Gilmore G., Reid N., 1983, MNRAS, 202, 1025

Gingold R. A., Monaghan J. J., 1977, MNRAS, 181, 375

Goldreich P., Lynden-Bell D., 1965, MNRAS, 130, 125

Goldreich P., Tremaine S., 1981, ApJ, 243, 1062

Grand R. J. J., Kawata D., Cropper M., 2012, MNRAS, 426, 167

Grand R. J. J., Kawata D., Cropper M., 2014, MNRAS, 439, 623

Green D. A., 2014, in IAU Symposium, Vol. 296, IAU Symposium, Ray A., McCray R. A., eds., pp. 188–196

Guedes J., Callegari S., Madau P., Mayer L., 2011, ApJ, 742, 76

Hammer F., Puech M., Chemin L., Flores H., Lehnert M. D., 2007, ApJ, 662, 322

Haywood M., 2012, in European Physical Journal Web of Conferences, Vol. 19, European Physical Journal Web of Conferences, p. 5001

Holmberg J., Nordström B., Andersen J., 2009, A&A, 501, 941

Jones T., Ellis R. S., Richard J., Jullo E., 2013, ApJ, 765, 48

Julian W. H., Toomre A., 1966, ApJ, 146, 810

Jurić M. et al., 2008, ApJ, 673, 864

Kormendy J., 1979, ApJ, 227, 714

Krumholz M. R., 2014, ArXiv e-prints

Kubryk M., Prantzos N., Athanassoula E., 2013, MNRAS, 436, 1479

Lacey C. G., Fall S. M., 1985, ApJ, 290, 154

Lemson G., Virgo Consortium t., 2006, ArXiv Astrophysics e-prints

Lépine J. R. D., Acharova I. A., Mishurov Y. N., 2003, ApJ, 589, 210

Li Y., Mo H. J., van den Bosch F. C., Lin W. P., 2007, MNRAS, 379, 689

Lin C. C., Yuan C., Shu F. H., 1969, ApJ, 155, 721

Lindblad B., 1958, Stockholms Observatoriums Annaler, 20, 4

Little B., Carlberg R. G., 1991, MNRAS, 251, 227

Loebman S. R., Roškar R., Debattista V. P., Ivezić Ž., Quinn T. R., Wadsley J., 2011, ApJ, 737, 8

Lowe S. A., Roberts W. W., Yang J., Bertin G., Lin C. C., 1994, ApJ, 427, 184

Luck R. E., Lambert D. L., 2011, AJ, 142, 136

Lucy L. B., 1977, AJ, 82, 1013

Lynden-Bell D., Kalnajs A. J., 1972, MNRAS, 157, 1

Mark J. W.-K., 1976, ApJ, 206, 418

Martínez-Serrano F. J., Serna A., Doménech-Moral M., Domínguez-Tenreiro R., 2009, ApJLett, 705, L133

Matteucci F., 2012, Chemical Evolution of Galaxies

Meidt S. E., Rand R. J., Merrifield M. R., 2009, ApJ, 702, 277

Meidt S. E., Rand R. J., Merrifield M. R., Shetty R., Vogel S. N., 2008, ApJ, 688, 224

Merrifield M. R., Rand R. J., Meidt S. E., 2006, MNRAS, 366, L17

Mestel L., 1963, MNRAS, 126, 553

Minchev I., Chiappini C., Martig M., 2013, A&A, 558, A9

Minchev I., Chiappini C., Martig M., 2014, ArXiv e-prints

Minchev I., Famaey B., 2010, ApJ, 722, 112

Minchev I., Famaey B., Combes F., Di Matteo P., Mouhcine M., Wozniak H., 2011, A&A, 527, A147

Minchev I., Famaey B., Quillen A. C., Dehnen W., Martig M., Siebert A., 2012, A&A, 548, A127

Navarro J. F., White S. D. M., 1993, MNRAS, 265, 271

Nieva M.-F., Przybilla N., 2012, A&A, 539, A143

Nomoto K., Kobayashi C., Tominaga N., 2013, ARA&A, 51, 457

Pagel B. E. J., 2009, Nucleosynthesis and Chemical Evolution of Galaxies

Patsis P. A., Kalapotharakos C., Grosbøl P., 2010, MNRAS, 408, 22

Pfenniger D., 1990, A&A, 230, 55

Prantzos N., 2009, in IAU Symposium, Vol. 254, IAU Symposium, Andersen J., Nordströara, m B., Bland-Hawthorn J., eds., pp. 381–392

Ptolemaeus C., 150 ap. J.-C., Almageste

Quillen A., Minchev I., Bland-Hawthorn J., Haywood M., 2009, MNRAS, 397, 1599

Rix H.-W., Bovy J., 2013, A&A Rev., 21, 61

Romero-Gómez M., Masdemont J. J., Athanassoula E., García-Gómez C., 2006, A&A, 453, 39

Roskar R., 2010, PhD thesis, University of Washington

Roškar R., Debattista V. P., Quinn T. R., Stinson G. S., Wadsley J., 2008a, ApJLett, 684, L79

Roškar R., Debattista V. P., Quinn T. R., Wadsley J., 2012, MNRAS, 426, 2089

Roškar R., Debattista V. P., Stinson G. S., Quinn T. R., Kaufmann T., Wadsley J., 2008b, ApJLett, 675, L65

Sales L. V. et al., 2009, MNRAS, 400, L61

Sánchez-Blázquez P., Courty S., Gibson B. K., Brook C. B., 2009, MNRAS, 398, 591

Schönrich R., Binney J., 2009, MNRAS, 396, 203

Sellwood J., Binney J., 2002, MNRAS, 336, 785

Sellwood J. A., 1980, A&A, 89, 296

Semelin B., Combes F., 2005, A&A, 441, 55

Shevchenko I. I., 2011, ApJ, 733, 39

Shu F. H., 1970, ApJ, 160, 89

Silk J., Mamon G. A., 2012, Research in Astronomy and Astrophysics, 12, 917

Skokos C., Patsis P. A., Athanassoula E., 2002, MNRAS, 333, 847

Springel V., 2000, MNRAS, 312, 859

Springel V., 2005, MNRAS, 364, 1105

Springel V., 2010, MNRAS, 401, 791

Springel V., Di Matteo T., Hernquist L., 2005, MNRAS, 361, 776

Springel V., Yoshida N., White S. D. M., 2001, NewA, 6, 79

Steinmetz M., 2012, Astronomische Nachrichten, 333, 523

Teyssier R., 2002, A&A, 385, 337

Teyssier R., Moore B., Martizzi D., Dubois Y., Mayer L., 2011, MNRAS, 414, 195

Toomre A., 1981, in Structure and Evolution of Normal Galaxies, Fall S. M., Lynden-Bell D., eds., pp. 111–136

Übler H., Naab T., Oser L., Aumer M., Sales L. V., White S. D. M., 2014, ArXiv e-prints

van Dokkum P. G. et al., 2013, ApJLett, 771, L35

Van Kampen N. G., 1955, Physica, 21, 949

Wang Y., Zhao G., 2013, ApJ, 769, 4

Wielen R., Fuchs B., Dettbarn C., 1996, A&A, 314, 438

Yuan C., Kuo C.-L., 1997, ApJ, 486, 750